Università
Ca'Foscari
Venezia

Scuola Dottorale di Ateneo

Graduate School

Dottorato di ricerca

in Scienze Chimiche

Ciclo XXVIII

Anno di discussione 2016

Development and application of laser ablation ICP-MS for the study of glass and its degradation

SETTORE SCIENTIFICO DISCIPLINARE DI AFFERENZA: CHIM/01

Tesi di Dottorato di Serena Panighello, matricola 820253

Coordinatore del Dottorato

Prof. **Maurizio Selva**

Tutore del Dottorando

Prof. **Ligia M. Moretto**

Co-tutori del Dottorando

Prof. **Emilio F. Orsega**

Dr. **Johannes T. van Elteren**

"A new scientific truth does not, generally speaking, succeed because the opponents are convinced or declare themselves educated, however because they die and the new generations from the beginning learn about it as the truth"

Max Planck (1858 - 1947)

"In so far as a scientific statement speaks about reality, it must be falsifiable; and in so far as it is not falsifiable, it does not speak about reality"

Karl Popper (1902 – 1994)

ABSTRACT

The present PhD project aims to study a wide selection of glass artifacts from different periods, in order to obtain information on their chemical composition, to trace back their raw materials, to advance hypotheses on their geographic origin and technology and to investigate the phenomena of degradation. Among the various analytical techniques, LA-ICP-MS (laser ablation inductively coupled plasma mass spectrometry) seems to be ideally suited for the analysis of glass due to its high sensitivity (detection limits in the ng g^{-1} range for some elements) and large linear range (9-10 orders of magnitude), whereas very little or no sample preparation is necessary. Since LA-ICP-MS is a microanalytical technique for direct solid sampling of solid material (via a high-energy, pulsed laser beam of several µm to several hundreds of µm in size), the LA-ICP-MS may be considered "quasi" non-destructive.

The study is divided in different but complementary steps since several approaches are necessary to acquire a complete “picture” of the chemical composition of glass and the phenomena related to the degradation of glass. Laser ablation can be executed in different modes, i.e. ablation on a spot (drilling) or along a line (line scan or raster mode) for retrieval of multi-elemental concentrations in the bulk, depth profiles and elemental maps. Depth profiling protocols were developed to study glass degradation phenomena for superficial and more corroded glass artifacts using laser drilling, either with a low (1 Hz) or a high (10 Hz) pulse repetition rate during 50 s, thereby generating detailed spatial information for ca. 20 elements over a small depth (7.5 µm) or less-detailed spatial information for 50-60 elements over a large depth (75 µm). 2D maps were generated from high-repetition rate laser ablation pulses along parallel lines and relatively long ICP-MS acquisition times, resulting in lateral information. 3D maps were generated from low-repetition rate laser ablation on a grid (50 pulses per grid point at 1 Hz) and extremely short ICP-MS acquisition times, followed by peak integration and extraction of depth maps along the z-axis, resulting in lateral and depth-related information. Using these various laser ablation modes spatial information (lateral resolution of several µm and depth resolution as low as 150 nm) could be obtained for up to ca. 60 (major, minor and trace) elements simultaneously.

The interpretation of ancient glass analysis data depends critically on the comparability of one’s own data to published data sets. Therefore, high quality calibration for quantitative analysis, and simultaneous analysis of control samples such as certified reference materials or other commonly used reference glasses, is imperative. For quantitative analysis of glass a sum normalization calibration protocol was used for all laser ablation modes based on summation of the elements as their oxides to 100 wt % and using relevant glass standards. The laser ablation ICP-MS data can be combined with data from other analytical techniques in order to obtain supplementary information related to the material. EPMA (electron microprobe analysis) was used to investigate the morphology, to generate elemental maps for detailed and small surfaces and to study the crystalline phases (e.g. opacifiers and inorganic or organic compounds generated from corrosion). UV-Vis spectroscopy was used to study ancient colored glass; it is a straightforward, non-destructive, low-cost and in-situ applicable technique in identifying authentic material and to obtain information about the origin of the color.

A selection of different archaeological, historical and artificially aged glasses were analysed by laser ablation ICP-MS (and other techniques) in order to obtain quantitative elemental bulk concentrations, depth profiles and 2D and 3D maps related to the different raw materials used for glass fabrication, glass degradation phenomena, heterogeneity, etc. Case studies will highlight the elemental leachability of both archaeological/historical and contemporary/industrial glasses. Another case study will show the altered blue pigment smalt (cobalt glass particles) in 17th century paint cross-sections.

PUBLICATIONS AND PRESENTATIONS

First author publications

Panighello S., Kavčič A., Vogel-Mikuš K., Tennent N.H., Wallert A., Hočevar S.B. and van Elteren J.T. (2015) Investigation of smalt in cross-sections of 17th century paintings using elemental mapping by laser ablation ICP-MS, Microchem. J., 125; pp. 105-115.

Panighello S., van Elteren J.T., Orsega E.F. and Moretto L.M. (2015) Laser ablation ICP-MS depth profiling to study ancient glass surface degradation, Anal. Bioanal. Chem., 407; pp. 3377-3391.

Panighello S., Orsega E.F., van Elteren J.T., Šelih V.S. (2012a) Analysis of polychrome Iron Age glass vessels from Mediterranean I, II and III groups by LA-ICP-MS, J. Archaeol. Sci., 39; pp. 2945-2955.

Panighello S., Parello M.C., Orsega E.F. (2013) Investigation on medieval glass from Poggio Diana Castle (Sicily) by LA-ICP-MS and UV-VIS Reflectance Spectroscopy – Proceedings of the 16th Symposium on Mediterranean Archaeology, Florence, Italy, 1–3 March 2012, edited by Luca Bombardieri, Anacleto D'Agostino, Guido Guarducci, Valentina Orsi and Stefano Valentini. *B.A.R. International Series* 2581 (II), Oxford University.

Panighello S., Šelih V.S., van Elteren J.T., Sommariva G. and Orsega E. F. (2012b) Elemental mapping of polychrome ancient glasses by laser ablation ICP-MS and EPMA-WDS: a new approach to the study of elemental distribution and correlation", Proc. SPIE 8422, *Integrated Approaches to the Study of Historical Glass*, 842202 (September 1, 2012).

Other publications

Wood M., Panighello S., Orsega E. F., Robertshaw P., van Elteren J. T., Crowther A., Horton M., Boivin N. (2015) Zanzibar and Indian Ocean trade in the first millennium CE: the glass bead evidence, submitted to Archaeol. Anthropol. Sci. (under revision).

Van Elteren J.T., Izmer A., Šala M., Orsega E.F., Šelih V.S., Panighello S. and Vanhaecke F. (2013) 3D Laser Ablation-ICP-Mass Spectrometry Mapping for the Study of Surface Layer Phenomena – A Case Study for Weathered Glass, J. Anal. At. Spectrom., 28, pp. 994-1004.

Orsega E.F., Caminneci V., Panighello S., Rizzo M.S. (2013) Physicochemical analysis of medieval glass from 14th-16th centuries found in the Sciacca Castle site (Sicily) by LA-ICP-MS and UV-VIS Reflectance Spectroscopy – Proceedings of the 16th Symposium on Mediterranean Archaeology, Florence, Italy, 1–3 March 2012 edited by Luca Bombardieri, Anacleto D'Agostino, Guido Guarducci, Valentina Orsi and Stefano Valentini. *BAR International Series*, 2581 (II), Oxford University Press.

Arizio E., Orsega E.F., Sommariva G., Falcone R. and Panighello S. (2012) EPMA - WDS mapping: a new approach to the investigation of glass weathering, Sciences at Ca' Foscari, 1; pp. 9-13.

Van Elteren J.T., Panighello S., Šelih V.S. and Orsega E.F. Optimization of LA-ICP-MS mapping of glass with decorative, coloured features – Application to multi-elemental analysis of a polychrome glass vessel fragment from the Iron Age, in Recent Advances in Laser Ablation ICP-MS for Archaeology, Springer-Verlag GmbH, Berlin, Germany (in press).

Oral Presentations

"Investigation of glass leaching processes by laser ablation ICP-MS. A selection of case studies", Glass reflections – Glass in the Year of Light, 7 - 9 September 2015, Cambridge (UK).

"Application of laser ablation ICP-MS depth profiling methods for the study of African glass beads" Living glass, GlassAC, 10 - 12 September 2014, Durham (UK).

"Application of Laser Ablation ICP-MS depth profiling methods for the study of ancient glass artifacts", YISAC, 21st Young Investigators' Seminar on Analytical Chemistry, 25 – 28 June 2014, Pardubice (CZE).

"Application of Laser Ablation ICP-MS technique in the study of ancient glass" XIV Congresso Nazionale di Chimica dell'Ambiente e dei Beni Culturali, 2 - 5 June 2013, Rimini (IT).

"Application of Laser Ablation ICP-MS in the study of glass corrosion via depth profiling protocols" YISAC, 20st Young Investigators' Seminar on Analytical Chemistry, 26 – 29 June 2013, Maribor (SLO).

Poster Presentations

"Investigation of smalt in paint cross-sections of 17th century paintings using elemental mapping by laser ablation ICP-MS", Technart, 27 – 30 April 2015, Catania (IT).

"Physico-chemical characterization of glass beads from Zanzibar by laser ablation ICP-MS" Things that travelled – Mediterranean glass in the first millennium AD, 28 - 29 November 2014, UCL, London (UK).

"Application of laser ablation-ICP-MS for the study of ancient glass" GlassAC 2014, 10 - 12 September 2014, Durham (UK) *(ePoster).*

Awards

October 10, 2013
First prize for the best research work at the Ca' Foscari PhD opening Ceremony with the poster:
Application of Laser Ablation ICP-MS in the Study of Glass Corrosion.

June 25-28, 2014
First prize for the best oral presentation at the 21th YISAC (Young Investigators' Seminar on Analytical Chemistry) in Pardubice, Czech Republic.
Title of the presentation:
Application of Laser Ablation ICP-MS depth profiling methods for the study of ancient glass artifacts.

September 10-13, 2014
2014 Paul Award for the best presentation at the New Researchers Forum during the SGT (Society of Glass Technology) annual Conference in Durham (UK).
Title of the presentation:
Application of laser ablation ICP-MS depth profiling methods for the study of African glass beads

CONTENTS

LIST OF ABBREVIATIONS AND ACRONYMS

AAS	Atomic Absorption Spectroscopy
AFM	Atomic Force Microscopy
BSE	Back-Scattered Electrons
CMG	Corning Museum of Glass
CPS	Counts Per Second
EDX	Energy Dispersive X-Ray Analysis
EPMA	Electron probe Micro-Analysis
fs	femto-second
FT-IR	Fourier Transform Infrared Spectroscopy
HMG	High Magnesia Glass
ICP-MS	Inductively Coupled Plasma Mass Spectrometry
LA-ICP-MS	Laser Ablation Inductively Coupled Plasma Mass Spectrometry
LMG	Low Magnesia Glass
LMLK	Low Magnesia Low Potash
MC-ICPMS	Multicollector Inductively Coupled Plasma Mass Spectrometry
MRMs	Microanalytical Reference Materials
NIST	National Institute For Standards and Tables
OES	Optical Emission Spectroscopy
OM	Optical Microscopy
PCA	Principal Component Analysis
PIGE	Proton Induced Gamma Ray Emission
PIXE	Particle Induced X-Ray Emission
ps	pico – second
REEs	Rare Earth Elements
SE	Secondary Electrons
SEM	Scanning Electron Microscopy
SIMS	Secondary Ion Mass Spectrometry
SLS	Soda-Lime-Silica
SRM	Standard Reference Material
TEM	Transmission electron Microscopy
TOF	Time of Light Mass Spectrometer
UV	Ultra-Violet
Vis	Visible
XRF	X-Ray Fluorescence
XPS	X-Ray Photoelectron Spectroscopy
XAS	X-Ray Absorption Spectroscopy

CHAPTER 1

THE HISTORY AND SCIENCE OF GLASS:

A LOOK INSIDE

1.1. Introduction

Elemental analysis is the primary tool for the characterization of ancient glass samples with regards to their raw materials (sands and fluxes) and added compounds, such as decolourizers, chromophores and opacifiers and to support hypotheses about mineral sources (e.g. mineral origin of cobalt or copper). The data obtained can then be related to other groups of glasses in order to validate assumptions about their primary and secondary provenance and production period (for a concise historical overview of glass production see Appendix 1).

Glass is an "old" material as confirmed by the numerous types of glass used in its long history (5000 years) for multifarious applications. Each glass typology (e.g. soda-lime, cristallo, gold ruby, lead crystal, etc.) is associated with a practical problem to be solved, e.g. the soda Solvay process to manufacture soda ashes for the glass production was instigated by the insufficient availability of the natural source of soda ashes, i.e. certain plants.

Fingerprinting of ancient glasses by means of elemental composition analysis may help in a better understanding of the fabrication recipes and the application of these glasses in everyday life. However, the analysis of archaeological glass remains a challenge for artefacts with physical and/or chemical damages on their surface as a result of chemical instability of ancient glass under aggressive environmental conditions, often endured for centuries or even millennia.

For archaeological (buried) glasses, the ground moisture brings about leaching of alkali elements from glass, leading to glass weathering or corrosion as evidenced by discoloration, iridescence or other superficial alterations. Historical and modern glasses are affected by other types of deterioration, known as atmospheric corrosion and crizzling as a result of exposure to high levels of humidity and/or atmospheric pollution at particular pH values.

In general two degradation mechanisms are involved: de-alkalization (commonly referred to leaching) and network dissolution (Newton and Davison, 1989). However, these mechanisms are not associated with ancient artifacts only but also with contemporary or industrial glass. The chemical durability of these last glasses should be unquestionable as their use is often directly related to human health (as containers for drugs, foods, beverages, etc.). Nevertheless, they are also affected by deterioration phenomena and inherent leaching of different elements. So, the chemical resistance and weathering behavior of these allegedly inert industrial glasses (e.g. soda-lime, borate and crystal [lead glass]) is largely studied nowadays.

Looking at the development of glass over the two last centuries it can be concluded that it closely follows the developments in the field of chemistry and it is common practice nowadays to study the physico-chemical properties of glass and its degradation through analytical chemistry.

Any elemental analysis technique for the scientific investigation of glass should have relevant characteristics such as (i) minimal or no sample damage, (ii) minimal sample preparation, (iii) fast and simultaneous determination of major, minor and trace elements, (iv) providing spatially resolved information, on-surface (laterally) and/or in-depth, (v) determination of isotopic abundances (Resano *et al*., 2010). LA-ICP-MS fulfills most of these characteristics and is ideally suited for chemical analysis and compositional fingerprinting of different materials (glass, metal, ceramic, cement, etc.) and heterogeneous systems such as paintings (Resano *et al*., 2007; Marin *et al*., 2014) through microprobing or bulk analysis.

The potential of LA-ICP-MS to generate bulk chemical data of glass samples through microanalysis has been studied in a wide number of research projects, mostly concerning glass from the past (Cagno *et al*., 2012; De Raedt *et al*., 2001; Dussubieux *et al*., 2007; Wagner *et al*., 2008; and references therein). To obtain a complete "picture" of the chemical composition of glass and the phenomena related to the degradation of glass, laser ablation can be executed in different modes, i.e. ablation on a spot (drilling) or along a line

(line scan or raster mode) for retrieval of multi-elemental concentrations in the bulk, depth profiles and elemental maps. Depth profiling protocols can be useful to study glass degradation phenomena for both superficially and profoundly corroded glass artifacts using laser drilling.

2D maps are useful for a fast preliminary visual inspection of the correlated elements in a polychrome glass or to study superficial degradation. 3D maps generated through spot drilling can be useful to study the heterogeneity of glass and weathering phenomena.

Although LA-ICP-MS offers many features that can be helpful in the characterization of cultural heritage objects, there are still many practical and analytical problems to be solved such as e.g. the difficulty to analyze large samples and the complications in the accurate quantitative analysis through matrix-matched calibration standards and quantification protocols, especially associated with imaging. The use of complementary techniques such as OM, SEM and UV-Vis reflectance spectroscopy, next to multi-element mapping and depth profiling by LA-ICP-MS, may lead to a further "quasi" complete characterization of the sample. This is schematically illustrated in Figure 1.1.

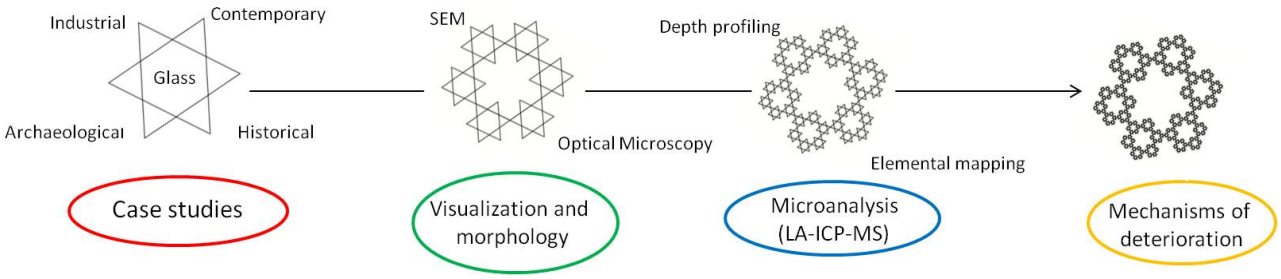

Figure 1.1. Schematic illustration of the sequence of steps in the glass degradation investigation, from degraded glass samples to interpretation of the analytical data. These steps are presented as a fractal system that grows and evolves in time, becoming more and more complex, giving more and more insight.

1.2. What is glass?

It is probably easier to start by recognizing that glass does not have a crystalline structure, it is a rigid material formed by heating a mixture of dry materials to a viscous state, then cooling the melting mass fast enough to prevent the formation of a regular crystalline structure. Glass has a disordered long-range structure, with short-range ordered arrangements inside. Being neither a liquid nor a solid, but sharing the features of both, glass is its own state of matter. Quartz is a crystal chemically similar to glass but in an ordered solid state.

Glass already exists in nature: the oldest known natural glass is contained in some meteorites that fell on Earth about 4500 million years ago. The most common natural glass on Earth is obsidian, produced when felsic lava extruded from a volcano cools rapidly with a minimum crystal growth. Figure 1.2 shows the silicate skeleton of a sponge, another natural glass, whose glassy fibers are of interest to researchers that study optical fibers and solar cells (Aizenberg *et al.*, 2004; Bullis, 1996).

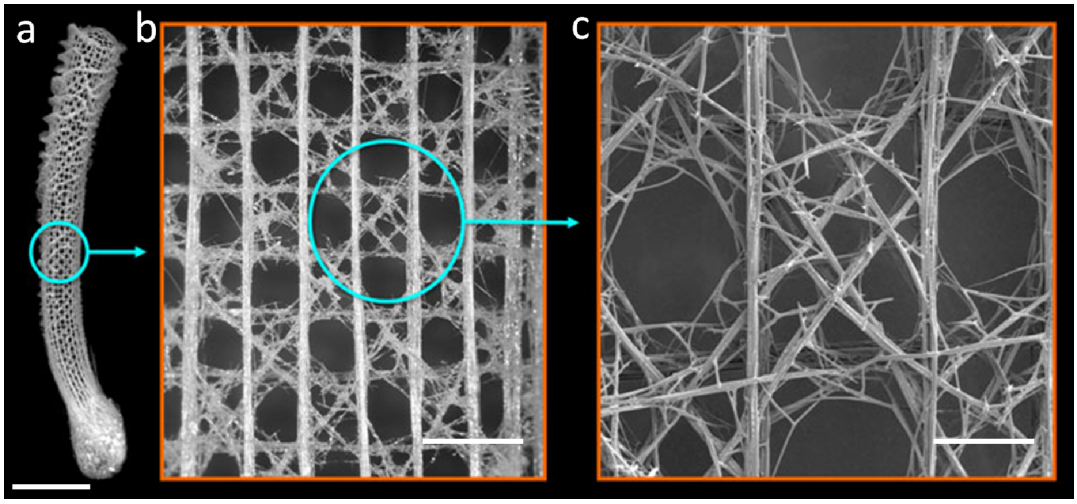

Figure 1.2. The Venus' flower basket, or Euplectella aspergillum sponge skeleton. It is one of the most primitive multicellular organisms still in existence with a grid-like skeletal architecture resembling a checkerboard pattern of open and closed latticework reinforced by diagonal bracings. Figure adapted from (http://wyss.harvard.edu/) and Weaver, *et al*, 2007. Scale bars: 5 cm (a); 5 mm (b); 2 mm (d).

The main constituents of the glass batch are: network formers, fluxes and stabilizers agents. Silicon dioxide is the most common former, but it melts at a very high temperature, thus a flux is added to allow the silicates structures melt at lower temperatures. Stabilizers keep the finished glass from dissolving, crumbling, or forming unwanted crystals; the most common is lime. The color of glass is due to metallic oxides, naturally present in the raw materials or intentionally added to the batch (see section 1.4).

1.3. Short historical overview of glass production

The glass technological history can be divided in two main phases, before and after the glass blowing invention, in the first century BC. This discovery had a strong influence on the cultural development of human society, as well as on its everyday life, with an impact probably similar to the one of plastic material nowadays.

Glass is a very ancient, artificial material and even today it is difficult to establish which civilization or culture can brag about its discovery, that probably happened accidentally. Pliny the Elder relates a legend, mentioned in the *Naturalis Historia,* regarding the discovery of glass that occurred by chance in the third millennium BC on the coast of Phoenicia. Some Phoenician merchants, docked in the area of River Belus in Palestine, lit a fire to cook on the banks, using as cooking base random blocks of Egyptian *nitrum* that was part of their cargo. Heating caused its reaction with the beach sand producing a glassy material (Pliny the Elder). It is only a legend, which cannot explain how the temperature reached in a simple campfire could lead to the melting of the silica sand with consequent formation of glass. However, it reflects some scientific aspects such as the mixing of raw materials necessary for making glass, silica sand as vitrifying agent and sodium carbonate (*nitrum*) as fluxing agent.

The real discovery of the glassy material in the form of *faïence* or glassy paste dates probably to the 3rd millennium BC in Mesopotamia (Iraq and Syria) and Egypt. At first the glass was used to produce jewelry or inlays to imitate hard or semiprecious expensive stones. Only around the 2nd millennium BC the production of different glass objects was introduced in Mesopotamia, in the form of vessels inspired by ceramic products and realized with the core-forming technique (Harden, 1981).

The first written information about the glassmaking process has been found in several Assyrian clay tablets from the 8th century BC discovered in the library of Nineveh palace, specifically in a tablet of

unknown origin (14th - 12th century BC) which describes a recipe for red glass, in a fragment from Babylon (12th century BC) and in a tablet from Bogazköi (Turkey). These sources confirmed that glass was obtained by melting a mixture of quartz stone (*immanakku*) and ash (*ahussu*) (Holmyard, 1931; Shortland and Tite, 2000; Moretti and Hreglich, 2013).

Late Bronze Age (1550-1200 BC). During the Late Bronze Age Egyptian and Mesopotamian glass was widely traded and exchanged, both as finished vessels, beads and other objects, often in bright polychrome styles and as monochrome glass ingots. Recent works (Shortland, 2005; Shortland *et al.,* 2007) identified systematic differences in trace element concentrations between Mesopotamian and Egyptian glass, further underlining the existence of an independent Egyptian glass industry.

Hellenistic (323 BC – 31 BC) and Roman (27 BC - 395 AD) time. During the Hellenistic and Roman time, glass was produced using *natron* (hydrated sodium carbonate) as a flux. In Roman times, thanks to the use of abundantly available natron and the invention of glassblowing that facilitated very much the shaping of objects, glass turned into an affordable commodity (Foy, 2000; Foy *et al,* 2000).

Late Roman (250 - 450 AD)/Byzantine period (from 330 AD). Only for the late Roman/Byzantine period, chemical analysis seems to evidence multiple glass making centers, most stemming from Egypt and the Levant. Based on the analysis of glass from large-scale production sites and from extended sets of finished objects, several chemically distinct groups have been classified (Freestone, 2005).

The use of mineral-natron based glass progressively ended with the end of the Western Roman Empire (5th AD) in Europe and of the Eastern Roman Empire (Byzantine). In the Middle-East and Mediterranean area (late 1st millennium AD) a different glass technology developed and during the Middle Age Roman glass was recycled. Historical sources underpin the assumption that political changes made it difficult to source Egyptian natron, and therefore alternative fluxes had to be found to maintain glassmaking (Shortland *et al.*, 2006). Countries at the East of the Roman Empire (Central Asia and India) had continued along the first millennium BC and the first millennium AD using plant ash as the main flux, with an apparently seamless tradition from Late Bronze Age plant-ash based recipes.

Middle Age. The Carolingian expansion led to the emergence of a new local glass industry based on wood ash as the main alkali. The change in raw material coincided with a change in glassmaking organization and distribution, from the long-distance network of the Roman Empire towards an excess of glass workshops. These latter produced – for almost a millennium – a lower quality glass. High-quality glass was imported in minute quantities from the Levant, such as the famous Hedwig beaker[1] which was probably brought to Europe during one of the crusades.

Venetian time. The Venetian monopoly in the trade with the Levant by the 12th - 13th century facilitated their exclusive access to high-quality plant ash sources, and led to the foundation of the famous Venetian glass industry (Freestone, 1992).

Potash glass, instead, with K_2O levels between 10 and 20%, was the glass type used for the stained glass windows in the cathedrals of Northern Europe, in particular from 1000 to 1400 AD.

Post Medieval Age. The low quality of the wood ash glass and the high price of the eastern glass, led to the development of new recipes and to the production of the well-known *façon de Venice* glass, a copy of the Venetian one, in particular in Amsterdam during the 15th century.

Soda glass production remained popular till the late 17th century, when the Englishman Ravenscroft invented lead crystal, with better optical properties. Lead crystal and Bohemian potash glass remained the most popular European production, until the industrial revolution and the discovery of the Solvay process (ca. 1860), leading to the production of affordable pure soda.

[1] http://www.britishmuseum.org/explore/highlights/highlight_objects/me/r/hedwig_glass_beaker.aspx

The great number of analyses regarding glass from the Mediterranean and European area reveals that until the end of the first millennium AD almost all the glass was soda-lime-silica and it can be divided into two categories based on the amount of Mg and K oxides. Generally Roman glass has values of these oxides less than 1.5%, while glass dating back to the Bronze Age and the Islamic and Venetian glass, contains values of Mg and K oxides higher than 1.5%; these distinct glasses are commonly labeled as "high magnesia" (HMG) and “low magnesia" (LMG) glasses. The glasses defined as "low magnesia" were produced using natron (hydrated sodium carbonate) as a flux, whereas those defined as "high magnesia" with a plant ash based flux (Shortland *et al.* 2006). The timeline in Figure 1.3 shows the used opacifiers, fluxes and decolourizes from the Bronze Age to the Islamic time.

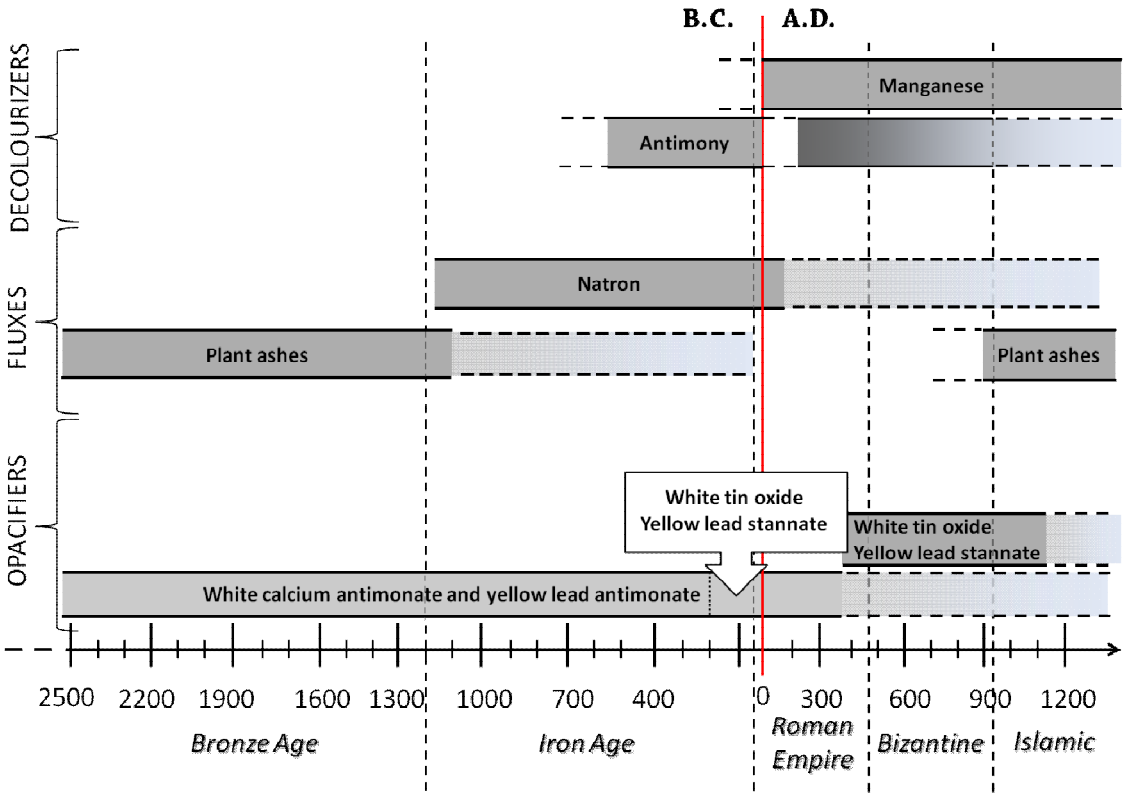

Figure 1.3. Timeline of the use of opacifiers, fluxes and decolourizers in the production of glass from the Bronze Age to the Islamic Age (Turner and Rooksby, 1961; Sayre and Smith, 1967; Henderson and Warren, 1983; Henderson, 1985; Nicholson and Henderson, 2000; Mass *et al*., 2002; Shortland, 2002; Tite *et al*., 2008; Lahlil *et al*., 2010).

1.4. Chemical composition of contemporary glass

In the Twentieth century the rapid industrial growth led to the use of very pure ingredients for glass manufacturing obtained by synthesis. This allowed an improvement to the phases of glass production and an easier work for the glassmakers.

The quality of glass products depends mainly on the careful choice of the raw materials used for their manufacture. This selection is based on different factors connected with the fact that glass consists of oxides and therefore the necessary raw materials are oxides or are compounds which give rise to oxides by decomposition in the heating phase. The oxides used in glass production can be discriminated in vitrifiers, fluxes and stabilizers, according to their function. The timeline in Figure 1.4 shows the used opacifiers and fluxes from the Islamic time to today.

Vitrifiers. The main vitrifying agents responsible for the structure of glass are SiO_2, B_2O_3 and P_2O_5. Silica is introduced through quartz sand, normally containing impurities such as feldspars, calcareous clay and iron oxides. Therefore, to obtain high-quality material, sand is subjected to a purification process. Based on the amount of impurities and the granulometry of the grains we can distinguish different kind of sands. It is worthwhile mentioning deposits of highly pure sands located in Fontainebleau and Nemour (South of Paris), along the border between France and Belgium and in Pola (Istria) used by glassmakers in Murano from the end of the 18th century until the 20th century (Moretti and Hreglich, 2013). From the 20th century the recipes of industrial glass (packaging and float glass) changed by introducing feldspar and nepheline to increase the content of alumina and silica because of their lower cost.

Boron oxide is added to glass and enamels to make it resistant to thermal shock (e.g. Pyrex® glass). It makes the glass more brilliant and improves the esthetic appearance. Phosphorus pentoxide is used in the production of phosphate glasses as well as opacifier.

Fluxes. The main fluxes, so-called because coadjuvants of the melting process, are sodium and potassium oxides. When the Solvay process was established (in 1861), the glass industry started to use synthetic soda instead of plant ashes as fluxing agent. With a similar process during the second half of the 19th century, potassium carbonate and nitrate were also produced. When potassium is used instead of sodium, there is an increase in viscosity, density and brilliance with a slight sacrifice in toughness and chemical resistance (Locardi, 1977). Lithium oxide is also used as fluxing agent; it increases the speed of the melt and gives a long working range to the glass but is more expensive than most of the other alkaline fluxes. It is used increasingly in the development of glass ceramics and in special glasses, e.g. the ones with a low expansion coefficient and UV and electrically resistant glasses.

Stabilizers. Calcium, magnesium, barium, lead, zinc, aluminum and boron oxides are used as stabilizing agents because they make the glass more durable and preserve it from dissolution caused by leaching or by the action of various chemical agents. The importance and the role played by these oxides were discovered during the beginning of the 19th century. In common glasses, calcium oxide is normally used since it makes glass mechanically and chemically more resistant. It can be introduced by natural components like limestone and dolomite, which are available in large deposits scattered all over the Europe (Moretti and Hreglich, 2013). Barium oxide was used in the past only by Chinese glassmakers since it was available in nature as whiterite. In the 19th century it was synthetically produced and it is used in particular for optical glasses. Lead oxide contributes to increase the density of the refractive index and the brilliance. Therefore, it is used for optical and electrical glasses and for the production of precious glass with a precise composition regulated by specific rules. Natural or synthetic compounds containing boron are increasingly used to produce technical glasses for special uses as pharmaceutical glass, low-thermal-expansion glass (Pyrex®) and glass fibres.

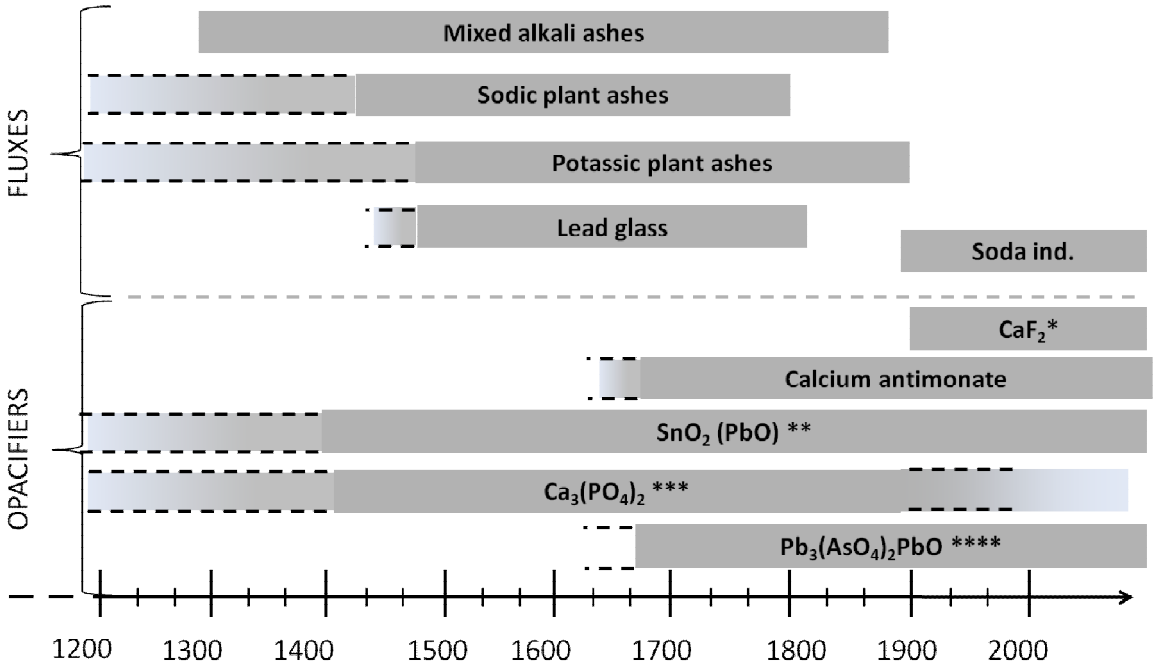

Figure 1.4. Timeline of several opacifiers and fluxes used in the production of glass from the Islamic Age to today (Verità, 2000). [*CaF_2 Calcium and sodium fluorides; **SnO_2 (PbO) Lead stannate (cassiterite in lead glass); ***$Ca_3(PO_4)_2$ Bone ash (calcium phosphate); ****$Pb_3(AsO_4)_2PbO$ Lead arsenate]

1.5. Colorants in glass

Glass coloration is a complex process that can be caused by the presence of: 1) crystalline phases visible with the naked eye (pigments); 2) colloidal particles (generally of metals ions or oxides, such as Cu, Ag, Au); 3) cations of the transition metals (ionic coloration).

Specifically color is a subjective physiological attribute of the human eye that is sensitive to electromagnetic radiation in the spectral range between 380 and 750 nm, defined as "visible light" (Weyl, 1951). The color of an object is given by reflected light in the visible wavelength range. The colors corresponding to the absorbed and reflected spectrum are called complementary. For example, an object that is able to absorb the radiation at 400-440 nm (violet light) will appear yellow-green; an object that absorbs in the range 600-700 nm (red light) appears blue-green. So the color of a glass depends on the absorption of the visible incident radiation (usually "white") by the glass and the interaction with the glass coloring agents.

The ionic colorants of glass are cations of transition metals (Ti, Cr, Mn, Fe, Co, Ni, Cu, ...) which, by absorbing part of the solar radiation (white light), give rise to the coloration. Some of these can impart different colors depending on their oxidation state.

Even a small change in the ligand field can cause variations in absorption and thus vary the color. In fact, the color in glass depends not only on the concentration of a specific transition element, and from its oxidation state (valence) that determines the number of electrons in the 3d orbitals, but also on the type of vitrifiers (SiO_2, B_2O_3, etc.) and fluxes (Na_2O, K_2O, etc.) and on the procedure of manufacture (furnace atmosphere with more or less oxidizing or reducing conditions). Henderson (2000) reports a series of factors that affect the coloring of the glass: 1) types of raw materials, their processing and furnace temperature (the use of a high temperature, 1400°C, influences the diffusion of the raw materials and coloring agents); 2) the use of transition metals ions; 3) the presence of opacifiers crystals; 4) the chemical environment and therefore the interaction between coloring elements and other elements in glass; 5) the

atmosphere of the furnace; 6) The cycle of heating and the highest temperature reached. Iron, for example, gives a green color to the glass as it is usually present as a mixture of ferrous ions Fe (II) (light blue) and ferric ions Fe (III) (yellow or brown). The value of the ratio Fe (II) / Fe (III) is strongly influenced by the presence of organic substances (plant material not combusted) in the batch, and the atmosphere of the melting furnace (Nassau, 2001). The cupric ions Cu (II) give to the glass a very bright aquamarine color. In Table 1.1 the main chromophores and the related colors are reported.

The Lycurgus cup (dichroic glass) is an example of man-made glass "back to the future": it is a first example of nanotechnology from Roman time. "The cup has a pea-soup green or jade-like appearance by reflected light but shows a deep magenta color by transmission" (Brill, 1965). The so-called Lycurgus effect is caused by the presence of colloidal gold and silver particles in glass. The size and density of the nano-particles affect the color.

Thanks to recent technologies some rare earths elements are also used to produce very colorful and high-brightness glass. An example is the use of didymium[2] salts which give a beautiful violet color to the glass. Neodymium oxides (Nd_2O_3) is used in glass melt from artists to obtain luminescent glass colors. The photoluminescence properties of rare earth elements are also of interest in several high-tech and environmental application areas, mainly concerning magnetic and optical devices.

Figure 1.5 shows two examples of contemporary colored glass art exhibited in big public contexts as the train station in Taiwan with the largest glass work in the world and the ceiling of a hotel in Las Vegas. For the ceiling in the Bellagio hotel two thousand hand-blown glass elements were installed.

Table 1.1. Principal chromophores and their coloring effects.

Color	Element/compound + chromophores ions
Blue	Cobalt oxide (Co^{2+})
Aquamarine	Copper oxide (Cu^{2+})
Light Blue	Iron oxide (Fe^{2+})
Amethyst	Manganese oxide Mn_2O_3 (Mn^{3+})
Violet	Manganese oxide with traces of cobalt oxide
Transparent yellow	Iron oxide (Fe^{3+}) - Uranium oxide (fluorescent)
Opaque yellow	Lead antimonate - Lead stannate - Cadmium sulfide - Colloidal solution of silver
Amber yellow	Sulphur-Iron (in reducing conditions) $Fe^{3+}(O^{2-})3S^{2-}$
Green	Chrome oxide (Cr^{3+}) - Iron oxide + Copper oxide - Cobalt oxide + Lead antimonate or stannate
Orange	Selenium - Cadmium sulfide and Cadmium sulpho-selenide
Red	Colloidal solutions of: Sulphur-cadmium selenide – Copper oxide or metal copper - Gold
Opaque white	Lead antimonate - Tin oxide - Lead arsenate - Calcium or sodium fluoride
Black	Mixture of iron oxides, manganese, cobalt and copper - Carbon and sulfur – manganese oxide (high concentration)

[2] Didymium in chemistry is a mixture of the rare earth elements praseodymium and neodymium.

Figure 1.5. The Dome of Light at Formosa Boulevard Station, Taiwan, designed by Italian artist Narcissus Quagliata, 2008 (a) and the glass sculpture "Fiori di Como" that hangs from the ceiling in Bellagio's lobby, Las Vegas, 1998 with the artist Dale Chihuly in front (b).

1.6. Glass degradation

1.6.1. Chemical stability

Glass resists very well to almost all chemical products at standard temperatures; this does not mean that it is not susceptible to attack, but that the reaction rates are generally very low and often decreasing in time. Glass is attacked to a significant degree, particularly at higher temperatures, only by hydrofluoric acid, strong alkaline solutions and concentrated phosphoric acid. Glass but even ceramic are electrically insulating materials where the chemical attack on the surface is mainly by acid-base type rather than electrochemical corrosion (White, 1992).

The attack of acids or acidic aqueous solutions on a glass can be considered a pure ion exchange between alkaline ions of the glass and H^+ (or H_3O^+) ions of the acid agent (Figure 1.6 - ACID). The speed of this attack, which involves the removal of alkali from the surface layers of the glass, is conditioned by the diffusion rate of alkali ions. By reducing the latter, it is possible to increase the glass chemical durability, e.g. by lowering the diffusivity of sodium ions by addition to the glass of alkaline-earth ions. This explains why it is important to introduce lime or another stabilizer agent in the bulk. No reaction occurs between the H^+ ions and the siliceous lattice until the constituent ions are strongly bound and free of any possibility of migration. The acid attack of the glass, linked to the diffusion mechanism, decreases as a function of the square root of the contacting time; consequently, the chemical durability of glass improves with time (Locardi, 1977).

The outstanding chemical durability of certain borosilicate glasses is due to their particular structure. These glasses have in fact a silica matrix in which a second phase of sodium borosilicate is dispersed. The reactivity towards acid solutions is similar to that of the silica lattice, because the borosilicate phase is practically impenetrable due to the high pressure required to force liquid water within so narrow capillaries.

The attack by alkaline solutions is determined by another mechanism. In this case the OH^- ion plays a determining role; it reacts with the lattice by breaking the oxygen bridges (Figure 1.6 - BASIC). If the glass remains in contact with the basic solution, this mechanism can lead to the formation of silicic acid anions ($SiO_4H_3^-$), which pass into solution, with a progressive total destruction of the lattice. The glass alkaline attack is a chemical reaction which is a linear function of time (and therefore more significant than the acid attack).

With regards to the interaction of pure water with glass: initially it takes place according to a mechanism of exchange between the H^+ ions of the water and the alkali ions of the glass; later, however, when the pH of the water increases due to the decrease of H^+ ions, the attack becomes alkaline with the breaking of the lattice and the dissolution of the glass. The prevalence of one of these mechanisms is also a function of the glass chemical composition and temperature.

1- An hydrated (de-alkalinized) silica layer is formed:

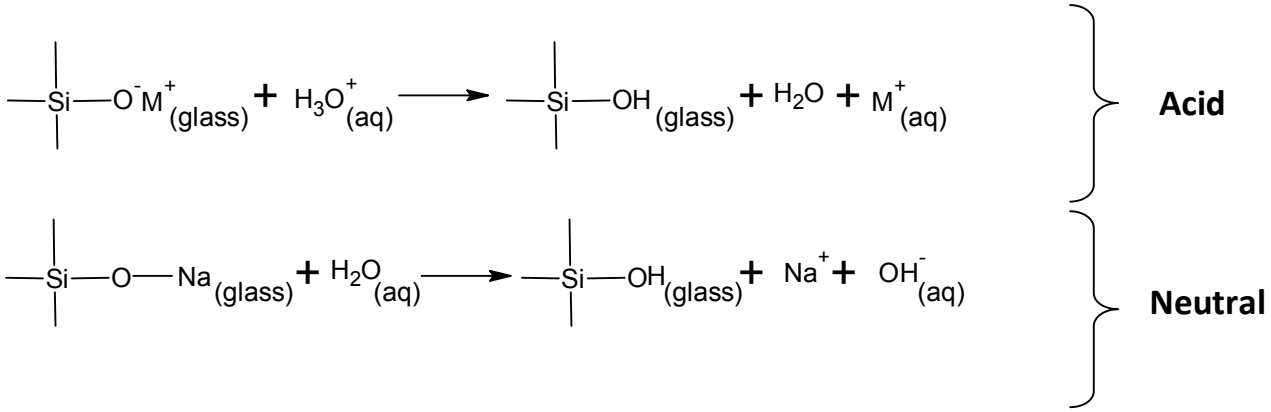

2- Dissolution of the silica network (hydrolysis):

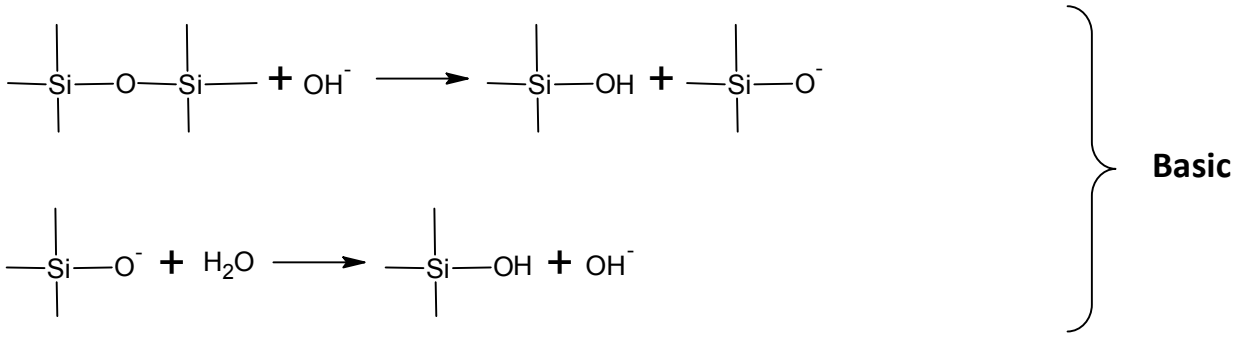

Figure 1.6. Schematic diagram of the glass degradation processes.

The atmospheric alteration of glass, in particular of plates, is associated with the water vapor contained in the air that is adsorbed on the glass surface, forming a uniform film which in normal conditions has a thickness of a few molecules of water. However, corrosion is negligible unless the air humidity is so high that partial condensation on the glass occurs. A subsequent increase of the temperature results in the evaporation of water from the glass surface that can lead to a dangerous increase in the alkalinity of the film if the alkaline solution is not removed, and therefore to a more energetic corrosive action. As a result, the glass surface can become iridescent or opaque.

1.6.2. Weathered archaeological glass

Glass found at archaeological excavations is normally exposed to particularly unfavorable environmental conditions. Depending on the physico-chemical proprieties of the burial environment and on the chemical composition of the glass itself, the appearance of the artifact can range from pristine to so heavily degraded that it is impossible to recognize because of total transformation into corrosion products. The

degradation of archaeological glasses is generally called weathering. Water is the primary cause of deterioration of silicate glasses and is the trigger of a series of reactions.

The first step is the penetration of molecular water into the glassy network through hydrolysis/condensation reactions (Paul, 1977; Bunker, 1994), inducing breaking of siloxane bonds. In the second step the most mobile cations (e.g. Na^+ and K^+) are slowly leached out and replaced by hydrogen ions from the water (Schreiner, 1991). Since the mobility of cations depends on their charge, size and on the glass composition itself, some glass types are more resistant to leaching than others; however, under the proper conditions any glass can show signs of degradation. When there are free water molecules inside the leached layer that are not replaced, the local pH increases (pH > 9). This can induce the attack of the silicate network by hydroxyl ions and the glass weathering. This leached layer, also called silica-rich, alkali deficient layer or hydrogen glass, has a lower density than the pristine/original glass (Paul, 1977; Panighello *et al*., 2015). If no change in environmental conditions occurs, this leached layer will gradually increase in thickness.

It is interesting to note that this layer occurs in a cyclic manner with additional layers every few years, generating a laminar structure. There are different theories that try to explain this process. One is related to physical stress generated at the interface between altered and healthy glass causing the formation of cracks. This process exposes the healthy glass to the weathering mechanism. It has also been suggested that the layering is caused by periodic or cyclic changes, such as seasonal variations in temperature and rainfall (Brill, 1961; Nuyts *et al.*, 2013).

Weathered glass can have a wide range of visual appearances from commonly found dulling, iridescence and opaqueness, to a total loss of the glassy nature with pits, cracks and discoloration. Generally the degradation of a glass is the combination of several of these manifestations.

1.7. The application of analytical chemistry to archaeological glasses

Archaeometry (or Archaeological Science) is the science of acquisition and interpretation of technical information, both qualitative and quantitative, that are implied in all the archaeological finds and their contexts, but that are evident only with the methodologies of the exact sciences. The chemical, physical, physico-chemical, mineralogical, petrographic, etc. results thus obtained for the archaeological artifacts will reveal a wealth of information related to chemical composition, physico-chemical parameters and manufacturing techniques. In turn the data may solve archaeological conundrums such as the provenance of the artifacts and of their raw materials, their trade routes, as well as their economic value. In the history of analytical chemistry many great scientists included the analysis of archaeological objects as part of their process of discovery.

The development of instrumental measurement techniques during the 1920s and 1930s such as optical emission spectroscopy (OES) gave new analytical methods applicable to archaeological chemistry. The immediate postwar years were alleged by a wide range of analytical techniques as X-ray analysis and electron microscopy, neutron activation analysis and mass spectrometry. During the late 1950s and early 1960s, the “New Archaeology” had a significant role on the use of analytical chemistry in the field because the approach to archaeology became more statistical and quantitative (Trigger, 1989).

“*No analytical technique has built in interpretative value for archaeological investigations; the links between physical properties of objects and human behavior producing the variations in physical states of artifacts must always be evaluated*” (DeAtley and Bishop, 1991).

In the case of glass, the material studied in this thesis, the investigation of the chemical composition allows to trace back the raw materials used for manufacturing and sometimes to advance reliable hypotheses on the area of origin. Fundamental aspects of glass production in the ancient world are still open to questions, in particular those regarding some phases of the production cycle (e.g. about the retrieval and processing of raw materials), the dissemination of the technological knowledge and the issue concerning the so-called "primary and secondary factories".

"*The inevitable result of these studies is an ever-increasing admiration for the glassmakers of early times. While everyone has long admired the manual dexterity and the skill and patience of these craftsmen, we are just beginning to realize that early experimentalists in glass also had an unexpected delicacy of control, if not a comprehension, of some of the complicated chemical factors involved in their processes*." (Brill, 1968)

The application of analytical chemistry in archaeology has a great significance, especially for glass. It was overrated for years because unlike ceramics (the most abundant available antique material), it is difficult to use for dating. The only way to obtain information regarding this man-made material is to differentiate the chemical compositions.

1.8. Analytical techniques

To provide an up-to-date description of the physico-chemical methods suitable for determining the composition of glass it is significant to take in consideration that each analytical method presents its own peculiar advantages and limitations. We already know that the main differences between glasses from diverse periods are more evident in the minor and trace elemental composition rather than in the major elemental composition, limiting the use of spectroscopic techniques such as colorimetric, atomic absorprion, Raman, FT-IR spectroscopy.

Analytical investigation of an archaeological artifact via chemical methods has its limitations instigated by *i*) artifact "health", i.e. the condition of an artifact is often far from ideal, being small, fragmentary, extremely degraded, contaminated from burial or storage media or often restored with unknown materials when it comes from a museum; *ii*) sampling restrictions, i.e. due to aesthetic, art-historical, monetary, etc. considerations artifacts cannot be damaged, thereby excluding invasive techniques including digestion (for bulk analysis with AAS or ICP-MS/OES) and destructive microanalytical techniques such as LA-ICP-MS; *iii*) sample heterogeneity and complexity, i.e. due to degradation and corrosion compounds or to a combination of several different materials accurate analysis is difficult; iv) instrumental selectivity and sensitivity, i.e. the need to use multi-element instrument with sufficiently low detection limits (low $\mu g\ g^{-1}$ range) and the availability of suitable (matching the sample composition as closely as possible) glass standards.

Without physical sampling of the object, i.e. using non-destructive microanalytical techniques, it is difficult to obtain reliable, quantitative information due to the presence of weathering or corrosion compounds on the surface. Despite these drawbacks the most used multi-elemental techniques for glass and glazes microanalysis are SEM-EDX (e.g., Lahlil *et al.,* 2010b), PIXE-PIGE (e.g., Šmit *et al.*, 2012), EPMA (e.g., Arletti *et al.*, 2010; Alberta *et al.*, 2011), TEM (e.g., Mata *et al.,* 2002; Lombardo *et al.,* 2013), micro-XRF (e.g., Naes *et al.*, 2008), SIMS (e.g., Rutten *et al.*, 2009) and LA-ICP-MS (e.g., Duwe and Neff, 2007; Pérez-Arantegui *et al.*, 2008; Robertshaw *et al.,* 2010). Often a combination of techniques is used to investigate elemental composition or distribution (e.g., Sokaras *et al.*, 2009; Carmona *et al.,* 2010; Šmit *et*

al., 2013). Looking at the techniques in detail it become obvious that each and every technique has its strengths and weaknesses denoted by one or more of the following characteristics: spatial resolution, range of detectable elements, feasibility of quantitative analysis, detection limits, dynamic range, required sample preparation, cost and accessibility (Behrends and Kleingeld, 2009).

The best technique for answering at all the questions related to the investigation of an object does not exist, but a combination of diverse techniques may yield the majority of the required information.

The still "young" LA-ICP-MS technique offers several possibilities for glass microanalysis, i.e. it is able to generate information on the bulk composition and spatial distribution using different measurement and data processing protocols which are still under heavy development.

LA-ICP-MS uses a high-energy laser to sample material from the object, in the order of µg-amounts, and as such can be regarded micro-destructive. However, the traces/craters generated by the laser upon ablation are invisible to the naked eye; in addition the analysis can be carried out directly on the object without any sample preparation. The different LA-ICP-MS protocols are directly related to the settings of the LA-ICP-MS system.

Ablation can be performed in two different modes, viz. spot (in-depth analysis) and line (lateral analysis). By focusing on a spot with a microscope and built-in CCS camera one can select the exact location for ablation and e.g. analyze local inclusions. The laser beam diameter can be varied from 5 µm or, even less (Van Malderen *et al*., 2015) to around 200-300 µm. Spot drilling is used for retrieval of deeper elemental information after drilling through the corroded layer and can be used to obtain bulk elemental concentrations. By choosing different LA spot drilling procedures, based on different laser pulse rates and ICP-MS acquisition times, element-depth relationships can be established for superficial layers. Line scanning can be used to collect elemental information along a line on the surface for better accuracy as "smoothing" and thus averaging occurs which is helpful for analysis of inhomogeneous samples. Furthermore, line scanning, or more specifically rastering, may also be used to generate 2D element maps. Under specific circumstances some authors (Gratuze *et al*., 2001) prefer to use line scanning instead of spot drilling for bulk analysis because of the better sensitivity (more details are given in Chapter 2) and the lower elemental fractionation effect (Neff, 2003).

Some disadvantages on the use of line scanning are connected with corrosion, that can become a major factor influencing the accuracy of the LA-ICP-MS data (Dussubieux *et al*., 2009). Although LA-ICP-MS facilitates the removal of superficial layers by performing pre-ablation passes, this may not result in accurate bulk analytical data when the alteration layer is more than a few micrometers thick.

Elemental mapping by LA-ICP-MS, compared to the commonly available contenders such as SEM-EDX and micro-XRF, has a lower lateral resolution than SEM-EDX but is far superior with regards to obtainable low detection limits, whereas LA-ICP-MS is relatively comparable to micro-XRF but with better accuracy, precision, sensitivity and analysis speed (Naes *et al.*, 2008). Figure 1.7 summarizes the detection limits and spatial resolutions of different microanalytical techniques.

With recent technical and instrumental improvements and improved 2D mapping protocols and data deconvolution approaches, lateral resolutions ≤ 1 µm have been demonstrated for LA-ICP-MS (Wang *et al.*, 2013; Van Malderen *et al.*, 2015).

Nevertheless, the Achille's heel of LA-ICP-MS remains the calibration procedure. It needs matrix-matched solid materials with a similar composition as the sample and the use of an internal standard to correct for ablation yields. This was studied by several authors (Gratuze *et al*., 2001; van Elteren *et al*., 2009; Neff, 2003; Liu *et al*., 2008) and is still under development.

Despite the fact that LA-ICP-MS has a relatively low native lateral resolution, generates micro damage on the sample's surface, is not designed for large samples (even though it is possible to design larger cells or sample in loco (Glaus *et al*., 2012; Glaus *et al*., 2013)), the technique is very versatile with a very large

dynamic range (analysis of concentrations from ng g^{-1} to % *w*/*w*), and the potential for imaging on scales from several µm to tens of mm (Woodhead *et al.*, 2007). Moreover the use of high resolution ICP-MS or TOF ICP-MS may offer greater opportunities for the analysis of isotopic ratios (Mao *et al*., 2011; Glaus *et al*., 2013; Kappel *et al*., 2013; Borovinskaya *et al*., 2013).

Finally, coupling LA-ICP-MS with another technique, e.g. SEM-EDX, allows the full characterization of a glass sample. The identification and structure of crystalline phases can be investigated by SEM-EDX as far as the morphology of the sample and the corroded layers are concerned, whereas minor and trace elements can be determined by LA-ICP-MS in different modes for bulk, surface, inclusions and depth profiling analysis.

Other improvements of the technique are under investigation with the use of lower wavelengths as femtosecond laser to reduce elemental fractionation (Russo *et al*., 2001; Günther and Hattendorf, 2005; Fernández *et al*., 2007).

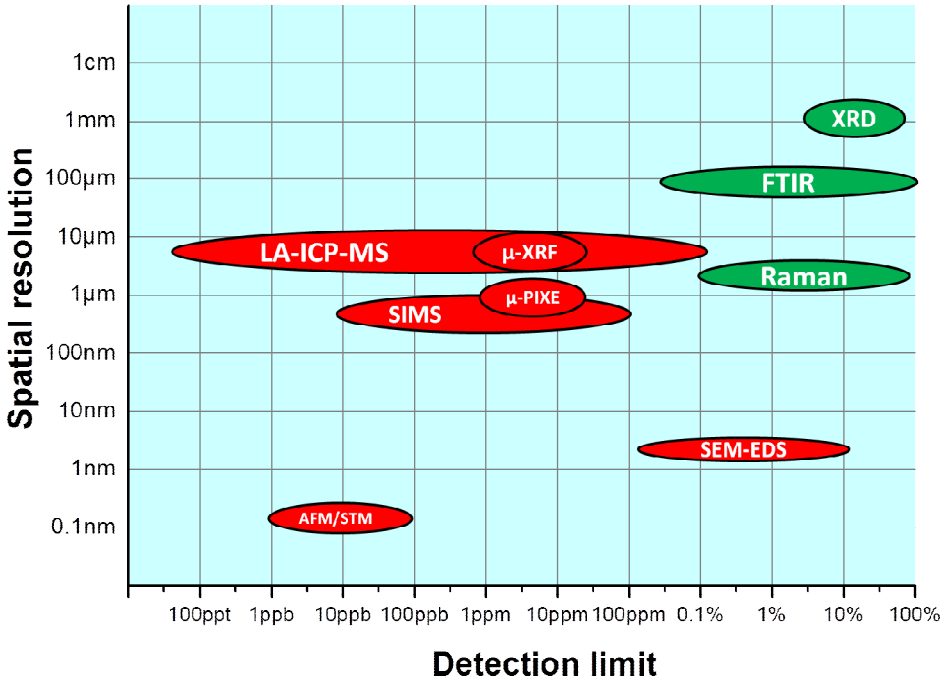

Figure 1.7. Detection limit vs spatial resolution for chemical composition/speciation techniques (red color) and techniques that are used for structural information (green color).

1.9. Aim of the study

The aim of this work is the development and application of spectroscopic techniques for the analysis of glass artifacts from different periods. Because the main composition of glass varies with the period/area of origin, it is in principle possible to assess the authenticity or the provenance of historical glass artifacts on the basis of their elemental composition. However, this is often challenging as glass was largely made by recycling of old glass through a variety of technological production steps (e.g. primary and secondary glass production), resulting in potentially "scrambled" data due to multiple sources. Furthermore, data can be affected by degradation, even if the surface looks pristine, adding to the data interpretation difficulties.

However, the quality of the glass compositional data retrieved not only depends on the "fabrication and environmental history" of the artifact, but to a large extent also on the characteristic performance of the analytical technique. Limitations may arise from the selectivity and sensitivity of the analytical technique for retrieval of quantitative, multi-element concentration data on the major, minor and trace level.

LA-ICP-MS, applied for most of the work presented in this thesis, is ultimately suitable for the direct elemental analysis of glass due to its multi-elemental characteristics (simultaneous analysis of 50-60 elements), high sensitivity (down to the low mg kg^{-1} level or even lower under certain operating conditions) and microanalytical probing possibilities (laser beam diameters as low as few µm may be selected). The last feature warrants the application of LA-ICP-MS for spatial elemental analysis, both laterally and in depth. By combining various laser ablation modes (Chapter 2), i.e. spot drilling and line scanning, depth profiling (Chapter 3), 2D (Chapter 4) and 3D (Chapter 5) imaging was elaborated for the study of surface-related degradation phenomena. The various laser ablation modes, and their associated elemental distribution patterns, were applied to the study of ancient, corroded glass to get insight into degradation phenomena. A special case of glass corrosion was studied by 2D mapping of degraded smalt particles (blue glass pigment) in paint cross-sections of several discolored 17th century paintings (Chapter 6) to highlight the quantitative performance characteristics of LA-ICP-MS of very small artifacts (size smalt particles in the order of 10-20 micrometer).

Furthermore, conventional quantification protocols were modified and optimized for imaging purposes based on a sum normalization protocol that sums all the elemental concentrations as their oxides to 100 wt %. Subsequent retrieval of the alteration layer density vs. depth for degraded glass surfaces was achieved with the modified quantification protocol (Chapter 3). To aid in the initial selection of the optimal LA-ICP-MS conditions for spatial resolution and analysis time in 2D imaging, a digital image of a polychrome glass was subjected to virtual 2D mapping, using existing software which simulates the actual LA-ICP-MS mapping process (Chapter 4).

1.10. References

Aizenberg J., Sundar V.C., Yablon A.D., Weaver J.C. and Chen G. (2004) Biological glass fibers: Correlation between optical and structural properties, PNAS, vol. 101, 10; pp. 3358-3363.

Alberta S., Gianmario M., Valentina P. (2011) The stained glass window of the southern transept of St. Anthony's Basilica (Padova, Italy): study of glasses and grisaille paint layers. Spectrochim Acta B 66; pp. 81-87.

Arletti R., Maiorano C., Ferrari D., Vezzalini G., Quartieri S. (2010) The First Archaeometric Data on Polychrome Iron Age Glass from Sites Located in Northern Italy, J Archaeolog Sci 37; pp. 703-712.

Behrends T. and Kleingeld P. (2009) Bench-top micro-XRF – a useful apparatus for geochemists? Geochemical News 138.

Borovinskaya O., Hattendorf B., Tanner M., Gschwinda S., Günther D. (2013) A prototype of a new inductively coupled plasma time-of-flight mass spectrometer providing temporally resolved, multi-element detection of short signals generated by single particles and droplets, J. Anal. At. Spectrom., 28; pp. 226-233.

Brill R.H.. (1961) The record of time in weathered glass, Archaeology 14 no. 1; pp. 18-22.

Brill R. H. (1965) The Chemistry of the Lycurgus Cup, Comptes Rendus, VII e Congrès International du Verre, Brussels, v. 2, paper 223; pp. 1-13.

Brill R.H. (1968). The Scientific Investigation of Ancient Glasses, Studies in Glass History and Design, papers read to Committee B sessions of the VIIIth International Congress on Glass, London, July 1-6, 1968, Sheffield, U.K.: Society of Glass Technology, n.d. [1969/1970], pp.47-68.

Brill R., (with a contribution by Brandt A. Rising) (1999) Chemical Analyses of Early Glasses, vol. 1-2. The Corning Museum of Glass, Corning, New York.

Bullis K. (2006) Silicon and Sun, MIT Technology Review.

Bunker B.C. (1994) Molecular mechanisms for corrosion of silica and silicate glasses. J Non-Cryst Solids 179(C):300–308.

Cagno S., Favaretto L., Mendera M., Izmer A., Vanhaecke F. and Janssens K. (2012). Evidence of early medieval soda ash glass in the archaeological site of San Genesio (Tuscany). J Archaeol Sci 39(5): 1540-1552.

Carmona N., Ortega-Feliu I., Gomez-Tubio B., Villegas M.A. (2010) Advantages and disadvantages of PIXE/PIGE, XRF and EDX spectrometries applied to archaeometric characterisation of glasses. Mater Charact 61; pp. 257-267.

DeAtley S. P. and Bishop R. L. (1991). Toward an integrated interface for archaeology and archeometry. In The Ceramic Legacy of Anna O. Shepard, eds. Bishop, R. L. and Lange, R. W., Boulder, CO, University Press of Colorado, pp. 358–380.

De Raedt I., Janssens K., Veeckman J., Vincze L., Vekemans B. and Jeffries T.E. (2001). Trace analysis for distinguishing between Venetian and façon-de-Venise glass vessels of the 16th and 17th century. J Anal Atom Spectrom 16(9): 1012-1017.

Dussubieux L., Golitko M., Ryan Williams P. and Speakman R.J. (2007). In Glascock M.D., Speakman R.J. and Popelka-Filcoff R.S. (Eds.) Archaeological Chemistry, Analytical techniques and Archaeological Interpretation 968: 349-363.

Dussubieux L., Robertshaw P. and Glascock M.D. (2009). LA-ICP-MS analysis of African glass beads: Laboratory inter-comparison with an emphasis on the impact of corrosion on data interpretation. Int J Mass Spectrom 284(1-3): 152-161.

Duwe S. and Neff H. (2007) Glaze and slip pigment analyses of Pueblo IV period ceramics from east-central Arizona using time of flight-laser ablation-inductively coupled plasma-mass spectrometry (TOF-LA-ICP-MS). J Archaeolog Sci 34; pp. 403-414.

Fernández B., Claverie F., Pécheyran C. and Donard O.F.X. (2007) Direct analysis of solid samples by fs-LA-ICP-MS, Trends in Analytical Chemistry, Vol. 26, No. 10; pp. 951-966.

Foy D. (2000) Technologie, géographie, économie: les ateliers de verriers primaires et secondaires en Occident. Esquisse d'une évolution de l'Antiquité au Moyen Âge, in Ateliers primaires et secondaires de verriers du second millénaire av. J.-C. au MoyenÂge (ed. M.-D. Nenna), Travaux de la Maison de l'Orient Méditerranéen 33, Lyon; pp. 147-170.

Foy D., Vichy M., and Picon M. (2000) Lingots de verre en Méditerranée (IIIe s. av. J.-C.- VIIe s. ap. J.-C.), approvisionnement et mise en oeuvre; les données archéologiques et les données de laboratoire, Annales of the 15th AIHV Congress, Venise-Milan, 1998, Lochem; pp. 51-57.

Freestone I. (1992) Theophilus and the composition of medieval glass. In: P. Vandiver et al. (eds.), Materials Issues in Art and Archaeology III, pp. 739-745.

Freestone I. (2005) The provenance of ancient glass trough compositional analysis, Mater. Res. Soc. Symp. Proc. Vol. 852.

Glaus R., Koch J. and Günther D. (2012) Portable Laser Ablation Sampling Device for Elemental Fingerprinting of Objects Outside the Laboratory with Laser Ablation Inductively Coupled Plasma Mass Spectrometry, Anal. Chem. 84; pp. 5358-5364.

Glaus R., Dorta L., Zhang Z., Ma Q., Berkec H. and Günther D. (2013) Isotope ratio determination of objects in the field by portable laser ablation sampling and subsequent multicollector ICPMS, J. Anal. At. Spectrom. 28, 801; pp. 801-809.

Gratuze B., Blet-Lemarquand M. and Barrandon J.N. (2001) Mass spectrometry with laser sampling: A new tool to characterize archaeological materials, J. Radioanal. Nucl. Chem., 247; pp. 645–656.

Günther D. and Hattendorf B. (2005) Solid sample analysis using laser ablation inductively coupled plasma mass spectrometry, Trends in Analytical Chemistry, Vol. 24, No. 3; pp. 255-265.

Harden D.B. (1981) Catalogue of Greek and Roman Glass in the British Museum. In: Core and Rod-formed Vessels and Pendants and Mycenaean Cast Objects, vol. 1. British Museum Publications.

Henderson J., Warren S.E. (1983) Analysis of Prehistoric lead glass. In: Aspinall A, Warren SE (eds) Proceedings of 22nd International Symposium on Archaeometry, Schools of Physics and Archaeological Sciences, Bradford; pp. 168-180.

Henderson J. (1985) The raw materials of early glass production. Oxford J Archaeol 4; pp. 267-291.

Henderson J. (2000) The Science and Archaeology of Materials. An Investigation of Inorganic Materials, William E. Boyd Ed. , Southern Cross University, Great Britain.

Holmyard Eric John (1931). Makers of Chemistry, Oxford, p. 14.

Kappel S., Boulyga S.F., Dorta L., Günther D., Hattendorf B., Koffler D., Laaha G., Leisch F., Prohaska T. (2013) Evaluation strategies for isotope ratio measurements of single particles by LA-MC-ICPMS, Anal. Bioanal. Chem., 405; pp. 2943-2955.

Lahlil S., Biron I., Cotte M., Susini J., Menguy N. (2010a) Synthesis of calcium antimonate nano-crystals by the 18th Dynasty Egyptian glassmaker. Appl Phys A 98; pp. 1-8.

Lahlil S., Biron I., Cotte M., Susini J., Menguy N. (2010b) New insight on the in situ crystallization of calcium antimonate opacified glass during the Roman period. Appl Phys A: Mater Sci Process 100; pp. 683-692.

Liu Y., Hu Z., Gao S., Günther D., Xu J., Gao C., Chen H. (2008) In situ analysis of major and trace elements of anhydrous minerals by LA-ICP-MS without applying an internal standard, Chemical Geology, 257; pp. 34–43.

Locardi B. (1977) Aspetti chimico-fisici riguardanti la produzione del vetro in: Vetri - Quaderni di chimica applicata (Eds.) Scarinci G., Toninato T. and Locardi B., Casa Editrice Ambrosiana, Milano (Italy), pp. 77-96.

Lombardo T., Gentaz L., Verney-Carron A., Chabas A., Loiseb C., Neff D., Leroy E. (2013) Characterization of complex alteration layers in medieval glasses. Corros Sci 72; pp. 10-19.

Mao X., Bol'shakov A. A., Choi I., McKay C.P., Perry D.L., Sorkhabi O., Russo R.E. (2011) Laser Ablation Molecular Isotopic Spectrometry: Strontium and its isotopes, Spectrochimica Acta Part B 66; pp.767-775.

Marin E., Padró A., Miquel A. and Garcia J.F. (2014) Characterization of paintings by laser ablation-inductively coupled plasma-mass spectrometry, Analytical Letters 48:1, pp. 167-179.

Mass J.L., Wypyski M.T., Stone R.E. (2002) Malkata and lisht glassmaking technologies: towards a specific link between second millennium B.C. metallurgist and glassmakers. Archaeometry 44; pp. 67-82.

Mata M.P., Peacor D.R., Gallart-Marti M.D. (2002) Transmission electron microscopy (TEM) applied to ancient pottery. Archaeometry 44; pp. 155-176.

Moretti C. and Hreglich S. (2013). Raw materials, recipes and procedures used for glass making in: Janssens K. (ed.) Modern methods for analyzing archaeological and historical glass 1, John Wiley & Sons, Ltd 23-47.

Naes B.E., Umpierrez S., Ryland S., Barnett C., Almirall J.R. (2008) A comparison of laser ablation inductively coupled plasma mass spectrometry, micro X-ray fluorescence spectroscopy, and laser induced breakdown spectroscopy for the discrimination of automotive glass. Spectrochim Acta B 63; pp. 1145-1150.

Nassau K. (2001) The Physics and Chemistry of color (The fifteen causes of color), 2nd edition, Wiley & Sons.

Neff H. (2003) Analysis of Mesoamerican plumbate pottery surfaces by laser ablation-inductively coupled plasma-mass spectrometry (LA-ICPMS), J. Archaeol. Sci., 30; pp. 21–35.

Newton R. and Davison S. (1989). Conservation of Glass, Butterworths, 1st edn., London.

Nicholson P.T., Henderson J. (eds) (2000) Glass in Ancient Egyptian Materials and Technology. Cambridge University Press, Cambridge.

Nuyts G., Cagno S., Hellemans K., Veronesi G., Cotte M., Janssens K. (2013), Study of the early stages of Mn intrusion in corroded glass by means of combined SR FTIR/μXRF imaging and XANES spectroscopy. Procedia Chemistry 8, pp. 239-247.

Panighello S., van Elteren J.T., Orsega E.F. and Moretto L.M. (2015) Laser ablation ICP-MS depth profiling to study ancient glass surface degradation, Anal. Bioanal. Chem., 407; pp. 3377-3391.

Paul A. (1977) Chemical durability of glasses; a thermodynamic approach. J Mater Sci 12; pp. 2246–2268.

Pérez-Arantegui J., Resano M., García-Ruiz E., Vanhaecke F., Roldán C., Ferrero J., Coll J. (2008) Characterization of cobalt pigments found in traditional Valencian ceramics by means of laser ablation-inductively coupled plasma mass spectrometry and portable X-ray fluorescence spectrometry. Talanta 74; pp. 1271-1280.

Pliny the Elder, The Natural History, ed. John Bostock, M.D., F.R.S., H.T. Riley, Esq., B.A.

Resano M., García-Ruiz E., Alloza R., Marzo M.P., Vandenabeele P. and Vanhaecke F. (2007) Laser Ablation-Inductively Coupled Plasma Mass Spectrometry for the Characterization of Pigments in Prehistoric Rock Art, Anal. Chem. 79, pp. 8947-8955.

Resano M,. García-Ruiz E. and Vanhaecke F. (2010) Laser ablation-inductively coupled plasma mass spectrometry in archaeometric research, Mass Spectrometry Reviews 29, pp. 55-78.

Robertshaw P., Benco N., Wood M., Dussubieux L., Melchiorre E., Ettahiri A. (2010) Chemical analysis of glass beads from medieval Al-Basra (Morocco). Archaeometry 52; pp. 355-379.

Russo R.E., Mao X., Liu H., Gonzalez J. and Mao S.S. (2001) Laser Ablation in Analytical Chemistry - A Review, Lawrence Berkeley National Laboratory.

Rutten F.J.M., Briggs D., Henderson J., Roe M.J. (2009) The application of time-of-flight secondary ion mass spectrometry (ToF-SIMS) to the characterization of opaque ancient glasses. Archaeometry 51; pp. 966-986.

Sayre E.V., Smith R.W. (1967) Some materials of glass manufactory in antiquity. In: Levey M (ed) Archeological Chemistry: 3rd Symposium on Archeological Chemistry, Atlantic City, New Jersey. University of Pennsylvania Press, Philadelphia; pp. 279-312.

Schreiner M. (1991) Glass of the past: the degradation and deterioration of medieval glass artifacts. Microchim Acta 104(1–6); pp. 255–264.

Shortland A.J. and Tite M.S. (2000).Raw materials of glass from Amarna and implications for the origins of Egyptian glass, Archaeometry, 42, 1, 141-151.

Shortland A.J. (2002) The use and origin of antimonate colorants in early Egyptian glass. Archaeometry 44; pp. 517-530.

Shortland A. (2005), The raw materials of early glasses: the implications of new LA-ICPMS analyses. In: Annales du 16e Congres de l'Association Internationale pour l'Histoire du Verre, London 2003, Nottingham, England, AIHV, pp.1-5.

Shortland A., Schachner L., Freestone I. and Tite M. (2006) Natron as a flux in the early vitreous materials industry: sources, beginnings and reasons for decline. Journal Archaeological Science 33, pp. 521-530.

Shortland A., Rogers N. and Eremin K. (2007) Trace element discriminants between Egyptian and Mesopotamian Late Bronze Age glasses. Journal of Archaeological Science 34, pp. 781-789.

Šmit Ž., Knific T., Jezeršek D., Istenič J. (2012) Analysis of early medieval glass beads - Glass in the transition period. Nucl Instr Meth B 278; pp. 8-14.

Šmit Ž., Milavec T., Fajfar H., Rehren Th., Lankton J.W., Gratuze B. (2013) Analysis of glass from the post-Roman settlement Tonovcov grad (Slovenia) by PIXE-PIGE and LA-ICP-MS. Nucl Instr Meth Phys Res B 311; pp. 53-59.

Sokaras D., Karydas A.G., Oikonomou A., Zacharias N., Beltsios K., Kantarelou V. (2009) Combined elemental analysis of ancient glass beads by means of ion beam, portable XRF, and EPMA techniques. Anal Bioanal Chem 395; pp. 2199-2209.

Tite M.S., Pradell T., Shortland A.J. (2008) Discovery, production and use of Tin-based opacifiers in glasses, enamels and glazes from the Late Iron Age onwards: a reassessment. Archaeometry 50; pp. 67-84.

Trigger B. G. (1989). A History of Archaeological Thought. Cambridge, Cambridge University Press.

Turner W.E.S., Rooksby H.P. (1961) Further historical studies based on X-ray diffraction methods of the reagents employed in making opal and opaque glasses. Jahrbuch des Römisch - Germanischen Zentral - Museums 8; pp. 1-16.

Van Elteren J.T., Tennent N.H., Šelih V.S. (2009) Multi-element quantification of ancient/historic glasses by laser ablation inductively coupled plasma mass spectrometry using sum normalization calibration, Anal. Chim. Acta 644(1–2); pp. 1–9.

Van Malderen S.J.M., Van Elteren J.T. and Vanhaecke F. (2015) Development of a fast laser ablation-inductively coupled plasma-mass spectrometry cell for sub-µm scanning of layer materials. J Anal. At. Spectrom 30; pp. 119-125.

Verità M. (2000) Tecniche di fabbricazione dei materiali musivi vitrei. Indagini chimiche e mineralogiche. Da Medieval Mosaic. Light, color, materials, Silvana Editoriale.

Wagner B., Nowak A., Bulska E., Kunicki-Goldfinger J., Schalm O. and Janssens K. (2008). Complementary analysis of historical glass by scanning electron microscopy with energy dispersive X-ray spectroscopy and laser ablation inductively coupled plasma mass spectrometry. Microchim Acta 162; pp. 415-424.

Wang H.A.O., Grolimund D., Giesen C., Borca C.N., Shaw-Stewart J.R.H., Bodenmiller B., Günther D. (2013) Fast chemical imaging at high spatial resolution by laser ablation inductively coupled plasma mass spectrometry. Anal Chem 85; pp. 10107-10116.

Weaver J. C., Aizenberg J., Fantner G.E., Kisailus D., Woesz A., Allen P., Fields K., Porter M.J., Zok F.W., Hansma P.K., Fratzl P., Morse D.E. (2007) Hierarchical assembly of the siliceous skeletal lattice of the hexactinellid sponge Euplectella aspergillum, Journal of Structural Biology 158; pp. 93–106.

Weyl W. A. (1951) *Coloured glasses*. Society of Glass Technology, England.

White W.B. (1992) Theory of corrosion of glass and ceramics. In: Clarke, D.E. and Zoitos, B.K., Eds. Corrosion of Glass, Ceramics and Superconductors. Noyes Publications, Park Ridge, 2, pp. 2-28.

Woodhead J.D., Hellstrom J., Hergt J.M., Greig A., Maas R. (2007) Isotopic and elemental imaging of geological materials by laser ablation inductively coupled plasma-mass spectrometry. Geostand Geoanal Res 31; pp. 331-343.

Chapter 2

Methodologies for the analysis of glass

2.1. Introduction

The preparation of glass samples for analysis is normally achieved incorporating small pieces of sample in acrylic resin and subsequent polishing of the surface (De Raedt *et al*., 2001; Wagner *et al*., 2008), while larger samples (more than ten centimeters) can be directly analyzed by techniques such as PIXE-PIGE (Šmit *et al*., 2005), XRF or LA-ICP-MS using a non-contact cell for large planar samples (Asogan *et al.*, 2009) or a recently developed portable laser ablation sampling device (Glaus *et al*., 2012; Glaus *et al*., 2013). The polishing action allows removing the degraded layer, even if it has a thickness of several millimeters. Glass degradation is a commonly encountered phenomenon for archaeological glasses that were buried for a long time.

Laser ablation facilitates the removal of superficial layers by performing pre-ablation prior to the actual quantification-ablation. Quantification procedures typically require the use of external standards with a similar type of matrix as the sample. For glass analysis NIST SRM glass standards and Corning glasses A, B, C and D are normally used. The latter ones were synthesized by Dr. Robert Brill of the Corning Museum of Glass (Corning, New York) to specifically mimic the composition of different historical glasses like Egyptian and Mesopotamian, Roman and Medieval ones. In order to correct for different ablation rates between sample and standard, an element with a known concentration in both materials is required as an internal standard. Often complementary techniques such as e.g. EPMA are used to determine the unknown internal standard concentration in the samples (Resano *et al*., 2010; Gratuze, 2013). However, by analyzing the major, minor and trace elements, and using one of the major elements as an internal standard, one can quantify all elements in glass by a normalization procedure which sums all the elements as their oxides to 100 wt % without actually knowing the internal standard concentration (Gratuze *et al*., 2001; Liu *et al*. 2008; van Elteren *et al*., 2009).

The micro damage of the surface caused by the laser is undeniable but in most cases invisible to the naked eye and the integrity of the entire precious object is preserved. LA-ICP-MS features micrometer spatial resolution as well, enabling the analysis of heterogeneous samples. This feature fosters the investigation of particular components in a sample, like inclusions in metal objects or fragments in pottery samples. Increasingly materials such as teeth and bones or stratified artworks such as ceramics, paintings, stuccoes and ancient metal objects are also be studied by sampling across or through (depth profiling) the in homogeneities.

LA-ICP-MS shows the best elemental sensitivity compared to the other non-destructive or minimally destructive techniques relying on solid sampling. Despite these advantages, imprecision owing to inhomogeneity, fractionation effects, matrix effects and the requirement for calibration standards with a composition similar to the samples, are still limiting the true potential of this technique.

The goal of this chapter is to present the various sampling modes of the LA-ICP-MS for the retrieval of quantitative, multi-elemental, spatial information related to degraded glass samples; the various sampling modes and their limitations and capabilities will be critically examined. Complementary analytical techniques will be discussed as well as a means of obtaining supplementary information related to the material.

2.2. Laser Ablation ICP-MS

Ca. 30 years ago, when the advantages of ICP-MS became commercially available, laser ablation was immediately applied creating a powerful technique for the direct elemental analysis of solid samples (Gray, 1985). The use of laser ablation eliminated the long and time consuming procedure for sample preparation prior to ICP-MS measurement while still having a sensitive technique for elemental and isotopic determination in solid samples. Besides the unnecessary sample preparation, the other advantages using ICP-MS hyphenated to laser ablation systems can be summarized as follows: less interferences due to the absence of solvents and acids, spatial resolution as low as a few µm is possible, elemental and isotopic information are obtainable, limits of detection are significantly lower to other solid sampling techniques and the speed of data acquisition allows large quantities of samples to be analyzed within a reasonable time (Russo *et al*., 2001; Günther and Hattendorf, 2005; Resano *et al*., 2010; Limbeck *et al*., 2015).

Conceptually, the ablation process is simple: "a short pulsed high power laser beam is focused onto a sample surface. The laser beam converts a finite volume of the solid sample instantaneously into its vapor phase constituents. The vapor then is analyzed by measuring atomic/ionic emission by transporting the vapor to another measurement system, such as the inductively coupled plasma (ICP)" (Russo *et al*., 2001).

2.2.1. Instrumentation

Two different quadrupole ICP-MS instruments were used for the experiments. Both ICP-MS instruments can be used in solution nebulization and laser ablation mode. An Agilent 7500ce (Palo Alto, USA) was used in combination with a Nd:YAG laser (New Wave Research UP 213, Fremont, USA). The other ICP-MS was an Agilent 7900 (Agilent Technologies, Santa Clara, USA) combined with a 193 nm ArF* excimer laser (Cetac Analyte G2, Teledyne CETAC Technologies, Omaha, USA). A schematic setup of a generic LA-ICP-MS system is shown in Figure 2.1 giving the main components which are further specified in Table 2.1 for the individual LA-ICP-MS systems. Laser ablation takes place in a so-called SuperCell™ (New Wave Research), a chamber with a small void volume especially designed for optimal flow dynamics, yielding fast transient signals and inherent high sensitivity or in a so-called HelEx II 2-volume cell, a large chamber for sampling of "flat" objects via a "roving" cup to counteract the large cell volume (Bleiner and Günther, 2001). In both cases helium was used to transport the ablated material from the ablation chamber to the inductively coupled plasma (ICP); argon was added as a make-up gas before the torch of the ICP. The ions formed in the ICP were extracted in the quadrupole mass spectrometers and separated according to their mass-to-charge ratios. The mass spectrometers were set up in time-resolved analysis mode, measuring one point per mass. The main differences between the ICP-MS instruments are sensitivity and speed of acquisition. In the chapters referring to the development of the different LA-ICP-MS methodologies for bulk analysis and elemental imaging (depth profiling and 2D/3D mapping) the actual operational conditions will be given.

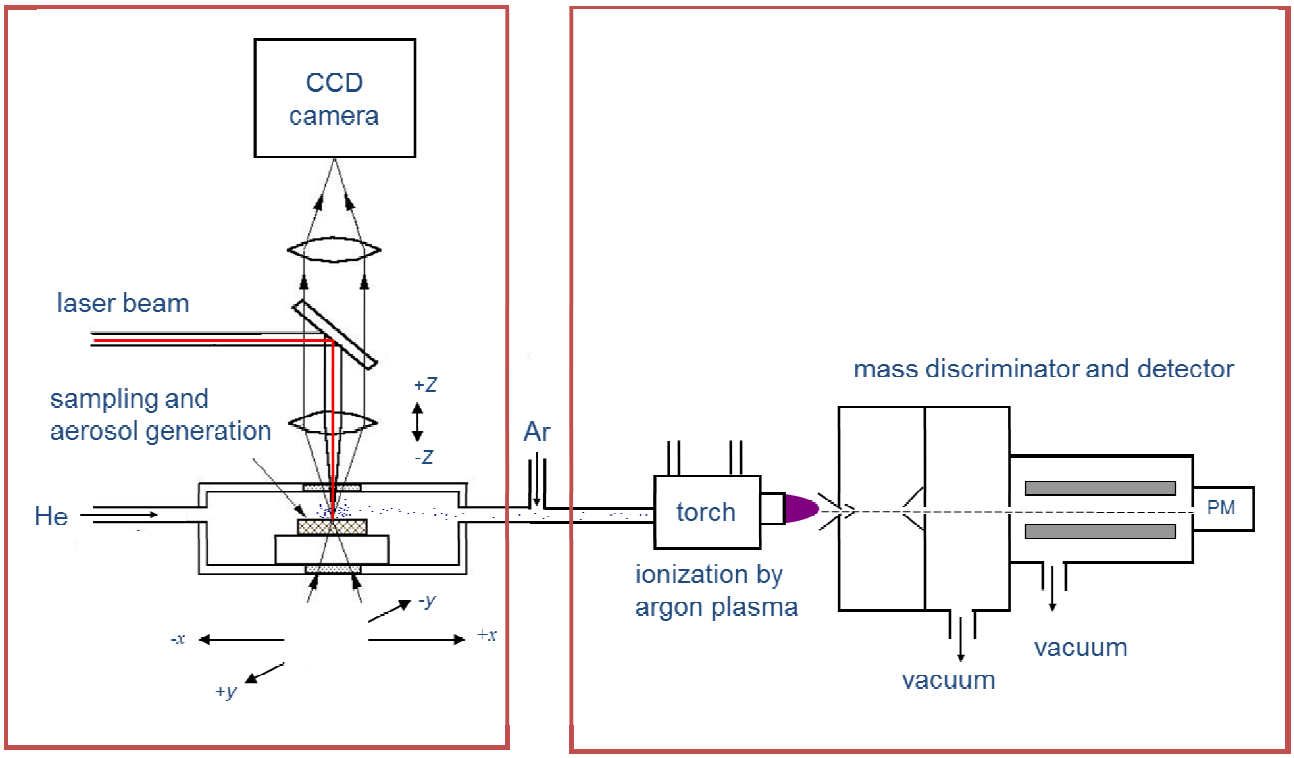

Figure 2.1. Schematic drawing of a LA-ICP-MS setup.

Table 2.1. Specifications of the LA-ICP-MS systems used in this work.

Laser Ablation	**NWR (New Wave Research)**	**Cetac Analyte G2**
Cell type	Super cell	HelEx II 2-volume cell
Laser source	Nd:YAG	Excimer
Wavelength	213 nm	193 nm
Pulse duration	4ns	<5ns
Crater diameter	From ~4 to ~250 µm	From ~1 to ~400 µm
Repetition rate	1-20 Hz	1 - 300 Hz
Energy density	Up to 30 J/cm^2	Up to 15 J/cm^2
Ablation modes	Single shot, burst, continuous	Single shot, burst, continuous
Light polarization	Polarized light source	Rotating cross-polarizers for both transmitted and coax lighting
ICP-MS	**Agilent 7500ce**	**Agilent 7900**
Mass separator	Quadrupole	Quadrupole
Detection limit	10 µg/kg - 10 mg/kg (depending on element and operating conditions)	1 µg/kg - 1 mg/kg (depending on element and operating conditions)
Minimum dwell time	1 ms (per element)	100 µs (per element)

2.2.2. Calibration strategy

Laser ablation in combination with ICP-MS is a powerful technique for major, minor and trace elemental analysis of solid samples. However, in comparison to the analysis of liquids, quantitative results are more difficult and very challenging in combination with spatial imaging of glass. The difficulty is due in particular to the inhomogeneity of the samples, matrix effects and elemental fractionation phenomena (Russo *et al*., 2000; Resano *et al*., 2010; Horn *et al*., 2000; Guillong and Günther, 2002; Günther and Hattendorf, 2005, Sylvester, 2008).

For accurate *in situ* elemental quantification of glasses with microanalytical techniques such as EPMA, SIMS, LA-ICP-MS, etc., the availability of microanalytical reference materials (MRMs) is essential. Currently, tens of microhomogeneous MRM glasses are used for microanalytical calibration, most notably from NIST (National Institute of Standards and Technology, USA), USGS (US Geological Survey), MPI-DING (Max Planck Institute for Chemistry, Germany), BAM (Federal Institute for Materials and Testing, Germany), and, recently, NRCG (National Research Center of Geoanalysis, China). In general, these MRMs can be divided into synthetic reference glasses (NIST SRM) and geological reference glasses (USGS, MPI-DING, and NRCG), with similar concentrations for all trace elements and based on homogeneous glasses of natural composition, respectively. An informative database is maintained with published and GeoRem preferred values by the Max Plank Institute of Chemistry (http://georem.mpch-mainz.gwdg.de).

For quantification of ancient glasses, these MRMs are useful but not necessarily the best as ancient glass compositions are usually very different from the ones of the MRMs mentioned above. To this end, a selected number of MRMs such as NIST SRM 610 and 612 are augmented with standards from the Corning Museum of Glass (CMG) which mimic ancient compositions. Hence, they are better suited for accurate quantification, especially when the elements are not present at trace levels such as in lead glasses. CMG A (not available anymore) and B match the composition of SLS Egyptian, Mesopotamian, Roman, Byzantine, and Islamic glasses. CMG C is a lead-barium glass similar to those found in East Asia, and CMG D is a high-Mg, high-Ca potash glass with typical medieval composition (Bertini *et al.*, 2013). CMG glasses were never meant to be used for microanalytical work as microhomogeneity issues may start to play a role as evidenced from the work by Vicenzi *et al.* (2002). However, they found that LA-ICP-MS indicates a high degree of chemical uniformity within all glasses at a beam size of 65 µm, typically <2 % relative (1 σ), whereas EPMA (and also SIMS) suggest a significant level of heterogeneity for a number of metals (Ba, Sn, Co, Cu, Sr, Sb, Zn, and/or Pb). Furthermore, the published bulk analytical data by Brill (1999) need to be reevaluated for some elements in the light of some recently published data by Dussubieux *et al.* (2009) and Wagner *et al.* (2012) (see Table 2.2). In particular, the results for Ba, Sn, B, Cr, and Bi in CMGB; P, Sb, Cr, and B in CMG C; and Pb, Ba, and Bi in CMG D were found to deviate significantly from Brill's data (300 % for Bi in CMG C, 130 % for Cr in CMG C, and from 16 to 100 % for the other elements listed above in CMG B, C, and D).

Our own LA-ICP-MS investigations, using a set of 12 standard glasses [NIST SRM 610 and 612 (National Institute of Standards and Technology), SGT 2, 3, 4, 5 (Society of Glass Technology), CMG B, C, D (Corning Museum of Glass), and DLH 6, 7, 8 (P&H Developments Ltd.)] with a conventional bulk analysis procedure (Van Elteren *et al.*, 2009 and 2013), led to data which match these new values very well as can be seen from Table 2.2.

Table 2.2. Reference data (in wt %) for some elemental oxides in three Corning Museum of Glass standards which deviate from the original values published by Brill, 1999.

	Brill	Wagner *et al.*, (2012)	Dussubieux *et al.*, (2009)	This work
CMG B				
BaO	0.12	0.077 ±0.002	0.08 ±0.02	0.076 ±0.002
SnO_2	0.04	0.0241 ±0.0002	0.021 ±0.001	0.024 ±0.001
B_2O_3	0.02	0.035 ±0.001	ND*	0.030 ±0.002
Cr_2O_3	0.005	0.0096 ±0.0003	ND	0.0095 ±0.0001
Bi_2O_3	0.005	0.0042 ±0.0001	ND	0.0036 ±0.0004
CMG C				
P_2O_5	0.14	0.068 ±0.001	0.07 ±0.03	0.102 ±0.006
MnO	ND	0.0011 ±0.0000	0.0013 ±0.0002	0.0014 ±0.0001
Sb_2O_5	0.03	0.0001±0.0000	0.0002 ±0.0001	0.0001 ±0.0001
Cr_2O_3	0.001	0.0023 ±0.0001	ND	0.0025 ±0.0001
Bi_2O_3	0.001	0.0040 ±0.0001	ND	0.0038 ±0.0002
CMG D				
PbO	0.48	0.241 ±0.003	0.23 ±0.01	0.23 ±0.012
BaO	0.51	0.291 ±0.005	0.38 ±0.09	0.293 ±0.007
Bi_2O_3	0.003	0.0012 ±0.0000	ND	0.0012 ±0.0001

*ND, not determined.

2.2.3. Sum normalization calibration protocol

The strategy employed for the analysis of glass samples in this work is based on an approach developed by van Elteren *et al.* (2009), comprising a so-called sum normalization calibration procedure based on summing the concentration of all matrix-containing elements as their oxides and normalizing them to 100 wt % using external calibrants. Internal standardization was applied to correct for variations of the sample introduction system, the plasma conditions, instrumental drift and matrix effect (Longerich *et al.*, 1996; Resano *et al*., 2010). However, since one cannot add an internal standard to a solid sample an extra step is needed to quantify one of the elements, normally a major constituent of the matrix homogeneously distributed in the sample, with a complementary technique such as e.g. EPMA.

Alternatively, one can use a random concentration for one of the major glass constituents and let the sum normalization protocol converge to the actual elemental concentrations as described below. Quantification is performed selecting SiO_2 as an internal standard, without actually knowing the concentration in the samples, by converting the elemental ICP-MS data I_i (in cps) in each selected point for each element *i*. To this end the output $I_{i,corr}$ is corrected for ablation differences by dividing I_i with (I_{Si}/50), with 50 being the arbitrary SiO_2 concentration in wt % (c_{Si}):

$$I_i(corr) = \frac{I_i}{I_{Si}/c_{Si}} \qquad \text{[Eq. 2.1]}$$

For the glass standards a similar protocol is followed but now with known SiO_2 concentrations yielding average elemental sensitivities F_i for each element *i*. The individual elemental oxide concentrations (c_i), based on a SiO_2 concentration of 50 wt %, are given by

$$c_i = \frac{I_i(corr)}{F_i} \qquad \text{[Eq. 2.2]}$$

The subsequent cumulated elemental oxide concentration c_t in the sample is denoted by

$$c_t = \sum_{i=1}^{n} c_i \qquad \text{[Eq. 2.3]}$$

After summation (Eq. 2.3) and normalization to 100 wt %, the actual, corrected elemental oxide concentrations c_i (= $\{I_{i,corr} \times 100\}/\{\sum[I_{i,corr}/F_i] \times F_i\}$) are found, with the SiO_2 concentration c_{Si} (in wt %) automatically corrected to its true value:

$$c_i(norm) = 100 \times \frac{c_i}{c_t} \qquad \text{[Eq. 2.4]}$$

Calcium and sodium are also used as internal standard in glass analysis (Shortland and Schroeder, 2009; Wagner *et al.*, 2008) but they are less common because their isotopes are more subjected to interferences. Figure 2.2 shows that the main criterion in the choice of an internal standard is the high concentration level and/or abundance. In this case the error generated using CaO as internal standard is very high, in particular for the elements SiO_2, K_2O and PbO.

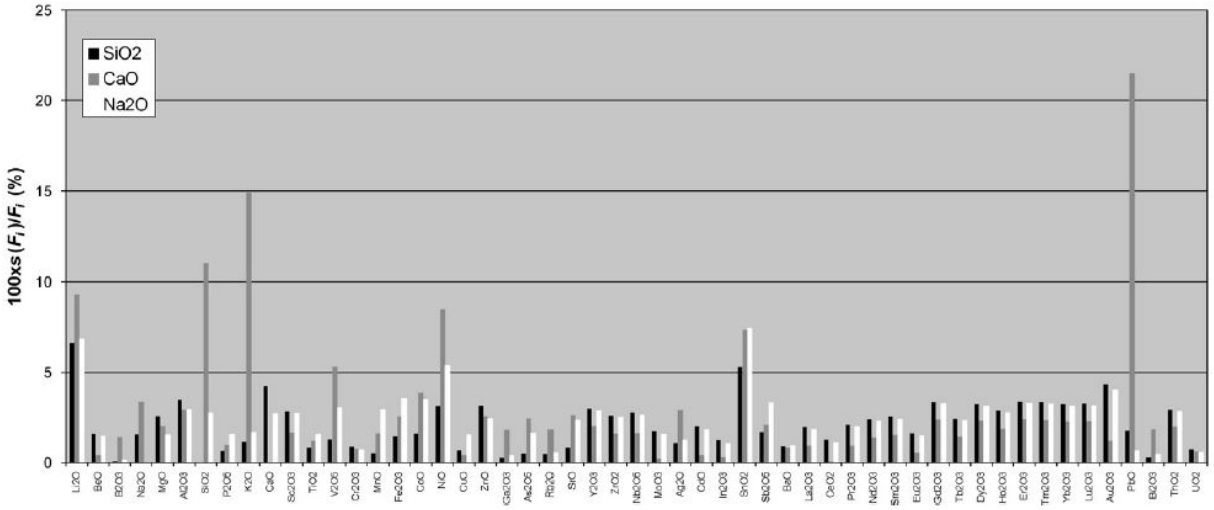

Figure 2.2. Relative standard error in the response factor F_i of the calibration graphs for elemental oxides *i* and the use of different internal standards (SiO_2, CaO or Na_2O); after Van Elteren *et al*. (2009).

It can be significant to understand and compare the composition of the glass samples on the basis of their primary raw materials (sands and fluxes). For this purpose usually a so-called reduced composition of the glass samples is considered (Brill, 1999): the amounts of the oxides supposed not significantly present in sands and fluxes, i.e. chromophores and opacifiers or others elements associated with them, but added

during the melting process to modify the base glasses, are subtracted from the total sum. The remaining oxides are recalculated to bring their sum to 100%. The oxides subtracted are normally Fe, Co, Cu, Sn, Sb and Pb. Iron oxide is subtracted when its content is higher than 0.3-1.0 wt % when it is considered a constituent of the sands used in the manufacture of ancient glasses. In practical use (Chapter 7) the values of the reduced oxides were in many cases markedly different from the original values, especially for opaque glass samples.

Statistical analysis is applied to better organize and interpret the enormous amount of data (major, minor and trace elements) generated by LA-ICP-MS. Cluster Analysis and Principal Component Analysis (PCA) are the pattern recognition methods that are used. Bivariate and multivariate statistical analyses were performed with Origin® and Statistica®, respectively.

2.2.4. Different analytical procedures

The potential of LA-ICP-MS to generate bulk chemical data of glass samples through microanalysis has been studied in a wide number of research projects, mostly concerning glass from the past (Cagno *et al.*, 2012; De Raedt *et al*., 2001; Dussubieux *et al*., 2007 and Wagner *et al*., 2008). The analytical approach to retrieve bulk compositional data, especially for ancient glass, is becoming customary practice to provide information about fabrication technology and provenance of the raw materials (sands, fluxes, chromophores, opacifiers, etc.) in order to address specific questions, particularly in disciplines such as conservation-restoration, archaeology, and geology. The analysis of archeological glass remains a challenge for samples with physical and/or chemical damage on the surface of the artifact as a result of chemical instability of ancient glass and often aggressive environmental conditions in which they remained, often for centuries or even millennia.

Although LA-ICP-MS facilitates the removal of superficial layers by performing pre-ablation passes, this may not result in accurate bulk analytical data when the alteration layer is more than a few micrometers thick (Hench, 1975) and the undegraded glass has not been reached. There are multiple factors which may cause the laser beam not to penetrate the alteration layer of an ancient or unstable glass. Next to the chemical composition and morphology of the alteration layer itself, also the characteristics of the laser ablation device (wavelength, ablation cell design, background gas, etc.) and the laser ablation settings (spot size, fluence, repetition rate, background gas flow rate, ablation mode, etc.) may be responsible.

The impact of corrosion on the accuracy of LA-ICP-MS results was recently studied by Dussubieux *et al*. (2009). They analyzed several African glass beads in two different laboratories using the line scanning mode (the firing laser traverses the sample surface in linear fashion at constant speed) and the spot analysis mode (the laser fires on a single point on the surface). They found that glass corrosion can become a major factor influencing the accuracy of the LA-ICP-MS data and concluded that the line scanning mode is more sensitive to corrosion artifacts than the spot analysis mode. Indeed, the use of the spot analysis mode may provide the right means to circumvent this problem (Wagner *et al*., 2008; Dussubieux *et al*., 2009; Gratuze, 2013). In addition, the crater generated by spot drilling is less visible than the ablation line. Spot drilling can be used not only for bulk analysis but also to generate depth profiling (1D) and 3D mapping in order to obtain more information about the elemental distribution in the sample. Glass sample material can be ablated also along line (line scan mode, raster) to retrieval of bulk elemental concentrations, and 2D elemental maps. The selection of one of the ablation modes depends primarily on the intended application, as well as on the characteristics of the sample. Laser ablation modes of operation are illustrated in Figure 2.3; a detailed description of the development of these modes is given in Chapters 3, 4 and 5, together with specific applications.

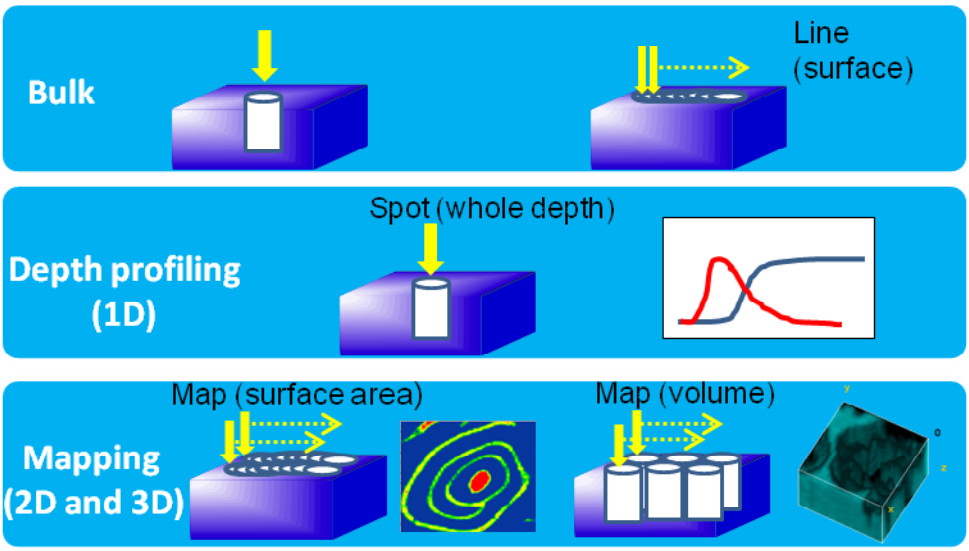

Figure 2.3. Laser ablation modes of operation.

2.2.4.1. Spot drilling / depth profiling

Depth profiling involves laser drilling down into a sample with the aim to retrieve the relationship between depth and chemical composition. Since the penetration rate is in the order of 0.1 µm per laser shot (van Elteren *et al.*, 2013) for 213 nm LA system, depth profiling yields a much higher resolution than line scanning of a cross section of the same sample which is limited by the size of the laser beam, in general >10 µm for serviceable sensitivities. However, when the beam profile deviates from the ideal top hat shape, material might mix at the layer interface leading to "blurred" depth profiles (Woodhead *et al.*, 2008), whereas too deep craters may lead to a decreasing signal as a result of particles not escaping from the crater effectively (Mank and Mason, 1999). By choosing different LA spot analysis drilling procedures, based on different laser frequencies, element-depth relationships can be established for superficial layers.

The laser frequency setting (normally from 1 to 50 Hz) is very important because it affects the sensitivity. At a higher frequency, more mass is ablated per second, and thus a higher count rate is obtained. However, when depth-profiling information is relevant for the intended application, it is important to keep in mind that the use of a lower frequency provides a better depth resolution.

The analysis of ancient glass will inevitably involve the effects of degradation as a result of leaching and corrosion. To study glass degradation phenomena, accelerated leaching can be performed (e.g. autoclaving, microwaving, etc. with various experimental variables simulating environmental conditions). In Figure 2.4 elemental depth profiles are given for a microwave leached (in acidic solution, 121^{o}C, 5 hours) lead crystal glass, showing the depletion gradient of Na_2O and K_2O in the 1-2 µm top layer and a marked loss of PbO at the utmost surface. Additionally, depth profiling of an ancient glass will give insight into the corrosion mechanisms and also the corrosion layer thickness and thus the depth for accurate retrieval of bulk concentrations. In Figure 2.5, depth profiles for Na, Al and K oxides from an African bead of the 8th century are shown. It presents a very low soda concentration with an enrichment of potash and alumina in the corroded layer. This is probably due to the precipitation on the glass surface of mineral phases from the soil. Detailed information on the approach to generate LA-ICP-MS glass depth profiles is given in Chapter 3.

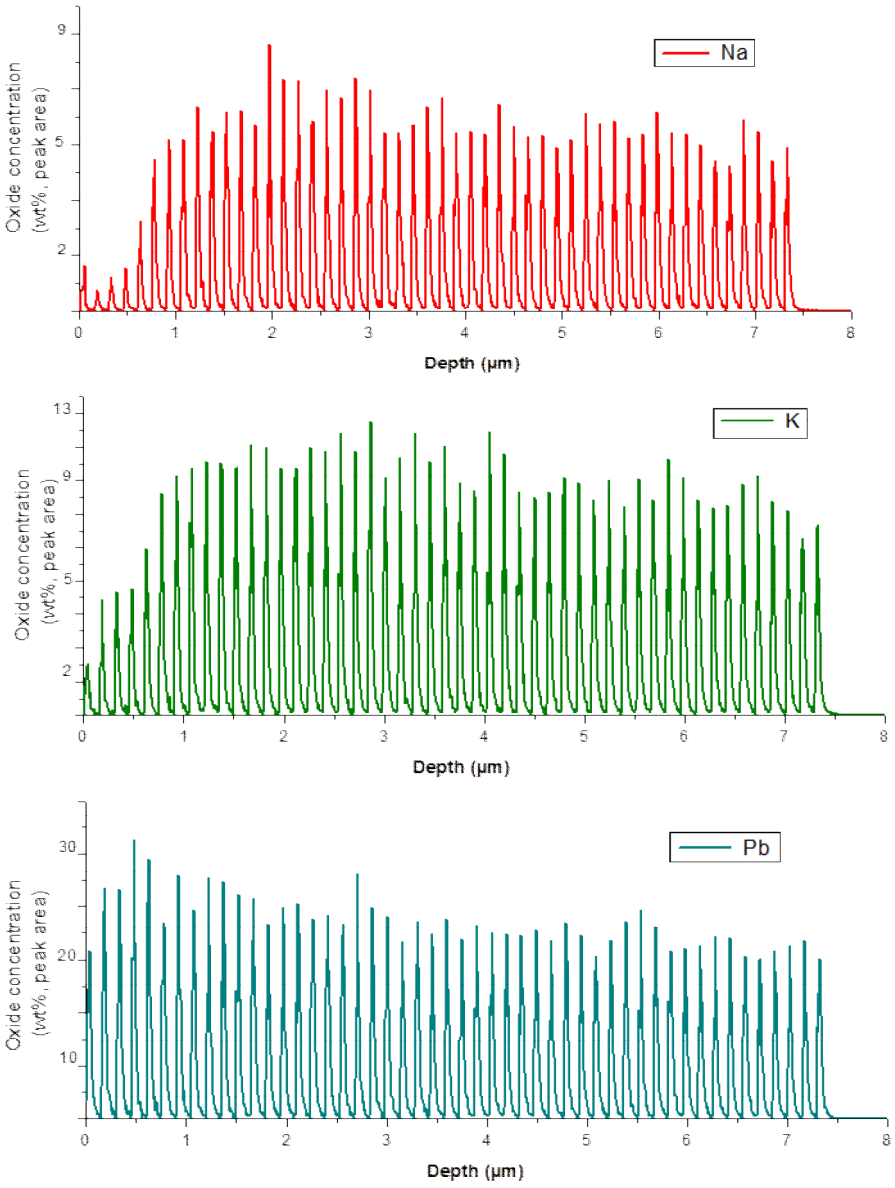

Figure 2.4. Laser ablation depth profiles of a lead glass using single pulse drilling (1 Hz).

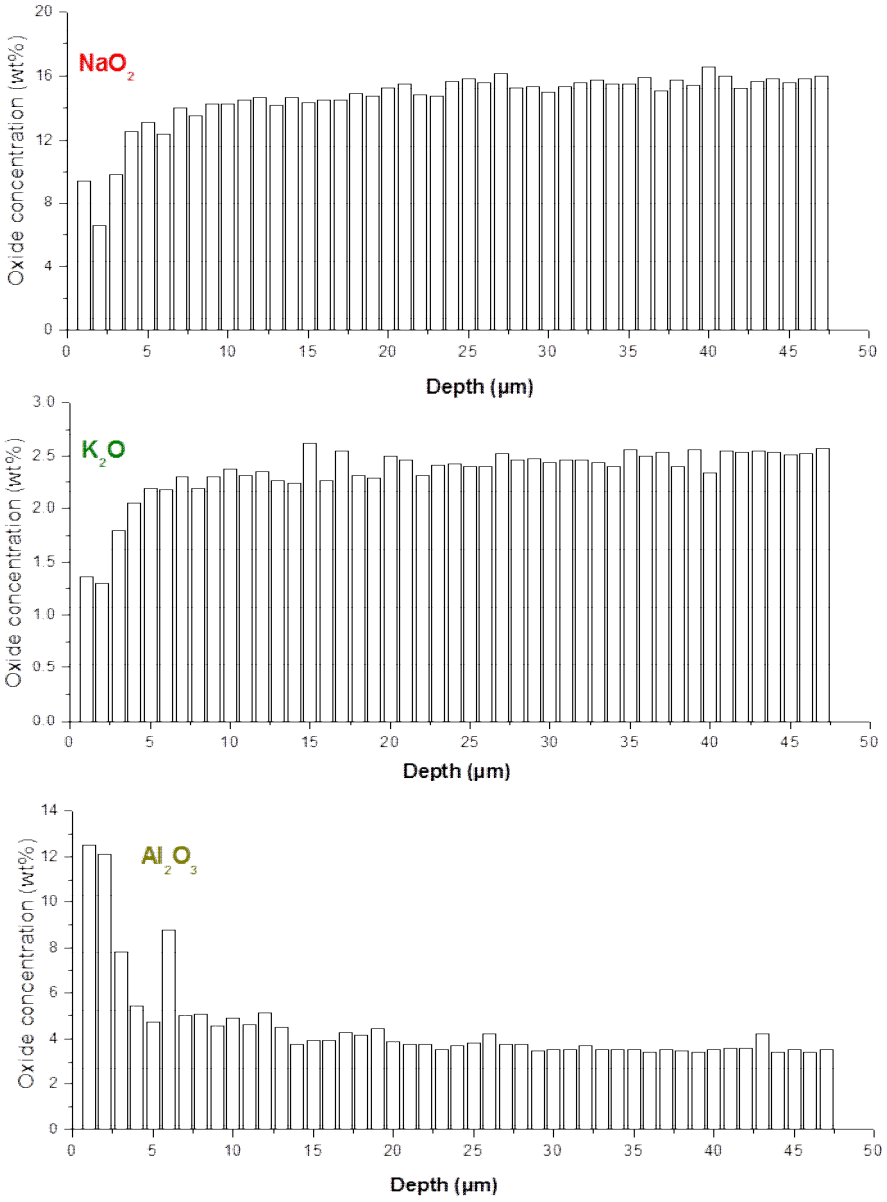

Figure 2.5. Laser ablation depth profiles of an archaeological glass using continuous pulse drilling (10 Hz).

2.2.4.2. Line profiling / 2D mapping

Line profiling or rastering modes covering a wider area are more suitable for bulk characterization of an inhomogeneous sample (Resano *et al*., 2010). Moreover, the sensitivity is often better for line profiling than for drilling as ablation rate and particle transport efficiency decrease as the beam penetrates deeper into the sample and the laser defocuses. Finally, some authors have pointed out that line profiling reduces elemental fractionation due to the shallow ablation profile and better heat dissipation, whereas particle size distributions show less variation in time in comparison with drilling (Sylvester, 2008; Resano *et al*., 2010). Additionally, line profiling and rastering are time- and spatially-resolved modes of ablation, allowing the generation of elemental maps covering large sample areas.

An elemental map is an image representing the spatial distribution of elements and their contents in a sample. It can be particularly useful for a preliminary visual inspection of the elemental superficial patterns of the samples and their comparison. Selection of the appropriate LA-ICP-MS conditions (fluence, beam diameter, repetition rate, scanning speed, gas flow rate and acquisition time) for generation of high-quality 2D elemental image maps is complex due to the mutual effects of the LA-ICP-MS conditions on the quality of the maps in terms of spatial resolution and signal-to-noise ratio within a given time frame for analysis. While it is possible to increase the resolution by decreasing the beam diameter, this invariably increases the analysis time and potentially the signal-to-noise ratio when trace level concentrations are to be measured.

In this work 2D mapping is applied to diverse polychrome glass samples (see Chapter 4). Since decorative coloured features in glass are determined by the presence of chromophoric elements (especially heavy metals in the form of ions or compounds, see Table 1.1 in Appendix 1), a digital image of the glass gives a rough representation of the chromophoric elemental distribution, and as such may be used for virtual mapping to simulate the 2D LA-ICP-MS elemental mapping process (an example is given in Figure 2.6).

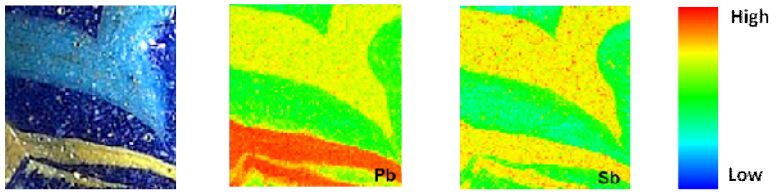

Figure 2.6. Comparison of elemental maps of a fragment of a pre-Roman vessel (first picture on the left). The elemental maps of Sb and Pb oxides are indicative of the use of lead and calcium antimonates as yellow and white opacifiers respectively (this example is described in Chapter 4).

Virtual mapping software has been previously developed (Triglav *et al.*, 2010); this is the conceptual model behind: when a laser beam with diameter D (μm) traverses the surface of the sample with a scanning speed S (μm s^{-1}), and the laser firing at an optimal fluence and a repetition rate R (s^{-1}), the amount of material sampled per pulse is directly proportional to the cross-sectional area A (μm^2) of the laser beam and the object. Since the ablation cell volume V (l) is relatively large and the gas flow rate F (l s^{-1}) has an upper limit, the washout of aerosol particles from the ablation cell is controlled by their residence time σ (= V/F) in the cell, resulting in an exponential washout of the particles from the cell expressed by $A \times \exp(-t/\sigma)$ for each pulse, assuming aerosol ablation under turbulent conditions. Thus, the aerosol concentration leaving the ablation cell is represented, as a function of time, by superimposition of tailing peaks as a result of exponential washout of subsequent pulses.

When this continuous time-related concentration signal is presented to the ICP-MS instrument, discrete measurement takes place as a function of the acquisition time *T* (s). The software translates this line scanning model into a virtual 2D mapping tool, with the understanding that maps consist of many parallel lines. With this 2D mapping tool the quality of the maps can be accurately predicted by virtual mapping of a digital image of e.g. a polychrome glass sample, as a function of the LA-ICP-MS conditions (see Chapter 4). However, the predicted quality can only be assessed in terms of 2D spatial resolution and analysis time as signal-to-noise ratios are based on actual elemental concentrations and can only be investigated experimentally. Detailed information on the approach to generate LA-ICP-MS glass maps is given in Chapter 4 and in Šelih and van Elteren (2011).

2.2.4.3. Spot drilling / 3D mapping

The field of 3D elemental imaging by LA-ICP-MS is still in its infancy, with the state of the art relying on (*i*) registered stacking of 2D maps generated by ablation of serial consecutive sections obtained by (cryo)microtoming [for "soft" materials as biological tissues (Becker *et al.*, 2010)] or (*ii*) laser drilling on a grid and rearrangement of the thus retrieved spatial LA-ICP-MS data in individual 2D depth maps along the *z*-axis for materials that cannot be sectioned [for "hard" materials as glass, bronze, etc. (Chrinos *et al*., 2014; Van Malderen *et al*., 2015)].

3D maps (Figure 2.7) are generated from low-repetition rate laser ablation on a grid (50 pulses Hz per grid point at 1 Hz) and extremely short ICP-MS acquisition times, followed by peak integration and extraction of depth maps along the z-axis, resulting in lateral and depth-related information (e.g. 90 µm x 90 µm x 0.15 µm voxels).

Layer-by-layer chemical imaging provides important information on the elemental distribution of materials as a function of depth. This imaging tool becomes more important the more inhomogeneous is the sample.

Spatial and depth (or axial) resolution is related to the sample physical characteristics (e.g. roughness, porosity, etc.) (Chrinos *et al*., 2014). Detailed information on the approach to generate LA-ICP-MS glass maps are given in Chapter 5 and in van Elteren *et al*., 2013.

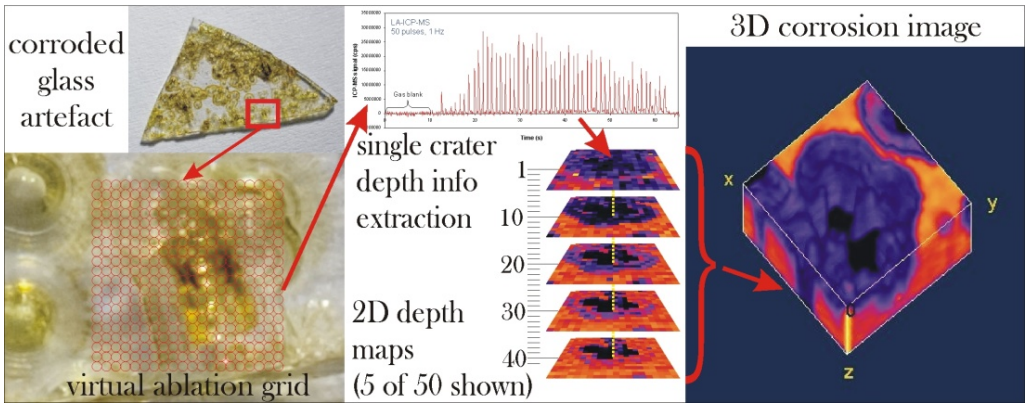

Figure 2.7. Workflow for retrieval of 3D imaging data via LA-ICP-MS analysis of a severely weathered glass area (van Elteren *et al*., 2013).

2.3. Complementary techniques

Different techniques were used in addition to LA-ICP-MS with the aim to obtain supplementary information regarding the target under investigation. EPMA-WDS mapping can be effective in understanding spatial distribution of elements in glass with a spatial resolution <1 μm. SEM-EDX is used to identify opacifier agents and to better study the mechanisms of degradation. Finally UV-Vis Reflectance Spectroscopy can be useful for the identification of pigments and chromophores in polychrome artworks.

2.3.1. X-ray microanalytical techniques

Electron probe microanalysis (EPMA) is an analytical technique that is used to establish the composition of small areas on a sample. It works by bombarding a micro-volume of a sample with a focused electron beam (typical energy, 5-30 keV) using a series of electromagnetic lenses, and collecting the X-ray photons emitted by the different elements. The characteristic X-rays are detected at particular wavelengths, and their intensities are measured to determine concentrations. This analytical technique has a high spatial resolution and sensitivity. Additionally, the electron microprobe can function like a scanning electron microscope (SEM) and obtain highly magnified secondary- and backscattered-electron images of a sample.

2.3.2. WDS (wavelength dispersive spectrometry) and mapping

EPMA WDS elemental maps were obtained with a Jeol JXA-8800R SuperProbe Electron Probe Microanalyzer equipped with four wavelength-dispersive spectrometers. Wavelength-dispersive spectrometers are tuned to the characteristic X-ray of interest for analysis; this is done by scattering of X-rays from a crystal positioned between a sample and the detector. By changing the angle of incidence of the X-rays, the crystal will constructively diffract X-rays of specific wavelengths. For calibration, NBS (National Bureau of Standards) standard 620, a soda lime flat glass, was used. The samples were embedded in a resin block, the surface of the resin was polished and a carbon coating was applied. The spatial resolution of X-ray maps is approximately 1 micron (Tanaka *et al*., 2008). Such mapping can delineate sub-micron particles or can be carried out across surfaces up to 90 mm on a side. In Table 2.3 the specifications of the instrument are reported.

Table 2.3. Jeol EPMA instrument features.

EPMA WDS	***JXA-8800R***
Detection Limit	From 300 to 30 ppm
Detectable element range	From $_{4}$Be to $_{92}$U
Detectable wavelength range	0.087 to 9.3 nm
Map resolution	~ 1 μ
Map acquisition time	10^{6} s/mm^{2}
Number of x-ray spectrometers	4
Sample size	150mm x 150mm x 50mm
X – Y range	90mm x 90mm
Accelerating voltage	0.2 to 30kV (100V steps)
Probe current range	10^{-12} to 10^{-5} A
Scanning image magnification	x40 to 300,000 (WD: 11mm)

2.3.3. EDS (Energy Dispersive Spectrometry)

In this work energy-dispersive spectrometry (EDS) system is used for rapid identification of phases and elemental analysis. Unlike wavelength-dispersive spectrometry (WDS), the EDS system does not "tune in" specific X-rays. Instead, a solid-state detector collects and counts all of the emitted X-rays at once, and it divides the energy spectrum into different "channels" or ranges. The EDS system can be used for quantitative analysis (one simply counts the X-rays received in the channels that correspond with a peak of interest), phase identification and rapid particle analysis. For many combinations of elements, however, the EDS system is less desirable than WDS because of its limited spectral resolution (overlapping peaks) and limited sensitivity.

2.3.4. SEM (Secondary Electron Microscopy)

Secondary electron (SE) images are used to provide topographic information about a sample. The spatial resolution for SEM imaging is approximately 100 to 200 nm, depending on the accelerating voltage, beam current, and other operating conditions. Back scattering electron (BSE) images show atomic number differences in a sample. A certain fraction of the electrons in the beam are scattered "backward" out of the sample as a result of interactions with its nuclei, and these "backscattered" electrons can be used to form images. The number of electrons that are backscattered increases with an increasing mean atomic number of the material. In a BSE image, the brighter the area, the heavier the mean atomic mass of that material.

2.3.5. Surface profilometry and confocal optical microscopy

Optical and contact profilometry was used to establish the ablation rate (µm of material removed per pulse) by measuring the crater depths as a function of the number of pulses. A stylus surface profiler (KLA Tencor Alpha-Step 500) was used for the measurement of the ablation crater shape (width and depth) in Chapter 3 with 0.4 µm-lateral steps and 2.5 nm of vertical resolution. The scan width was usually around 500 µm. Several scans were repeated on each crater to check the LA reproducibility. Measurement of the crater depth facilitated depth calibration as a function of the LA variables by converting the drilling time into a depth value.

The penetration depths upon ablation with 1, 2, 5, 10, 20, 30, 40 and 50 pulses according to the LA conditions for drilling were measured by a vertical scanning interferometer (VSI) in Chapter 5; the data were analyzed by WYKO Vision^{TM} software. Furthermore, confocal optical microscopy (Carl Zeiss, LMS 700, Germany) was used for 3D surface topography characterization of a single corrosion spot to study the effect of prolonged leaching on the physical manifestation on the glass surface.

2.3.6. Ultraviolet / Visible Reflectance Spectroscopy

Two instrumental principles are normally used to numerically measure the color: colorimetry and spectrophotometry. While the former is mainly used in the production phase and in the visual inspection to measure color differences and colored folders, the spectrophotometer finds application in laboratories for research and development of analysis with high accuracy.

The main difference between a colorimeter and a spectrophotometer is that with the first only numeric data in various color spaces are obtained while the second also provides a spectral reflectance graph. The light produced by a pulsed Xenon lamp illuminates the sample at an established angle and the diffused light is collected within the integrating sphere that spreads it uniformly into its inner surface, providing an

average over all angles of illumination and observation. Light enters the main spectral sensor and it is splitted into wavelengths (from 360 to 740 nm) by a holographic diffraction grating.

The spectrophotometric measurements were carried out with a double-beam spectrophotometer (Konica Minolta CM-2600d), working in the wavelength range from 360 to 740 nm, with a sensitive area of 3 mm making up the L* a* b* coordinates of the CIE system, according to the following conditions: SCI / SCE, D65, 100% UV, observer at 10 °. The samples were analyzed in fine powder form and in quantities of a few mg.

Table 2.4. Capabilities of the different techniques mentioned in this work.

	LA-ICP-MS	**SEM-EDX**	**EPMA-WDS**	**UV-Vis Reflectance spec.**
Data	Quantitative	Semi-quantitative	Quantitative	Qualitative
Detection limit	< μg g^{-1}	0.5 wt.% for most elements	> 500 ppm	5-10%
Beam size	5-200/300 μm	10-1000 nm	10-1000 nm	3 – 8 mm
Spatial Resolution	> 1 μm	< 1 μm	< 1 μm	
Detectable elements	Major, minor and trace	Major	Major, minor and trace	Coloring ions
Analyses	Bulk, surface, inclusions, mapping, depth profiling	Surface, inclusions, mapping, imaging (physical structure, topography), crystallography	Bulk, surface, inclusions, mapping	Identification of the coloring agents
Purposes in glass analysis	Silica sources, fluxing and stabilizing agents, coloring or opacifier agents, degradation phenomena	Opacifiers, degradation phenomena	Silica sources, fluxing and stabilizing agents, coloring or opacifier agents, degradation phenomena	Coloring and/or opacifier agents
Main limitations for glass analysis	- Size of the sample for some laser ablation chambers - Minimum amount of sample required for analysis (μg) - Elemental fractionation effect	-Sample preparation, -Sample size, -Limited detection of elements below Na in the periodic table (e.g. B), Detection limit depending on the element	-Sample preparation, -Sample size, -Limited detection of elements below Na in the periodic table, -X-ray detection limit depending on the element -no isotopic analysis	- Information related only to the oxidation state of the ions - Better performances with glass powder

2.4. Samples

For the development of the different laser ablation modes (depth profiling, 2D and 3D mapping) several archaeological and historical glasses were selected on the basis of their characteristics (different types of deterioration as a result of age, chemical composition and/or exposure conditions).

For the development of 2D elemental mapping methodologies two polychrome glass samples were preferred for a preliminary study of association between the elements, in order to obtain information about sands, chromophores, fluxes, opacifiers and minerals. 2D mapping was also applied to study the surface degradation of mirror glasses by EPMA - WDS mapping.

For the development of 3D mapping methodologies a weathered ancient glass fragment from a drinking glass was used.

Bulk analysis was performed on different set of samples from diverse archaeological sites, in order to answer at specific questions related to the technology and provenance of the artifacts, e.g. (in order of importance):

- What is it made of? (i.e. mineral soda or plant ash)
- How was it made? (blown, cast, machine made)
- What color is it? (subjective perception, metamerism)
- From what colorant? (i.e. pigment)
- What diagnostic features does it have? (Rim, base, folds, decoration)

More information related to the samples are found in the following chapters.

2.5. References

Asogan D., Sharp B.L., O' Connor C.J.P., Green D.A. and Hutchinson R.W. (2009) An open, non-contact cell for laser ablation-inductively coupled plasma-mass spectrometry, J. Anal. At. Spectrom. 24; pp. 1012-1017.

Becker J. S., Zoriy M., Matusch A., Wu B., Salber D., Palm C. (2010) Bioimaging of metals by laser ablation inductively coupled plasma mass spectrometry (LA-ICP-MS), Mass Spectrom. Rev., 29; pp. 156–175.

Bertini M., Izmer A., Vanhaecke F., Krupp E.V. (2013) Critical evaluation of quantitative methods for the multi-elemental analysis of ancient glasses using laser ablation inductively coupled plasma mass spectrometry, J. Anal. At. Spectrom. 28; pp. 77–91.

Bleiner D. and Günther D. (2001) Theoretical description and experimental observation of aerosol transport processes in laser ablation inductively coupled plasma mass spectrometry, J. Anal. At. Spectrom, 16(5); pp. 449-456.

Brill R.H. (1999) Chemical analyses of early glasses. The corning museum of glass. Corning, New York.

Cagno S., Favaretto L., Mendera M., Izmer A., Vanhaecke F., Janssens K. (2012) Evidence of early medieval soda ash glass in the archaeological site of San Genesio (Tuscany), J. Archaeol. Sci. 39(5); pp. 1540–1552.

Chirinos J.R., Oropeza D.D., Gonzalez J.J., Hou H., Morey M., Zorba V. and Russo R.E. (2014) Simultaneous 3-dimensional elemental imaging with LIBS and LA-ICP-MS, J. Anal. At. Spectrom. 29; pp. 1292-1298.

De Raedt I., Janssens K., Veeckman J., Vincze L., Vekemans B. and Jeffries T.E. (2001) Trace analysis for distinguishing between Venetian and façon-deVenise glass vessels of the 16th and 17th century, J. Anal. At. Spectrom. 16, pp. 1012-1017.

Dussubieux L., Golitko M., Ryan Williams P., Speakman R.J. (2007) In Glascock M.D., Speakman R.J., Popelka-Filcoff R.S. (Eds.) Archaeological chemistry, analytical techniques and archaeological interpretation 968; pp. 349–363.

Dussubieux L., Robertshaw P., Glascock M.D. (2009) LA-ICP-MS analysis of African glass beads: laboratory inter-comparison with an emphasis on the impact of corrosion on data interpretation, Int. J. Mass Spectrom. 284(1–3); pp. 152–161.

Glaus R., Koch J. and Günther D. (2012) Portable Laser Ablation Sampling Device for Elemental Fingerprinting of Objects Outside the Laboratory with Laser Ablation Inductively Coupled Plasma Mass Spectrometry, Anal. Chem. 84 (12); pp. 5358-5364.

Glaus R., Ladina D., Zhang Z., Ma Q., Berkec H. and Günther D. (2013) Isotope ratio determination of objects in the field by portable laser ablation sampling and subsequent multicollector ICPMS, J. Anal. At. Spectrom., 28; pp. 801-809.

Gratuze B., Blet-Lemarquand M. and Barrandon J.N. (2001) Mass spectrometry with laser sampling: A new tool to characterize archaeological materials, J. Radioanal. Nucl. Ch., vol. 247, 3; pp. 645-656.

Gratuze B. (2013) In: Janssens K. (ed) Modern methods for analyzing archaeological and historical glass, 1st edn. JohnWiley & Sons, Ltd, Chichester; pp 201–234.

Gray A. L. (1985) Solid sample introduction by laser ablation for inductively coupled plasma source-mass spectrometry, Analyst, 110(5); pp. 551-556.

Guillong M. and Günther D. (2002) Effect of particle size distribution on ICP-induced elemental fractionation in laser ablation-inductively coupled plasma-mass spectrometry., J. Anal. At. Spectrom., 17; pp. 831–837.

Günther D. and Hattendorf B. (2005) Solid sample analysis using laser ablation inductively coupled plasma mass spectrometry, TrAC Trends Anal Chem 24(3); pp. 255-265.

Hench L.L. (1975) Characterization of glass corrosion and durability, J. Non-Cryst. Solids 19(C); pp. 27–39.

Horn I., Rudnick R.L., McDonough W.F. (2000) Precise elemental and isotope ratio determination by simultaneous solution nebulization and laser ablation-ICP-MS: application to U–Pb geochronology, Chemical Geology, 164; pp. 281-301.

Limbeck A., Galler P., Bonta M., Bauer G., Nischkauer W. and Vanhaecke F. (2015) Recent advances in quantitative LA-ICP-MS analysis: challenges and solutions in the life sciences and environmental chemistry, Anal Bioanal Chem, 407 (22); pp. 6593-6617.

Liu Y., Hu Z., Gao S., Günther D., Xu J., Gao C., Chen H. (2008) In situ analysis of major and trace elements of anhydrous minerals by LA-ICP-MS without applying an internal standard, Chemical Geology*,* 257; pp. *34*–43.

Longerich H. P., Jackson S. E. and Gunther D., (1996) J. Anal. At. Spectrom., 11; pp. 899-904.

Mank A.J.G. and Mason P.R.D. (1999) A critical assessment of laser ablation ICP-MS as an analytical tool for depth analysis in silica-based glass samples, J. Anal. Atom. Spectrom. 14; pp. 1143–1153.

Resano M., García-Ruiz E. and Vanhaecke F. (2010) Laser ablation inductively coupled plasma mass spectrometry in archaeometric research, Mass Spectrometry Reviews 29; pp. 55-78.

Russo R.E., Mao X.L., Borisov O.V. and Haichen Liu (2000) Influence of wavelength on fractionation in laser ablation ICP-MS, J. Anal. At. Spectrom., 15; pp. 1115-1120.

Russo R.E., Mao X., Liu H., Gonzalez J. and Mao S.S. (2001) Laser Ablation in Analytical Chemistry - -A Review, eScholarship University of California; pp. 1-49 (http://escholarship.org/uc/item/1vt758q7).

Šelih V.S., Van Elteren J.T. (2011) Quantitative multi-element mapping of ancient glass using a simple and robust LA-ICP-MS rastering procedure in combination with image analysis, Anal. Bioanal. Chem. 401; pp. 745-755.

Shortland A.J. and Schroeder H. (2009) Analysis of first millennium BC glass vessels and beads from the Pichvnari necropolis, Georgia, Archaeometry 51, 6, pp. 947-965.

Šmit Ž., Janssens K., Bulska E., Wagner B., Kos M., Lazar I. (2005) Trace element fingerprinting of façon-de-Venise glass, Nucl. Instr. Meth. Phys. Res. B 239, pp. 94-99.

Sylvester P. (2008) Matrix effects in LA-ICP-MS, in Laser Ablation ICp-MS in the Earth Sciences Current practices and outstanding issues (Ed.) Sylvester Paul, Short Course delivered in association with Goldschmidt 2008, Vancouver, B.C., 19–20 July; pp. 67-76.

Tanaka M., Takeguchi M. and Furuya K. (2008) Wavelength dispersive X-ray spectroscopy of thick and thin samples for electron microscopes, Surf. Interface Anal., 40; pp. 1684-1687.

Triglav J., Van Elteren J.T., Šelih V.S. (2010) Basic modeling approach to optimize imaging by laser ablation ICP-MS, Anal. Chem. 82; pp. 8153-8160.

Van Elteren J.T., Tennent N.H., Šelih V.S. (2009) Multi-element quantification of ancient/historic glasses by laser ablation inductively coupled plasma mass spectrometry using sum normalization calibration, Anal. Chim. Acta 644(1–2); pp. 1–9.

Van Elteren J.T., Izmer A., Šala M., Orsega E.F., Šelih V.S., Panighello S., Vanhaecke F. (2013) 3D laser ablation-ICP-mass spectrometry mapping for the study of surface layer phenomena-a case study for weathered glass, J. Anal. Atom. Spectrom. 28(7); pp. 994–1004.

Van Malderen S.J.M., van Elteren J.T. and Vanhaecke F. (2015) Submicrometer Imaging by Laser Ablation-Inductively Coupled Plasma Mass Spectrometry via Signal and Image Deconvolution Approaches, Anal. Chem. 87; pp. 6125-6132.

Vicenzi E.P., Eggins S., Logan A., Wysoczanski R. (2002) Microbeam characterization of corning archeological reference glasses: new additions to the Smithsonian microbeam standard collection, J. Res. Natl. Inst. Stan. 107(6); pp. 719–727.

Wagner B., Nowak A., Bulska E., Kunicki-Goldfinger J., Schalm O. and Janssens K. (2008) Complementary analysis of historical glass by scanning electron microscopy with energy dispersive X-ray spectroscopy and laser ablation inductively coupled plasma mass spectrometry, Microchim Acta 162, pp. 415-424.

Wagner B., Nowak A., Bulska E., Hametner K., Günther D. (2012) Critical assessment of the elemental composition of Corning archeological reference glasses by LA-ICP-MS, Anal. Bioanal. Chem. 402; pp. 1667–1677.

Woodhead J., Hellstrom J., Paton C., Hergt J., Grieg A., Maas R. (2008) In laser ablation-ICP-MS in the earth sciences: current practices and outstanding issues. In: Sylvester PJ (Ed.). Mineral Association of Canada, Vancouver, B.C., pp. 135–145.

Chapter 3
Development of depth profiling methodologies*

* Part of this chapter was published in Panighello *et al*. 2015 and presented at Glass reflections – Glass in the Year of Light, 7 - 9 September 2015, Cambridge (UK).

3.1. Introduction

In general the analysis of archaeological glass represents a challenge for a wide variety of objects because of the presence of physical and/or chemical damage on the surface of the artifact, also known as weathering or corrosion. To retrieve accurate bulk elemental information by laser ablation – ICP-MS, the original, pristine glass needs to be "reached", thereby penetrating the alteration layer which is often more than 10 µm thick. To study this alteration layer the laser is operated in the drilling mode, either with a low (1 Hz) or a high (10 Hz) pulse repetition rate for a period of 50 s yielding detailed spatial information for ca. 20 elements over a shallow depth (ca. 5 µm) or less-detailed spatial information for 50-60 elements over a greater depth (ca. 50 µm). Quantitative elemental depth profiles (in wt %) are obtained with the sum normalization calibration protocol presented in Chapter 2, based on summation of the elements as their oxides to 100 wt %.

The increase of SiO_2 (in wt %) in the alteration layer is associated to the volumetric mass density change in the glass as a result of depletion of Na_2O and K_2O. Also the interaction of the number of laser shots with the alteration layer is shown experimentally via depth measurements using profilometry.

Chemical and physical changes in four ancient glass artifacts, directly and indirectly measureable by laser drilling, are studied as a function of internal and external factors such as age, composition and exposure conditions.

3.2. Evaluation of depth profiling procedure

By choosing two LA spot analysis drilling procedures, viz. one based on 1 Hz drilling and ultrafast pulse monitoring of up to 20 elements, and the other one based on 10 Hz drilling and monitoring of a continuous signal for 50-60 elements. Element-depth relationships can be established for superficial layers less than 10 µm thick for the former drilling procedure and much ticker layers more than 50-100 µm thick for the latter drilling procedure. The latter procedure also allows for accurate measurement of bulk concentrations of heavily corroded artifacts but we need to be aware that a 10 Hz drilling regime gives less detailed and less accurate spatial depth information as the elemental concentrations retrieved are an average of several pulses whereas the 1 Hz drilling regime facilitates spatial resolution per shot with pulse mixing, signal tailing and thermal diffusion eliminated. In Table 3.1 the operational conditions are given for both LA drilling procedures and in Figure 3.1 the ICP-MS output for both depth profiling procedures is schematically illustrated.

Table 3.1. LA-ICP-MS operating conditions for the two LA spot analysis drilling procedures.

	1 Hz drilling	10 Hz drilling
Laser (NWR UP213)		
Beam diameter	100 µm	100 µm
Fluence	7.5 J/cm^{-2}	7.5 J/cm^{-2}
Repetition rate	1 Hz	10 Hz
Penetration rate	ca. 0.1 µm s^{-1}	ca. 1.1 µm s^{-1}
Dwell time	50 s	50 s
ICP-MS (Agilent 7500ce)		
Number of elements measured	20 (^{23}Na, ^{24}Mg, ^{27}Al, ^{29}Si, ^{31}P, ^{39}K, ^{43}Ca, ^{55}Mn, ^{57}Fe, ^{59}Co, ^{60}Ni, ^{63}Cu, ^{66}Zn, ^{88}Sr, ^{90}Zr, ^{115}In, ^{118}Sn, ^{121}Sb, ^{137}Ba, ^{208}Pb)	54 (^{7}Li, ^{9}Be, ^{11}B, ^{23}Na, ^{24}Mg, ^{27}Al, ^{29}Si, ^{31}P, ^{39}K, ^{43}Ca, ^{45}Sc, ^{47}Ti, ^{51}V, ^{53}Cr, ^{55}Mn, ^{57}Fe, ^{59}Co, ^{60}Ni, ^{63}Cu, ^{66}Zn, ^{69}Ga, ^{75}As, ^{82}Se, ^{85}Rb, ^{88}Sr, ^{89}Y, ^{90}Zr, ^{93}Nb, ^{95}Mo, ^{107}Ag, ^{111}Cd, ^{115}In, ^{118}Sn, ^{121}Sb, ^{137}Ba, ^{139}La, ^{140}Ce, ^{141}Pr, ^{146}Nd, ^{147}Sm, ^{153}Eu, ^{157}Gd, ^{159}Tb, ^{163}Dy, ^{165}Ho, ^{166}Er, ^{169}Tm, ^{172}Yb, ^{175}Lu, ^{197}Au, ^{208}Pb, ^{209}Bi, ^{232}Th, ^{238}U)
Total acquisition time (per element)	60 ms (1 ms per element)	0.64 s (10 ms per element)

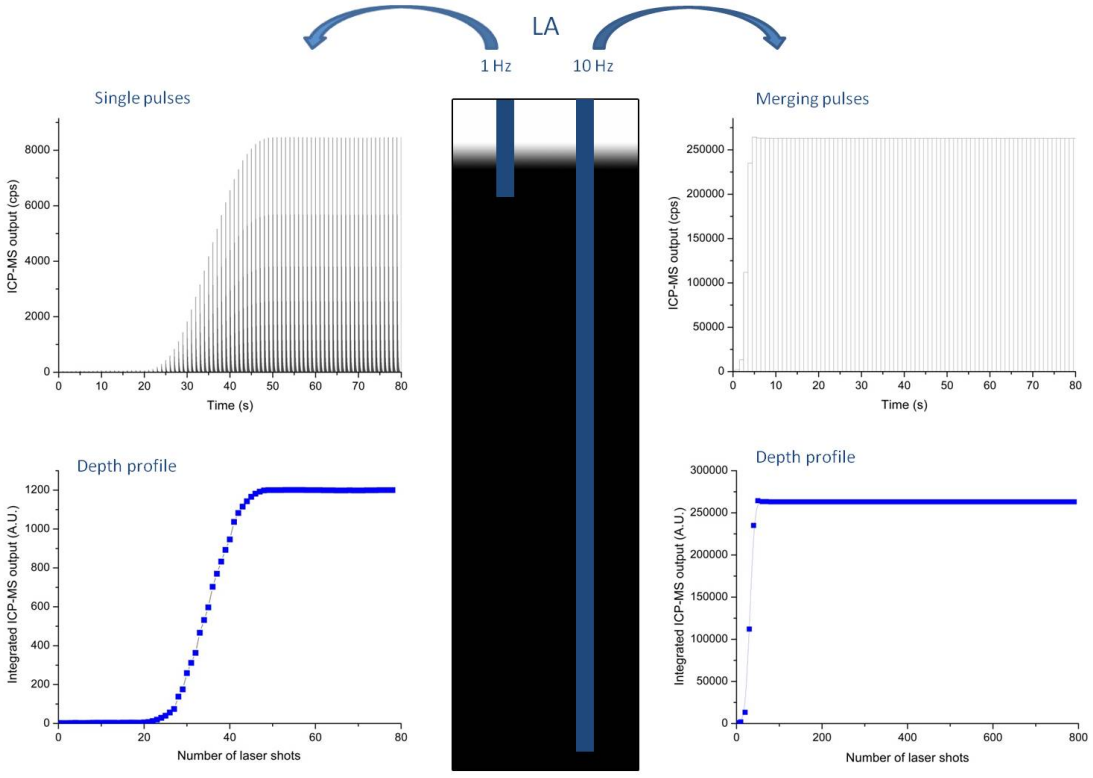

Figure 3.1. Illustration of the two laser drilling procedures (1 and 10 Hz) applied to a corroded glass (white = corroded glass, black = pristine glass); in both cases the dwell time was identical (80 s) but the pristine glass (at ca. 5 µm depth from the surface) was reached in ca. 50 and 5 s for the 1 and 10 Hz drilling procedure, respectively. The ICP-MS output associated with a depleted element were either peaks related to single pulses in the 1 Hz drilling procedure or user-selected time intervals for the 10 Hz drilling procedure. Upon integration of the peaks or averaging over the user-selected time intervals, and subsequent sum-normalization (see section 3.3.), the elemental depth profiles were obtained.

3.3. Quantification protocol

Conversion of the individual LA-ICP-MS depth profile data *I(N)* (in cps for *N* laser shots) to concentration data (in wt %) is performed with a previously reported sum normalization routine (see Chapter 2) (van Elteren *et al*., 2009; Šelih and van Elteren, 2011), summating *n* elements (54 major, minor and trace elements for the 10 Hz drilling procedure or 20 major and minor elements for the 1 Hz drilling procedure, see Table 3.1) as their oxides to 100 wt % upon drilling through the alteration layers (for most samples this might only be achieved with the 10 Hz drilling procedure). For internal standardization SiO_2 was used, without actually knowing the concentration in the samples, by converting the elemental ICP-MS depth profile data $I_i(N)$ for each element *i*. To this end the output $I_{i,corr}(N)$ was calculated, i.e. $I_i(N)$ corrected for ablation differences through division by $(I_{Si}(N)/50)$, with 50 being the arbitrary SiO_2 concentration in wt %.

This procedure also corrects for potential output changes as a result of ablation variations due to pulse inconsistency and/or depth-related issues. For the calibration standards a similar protocol was followed but now with known SiO_2 concentrations yielding average elemental sensitivities R_i for each element *i*.

The individual elemental oxide concentrations in the depth profile, based on a SiO_2 concentration of 50 wt %, are given by $I_{i,corr}(N)/R_i$. After summation ($\sum[I_{i,corr}(N)/R_i]$) and normalization to 100 wt %, the actual elemental oxide wt % concentrations $c_{wt,i}(N)$ in the depth profiles (= $\{I_{i,corr}(N)\times100\}/\{\sum[I_{i,corr}(N)/R_i]\times R_i\}$) are found, with the SiO_2 wt % concentration $c_{wt,Si}(N)$ automatically corrected to its true value. This calibration approach shows gradually decreasing SiO_2 wt % concentrations $c_{wt,Si}(N)$ with depth (= number of shots *N*) in the glass for all ancient artifacts (see section 3.6), and concomitant increasing alkali and alkaline earth element concentrations, until the pristine glass is reached ($N=\infty$). However, it is reasonable to assume that for high-silica content glass [SiO_2 : Na_2O or K_2O ratios around 3 (Paul, 1977)] the SiO_2 vol % concentrations ($c_{vol,Si}(N)$) with depth (= number of shots *N*) remain constant ($c_{vol,Si}$). This implies that the glass densities are gradually decreasing towards to glass surface ($N=0$). Alteration layer densities D_N (in g cm^{-3}) as a function of the number of shots *N* were derived from the relationship $D_N = c_{vol,Si}/c_{wt,Si}(N)$, where $c_{vol,Si}$ was calculated from $c_{wt,Si}(\infty)\times D_\infty$, with $c_{wt,Si}(\infty)$ the SiO_2 wt % concentration in the pristine glass and D_∞ the theoretical glass density derived from the composition of the pristine glass after (Fluegel, 2007).

The retrieval of volumetric mass density profiles D_N for glass alteration layers is schematically illustrated in Figure 3.2.

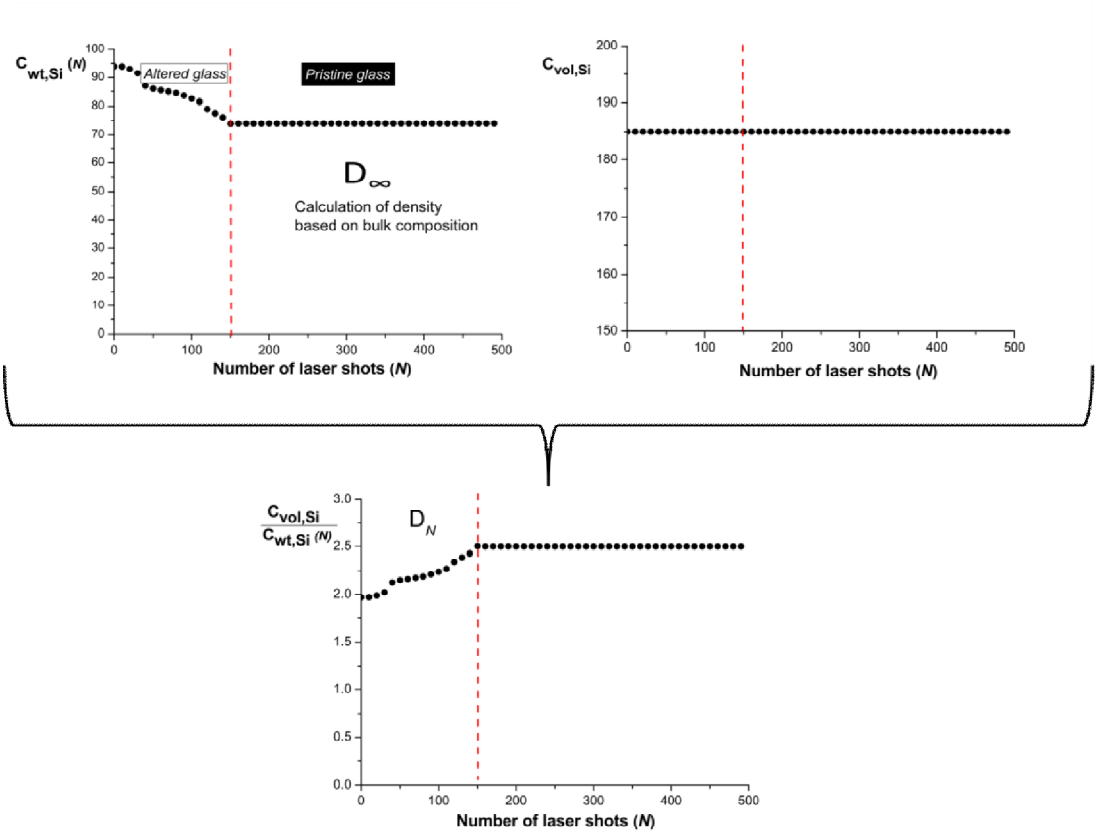

Figure 3.2. Illustration of the quantification protocol for the volumetric mass density profiles.

In Figure 3.3 the calibration routines are illustrated for a hypothetical, weathered glass with different compositions in the pristine bulk and the leached layer depleted in alkali ions. For some samples in this study it was found that the summated oxide concentrations in the alteration layers can be up to ca. 20 wt % lower than in the pristine glass.

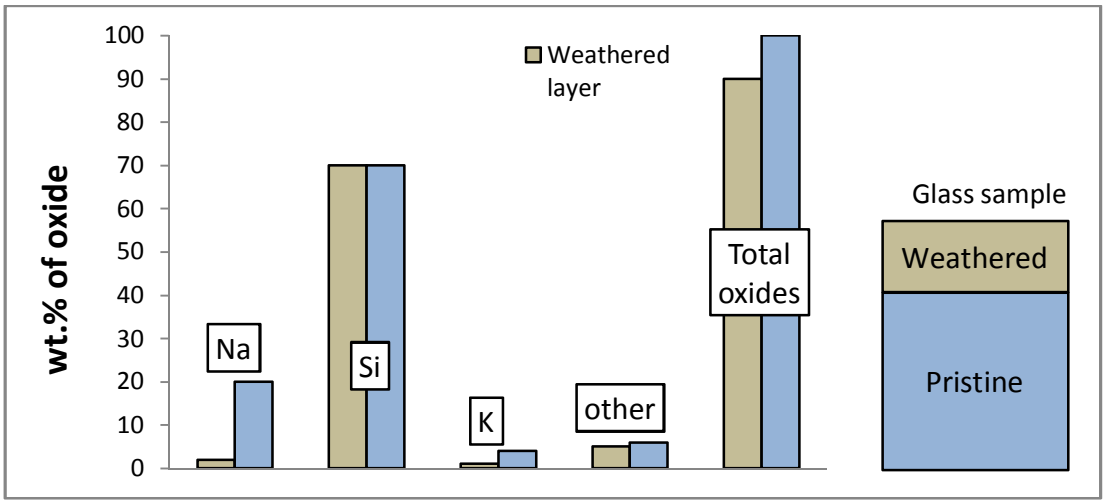

Figure 3.3. Elemental composition in a hypothetical weathered glass in the pristine bulk and the outermost weathered layer; with the sum normalization calibration protocol all the elements in the pristine glass are normalized to 100 wt %, whereas with the modified calibration protocol the correct elemental concentrations were deduced for the outermost weathered layer using the SiO_2 concentration in the pristine bulk as an internal standard concentration.

3.4. Samples

Several archeological, degraded glasses, presenting different types of deterioration as a result of age, chemical composition, and/or exposure conditions, were selected for this study. As shown in Figure 3.4, these samples are (a) an uncolored Roman glass found at an archeological site in Tortosa, Spain (first–second century CE), with an iridescent surface layer that produces optical interference patterns; (b) a blue-green glass bead (FK002) with an altered, porous surface from Fukuchani, Zanzibar, Tanzania, excavated at an archeological site dating from sometime between the sixth and early tenth century; (c) a gold-glass bead or metal-foil bead, highly corroded and found in Tanzania (village of Kaole, dating from the thirteenth to sixteenth century CE), with thick corrosion layers which make it difficult to recognize the location of the metal foils; and (d) a fragment (CMG 449, Corning Museum of Glass) of an eighteenth century French wine glass with a “crizzled” or “weeping” surface (Newton, 1985; Koob, 2006), showing a network of small cracks when magnified (×40).

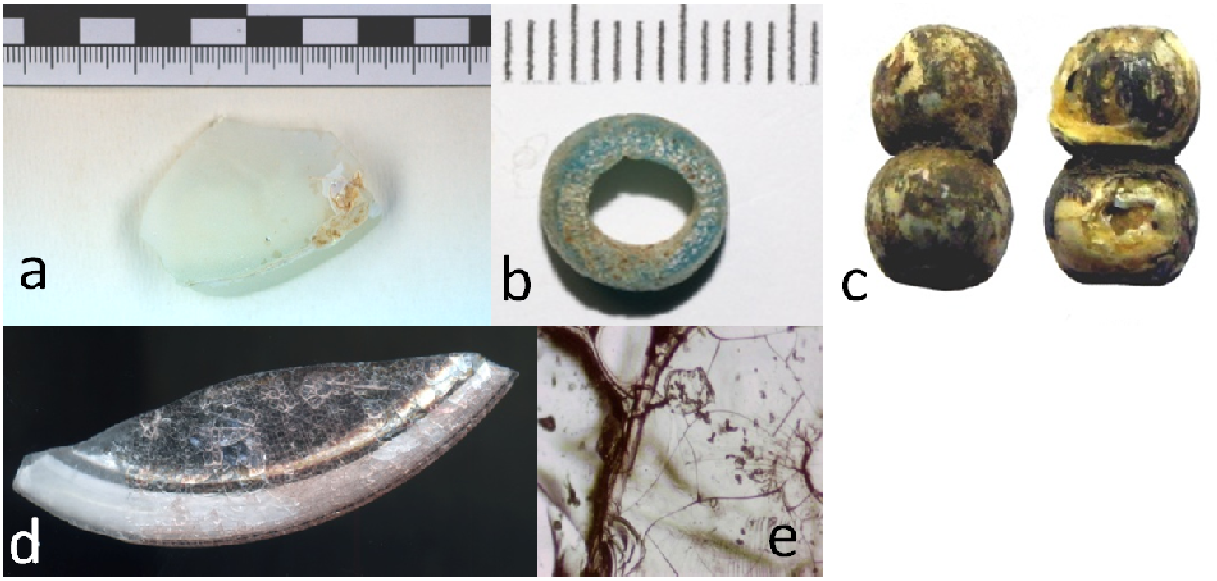

Figure 3.4. Selected glass artifacts with visible alteration layers: Roman glass (a), African glass bead (b), metal-foil glass bead (c), crizzled glass CMG 449 (d) and magnified details [x40]of CMG 449 sample (e).

3.5. Validation of depth profiling procedure

Depth calibration was attempted through ablation of a very homogeneous industrial glass (chemical composition and more details of this glass can be found in van Elteren *et al*., 2013) and the Roman glass sample (Figure 3.4a); profilometry was used to measure the depth of the craters. To this end 100 µm ablation craters were produced with different depths using a laser fluence of 7.0 J cm^{-2}, a repetition rate of 1 or 10 Hz and various dwell times (from 2 to 160 s). In this way the crater depths can be associated with the number of laser shots for both the 1 and 10 Hz laser ablation depth profiling procedures described in section 3.2. In Figure 3.5 it can be observed that for the industrial glass with the 1 Hz procedure (number of laser shots: 2, 5, 10, 20 and 50) the shot-depth linear correlation is very good, whereas for the 10 Hz procedure (number of laser shots: 200, 300, 500, 700, 1000 and 1600) the shot-depth linear correlation start to deviate from linearity. When merging the data of both methods they could be fitted well

(R^2=0.9985) by an asymptotic exponential curve (y = a[1-e^{-bx}]). The linear part of the graph (0-50 shots) falls within its uncertainty limit on the exponential curve; the higher 10 Hz shots seem to reach an asymptote, probably due to particles not escaping from the crater effectively as reported by Mank and Mason, 1999, and misfocusing, as during drilling the laser is focused on the surface of the glass all the time. It should be noted that due to non-linearity in the depth calibration at higher shot numbers (Figure 3.5) a visible "compacting" of measurement points emerges (seen in most Figures in section 3.6). However, application of this depth calibration approach to (heavily) corroded glass artifacts was not so straightforward, probably due to surface roughness, cracks, unevenness, etc., resulting in inaccurate depth calibration as shown in Figure 3.5 for the Roman glass sample. We can observe a rather erratic laser sampling process for the first 300 shots, with an initial fast upshot followed by a sharp decrease. This suggests a more efficient ablation efficiency of the alteration layer than the industrial glass, but with a high degree of instability as it seems to collapse on/in itself, thereby restarting ablation of the collapsed material. Thus, the ablation behavior of (severely) corroded artifacts is strongly influenced by the composition, heterogeneity, morphology, etc. of the alteration layers, making depth calibration unreliable. For this purpose we omitted the depth calibration approach and used shots to indicate the penetration of the glass and construct depth profiles indicating elemental oxide wt % concentrations vs. number of shots.

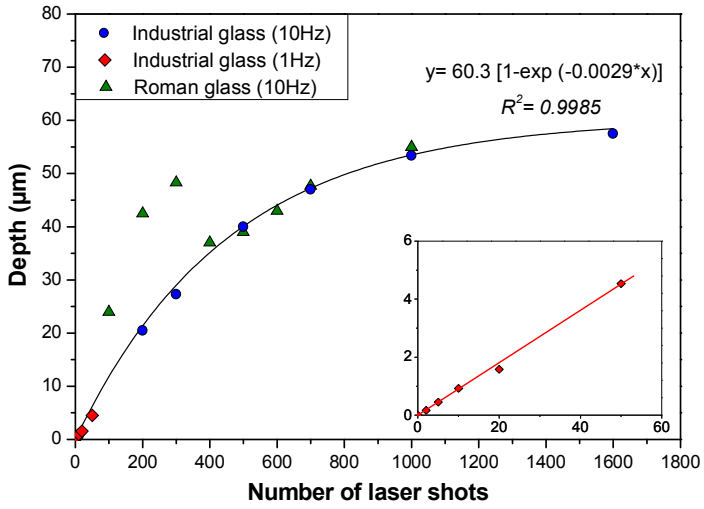

Figure 3.5. Depth vs. applied number of laser shots for a homogeneous glass upon laser ablation with the 1 Hz and 10 Hz depth profiling procedures and a best fit with an exponential asymptotic curve. The insert shows the linear fit of the depth vs. applied number of laser shots by the 1 Hz procedure. The 10 Hz depth profiling ablation procedure was applied to a real corroded sample (Roman glass).

To analytically validate the LA-ICP-MS depth profiling procedures described in section 3.2., the glass reference standard NIST SRM 610 was subjected to laser drilling (five spots) with a beam diameter of 100 µm and repetition rates of 1 or 10 Hz and ICP-MS recording of 20 or 54 elements, respectively. In Figure 3.6 the results for both depth profiling procedures are given for Na_2O, Al_2O_3 and ZnO, after quantification by sum normalization, showing good agreement between both procedures during the first 50 shots of the depth profile. Additionally, the depth profiles obtained with the 10 Hz procedure are constant up to a depth of ca. 500 shots with average concentrations matching the reference values in the GeoRem database (see inserted tables in Figure 3.6). These results indicate that depth profiling with both procedures yields accurate data for a small depth (<50 shots) with high resolution using the 1 Hz procedure and for a larger depth (<500 shots) with lower resolution using the 10 Hz procedure.

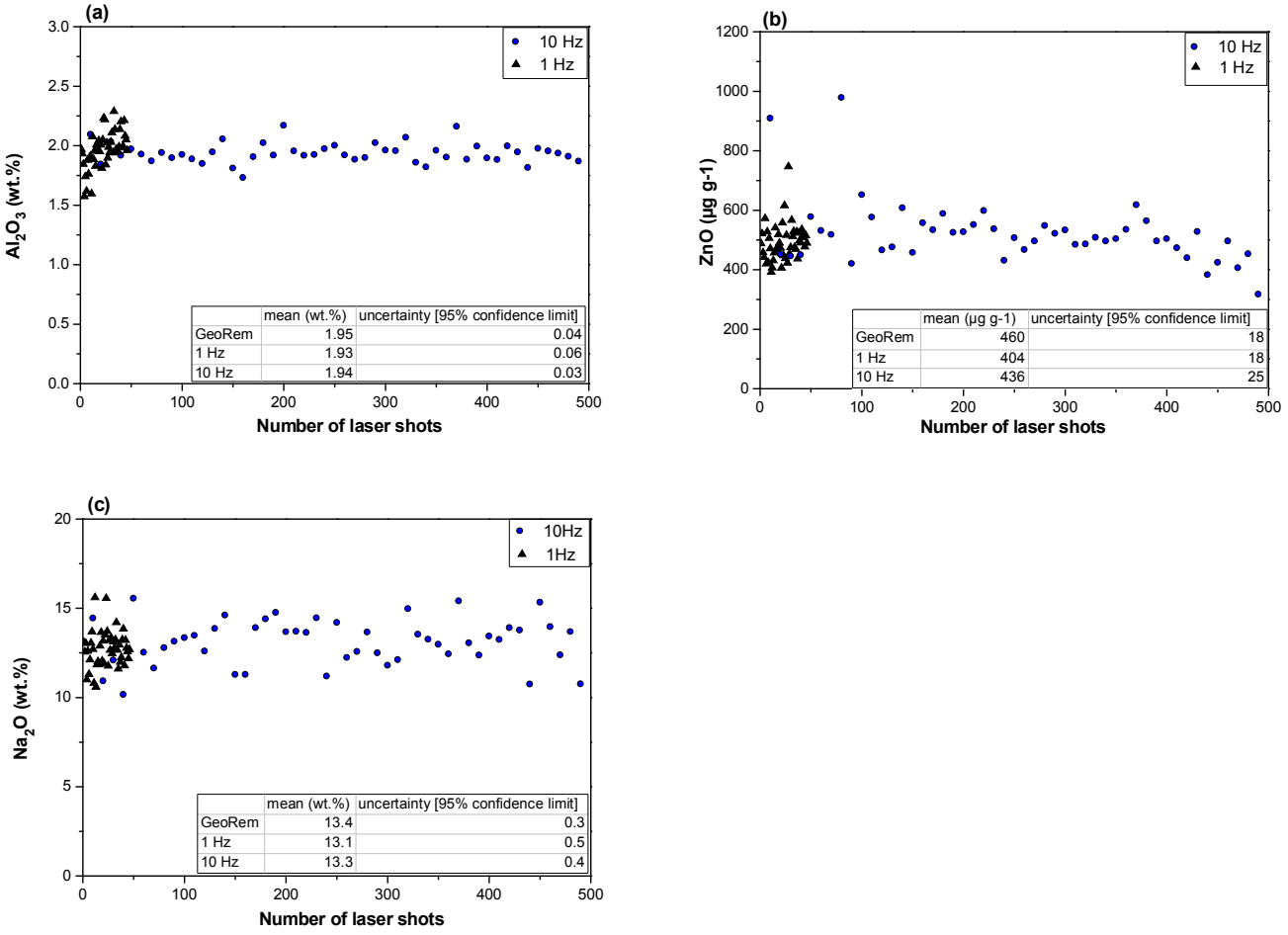

Figure 3.6. Typical depth profiles for Al_2O_3 (a), ZnO (b) and Na_2O (c) in NIST SRM 610 with 1 and 10 Hz drilling procedures. In the insert tables GeoRem preferred data (mean ± uncertainty [95% confidence limit]) are reported for Al_2O_3, Zn and Na_2O in NIST SRM 610, and compared to the results (mean ± uncertainty [95% confidence limit]) obtained with the two LA drilling procedures.

3.6. Depth profiling of various weathered glasses by LA-ICP-MS

The wide range of variables affecting the depth profile analysis of a weathered glass needs caution when interpreting the results. The depth profiling procedures developed may reveal systematic changes in glass composition with depth and give an indication about the elemental concentration and the type of degradation, but a general knowledge of the material and its alteration processes is essential. The chemical structure of an altered glass can contain several layers with different volumetric mass densities and include cracks, flaking surfaces, etc. which may affect the ablation process.

The symptoms of glass degradation reflect the chemical instability as a consequence of the manufacturing technology and the exposure of the glass to particularly aggressive environments. In aqueous corrosion, leached alkali ions are removed by the leaching solution, but the weathered glass surface retains the leached alkali ions, which accumulate and may lead to salt formation. Depth profiling by LA-ICP-MS appears to be the perfect analytical tool to characterize these kind of artifacts because it

respects the integrity of all the layers of the object (altered or not), but we must realize that the altered surface has a different chemical/physical composition then the pristine glass.

The glass artifacts studied here (Figure 3.4) originate from different historical periods and different environmental conditions. The Roman and African glasses, buried for centuries in moist soil, show heterogeneous and laminated surfaces. In general the studied African beads present corroded layers thicker than the Roman glasses because of their less stable chemical composition (Table 3.2) and different burial history. The data indicate that leaching must have been the main degradation mechanism based on SiO_2 : Na_2O or K_2O ratios around 3 (Paul, 1977), justifying the assumption of a constant SiO_2 vol % concentration from the pristine glass to the outermost alteration layer, enabling retrieval of volumetric mass density depth profiles according to the procedure described in section 3.3. In the remainder of the document the volumetric mass density profiles of all glass artifacts shown in Figure 3.4 will be compared and related to the Na_2O+K_2O concentrations.

Table 3.2. Chemical composition of the bulk (averaged for a depth of about 50 µm, obtained with the 10 Hz drilling procedure) of Roman glass, African bead, metal-foil glass and crizzled glass (in wt % of the major and some minor oxides); the mean and standard deviation for 5 measurements are given. The metal-foil beads consisted of several layers which made retrieval of an exact bulk concentration difficult; for this reason the data for this artifact are given in brackets.

	Roman glass	**African bead**	**Metal-foil bead**	**Crizzled glass**
	mean±sd (wt %)	mean±sd (wt %)	mean±sd (wt %)	mean±sd (wt %)
Na_2O	20.8±0.8	20.8±0.2	(0.97±0.52)	0.85±0.06
MgO	0.45±0.02	0.325±0.003	(0.93±0.36)	0.049±0.004
Al_2O_3	1.78±0.06	9.15±0.05	(6.5±0.9)	0.66±0.05
SiO_2	69.7±0.9	61.7±0.3	(79.1±3.3)	75.7±0.8
P_2O_5	0.021±0.003	0.038±0.001	(0.11±0.04)	0.09±0.01
K_2O	0.396±0.043	2.13±0.01	(0.15±0.07)	19.7±2.2
CaO	5.2±0.4	2.44±0.03	(7.1±1.7)	0.44±0.04
MnO	0.015±0.001	0.064±0.002	(0.4±0.2)	0.87±0.05
Fe_2O_3	0.35±0.03	1.469±0.027	(2.6±0.4)	0.140±0.004
CuO	0.001±0.000	0.874±0.009	(0.004±0.000)	0.005±0.000
SrO	0.041±0.003	0.037±0.001	(0.060±0.004)	0.003±0.000
ZrO_2	0.007±0.001	0.090±0.003	(0.039±0.006)	0.017±0.002
Sb_2O_5	0.99±0.08	0.001±0.000	(0.000±0.000)	0.000±0.000
PbO	0.001±0.0002	0.087±0.002	(0.011±0.004)	0.001±0.000

3.6.1. Roman glass

The Roman glass (Figure 3.4a) is a soda-lime-silica based glass with a low content of potassium, magnesium and phosphorus oxides, indicating the inorganic origin of the flux (*natron*). It is transparent and uncolored with Sb_2O_5 as a decolorizing agent (Table 3.2). It presents iridescent lamellae as alteration products, mainly composed of a hydrated silica gel, due to depletion of alkali and alkaline earth elements. The optical phenomena are due to the interaction between light and silica layers containing metallic ions interspersed with air. These chemical changes are further revealed by the depth profiles of Na_2O and K_2O (Figure 3.7). The depth profiles by the 1 Hz drilling procedure suggest a silica-rich protective layer on the top of the glass due to selective alkali leaching and the depth profiles by the 10 Hz drilling procedure indicate that after about 350 shots it is possible to assume the end of the corroded layer and to calculate the composition of the pristine glass. At first glance the unusual decrease of Na_2O and K_2O at the surface (Figure 3.7a) looks like an analytical artifact; however, the "raw" depth profiles in counts per second (not shown) have the same decreasing trend. Since the glass was buried for centuries it is challenging to try to understand the real reason for this behaviour. It is possible that the top alteration layer has weathered much less than deeper alteration layers (Newton, 1971) and that in this top alteration layer there are mineral compounds such as carbohydrates, nitrates and sulfates that may have immobilized the elemental cations.

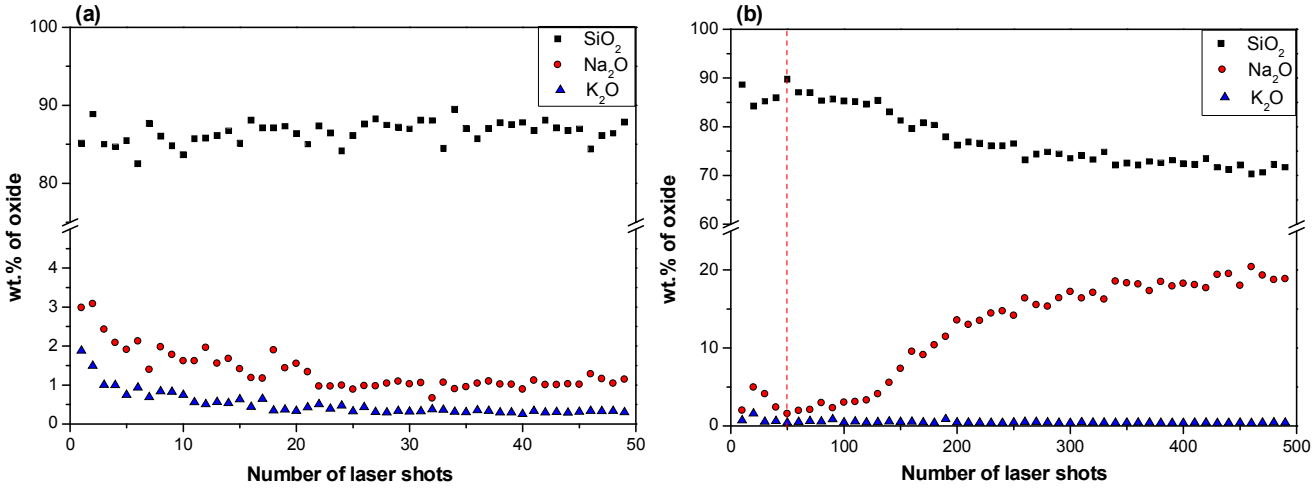

Figure 3.7. LA-ICP-MS depth profiling on the Roman glass; 1 Hz (a) and 10 Hz (b) drilling; the vertical dashed line in (b) shows the limit of the 1 Hz drilling procedure

3.6.2. African glass bead

At the glass-corrosion interface of an African glass bead (Figure 3.4b) a depletion of soda is evident, with concentrations from 0.9 to 20 wt % (Figure 3.8a). Normally corroded glass is depleted in Na, K, Mg and Ca, depending on the type of corrosion, i.e. atmospheric or underground. In this case there is an enhancement of magnesia, potash, lime and alumina (not shown) in the corroded layer compared to the pristine glass (Figures 3.8a and b and Table 3.2). This is due to the precipitation of mineral phases from the soil onto the glass surface. The presence of potassium in the soil can be due to its composition (feldspars, clays) or could indicate the past occurrence of a fire and the subsequent production of potassium carbonate or wood ashes (Dussubieux *et al.*, 2009). The penetration of an element into the leached glass diminishes the gradient of the chemical potential of the element at the solid/liquid interface, hindering diffusion of the associated cation from the glass to the outside. Most of the heavy metals/trace elements (Mn, Cu, Ti and Zr) present positive concentration gradients from the bulk to the surface in the first corroded layer (about 50 shots, see Figures 3.8c and d). This indicates that they probably originate from the soil.

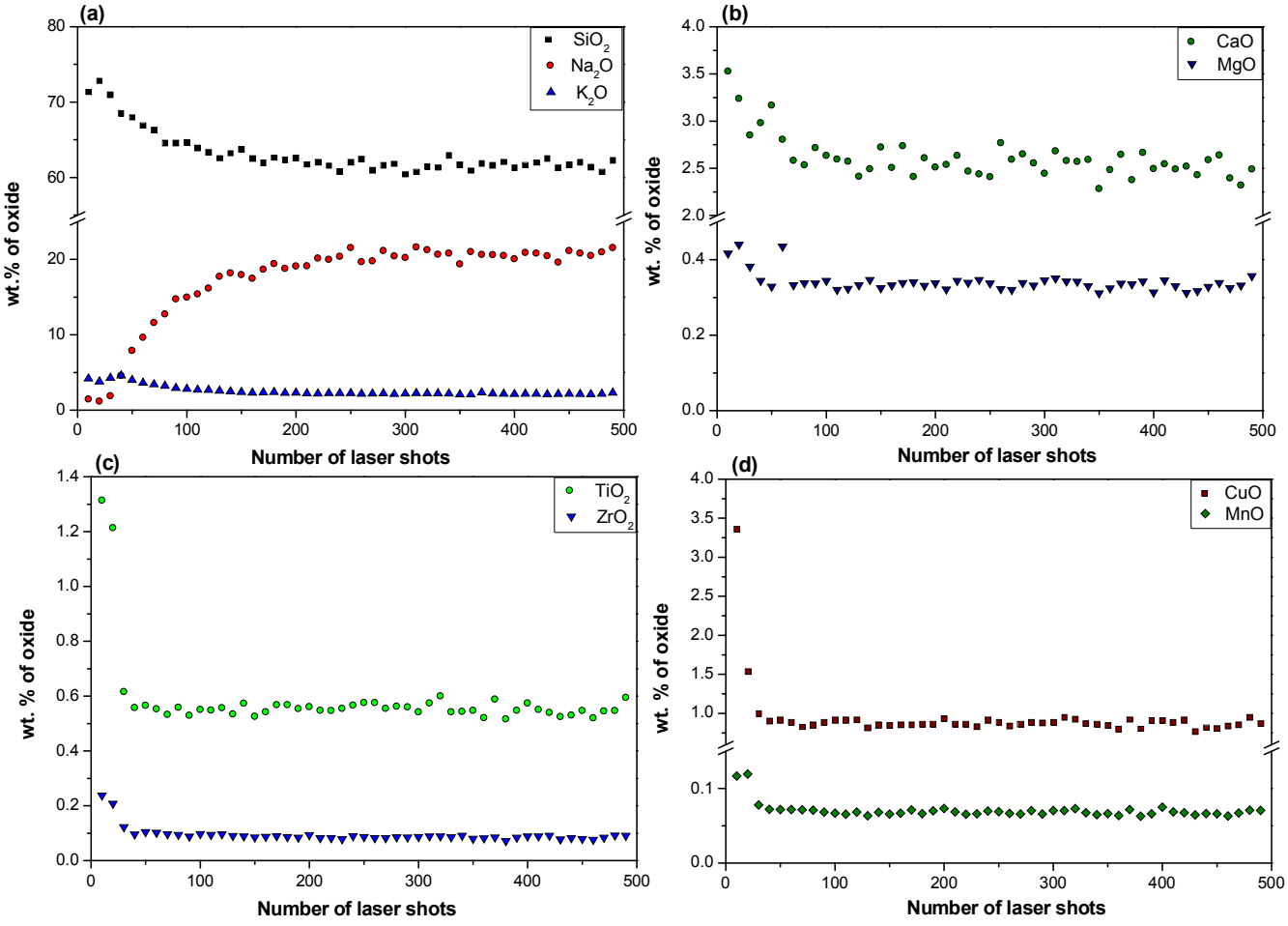

Figure 3.8. LA-ICP-MS depth profiling on the African blue-green bead from the archaeological site of Fukuchani (Zanzibar) for various elements with the 10 Hz drilling procedure.

3.6.3. Metal-foil glass bead

In the case of a highly or extremely corroded glass (Figure 3.4c) the analysis cannot produce data from which one can easily reconstruct the initial composition of the glass (Table 3.2). This is the case with the so-called metal–foil glass beads found in the village of Kaole, Tanzania. Their main feature is the technology of production with a three-layered sandwich structure: *gold or silver foil is wrapped over a clear glass tube which is then encased in another slightly larger tube. That assembly is reheated and pinched at intervals to form a long tube of bead shapes. These are later cut into single or multiple beads* (Greiff and Nallbani, 2008; Sode *et al*., 2010; Wood M. personal communication). The layered structure of one of the beads is evident in Figure 3.4c, where part of the outer layer is missing and the metal layer is visible. The laser was operated in the 10 Hz drilling mode at five different microlocations to get information about the composition of the depth layers without cutting the sample. Compositional variation and corrosion layers make it difficult to give an interpretation of the data resulting in craters with different elemental profiles. From Figure 3.9 it is evident that at a depth associated with 500 shots there is still corrosion measurable; the depth profiles show the presence of subsequent layers with different elemental composition. They show an apparent enrichment of SiO_2 and alumina, followed by their gradual decrease towards the inside, after 350 shots. The Na_2O, K_2O, CaO and MgO depth profiles, after a flat trend in the 0-350 shot range, show a sharp rise at the interface around 350 shots (Figures 3.9b and c). This enhancement is markedly pronounced in the case of CaO, which concentration increases from about 5 to 14 wt %. Similar to the African glass bead discussed above, some of the heavy metals are present at very high levels on the surface of the glass; in Figure 3.9c it can be seen that Fe_2O_3 in the depth profile ranges from 2.5 to 7.5 wt %.

Even though the concentrations of Au and Ag cannot be established correctly due to heterogeneity issues, and the fact that we use the sum normalization routine based on oxides for data processing, we can clearly see their presence (Figure 3.9d). Although this particular metal-foil glass bead artifact is highly corroded and causes problems to reconstruct the original composition of the glass, this is not characteristic for glass beads of this period (13th-16th century), but mainly due to corrosion phenomena such as soil composition and burial conditions such as pH, moisture content and temperature.

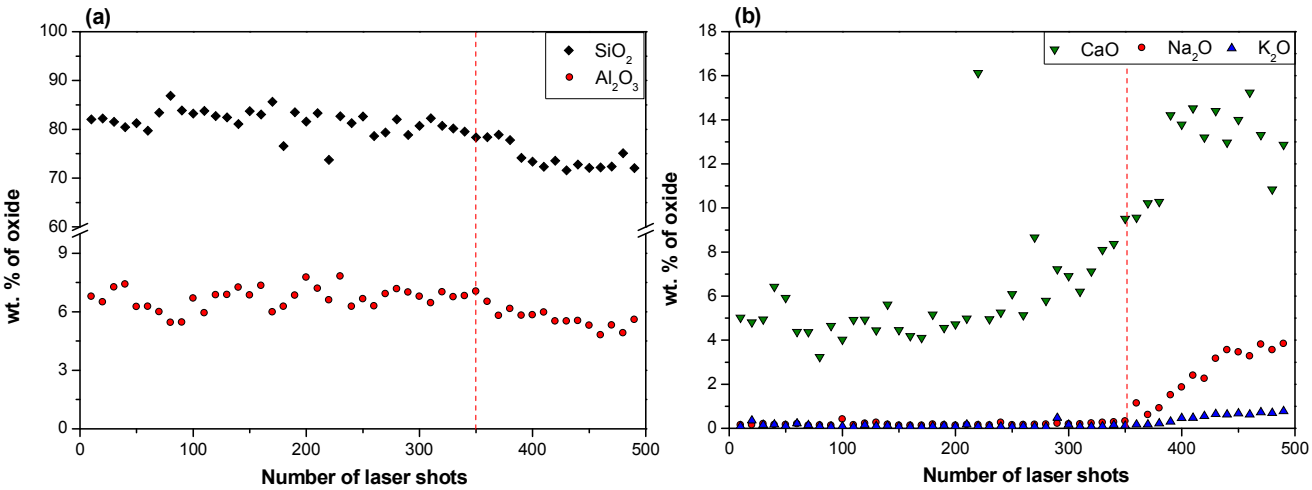

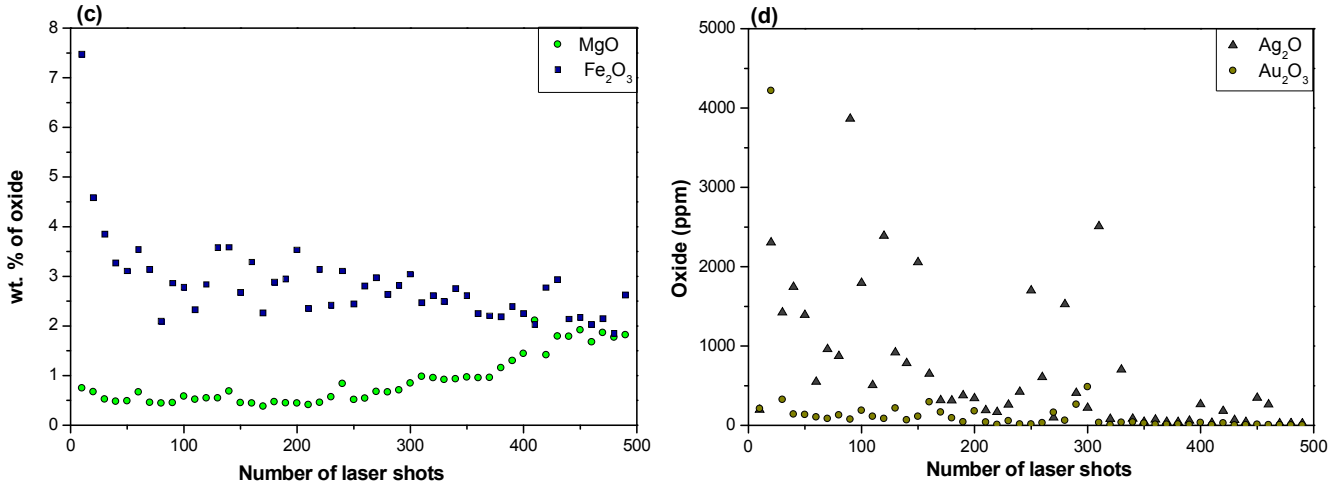

Figure 3.9. LA-ICP-MS depth profiling on the gold-glass bead from the archaeological site of Kaole (Tanzania) for various elements with the 10 Hz drilling procedure; the vertical dashed lines in (a) and (b) shows the changes in bulk composition.

3.6.4. Crizzled glass

The last glass degradation example is a fragment from a French wine glass (Figure 3.4d), ca. 1750 (CMG-449). It is a colorless glass object kept in a museum that presents a visible decay on the surface with pink areas. This type of deterioration depends on the chemical composition and on the manufacturing technology of the artifact. Glass with this kind of degradation is usually called “sick”, “weeping”, “sweating” or “crizzling” (Kunicki-Goldfinger, 2008; Gentaz *et al*., 2011; Koob, 2006). The deterioration of these *unstable* glasses has been the subject of keen interest, in particular of conservators trying to work out how to stop the degradation.

The elemental bulk concentrations in CMG-449, based on average concentrations associated with a depth of 500 shots, are given in Table 3.2. We can see that SiO_2 and K_2O make up more than 95% of the bulk concentration. Moreover, the contents of CaO, MgO and Al_2O_3 are very low, i.e. 0.4, 0.05 and 0.6 wt % respectively, and are probably the main reason for the *crizzling* effect. The elemental depth profiles in Figure 3.10 show the behavior of the K, Na, Mg and Pb oxides. Glass objects affected by crizzling typically have a composition that is high in alkali (K for the present glass) and low in lime. This particular glass presents an unusual content of lime that is three times lower than the normal amount needed to stabilize a glass (Koob, 2006). K and Na oxide concentrations are significantly depleted on the surface (Figures 3.10a and c); in contrast, the PbO concentration is higher on the surface (Figure 3.10d), which is probably due to contamination from the environment.

The pink color of the glass is probably a result of the process of solarisation, when Mn^{2+} oxidizes to Mn^{3+}. This glass artifact was previously analyzed by Brill, 1975 and 1999; he referred to this glass as heavily crizzled. By comparing the pristine glass composition with the crizzling layer composition (Table 3.3) he concluded that potassium and sodium must have been leached out, probably as a result of washing of the glass. He calculated the hydration/alkali depletion rate to be 0.3 µm per year by microscopic inspection of the thickness of the crizzling layer and the age of the glass.

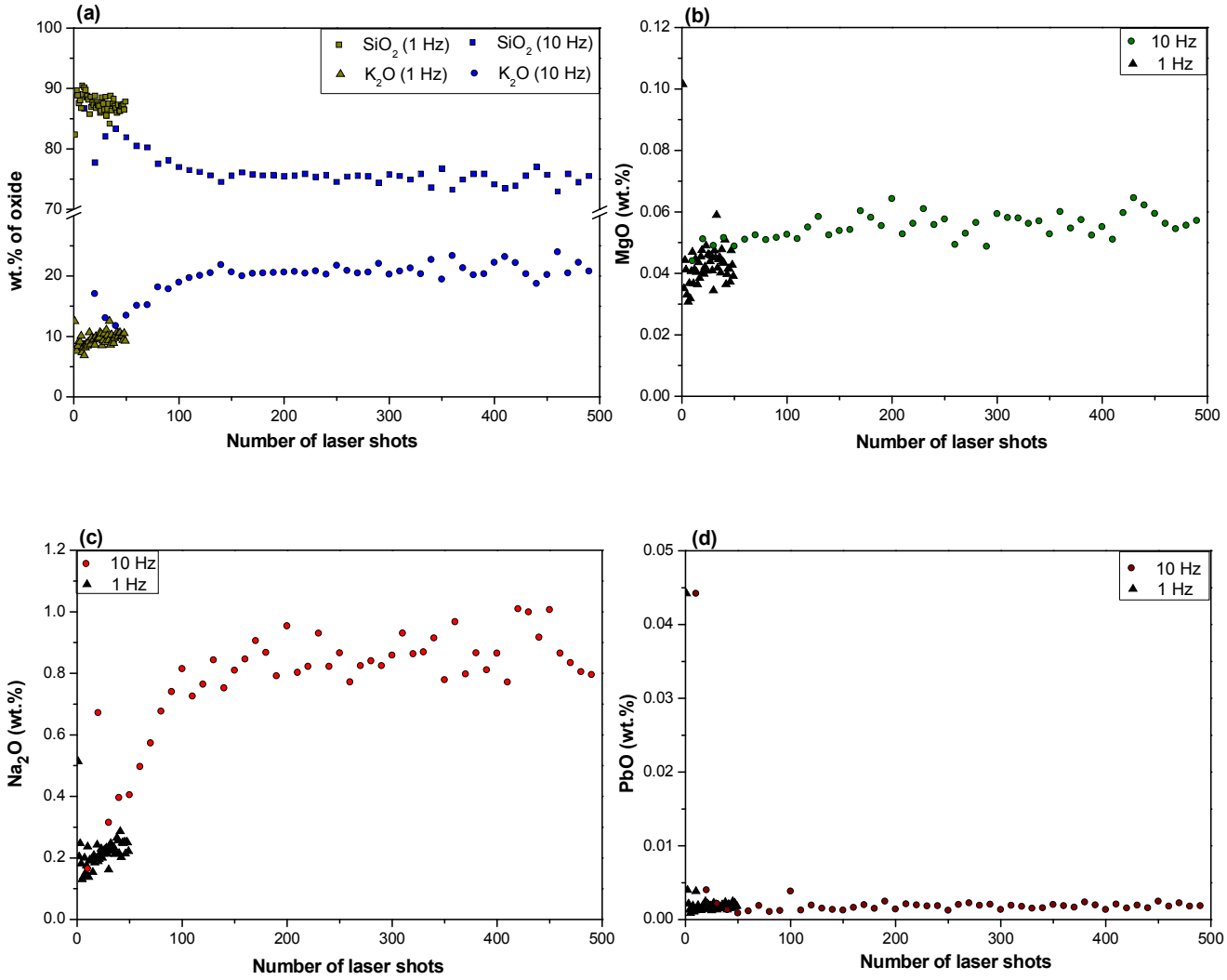

Figure 3.10. LA-ICP-MS depth profiling on CMG 449 glass from the Corning Museum of Glass for various elements with the 1 Hz and 10 Hz drilling procedures.

Table 3.3. Chemical composition (in wt %) of the bulk and the crizzling layers of CMG 449 by Brill (1999); the majority of the analyses was made by atomic adsorption spectroscopy and SiO_2 was measured gravimetrically.

	bulk	crizzling layers
SiO_2	76.47	79.31
Na_2O	0.8	0.17
K_2O	19.2	7.24
CaO	0.24	0.33
MgO	0.01	0.029
Al_2O_3	0.58	0.61
Fe_2O_3	0.098	0.087
MnO	0.54	0.62

3.7. Volumetric mass density depth profiles

The volumetric mass density of a glass is a function of its chemical composition and can vary from 2.4 to 5.9 g cm^{-3} (Newton and Davison, 1989). Its value generally increases when other oxides are added to the pure silica to occupy the empty spaces of the network; the volumetric mass density can be calculated based on the glass composition (Gentaz *et al.*, 2011) (a model calculator for room temperature glass densities is freely available [http://glassproperties.com/density/room-temperature]).

The alteration layer, also called the "gel layer", has a different chemical composition and a lower bulk density than the original glass (Adams, 1992). Using the model calculator and the calculation routine mentioned in section 3.3, the volumetric mass density profiles of the alteration layers of the ancient glasses under study were determined (Figure 3.11a). For the Roman glass sample the density varies from a low of 2.0 g cm^{-3} at the surface of the alteration layer to the common soda lime silica glass density of 2.5 g cm^{-3} (Newton and Davison, 1989). This common density is reached in ca. 300 shots and corresponds approximately to reaching the pristine glass (Figure 3.7). The volumetric mass density of both the corroded African bead and the crizzled glass slightly increases from ca. 2.1 to 2.3-2.5 g cm^{-3}, and the pristine glass is reached in ca. 200 shots. The density of the highly corroded glass could not be calculated due to its high heterogeneity as a result of the sandwich structure. The density depth profiles show that the volumetric mass density of the Roman glass alteration layer is lower than that of the two other glasses. A lower volumetric mass density suggests a higher depletion of alkali elements in the alteration layers, as indicated by less steep concentration depth profiles of Na_2O in the Roman glass (Figure 3.7) compared to Na_2O and/or K_2O concentration depth profiles in the other two glasses (Figures 3.8 and 3.10).

Figure 3.11b illustrates how the volumetric mass density of the alteration layer is related to the Na_2O+K_2O concentration in that layer. A very good linear correlation (R^2 = 0.995) is found for the crizzled glass suggesting that the volumetric mass density change is completely determined by depletion of Na_2O and/or K_2O, in contrast to the other two glasses which show a lot of noise. This noise is probably related to contamination of the alteration layers, resulting in (slightly) biased data for Na_2O and/or K_2O in the outermost alteration layer, possibly due to calculation errors in the sum normalization calibration approach. This finding seems to be in line with the fact that the crizzled glass is the youngest glass that was less affected by external contamination sources (soil, sediment, seawater, etc.), whereas the Roman glass and the African glass bead were excavated from the soil with lots of opportunity for contamination.

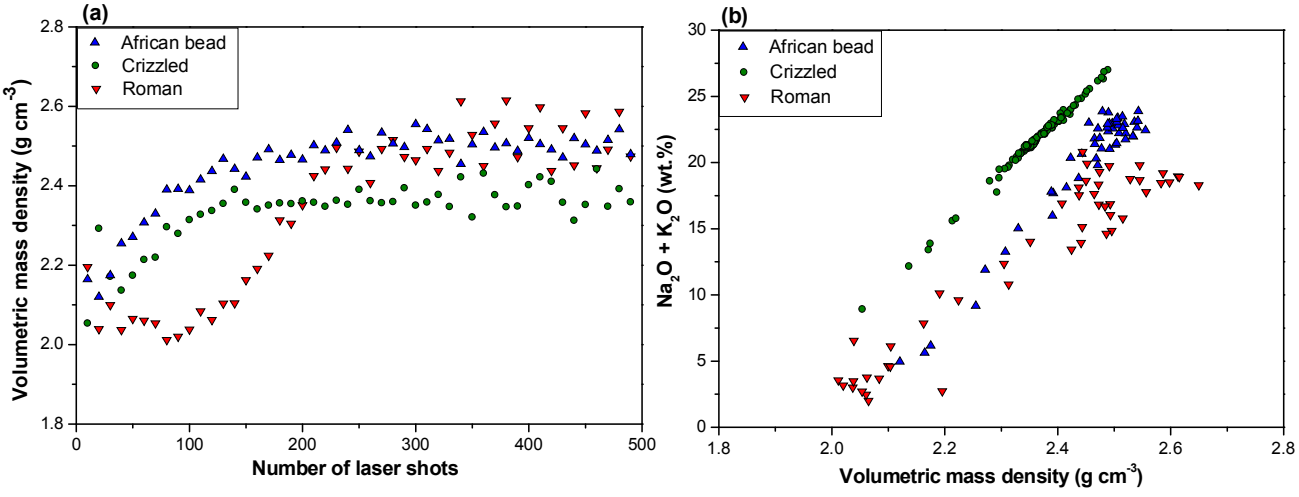

Figure 3.11. Volumetric mass density depth profiles of the glass samples (a) and their relationship with the depth profiles of the alkali elements, expressed as wt % concentrations of Na_2O+K_2O vs. volumetric mass density (b).

3.8. Conclusions

Four altered glass artifacts with diverse deterioration, from different centuries and provenance, were studied with LA-ICP-MS operated in drilling mode with a low and/or a high repetition rate. Depth profiles with quantitative elemental information for all their compositional layers (altered, pristine bulk, inclusions, metal foils, etc.) could be obtained with minimal damage to the artifact. Nevertheless, so far it is difficult to perform depth calibration of the depth profiles due to different ablation characteristics of degraded glasses compared to standard glasses. More work is needed to further understand the relationship between laser sampling conditions (for depth profiling) and the associated ablation rate for corroded glasses comprising pure glass structures and "gel" layers. In this chapter we also demonstrated a novel procedure to indirectly measure the volumetric mass density along the glass depth for high-silica content glasses to get insight into its possible relationship with ablation efficiency. However, other parameters such as matrix composition, optical absorption, etc. may influence the ablation efficiency as well (Russo *et al*., 2000; Gonzalez *et al*., 2002).

The results presented in this chapter (bulk concentrations, elemental depth profiles, volumetric density profiles, etc.) allowed us to *speculate* on the glass degradation phenomena identified in each sample:

1) The crizzled glass is a potasic glass (K_2O concentration, 19.7 wt %) with a very low CaO concentration (0.44 wt %) to stabilize a glass. Hence, deterioration may already occur at (humid) ambient conditions as a result of leaching of K^+ ions, thereby generating deep perpendicular cracks that enhance the glass decay.

2) Even though the metal-foil bead has a high, but difficult to quantify, CaO concentration (ca. 7.1 wt %) it is severely corroded; it can be assumed that aggressive exposure conditions in combination with the presence of different compositional layers (glass and metal) may have had a substantial role in its degradation.

3) The Roman glass is a sodic glass (Na_2O concentration, 20.8 wt %) with a CaO concentration of 5.2 wt %. The dulling of the surface refers to a leaching process resulting in many thin layers leading to iridescence, which is caused by "the interference between rays of light reflected from thin alternating layers of air and weathered glass crusts" (Newton and Davison, 1989). Laser ablation drilling of these thin layers, depleted in alkali and earth alkali elements, and with a lower volumetric mass density, is more efficient than of the pristine glass.

4) The African glass bead is a soda-lime-silica glass with a CaO concentration of 2.44 wt %, but with a distinctly different source of the flux then the Roman glass, i.e. a plant ash instead of a mineral (natron). The alteration layer is also depleted in Na_2O, but it presents (trace) elements as potash and cuprite in the outermost surface layer, probably as a result of contamination from the soil.

Volumetric mass density measurements, based on a novel approach relating the wt% and vol% elemental concentration depth profiles, allowed to measure the density of the alteration layers, a property normally not easily retrieved. This approach may also be beneficial for other glass sectors (forensics and glass manufacture) interested in density specifications for thin glass layers, laminated glass, etc. In this study we found that the glass density is directly related to the depletion of Na_2O and K_2O in the alteration layer.

3.9. References

Adams B.P. (1992) Ch.2 in Clark D.E. and Zoitos B.K. (eds.), Corrosion of Glass, Ceramics and Ceramic Superconductors: Principles, Testing, Characterization and Applications, Noyes Pubblications, Park Ridge; pp. 29-50.

Brill R.H. (1975) Crizzling - A Probem in Glass Conservation. Conservation in Archaeology and the Applied Arts, Stockholm Congress, London, IIC; pp. 121-134.

Brill R.H. (1999) Chemical Analyses of Early Glasses. The Corning Museum of Glass. Corning, New York.

Dussubieux L., Robertshaw P. and Glascock M.D. (2009) LA-ICP-MS analysis of African glass beads: Laboratory inter-comparison with an emphasis on the impact of corrosion on data interpretation. Int J Mass Spectrom 284(1-3); pp. 152-161.

Fluegel A. (2007) Global Model for Calculating Room-Temperature Glass Density from the Composition. J Am Ceram Soc 90 [8]; pp. 2622-2625.

Gentaz L., Lombardo T., Loisel C., Chabas A. and Vallotto M. (2011) Early stage of weathering of medieval-like potash-lime model glass: evaluation of key factors. Environ Sci Pollut Res 18; pp. 291-300.

Gonzalez J., Mao X. L., Roy J., Mao S. S., and Russo R. E. (2002) Comparison of 193, 213 and 266 nm laser ablation ICP-MS. J Anal At Spectrom 17(9); pp.1108-1113.

Greiff. S. and Nallbani E. (2008) When Metal Meets Beads – technological study of early medieval metal foil beads from Albania. MEFRM: Mélanges de l'École française de Rome : moyen-âge 120(2); pp. 355-375.

Koob S. P. (2006) Conservation and care of glass objects. Published by Archetype Publications in association with The Corning Museum of Glass, New York.

Kunicki-Goldfinger J.J. (2008) Unstable historic glass: symptoms, causes, mechanisms and conservation, Reviews in Conservation 9; pp. 47-60.

Mank A.J.G. and Mason P.R.D. (1999) A critical assessment of laser ablation ICP-MS as an analytical tool for depth analysis in silica-based glass samples. J Anal Atom Spectrom 14; pp. 1143-1153.

Newton R.G. (1971) The enigma of the layered crusts on some weathered glasses, a chronological account of the investigations. Archaeometry 13; pp. 1-9.

Newton R.G. (1985) Durability of Glass – a review. Glass Technol 26(1); pp. 21–38.

Newton R. and Davison S. (1989) Conservation of Glass, Butterworths, 1st edn., London.

Panighello S., van Elteren J.T., Orsega E.F. and Moretto L.M. (2015) Laser ablation-ICP-MS depth profiling to study ancient glass surface degradation, Anal Bioanal Chem 407(12); pp. 3377-3391.

Paul A. (1997) Chemical Durability of Glasses; a Thermodynamic Approach. J Mater Sci 12; pp. 2246-2268.

Russo R. E., Mao X. L., Borisov O. V., and Liu H. C. (2000) Infuence of wavelength on fractionation in laser ablation ICP-MS. J Anal At Spectrom 15(9); pp. 1115-1120.

Šelih V.S. and van Elteren J.T. (2011) Quantitative multi-element mapping of ancient glass using a simple and robust LA-ICP-MS rastering procedure in combination with image analysis. Anal Bioanal Chem 401(2); pp. 745-755.

Sode T., Feveile C. and Schnell U. (2010) In: Begründet von Claus Dobiat und Klaus Leidorf Herausgegeben von Claus Dobiat, Peter Ettel und Friederike Fless (Eds.) INTERNATIONALE ARCHÄOLOGIE - Studia honoraria - Band 31; Verlag Marie Leidorf GmbH. Rahden/Westf.

Van Elteren J.T., Tennent N.H. and Šelih V.S. (2009) Multi-element quantification of ancient/historic glasses by laser ablation inductively coupled plasma mass spectrometry using sum normalization calibration. Anal Chim Acta 644(1-2); pp. 1-9.

Van Elteren J. T., Izmer A, Šala M., Orsega E.F., Šelih V.S., Panighello S. and Vanhaecke F. (2013) 3D laser ablation-ICP-mass spectrometry mapping for the study of surface layer phenomena-a case study for weathered glass. J Anal Atom Spectrom 28(7); pp. 994-1004.

Chapter 4
Development of 2D Elemental mapping methodologies*

* Part of this chapter was published in Panighello *et al*. 2012b; Arizio *et al*. 2012 and accepted for a book chapter in Van Elteren *et al*., Springer-Verlag GmbH.

4.1. Introduction

2D elemental mapping of glass surfaces by LA-ICP-MS is an interesting technique to elucidate past technologies, establish provenance or understand deterioration processes of ancient, polychrome glass by visualization of the elemental distribution of the glass surface. However, selection of the appropriate LA-ICP-MS conditions for generation of high-quality elemental maps with the highest spatial resolution, lowest signal-to-noise ratio and shortest analysis time is normally a trial-and-error process. In this chapter a computational-experimental strategy is described to optimize the LA-ICP-MS conditions for 2D elemental mapping of polychrome glass by finding the best balance between fluence, beam diameter, repetition rate, scanning speed, gas flow rate and acquisition time. To aid in the initial selection of the optimal LA-ICP-MS conditions for spatial resolution and analysis time, a digital image of a glass surface has been subjected to virtual 2D mapping, using existing software which simulates the actual LA-ICP-MS mapping process. To verify whether these initial conditions would result in an acceptable signal-to-noise ratio during the actual LA-ICP-MS mapping process, they are used to experimentally determine the detection limits for each element via a simple line scan on a "blank" glass, and consequently predict the noise floor in the maps. This strategy is successfully validated (using a modern *murrina*) and applied to two different polychrome glasses, one from the Iron Age and the other one from the Roman Age to get more insight into their elemental composition and the mineral sources involved.

The 2D elemental mapping approach is finally compared to EPMA WDS mapping. EPMA-WDS elemental mapping is performed on selected surface areas and on broken edge sections of the Iron Age polychrome glass sample, at the interface between bulk and decorations and on a mirror glass from the 17th century. LA-ICP-MS elemental mapping can be functional to the determination of the glass chemical composition patterns and of associations between elements, while WDS elemental mapping is mainly aimed to identify the distribution of crystalline phases or to visualize concentration gradients of elements at the interfaces of different areas, such as bulk and decorations. Both the techniques can be functional to the study of glass superficial weathering.

4.2. Samples

For the development of 2D elemental mapping methodologies two polychrome glass samples were selected for a preliminary study of association between the elements, in order to obtain information about the sands, the chromophores, the fluxes, opacifiers and minerals.

The example presented in Figure 4.1a, used to evaluate the 2D mapping procedure, is an opaque polychrome glass vessel fragment from the Iron Age (5th century BC) from the museum of Adria (Northern Italy). More details on the provenance of the sample can be found in Chapter 7. It presents a blue bulk with opaque yellow and turquoise decorations. The body part is translucent and shows the presence of bubbles and devitrification crystals. This vessel was made using the "core-forming technique." Before the invention of glass-blowing around the first century AD, this was the most common method of manufacture of glass vessels.

This technique involved "*the shaping of a clay core, which was then dipped into molten glass. Decoration was then trailed onto the surface of the vessel, often in contrasting colours. These trails of glass could then be combed into close-set zigzag patterns and either left in relief or, more commonly, flattened by marvering. Finally, a rim-disc, foot-ring or handles could be added. On cooling, the core was carefully scraped out*" (Harden and Tatton-Brown, 1981).

Stylistically, this vessel falls within Harden's Mediterranean Group I, *aryballos* form 2 (Harden and Tatton-Brown, 1981). This group denotes the first of three successive industries which manufactured large amounts of core-formed vessels traded in the Mediterranean context. According to the most probable hypothesis this industry was developed mainly on Rhodes Island (Walton *et al.*, 2009), following the migration of craftsmen from the Near East.

In Figure 4.1b the analyzed sample is a fragment of glass bowl from the Roman period produced using the traditional Hellenistic technique of casting over a mold (Bonomi, 1996). The vessel was casted from a montage of slices cut from a fused cluster of white and yellow glass rods in a matrix of blue glass. The depth of colored layer is variable and it is dependent on the thickness of the vessel.

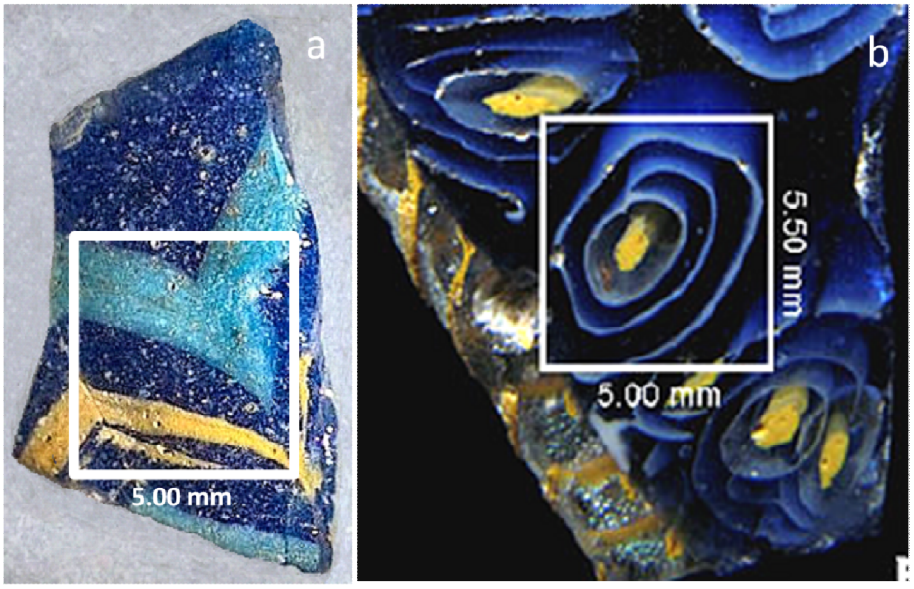

Figure 4.1. Detail of the glass fragments used for the development of 2D mapping methodologies. (a) glass fragment from an Iron Age glass vessel from the Archaeological museum of Adria; (b) Roman glass fragment. The mapped areas are defined by a white rectangle.

2D mapping was also applied to study the surface degradation of mirror glasses by the EPMA WDS technique. Figure 4.2 shows a fragment of glass from a mercury-tin amalgam mirror from the end of the 17th century, of unknown origin.

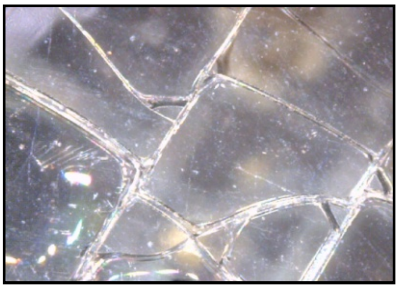

Figure 4.2. Detail of a macro image of the mirror glass.

4.3. Sample handling and glass calibration standards

For mapping purpose the archaeological artifact shown in Figure 4.1a was securely mounted on a glass slide with double-sided tape, next to a reference glass (NIST SRM 610) serving as an external standard with nominal elemental concentrations of ca. 500 µg g^{-1} (for published and consensus values see http://georem.mpch-mainz.gwdg.de). For establishing the elemental detection limits a synthetic "blank" glass (DLH6, P&H Developments Ltd.), prepared according to the coprecipitated gel technique (Hamilton and Hopkins, 1995), was used with a base composition of 72 % *w*/*w* SiO_2, 2 % *w*/*w* Al_2O_3, 12 % *w*/*w* CaO and 14 % *w*/*w* Na_2O. To validate the computational-experimental strategy for 2D LA-ICP-MS mapping a modern *murrina* from Murano, Venice (Italy) was used, both for LA-ICP-MS elemental oxide mapping and mapping simulation based on a digital image of the object. The *murrina* was embedded in epoxy resin in which carbon powder was mixed for better visibility of the glass structures. Hence, in the polished block (Figure 4.3) the translucent parts of the glass are black and the dark blue colour of the outer rim of the *murrina* is obscured by the black background colour as shown in the digital image of the murrina in Figure 4.3.

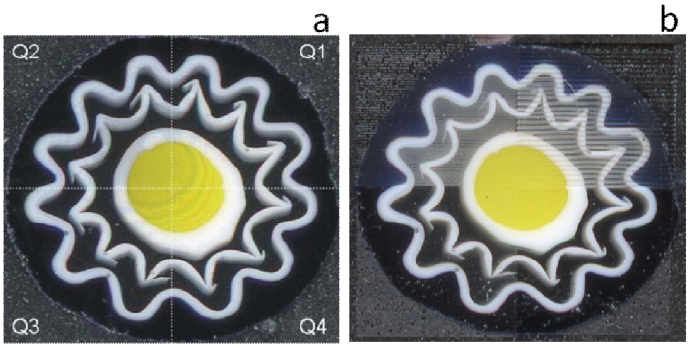

Figure 4.3. Digital image of the modern murrina used for virtual and experimental LA-ICP-MS image mapping (a) and damage induced by LA scanning of the quadrants Q1-Q3 of the glass using three different sets (Table 4.1) of LA-ICPMS conditions (b); quadrant Q4 served as a visual reference in the elemental image maps.

4.4. Evaluation of 2D mapping procedure

Each map consisted of many parallel line scans, with no space between adjacent scans, which were acquired and saved individually by a remotely triggered ICP-MS line scan sequence routine. The individually collected line scans with time-resolved data for each element (in cps) were saved and later converted into elemental oxide concentrations (in % *w*/*w*) (see Chapter 2). To test the LA-ICP-MS conditions for mapping of the *murrina* (Figure 4.3), three sets of LA-ICP-MS conditions were selected (Table 4.1) and the imaginary quadrants (Q1-Q3) mapped; quadrant Q4 served as a visual reference. As can be seen from Figure 4.3b the damage to the surface of the *murrina* is very dependent on the LA-ICP-MS conditions selected (fluence and repetition rate were kept constant for mapping of the quadrants), resulting in minimal damage to Q3 (25 µm / 36 µm s^{-1}) and destructive damage to Q1 (100 µm / 9 µm s^{-1}) and Q2 (55 µm / 16 µm s^{-1}); ablation of Q3 can be regarded as a kind of dulling of the surface.

Table 4.1. Operating conditions of the LA-ICPMS instrument for mapping of the quadrants (Q1-Q3) of the modern murrina (Figure 4.3a).

Laser ablation	***New Wave Research UP 213***
Wavelength	213 nm
Pulse length	4 ns
Spot size	100 (Q1), 55 (Q2), 25 (Q3) µm
Fluence	ca. 7 J cm^{-2}
Repetition rate	10 Hz
Scanning speed	9 (Q1), 16 (Q2), 36 (Q3) µm s^{-1}
Grid spacing	100 (Q1), 55 (Q2), 25 (Q3) µm
He flow rate	0.95 l min^{-1}
Make-up Ar flow rate	0.75 l min^{-1}
ICP-MS	***Agilent 7500ce***
Rf power	1500 W Sampling
depth	6.5 mm
Isotopes measured	^{7}Li, ^{9}Be, ^{11}B, ^{23}Na, ^{24}Mg, ^{27}Al, ^{29}Si, ^{31}P, ^{39}K, ^{43}Ca, ^{45}Sc, ^{47}Ti, ^{51}V, ^{53}Cr, ^{55}Mn, ^{57}Fe, ^{59}Co, ^{60}Ni, ^{63}Cu, ^{66}Zn, ^{69}Ga, ^{75}As, ^{82}Se, ^{85}Rb, ^{88}Sr, ^{89}Y, ^{90}Zr, ^{93}Nb, ^{95}Mo, ^{107}Ag, ^{111}Cd, ^{115}In, ^{118}Sn, ^{121}Sb, ^{137}Ba, ^{139}La, ^{140}Ce, ^{141}Pr, ^{146}Nd, ^{147}Sm, ^{153}Eu, ^{157}Gd, ^{159}Tb, ^{163}Dy, ^{165}Ho, ^{166}Er, ^{169}Tm, ^{172}Yb, ^{175}Lu, ^{197}Au, ^{208}Pb, ^{209}Bi, ^{232}Th, ^{238}U (54 masses in total)
Acquisition time/pixel	11.11 (Q1), 3.44 (Q2), 0.69 (Q3) s
Measurement mode	Time-resolved, TRA(1) Plasma gas flow
rate	15 l min^{-1}
Auxillary gas flow rate	1 l min^{-1}
Total analysis time/map	2.8 h

4.5. Quantification and image analysis

The individual line scans making up the elemental maps were sequentially stitched together into a 2D CSV file using an in-house macro. This macro converts the response of the line scans into 2D matrices with pixels conveying their content (cps/element). Since the content of often tens of thousands of pixels needs to be converted into % *w*/*w* for each element, a custom quantification routine (in Microsoft® Office Excel 2003, Microsoft Corporation, Redmond, WA, USA) was used based on summating 54 elements as their oxides to 100 % *w*/*w*. Similar approaches have been successfully applied before, using an array of glass standards or a single standard (Gratuze *et al.*, 2001; van Elteren *et al.,* 2009; Liu *et al.*, 2008; Šelih and van Elteren, 2011). Since the use of a single standard greatly reduces the analysis time and simplifies processing of the pixels, NIST SRM 610 was used for calibration purposes to generate quantitative data, similar to earlier published work (Šelih and Van Elteren, 2011). In short, the sum normalization calibration approach converts the raw signal intensity I_i (in cps) of the elemental oxide *i* (1 to *n*) in each pixel into an unnormalized concentration $c_i(unnorm)$ (in % *w*/*w*):

$$c_i(unnorm) = \frac{I_i}{I_{i,N610} / c_{i,N610}} \qquad \text{[Eq. 4.1]}$$

with $I_{i,N610}$ and $c_{i,N610}$ the raw signal intensity (in cps) and the elemental oxide concentration *i* (in % *w*/*w*) in NIST SRM 610, respectively. From Eq. (4.1) it is clear that after summation and normalization to 100 % *w*/*w* the normalized elemental oxide concentrations $c_i(norm)$ (in % *w*/*w*) can be retrieved:

$$c_i(norm) = 100 \times \frac{c_i(unnorm)}{\sum_{i=1}^{n} c_i(unnorm)} \qquad \text{[Eq. 4.2]}$$

This sum normalization approach not only yields accurate data, but for mapping of large surfaces the procedure is also not very susceptible to defocusing issues as a result of surface unevenness (Šelih and van Elteren, 2011). However, it should be stressed that for small beam diameters it is difficult to keep the laser focused (in the order of the beam diameter) for extended periods of time (many hours); we found out that a beam diameter ≤12 μm yielded elemental image maps of varying quality. Processing of the elemental oxide concentrations (in % *w*/*w*) into elemental maps (in .JPEG format) was achieved by Origin 7.5 SR4 (OriginLab Corporation, Northampton, MA, USA) and Sigmaplot (Systat Software Inc.); in general 256 shades of gray (8-bit image) were used for image analysis whereas for visual presentation pseudocolours were applied (from dark blue to bright red). The 8-bit elemental maps were imported into the image analysis software ImageJ (National Institute of Health, USA) for detailed digital analysis of the glass artefacts, using a simple calibration which links the shades of gray (256 brightness levels from 0 [black] to 255 [white]) to the oxide concentrations. With a tracing tool areas on the glass artefact were selected for localized elemental analysis.

4.6. Software for virtual LA-ICP-MS mapping

To aid in the selection of appropriate LA-ICP-MS mapping conditions, finding the best balance between spatial resolution, analysis time and signal-to-noise ratio, a previously developed LA-ICP-MS mapping software package (Triglav *et al.,* 2010) was used. After uploading a digital image in the software (the pre-Roman glass shown in Figure 4.1a it is subjected to permutations simulating the LA-ICP-MS mapping action (see the screenshot in Figure 4.4). The virtual LA-ICP-MS conditions (beam diameter, repetition rate, scanning speed, flow rate and acquisition time) can be freely selected; laser fluence cannot be selected as optimum coupling to the target material occurs in a fairly narrow fluence range (Phipps *et al.*, 2006; Xu, 2002). The virtual map generated is based on a computational approach comprising the following steps:

1) scaling of the digital image to its actual size (5 mm ×5 mm in this case),
2) creating of the LA-ICP-MS pixel grid and averaging of the RGB 0÷255 content of the photographic pixels,
3) determining the distortion of each pulse caused by exponential washout from the ablation cell,
4) gathering of the appropriate number of pixels (= $R \times T$) to generate the final virtual map in pseudocolours.

Since the computational approach does not take into account the elemental concentrations it is essential to investigate how the noise levels in the maps are related to the trace elemental concentrations for selected sets of LA-ICP-MS conditions. Although the software is kitted out with a noise generator, in this work on glass mapping it was found more convenient to investigate the anticipated noise in the elemental image maps by establishing multi-elemental detection limits via simple line scanning of the “blank” glass DLH6 and determining the concentrations via the sum normalization approach. The detection limits were calculated based on three times the standard deviation of the noise in this “blank” glass.

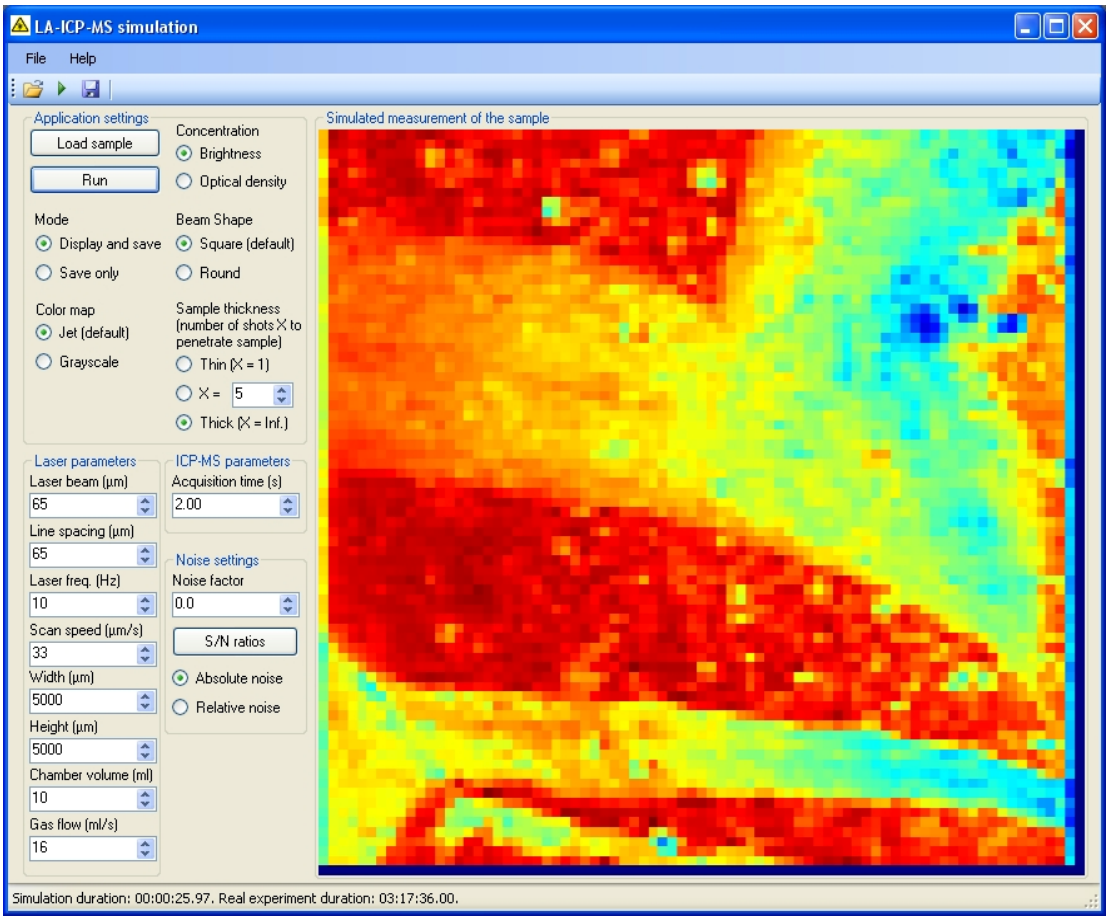

Figure 4.4. Screenshot of the LA-ICPMS software for virtual mapping; in this instance a digital image of the pre Roman glass shown (Figure 4.1a) has been uploaded in the software and the resulting virtual image map for the optimized LA-ICPMS conditions is shown.

4.7. Validation of the combined computational and experimental strategy

Experimental murrina 2D mapping details – a modern *murrina* (Figure 4.3a) was subjected to three sets of LA-ICP-MS mapping conditions (Table 4.1), and the actual LA-ICP-MS elemental image maps were compared to the findings of the computational-experimental strategy. This allowed us to prove that the computational-experimental strategy is suited to optimize the LA-ICP-MS conditions for generation of high-quality multi-elemental 2D image maps of decorative features in glass artefacts. The sample was divided into four imaginary quadrants (each of 3.2 mm × 3.0 mm) of which three were virtually and experimentally mapped, each with a different set of LA-ICP-MS conditions but equal analysis times (2.8 h). Square pixels were considered, implying that *D* (beam diameter) = *S* (scanning speed) × *T* (acquisition time). Based on the LA-ICP-MS conditions listed in Table 4.1, the relative theoretical elemental sensitivity values (in signal [cps] per concentration [% *w*/*w*]) were 1:0.30:0.06 for Q1:Q2:Q3. The experimental values of the elemental relative sensitivity (averaged over 54 elements upon ablation of NIST SRM 610) were 1:0.38±0.05:0.12±0.04, quite close to the theoretical values. Discrepancies were possible due to the fact that scanning speeds were different, resulting in different degrees of collateral damage to the glass surface and hence slight sensitivity variations.

Evaluation of experimental 2D map quality – after ablation of the quadrants, 54 elemental oxide maps were generated under the three sets of LA-ICP-MS conditions. In Figure 4.5 a small selection of the 54

elemental oxide maps is presented as composite maps of three different elemental maps (Q1, Q2 and Q3) for some major, minor and trace elements, and the digital image (Q4).

It can be seen that the image sharpness increases from Q1 to Q3, although for the trace elements it is obvious that the small pixel size in Q3 causes the noise floor for the trace elements to rise so much that unintelligible maps with inaccurate elemental oxide concentrations are obtained (visible from variations in colour patterns in the three quadrants).

Additionally, it is clear that retrieving accurate and precise data from the narrow, white, wavy patterns for Q1 is challenging due to the large pixelation; As_2O_3 and PbO concentrations in these areas are measured with a precision of ~ 60 % for Q1 compared to ~ 20 % for Q2. The LA-ICP-MS conditions used for mapping of quadrant Q2 seem to be the best compromise for yielding appropriate spatial resolution and adequate signal-to-noise ratios.

Technological fabrication information extracted from the maps – the compositional data extracted from all 54 maps (based on the measurement of Q2) reveal the following (concentrations ± standard errors): 1) the opaque, white, wavy patterns are associated with lead arsenate (10.8±0.8 % *w*/*w* As_2O_5 and 30.6±2.8 % *w*/*w* PbO), which is a weak (*opaline*) opacifier; 2) the yellow spot in the *murrina* centre is produced by colloidal dispersion of cadmium sulphide (measured as CdO [0.31±0.16 % *w*/*w*]), with a minor part of selenium-cadmium sulphide, under reducing conditions; the reducing agent is zinc metal powder that oxidizes to zinc oxide (9.1±2.1 % *w*/*w*); the latter acts also as a stabilizer in this glass poor in lime (1.3±0.3 % *w*/*w*); 3) the dark blue outer edge is due to the presence of cobalt oxide (0.31±0.08 % *w*/*w*), with a minor contribution of copper oxide (0.0020±0.0005 % *w*/*w*); 4) the translucent bulk glass matrix consists of SiO_2 (66.1±4.1 % *w*/*w*), Na_2O (21.3±3.6 % *w*/*w*), CaO (7.9±1.8 % *w*/*w*), B_2O_3 (1.3±0.3 % *w*/*w*), K_2O (1.6±0.2 % *w*/*w*) and Al_2O_3 (0.81±0.12 % *w*/*w*). These data indicate that the *murrina* is a silica-soda-lime glass where boron has been added as a fluidifying agent.

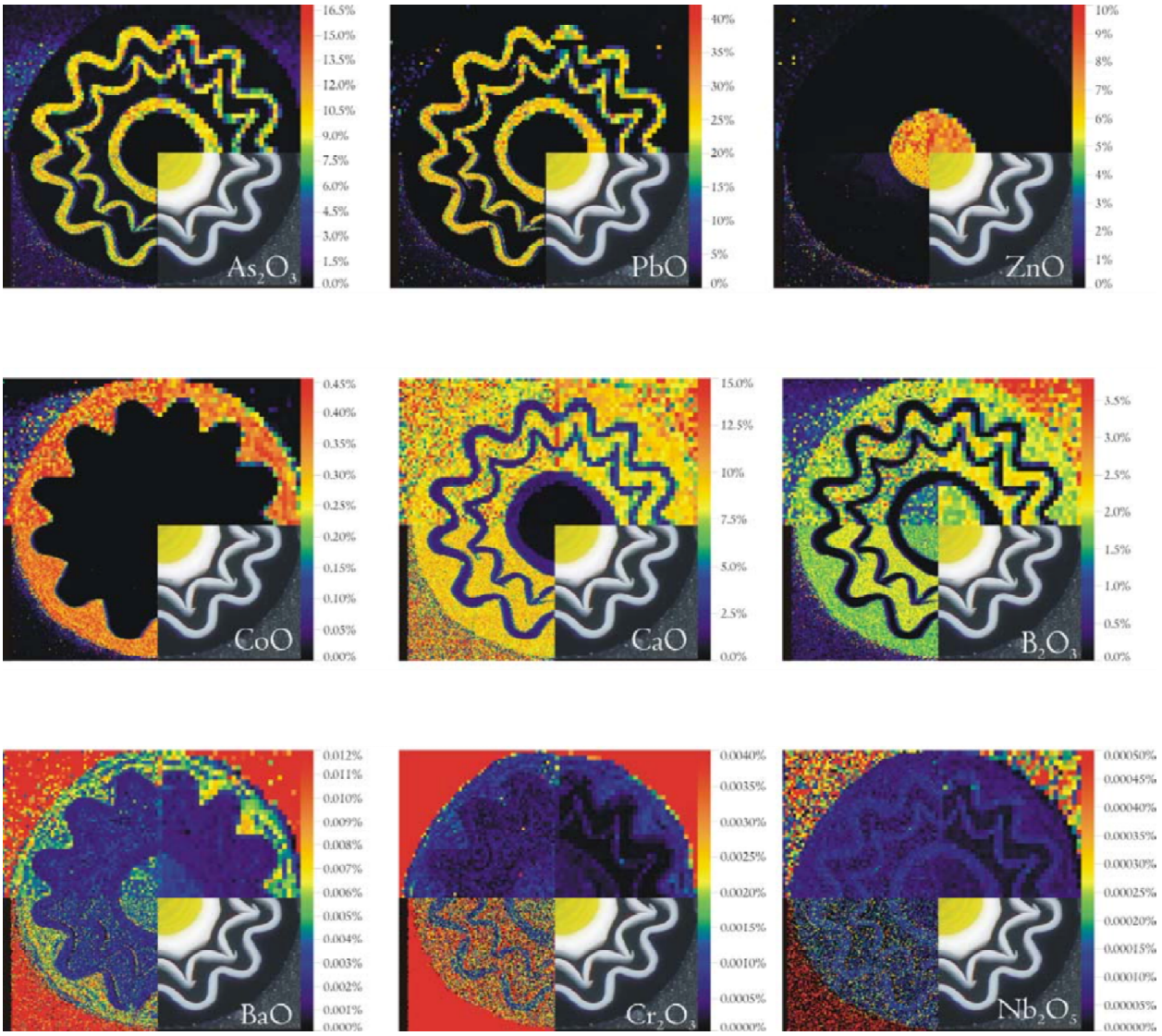

Figure 4.5. Selected composite elemental image maps after actual LA-ICPMS mapping of three quadrants of the murrina (Figure 4.1a) using three different conditions (Table 4.1); the visual image in the fourth quadrant serves as a reference. Lower image densities are mapped onto "cool" colors and higher densities onto "hot" colors. Low density images are shown in blue or violet, and high density images appear as orange or red.

4.8. Computational and experimental strategy

Virtual murrina mapping details – to investigate whether the best LA-ICP-MS conditions can be singled out by a computational–experimental strategy as well, we uploaded not only the digital image of the *murrina* (Figure 4.1a) in the software but also its negative image to emphasize both high and low elemental concentrations in similar parts of the glass. E.g., the translucent part of the *murrina* contains high concentrations of main elements, but most other elements are expected to be present at trace levels; thus, uploading the (positive) digital image of the *murrina* will yield an image map with a low contribution of the main elements since the black in the image is associated with a zero RGB brightness value. However, the corresponding negative digital image will appropriately address this issue. In Figure 4.6, the results of the virtual 2D maps of the *murrina* (both of the positive and negative digital image) for the three different quadrants are shown. As expected, the virtual 2D maps increase in quality from quadrant Q1 to Q3, with

quadrant Q1 also showing too large pixelation for accurate and precise measurement on the white wavy patterns, in agreement with the actual LA-ICP-MS mapping results.

Since the LA-ICP-MS conditions used for virtual mapping of quadrant Q3 yield the best virtual map, they seem the most obvious choice for experimental mapping.

However, due to introduction of instrumental noise associated with the small pixel size (25 µm × 25 µm), especially for trace level concentrations, these conditions might not be indicative for the best possible elemental image maps.

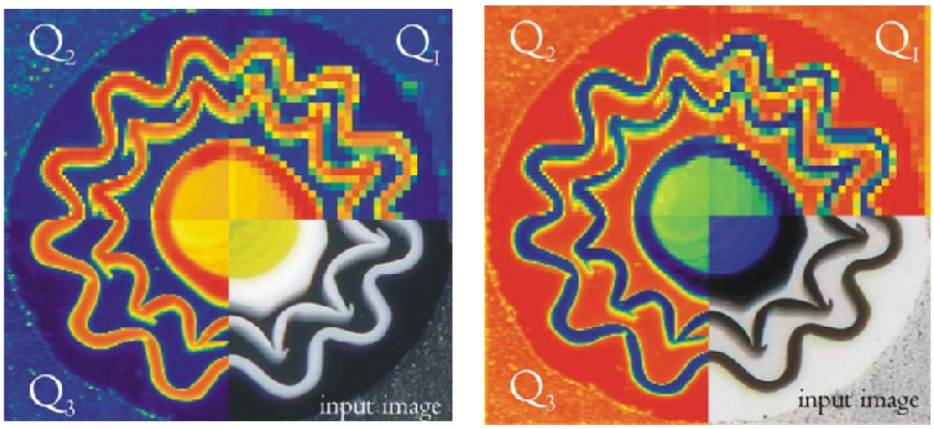

Figure 4.6. Composite image maps after virtual LA-ICPMS mapping of the three quadrants of the murrina (Figure 4.1a) using three different conditions (Table 4.1) for the positive (top) and negative (bottom) digital image; the visual image in the fourth quadrant serves as a reference.

Evaluation of virtual map quality – To envisage how these conditions might influence the noise floor of the 2D maps, the "blank" glass DLH6 was measured in single line scan mode to retrieve the concentrations of 54 elemental oxides according to the sum normalization procedure. In Figure 4.7 the detection limits for 50 elemental oxides (except the glass basic main oxides SiO_2, Al_2O_3, CaO and Na_2O) are presented as three times the standard deviation of the noise in the "blank" glass (in % *w*/*w*) for the three different LA-ICP-MS conditions. As a general trend, the detection limits increase from Q1 to Q3; averaged over all the elemental oxides the detection limit ratios are 1:3.3:40 for Q1:Q2:Q3. For prediction of the anticipated noise in the actual LA-ICP-MS elemental image maps, using Figure 4.7, we can assume that the main elements (Ca, B, As, Pb, Zn and Co) have concentration levels well above their detection limits for all three LA-ICP-MS conditions.

This suggests that all these elements can be measured satisfactorily in all the three quadrants, as confirmed by the actual elemental oxide maps in Figure 4.5. For the trace elements Ba, Cr and Nb, the LA-ICP-MS conditions for quadrant Q3 resulted in elemental oxide detection limits of 3.59×10^{-3}, 4.50×10^{-3} and 2.47×10^{-3} % *w*/*w*, respectively. Knowing that the actual concentrations of BaO, Cr_2O_3 and Nb_2O_5 in the bulk of the *murrina* (measured on the outer rim of quadrant Q2) are $5\times10^{-3}\pm2\times10^{-3}$, $9\times10^{-4}\pm3\times10^{-4}$ and $9\times10^{-5}\pm3\times10^{-5}$ % *w*/*w*, respectively, it is clear that the LA-ICP-MS conditions for Q3 cannot produce reliable 2D maps, as shown in Figure 4.5. The LA-ICP-MS conditions for Q2 fare much better, with elemental oxide detection limits of 1.26×10^{-4} % *w*/*w* BaO, 3.62×10^{-4} % *w*/*w* Cr_2O_3 and 6.30×10^{-5} % *w*/*w* Nb_2O_5, which are all below the actual measured concentrations in the *murrina*. Thus, our computational-experimental strategy faithfully predicted the LA-ICP-MS conditions for Q2 to yield the best quality elemental maps.

Although pre-knowledge on elemental oxide concentrations has been used in the prediction, in general we may assume that concentrations of ca. 10^{-4} % *w*/*w* are borderline cases and LA-ICP-MS conditions yielding detection limits below 10^{-4} % *w*/*w* are better excluded. What cannot be predicted is the elemental

heterogeneity, although this will only give rise to more noise in the maps and not necessarily to unintelligible maps.

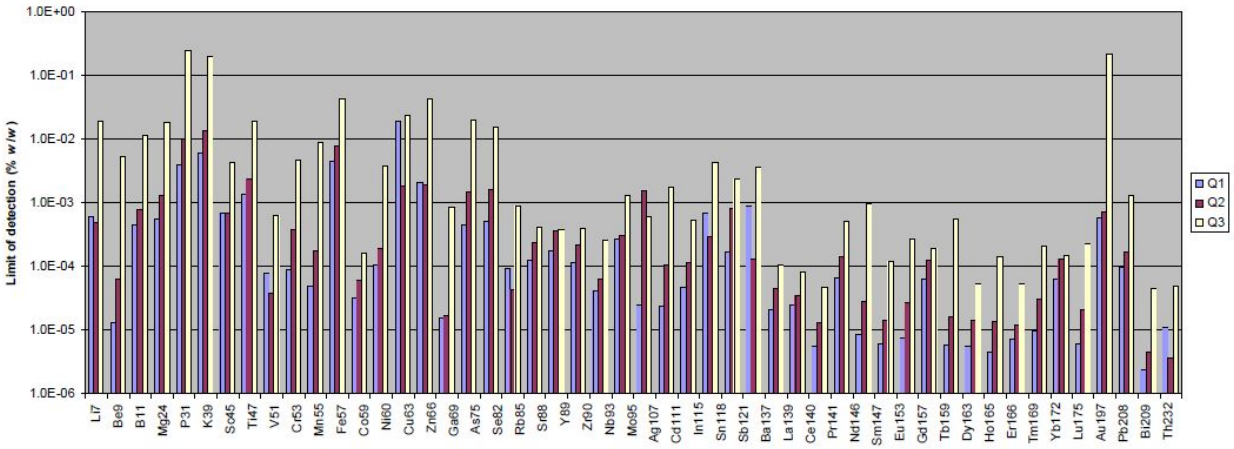

Figure 4.7. Limits of detection for the elemental oxides based on three times the standard deviation in the "blank" glass DLH6 (400 pixels) upon LA-ICPMS single line scanning under three different conditions (Table 4.1).

4.9. Application to 2D mapping of ancient glass

4.9.1. LA-ICP-MS mapping of the Iron Age polychrome glass

The computational-experimental strategy described above was used to predict the best possible LA-ICP-MS conditions for experimental 2D mapping of the pre-Roman glass shown in Figure 4.1a. These optimal conditions were as follows: laser beam, 65 µm (square); grid spacing, 65µm; repetition rate, 10 Hz; scanning speed, 32 µm s^{-1}; acquisition time/pixel, 2s (the remaining standard conditions can be found in Table 4.1). The resulting 2D map upon virtual ablation of the pre-Roman glass is shown in Figure 4.9 and shows that a high-quality map can be obtained in a relatively short analysis time (3.3h).

Preliminary observations of the glass sample by optical and electron microscopy detected a highly inhomogeneous texture, both on the external surface and on the broken section indicated in Figure 4.8a.

The glass bulk showed a very rough general texture and a wide-scale distribution of crystalline aggregates and bubbles in the glass (Figure 4.8b). These features can considerably affect the precision of the elemental quantification by a microanalytical technique such as LA-ICP-MS. From the elemental mapping results (Figure 4.9) this glass can be classified as a soda-lime-silica glass, based on its contents (concentrations ± standard deviations): silica (70.0±6.8% *w*/*w*), soda (17.0±3.9 % *w*/*w*) and lime (7.0±1.4 % *w*/*w*), and low potash (0.50±0.02 % *w*/*w*) and magnesia content (0.54±0.01 % *w*/*w*). Moreover, it presents a very low level of heterogeneously distributed phosphorous oxide (0.041±0.004 % *w*/*w*). Low K_2O, MgO and P_2O_5 contents correspond to the use of natron as fluxing agent (Verità, 2002; Shortland *et al.,* 2006; Reade *et al.,* 2009; Shortland and Schroeder, 2009). Particular elemental maps from Figure 4.9 were selected (see Figure 4.10) to highlight correlations between elements and their association with the features of the artefact concerning chromophores, opacifiers and their mineral sources.

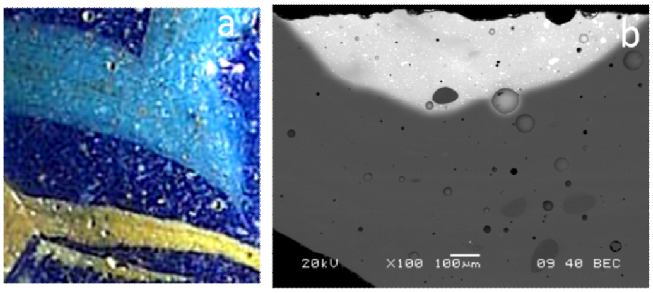

Figure 4.8. (a) mapped area and (b) SEM image of the broken section with the yellow decoration on the top and the blue bulk with bubbles and mineral inclusions.

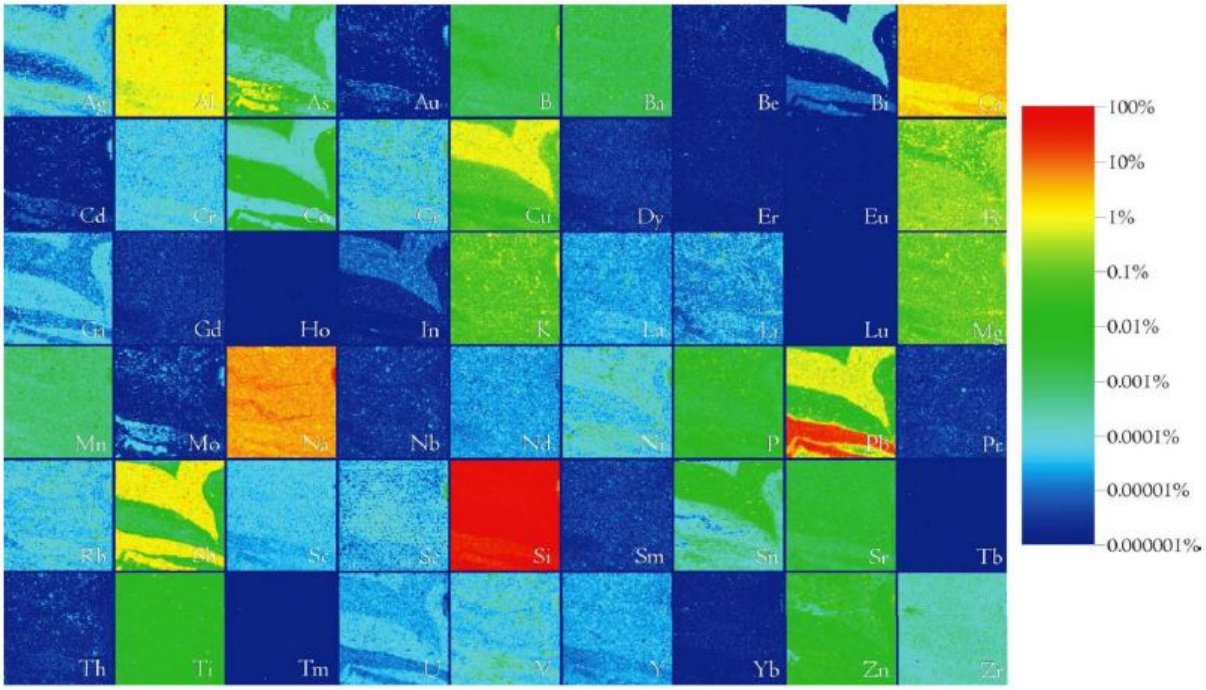

Figure 4.9. LA-ICP-MS elemental oxide maps of the Iron Age glass. Since the elemental oxide concentrations in all maps are scaled from 10 to 10 % *w*/*w* a logarithmic scale was used for visualization of all elemental oxides simultaneously. For an explanation of the color scale see Figure 4.5.

Analysis of chromophores and opacifiers – The Co and Cu maps (Figure 4.10a) show that the deep blue features can be attributed to the presence of CoO (0.088±0.021% *w*/*w*) and CuO (0.55±0.22 % *w*/*w*). The application of elemental mapping proves to be particularly suitable for the analysis of opaque glasses. The opacity of glass is due to the presence of a dispersion of crystals in the glass matrix (Henderson *et al.,* 2000). The 2D maps in Figure 4.10 indicate that the opaque turquoise and yellow decorations contain opacifiers based on antimony. Antimony-based opacifiers were used from the beginning of glass production in the Near East and Egypt around 1500 B.C. (Tite *et al.,* 2008). The opacity and colour of the yellow glass can be attributed to the presence of lead antimonate ($Pb_2Sb_2O_7$; measured as Sb_2O_5 [3.2±1.3 % *w*/*w*] and PbO [30.0±6.0 % *w*/w]). White calcium antimonate opacifier ($Ca_2Sb_2O_7$ or $Ca_2Sb_2O_6$; measured as CaO [6.8±0.4 % w/w] and Sb_2O_5 [3.2±1.2 % w/w]) and aquamarine-blue copper oxide (2.5±0.6 % w/w) are responsible for the turquoise hue. Calcium was not intentionally added to the glass batch since lime was a

natural component of the sand. Lead is present in strong excess in the yellow glass and in a more limited amount in the turquoise glass (2.3±1.1 % *w*/*w*). This element, with its low concentration and heterogeneous distribution in the blue glass (0.8±0.5 % *w*/*w*), found also in some other Iron Age glasses (Arletti *et al.,* 2010), probably entered the batch with the cobalt mineral. The presence of lead in the turquoise glass may have led to the formation of only a small amount of lead antimonate, or more probably it completely dissolved in the batch, without contributing to its opacity (Arletti *et al.*, 2008). Figure 4.10c also shows the 2D maps rendered as 3D maps for Sb and Pb with linear scaling, convincingly demonstrating their distribution in the glass and the potential of LA-ICP-MS for elemental mapping of glass.

Mineral sources – Elemental image maps also allow us to speculate on the composition of the ores used as the sources of chromophores and opacifiers based on the correlation between the elements. The study of the mineral sources for chromophores and opacifiers is rather complex and it is often difficult to state useful associations between elements. Several studies have investigated the nature and origin of the cobalt ores used for blue coloured glass (Henderson, 1985; Gratuze and Picon, 2006; Gratuze *et al.*, 1992; Gratuze *et al.,* 1996; Gratuze*,* 1997; Shortland *et al.*, 2006; Towle *et al.*, 2001). They were based on the analysis of the elements associated with cobalt, such as aluminium, copper, manganese, iron, nickel, zinc, arsenic, antimony and lead.

From the elemental oxide maps in Figure 4.10d it seems that in the dark blue glass cobalt is associated with copper and some impurities such as gallium and uranium. Cobalt may occur in combination with copper in heterogenites (mixtures of minerals as mindigite $2Co_2O_3 \cdot CuO \cdot 3H_2O$ and trieuite $2Co_2O \cdot CuO \cdot 6H_2O$) (Brady *et al.,* 2002), so that the presence of copper could be related to the addition of this kind of ore as a colouring agent. However, we cannot exclude that copper has been added to the glass batch independently to modify the cobalt blue hue, probably in the form of brass, as suggested by a % *w*/*w* Cu/Zn ratio of about 7, the same as one would expect in brass. This could also explain the correlation of cobalt and copper with Ga_2O_3 (0.0023±0.0011 % *w*/*w*), which is usually present in trace amounts in zinc. Uranium, as UO_2 (0.0019±0.0011 % *w*/*w*), might originate from the ores of copper and/or cobalt. The elemental oxide maps of the turquoise decoration in Figure 4.10e show that copper is associated with tin, lead and traces of indium and bismuth, although the occurrence of ^{115}In is most likely an interference caused by ^{115}Sn (natural abundance, 0.34 %) upon measuring higher levels (ca. 0.01 % *w*/*w* in this case) of ^{118}Sn (natural abundance, 24.44 %). The presence of copper, lead and tin suggests that two distinct possible materials could be identified as sources of copper: *i*) an ore containing all these three elements (Santopadre and Verità, 2000) and *ii*) slags from the working of bronze (Henderson, 1985). Antimony appears to be associated with traces of silver, arsenic and nickel, while lead correlates with traces of cadmium, arsenic and molybdenum. This suggests that the possible sources of lead and antimony could be sulphide ores containing galena (PbS) and stibnite (Sb_2S_3), respectively. The correlation of silver with antimony might be related to the use of cupellation litharge as a source for lead antimonate in the decorations (Mass *et al.*, 2002). This could also explain the presence of lead in the turquoise decoration. However, according to Rehren and Shortland (Rehren and Shortland, 2003; Shortland *et al.*, 2000), litharge as the source for antimony would be rather unlikely. Figure 4.11 shows the line scans after ablation.

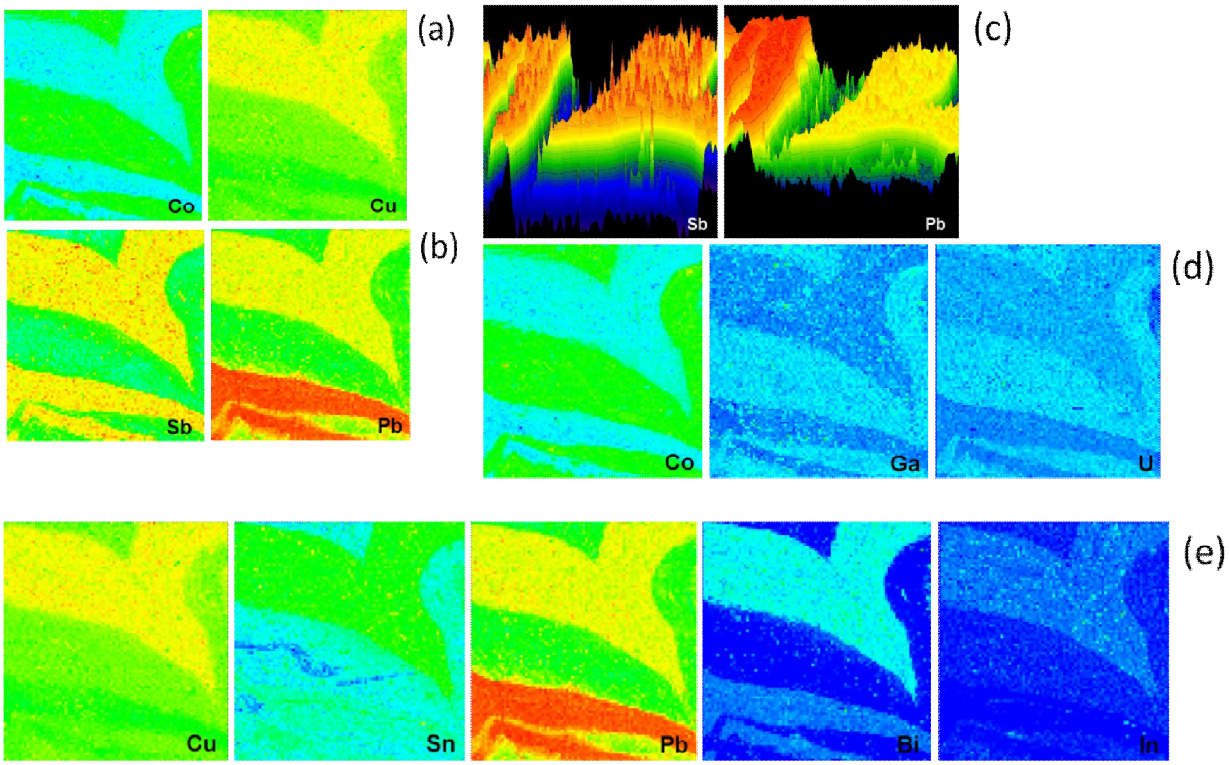

Figure 4.10. Selected elemental oxide maps of the Iron Age glass highlighting: 1) the correlations with the blue colourations (a) and the opaque and yellow decorations in 2D (b) and 2D rendered in 3D (c); 2) the provenance of some elements (d and e). For the explanation of colours see Figure 4.5. All maps a-e had logarithmic scaling as in Figure 4.7, except the 2D maps rendered in 3D in (c) which had linear scaling.

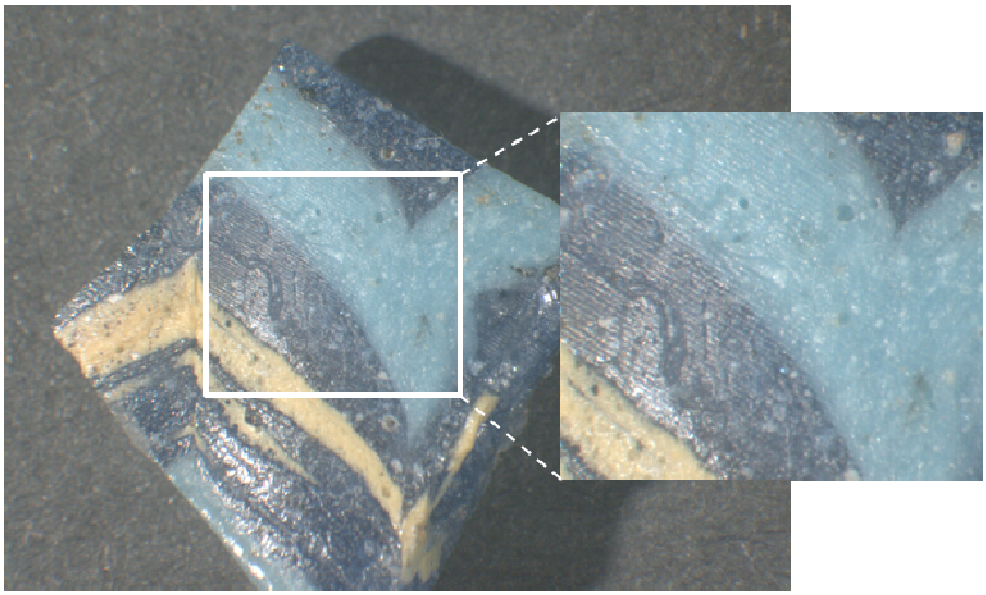

Figure 4.11. Photograph of the sample after ablation. The white rectangle shows the zoomed area on the right where the line scans are more visible.

4.9.2. *EPMA WDS mapping of the Iron Age polychrome glass*

WDS (Wavelength dispersive spectrometry) elemental maps were performed on the break-section of the Iron Age glass sample at the interface between bulk and decorations (Figure 4.12a). The selected area was a section of about 220x230 µm. The Cu map (Figure 4.12b) shows a concentration gradient at the interface between the blue and the turquoise decoration. Cu and Fe (here not presented) appear to have diffused more extensively than other elements, such as Pb, Sb, As and Sn. We noted also the non-homogeneous distribution of Ca, in contrast with Sb, that shows almost no diffusion in the near interface (Figure 4.12 c/d).

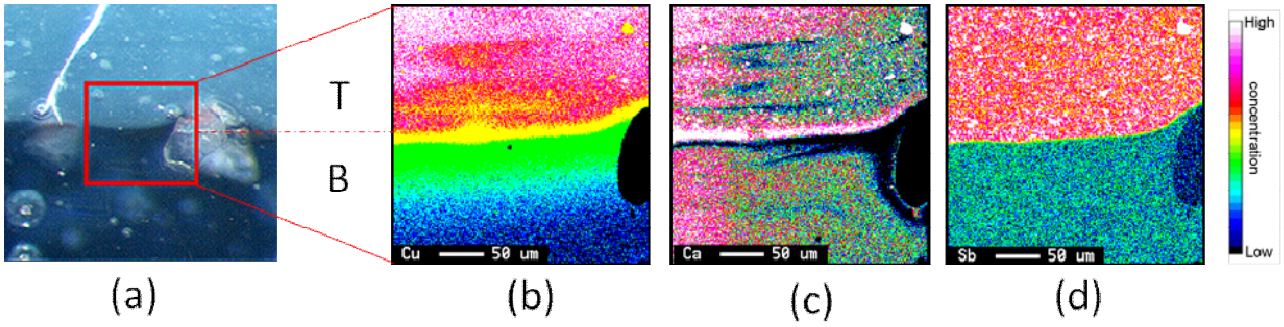

Figure 4.12. Picture of the glass sample analyzed (a) and WDS maps of Cu (b), Ca (c) and Sb (d) at the interface between the transparent blue bulk (B) and the opaque turquoise decoration (T). Every map has a different color scale.

4.9.3. *LA-ICP-MS mapping of the Roman polychrome glass*

The analyzed sample is a fragment of glass bowl (Figure 4.1b) from the Roman period. The quantitative elemental maps of each one of the 54 elements were performed on an rectangular area of the sample of about 5x5.50 mm (Figure 4.13), with 50 laser traces. The concentration values of the element oxides were visualized in pseudo-colors, both in 2D and 3D.

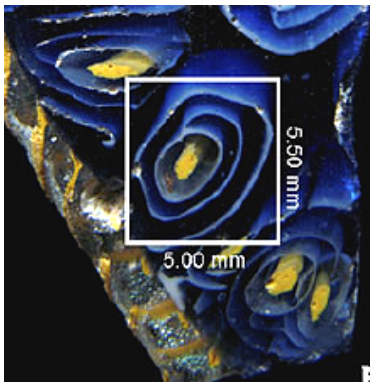

Figure 4.13. The analyzed Roman glass with the mapped area (white rectangle).

A first visual analysis of the elemental mapping shows that this glass can be classify as a soda-lime-silica glass with low potash and magnesia contents. This involves the use of a mineral sodic flux such as *natron*.

In Figure 4.14 the maps of Sb_2O_5, PbO and CaO are presented by way of examples. They are clearly indicative of the use of lead and calcium antimonates as yellow and white opacifiers respectively. It is well known that antimony-based opacifiers (yellow lead antimonate and white calcium antimonate) were used from the beginnings of glass production in the Near East and Egypt around 2500 B.C. through into the Roman period (Turner and Rooksby, 1959 and Tite *et al*., 2008).

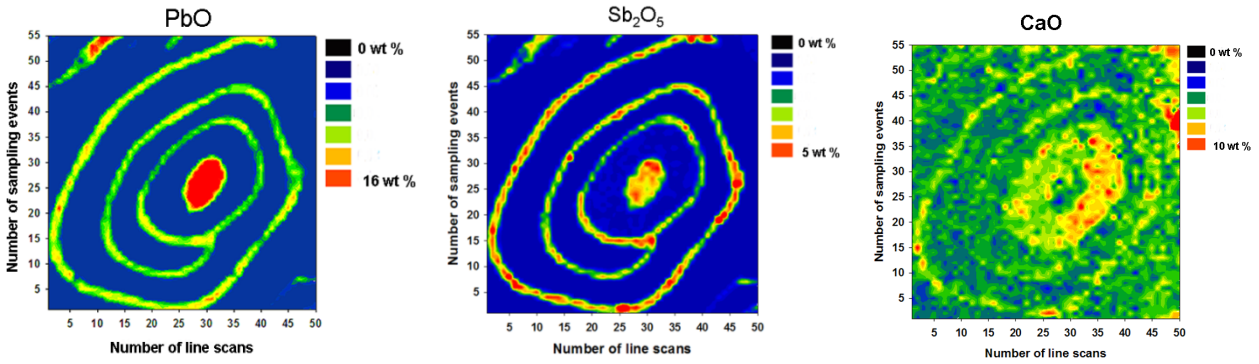

Figure 4.14. LA-ICP-MS 2D elemental maps of Pb, Sb and Ca oxides

Antimony and lead appear positively correlated in the yellow central spot and in the white spiral decoration (Figure 4.14); also Ca correlates with Pb and Sb. This indicates the presence of yellow lead antimonate in the central spot and of white calcium antimonate in the spiral, both as chromophores and opacifiers. Lead could have been added to the spiral decoration to improve the fluidity of the melt (Arletti *et al*., 2008 and Arletti *et al*., 2010).

Elemental maps may address to hypothesize the composition of the ores used as sources of chromophores and opacifiers, that are often difficult to identify. In the central spot and in the spiral, Pb and Sb appear associated to Bi and As respectively (Figures 4.14 and 4.15).

In the case of cobalt, a very powerful colorant responsible for the color of the blue area, it appears correlated with iron and nickel (Figure 4.16).

These examples of associations of elements, pure made by visual inspection of the maps, may be useful guides to hypothesize or exclude the nature of the sources for antimony, lead and cobalt, which in many cases related to ancient glasses are still not well understood.

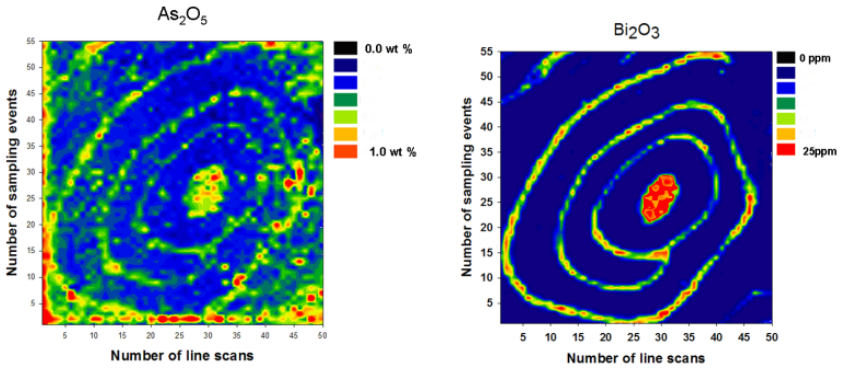

Figure 4.15. LA-ICP-MS 2D elemental maps of As and Bi

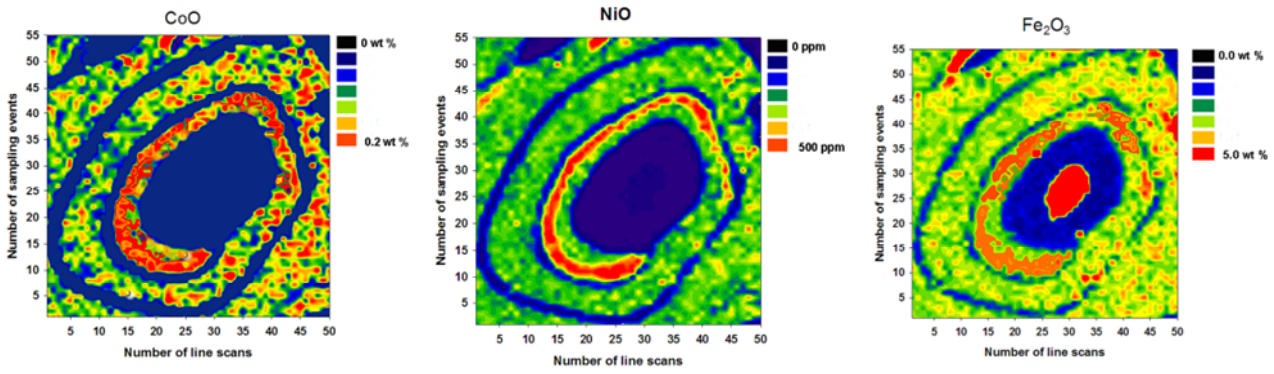

Figure 4.16. LA-ICP-MS 2D elemental maps of Co, Ni and Fe

An alternative, and sometimes more "revealing" way, to present the surface distribution of an element is via a 2D map with 3D rendering which contains the lateral distribution coordinates on the *x* and *y* axes and the concentration values on the *z*-axis (see Figure 4.17).

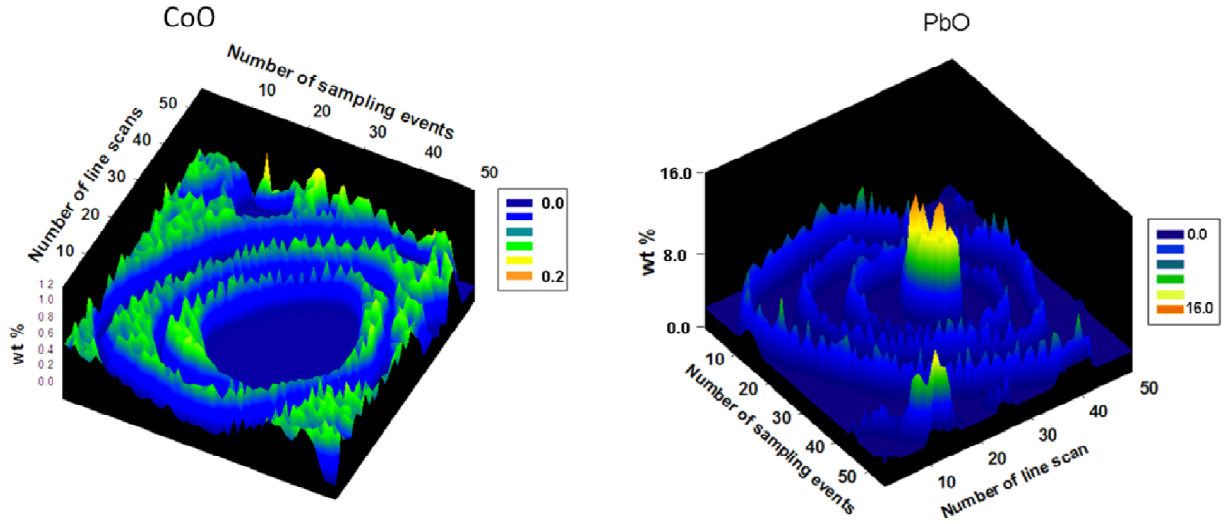

Figure 4.17. LA-ICP-MS 2D elemental maps of CoO and PbO, rendered in 3D.

4.9.4. EPMA-WDS mapping of a mirror glass

WDS maps may also be used to study the deterioration phenomena of glass. In order to assess the suitability of WDS maps to visualize the morphology of glass weathering, both the surface and the broken edge section of a silica-potash-lime glass (see Table 4.2) were mapped. This glass is a sample from a mercury-tin amalgam mirror (Figure 4.2) of unknown origin dates back to the end of the 17th century.

Table 4.2. Chemical composition by WD-XRF on the bulk and surface of the mapped glass sample

Oxides of the mapped elements	Bulk (% wt)	Surface (% wt)
SiO_2	68.2	80.9
Na_2O	2.0	0.8
K_2O	22.4	7.4
SO_3	0.4	0.8

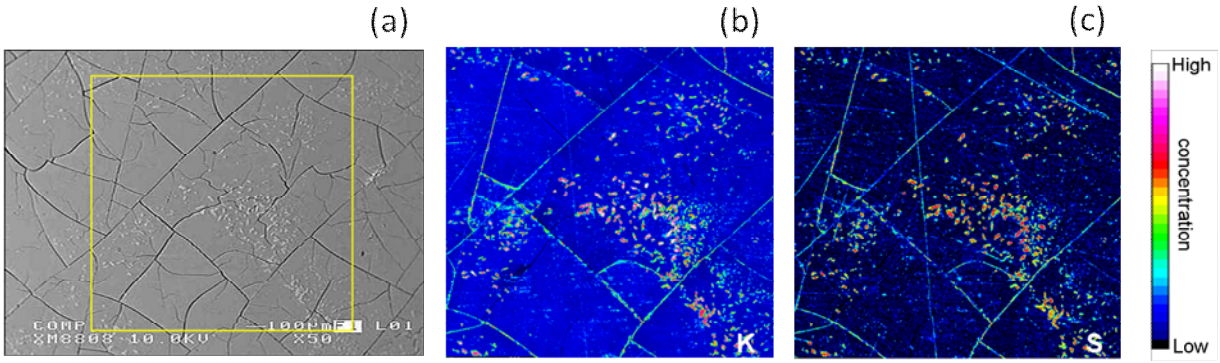

Figure 4.18. SEM/SE image of the glass mapped surface (a), WDS map of K (b) and WDS map of S (c). The selected area was a section of about 2x2 mm.

The hydrolytic attack to a glass surface consists of ion exchange reactions (leaching) between the glass network modifying ions, such as Na^+, K^+, Ca^{2+}, Mg^{2+}, and the water ion H_3O^+. This mechanism leads to the formation of a hydrated and alkali depleted glass layer. When the pH of the aqueous solution on the glass surface is > 9, glass corrosion can occur, causing network hydrolysis. These two glass alteration mechanisms are well explained in the literature (Cox *et al*., 1979; Newton and Fuchs, 1988; Davison, 2003; Falcone *et al*., 2011). In glasses exposed to the atmosphere, the extracted modifier ions can react with species present in the environment, such as CO_2, SO_x, NO_x, to form the respective salts. As a consequence, neo-crystallizations of different composition can be formed on the glass surface, depending on the composition of the glass and on the species present in the environment. The K and S maps of Figure 4.18 show the presence of potassium sulphates on the surface, as suggested also by the spindle-shaped crystals (Falcone *et al*., 2010), indicating that the extracted K can react with the SO_x species present in the environment.

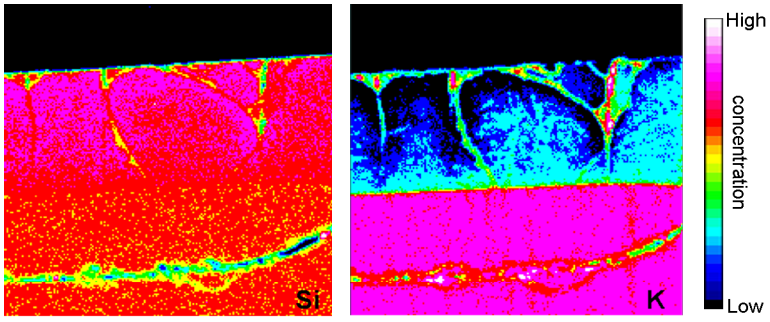

Figure 4.19. WDS maps of Si and K on the cross section of the sample. The selected area was a section of about 190x190 µm.

The maps of Figure 4.19 show the patterns along a broken edge section of the sample; from the pristine glass (lower layer) to the weathered phase (upper layer) an inverse correlation between Si and K is apparent, as a consequence of K depletion through leaching. In the weathered area there are a lot of cracks due to the loss of glass stability as the result of the deterioration processes (Davison, 2003).

Table 4.2 reports the composition of the potassic glass both in the bulk and on the surface, where an hydrated silica-rich layer due to the extraction of potash ions is present. It is well known that "*potash glasses have about half the durability of soda glasses because the potassium ions are larger than those of sodium ions, and take up more space in the glass network*" (Davison, 2003).

Glass weathering is often a very complex phenomenon and the study of its dependence on different environmental components and conditions is still not well understood. The nature and pattern of the leached superficial layer of glass is very important to determine the glass durability and deterioration factors and elemental mapping could be successfully assist the studies in this field.

4.10. Conclusions

By evaluating the computational-experimental strategy for elemental image mapping of a modern *murrina*, it is evident that prediction of the LA-ICP-MS conditions for optimal 2D elemental image mapping prior to actual mapping can be carried out efficiently and effectively. The steps to be taken are as follows: 1) make a digital image of the polychrome glass sample; 2) upload this image in the free virtual mapping software; 3) plug in numbers for the relevant LA-ICP-MS parameters and "play" with them to obtain the best image in the shortest analysis time and the highest spatial resolution; 4) use these virtually optimized parameters to make a line scan on a reference glass (NIST SRM 610) and a "blank" glass; 5) calculate the elemental detection limits to predict the noise floor in the elemental maps. When set up properly this process should take no longer than ca. one hour but might save many hours of analysis time or even prevent one from choosing the wrong LA-ICP-MS parameters; one should also be aware that the mapping process cannot be repeated again on the same glass surface, and therefore choosing optimal parameters in advance is particularly valuable. The LA-ICP-MS optimization strategy was successfully applied for quantitative multi-elemental mapping of two polychrome glass vessel fragments from the Iron Age and the Roman Age. The purpose of this test was to show how elemental mapping can contribute to the overall information retrieval on elemental distribution and homogeneity in the glass surface to gain insight into the presence of chromophores, opacifiers and their associated ores in an easy way, i.e. by visual inspection of the maps.

While LA-ICP-MS elemental mapping can be functional for retrieval of spatial elemental information and elemental correlations at moderate spatial resolution but high sensitivity, WDS elemental mapping is mainly aimed to identify the distribution of crystalline phases and grains at high spatial resolution but lower sensitivity, and to visualize concentration gradients of elements at the interfaces of different areas, such as bulk and decorations. Nevertheless, both elemental mapping techniques are complementary and can be used to study the distribution and morphology of the different types of degradation on glass surfaces.

4.11. References

Arletti R., Vezzalini G., Quartieri S., Ferrari D., Merlini M., Cotte M. (2008) Polychrome glass from Etruscan sites: first non-destructive characterization with synchrotron μ-XRF, μ-XANES and XRPD. Appl Phys A 92; pp. 127-135.

Arletti R., Maiorano C., Ferrari D., Vezzalini G., Quartieri S. (2010) The First Archaeometric Data on Polychrome Iron Age Glass from Sites Located in Northern Italy, J Archaeolog Sci 37; pp. 703-712.

Brady G.S., Clauser H.R., Vaccari J.A. (2002) Materials handbook 15th edition. McGraw-Hill, New York.

Bonomi S. (1996) Vetri antichi del museo archeologico nazionale di Adria, Venezia: Giunta Regionale del Veneto: Comitato nazionale italiano Association internazionale pour l'histoire du verre (Corpus delle collezioni archeologiche del vetro nel Veneto).

Cox G.A., Heavens O.S., Newton R.G. and Pollard A.M, (1979) A study of the weathering behaviour of medieval glass from York Minster, J. Glass. Stud., 21; pp. 54–75.

Davison S. (2003) Conservation and Restoration of Glass. Butterworth Heinemann, Oxford; pp. 169-198.

Falcone R., Licenziati F., Orsega E.F., Verità M. (2011) The dependence of the weathering of soda-lime-silica glass on evironmental parameters: a preliminary investigation, Glass. Technol. 52 (1); pp. 23-29.

Falcone R., Nardone M., Sodo A., Sommariva G., Vallotto M. and Verità M. (2010) SEM-EDS, EPMA and MRS analysis of neo-crystallisations on weathered glasses, IOP Conf. Series: Materials Science and Engineering 7.

Gratuze B., Soulier I., Barrandon J.N., Foy D. (1992) De l'origine du cobalt dans les verres, Revue d'Archéométrie 16; pp. 97-108.

Gratuze B., Soulier I., Blet M., Vallari L. (1996) De l'origine du cobalt: du verre à la céramique, Revue d'Archéométrie 20; pp. 77-94.

Gratuze B. (1997) L'apport des analyses de verres archéologiques: etudes de cas. In: Techne, Verres–Emaux–Glaçures. Paris Laboritoire de recherche des musées de France n. 6; pp. 8-18.

Gratuze B., Blet-Lemarquand M., Barradon J.N. (2001) Mass spectrometry with laser sampling: A new tool to characterize archaeological materials, J. Radioanal. Nucl. Chem. 247; pp. 645-656.

Gratuze B., Picon M. (2006) Utilisation par l'industrie verrière des sels d'aluns des oasis égyptiennes au début du premier millénaire avant notre ère. In: Borgard P., Brun J.P., Picon M. (eds) L'Alun de Mediterranie. Naples/Aix-en-Provence, Centres Jean Bérard et Camille Jullian, Collection du Centre Jean Bérard 23; pp. 269-276.

Harden D.B. and Tatton-Brown V.A. (1981) Catalogue of Greek and Roman glass in the British Museum Vol. 1. Core and rod-formed vessels and pendants and Mycenaean cast objects. London, British Museum Publications.

Hamilton D.L., Hopkins T.C. (1995) Preparation of glasses for use as chemical standards involving the coprecipitated gel technique. Analyst 120; pp. 1373-1377.

Henderson J. (1985) The raw materials of early glass production, Oxford J. Archaeol. 4; pp. 267-291.

Henderson J. (2000) The Science and Archaeology of Materials: An investigation of inorganic materials. Routledge, New York.

Liu Y., Hu Z., Gao S., Gunther D., Xu J., Gao C., Haihong C. (2008) In situ analysis of major and trace elements of anhydrous minerals by LA-ICP-MS without applying an internal standard. Chem Geol 257; pp. 34-43.

Mass J.L., Wypyski M.T., Stone R.E. (2002) Malkata and lisht glassmaking technologies: towards a specific link between second millennium B.C. metallurgist and glassmakers, Archaeometry 44; pp. 67-82.

Newton R.G. and Fuchs D. (1988) Chemical analyses and weathering of some medieval glass from York Minster, Glass. Technol., 29; pp. 43–8.

Phipps C., Luke J., Funk D., Moore D., Glownia J., Lippert T. (2006). Laser impulse coupling at 130 fs. Appl Surf Sci 252; pp. 4838–4844.

Reade W., Freestone I.C., Bourke S. (2009) Innovation and continuity in Bronze and Iron Age glass from Pella in Jordan. In: Janssens K., Degryse P., Caen J., Van't dack L. (eds) Annales du 17 Congrès de l'Association Internationale pour l'Histoire du Verre, Anvers, 2006. AIHV and University Press Antwerp, Brussels; pp. 47-54.

Rehren T., Shortland A.J. (2003) Comments on J.L. Mass, M.T. Wypyski and R.E. Stone, Malkata and Lisht glassmaking technologies: towards a specific link between second millennium B.C. metallurgists and glassmakers and reply, Archaeometry 44; pp. 67-82.

Santopadre P., Verità M. (2000) Analyses of the production technologies of Italian vitreous materials of the Bronze Age, J. Glass. Stud. 42; pp. 25-40.

Šelih V.S., Van Elteren J.T. (2011) Quantitative multi-element mapping of ancient glass using a simple and robust LA-ICP-MS rastering procedure in combination with image analysis. Anal Bioanal Chem 401; pp. 745-755.

Shortland A.J., Nicholson P.T., Jackson C.M. (2000) Lead isotopic analysis of Eighteenth-Dynasty Egyptian eyepaints and lead antimonate colorants, Archaeometry 42; pp. 153-157.

Shortland A.J., Schachner L., Freestone I., Tite M. (2006) Natron as a flux in the early vitreous materials industry: sources, beginnings and reason for decline, J Archaeolog Sci 33; pp. 521-530.

Tite M.S., Pradell T., Shortland A.J. (2008) Discovery, production and use of Tin-based opacifiers in glasses, enamels and glazes from the Late Iron Age onwards: a reassessment. Archaeometry 50; pp. 67-84.

Shortland A.J. and Schroeder H. (2009) Analysis of First Millennium BC Glass Vessels and Beads from the Pichvnari Necropolis, Georgia. Archaeometry 51; pp. 947-965.

Towle A., Henderson J., Bellintani P., Gambacurta G. (2001) Frattesina and Adria: report of scientific analyses of early glass from the Veneto. PADUSA, Bollettino del Centro Polesano di studi storici, archeologici ed etnografici; anno XXXVII, Rovigo; pp. 7-68.

Triglav J., Van Elteren J.T., Šelih V.S. (2010) Basic modeling approach to optimize imaging by laser ablation ICPMS, Anal Chem 82; pp. 8153-8160.

Turner W. E. S. and Rooksby H. P. (1959) A study of opalising agents in ancient opal glasses throughout three thousand four hundred years, Glastechnische Berichte, 32K, VII, pp. 17–28.

Van Elteren J.T., Tennent N.H., Šelih V.S. (2009) Multi-element quantification of ancient/historic glasses by laser ablation inductively coupled plasma mass spectrometry using sum normalization calibration, Anal Chim Acta 644; pp. 1-9.

Verità M., Renier A., Zecchin S. (2002) Chemical analyses of ancient glass findings excavated in the Venetian lagoon, J. Cult. Herit. 3; pp. 261-271.

Walton M.S., Shortland A.J., Kirk S., Degryse P. (2009) Evidence for the trade of Mesopotamian and Egyptian glass to Mycenaean Greece, J. Archeolog. Sci. 36; pp. 1496-1503.

Xu X. (2002) Phase explosion and its time lag in nanosecond laser ablation, Appl Surf Sci 197–198; pp. 61–66.

Chapter 5
Development of 3D mapping methodologies*

* Part of this chapter was published in Van Elteren *et al*. 2013.

5.1. Introduction

In this chapter a multi-elemental 3D laser ablation-ICP-mass spectrometry mapping procedure is elaborated for high resolution depth information retrieval to investigate surface layer phenomena in degraded glass. The procedure is based on 50 laser pulses per grid point at a pulse rate of 1 Hz, combined with the use of an ablation cell with good flow dynamics (short washout time) and ultrafast ICP-MS monitoring with subsequent integration of each pulse in time. This experimental setup circumvents the commonly encountered problems of pulse mixing and signal tailing, whereas also limiting the thermal diffusion into the bulk. Nevertheless, deviation of the crater profile from the ideal flat-top shape might still lead to material mixing at the layer interface. However, the conceptual limitations of fixed focus laser drilling such as signal blurring, loss of depth resolution, re-ablation of earlier deposited material on the ablation crater walls or surface, etc. (Woodhead *et al*., 2008) are greatly reduced with this novel drilling procedure. Elaborate data processing and manipulation of the huge amount of ICP-MS data retrieved requires development of dedicated software routines to link each laser pulse to unique 3D information which may be displayed in various ways using specialized image processing programs.

The merits of the drilling procedure were investigated by multi-elemental 3D imaging of a medieval, corroded glass artifact with areas displaying different degrees of deterioration. When glass dissolves, ion exchange leaching via counter-current diffusion and/or network hydrolysis remove the mobile metals and leave a less-reactive substructure near the surface (Casey, 2008). The dominance of either reaction is dependent on the chemical composition and surface structure of the glass, as well as the environmental conditions such as pH, temperature and humidity. Application of LA-ICP-MS to 3D glass analysis is appealing in that most methods such as XPS, SIMS, AFM, PIXE, PIGE, X-ray scattering, neutron scattering, etc. focus on surface analysis or very shallow depth resolution (Doménech-Carbó *et al*., 2009). Investigation of the degradation mechanisms in deeper layers under the surface with these techniques requires analysis of a cross-sectional fragment of the glass. Recently, a study with µ-XRF was undertaken to obtain direct depth-resolved information via the surface from a historical object in the reverse-glass painting technique by a confocal arrangement of the X-ray optics (Kanngießer *et al*., 2008) The 3D mapping procedure developed not only merits better and easier study of glass degradation mechanisms but also forms a basis for application to other scientific topics. In order to better understand the weathering mechanism WDS mapping was applied to the same sample with a spatial resolution of 1 µm, although recently submicrometer images of the same sample were generated via LA-ICP-MS through a deconvolution approach (Van Malderen *et al*., 2015).

5.2. Sample

The 3D mapping approach was applied to an ancient glass fragment, probably part of a drinking glass, with weathered areas (see Figure 5.1). The artifact from Poggio Diana castle (Sicily) was excavated from a pit used for storage of grain and dates from the second half of the 14th century to the beginning of the 15th century (more information on the sample can be found in Panighello *et al*., 2013). Prior to analysis, the sample was washed with a solution of ca. 0.15 mol l^{-1} HCl and mounted on a glass slide with double-sided tape. For measurement of the bulk composition of the glass, an uncorroded area on the sample was chosen and subjected to deep laser drilling using a GeoLas 193 nm ArF* excimer-based LA system (MicroLas, Germany) interfaced with a Perkin-Elmer Sciex DRCPlus quadrupole-based ICP-MS instrument (Canada). In Table 5.1 the operational conditions are given. Quantification was carried out using the sum normalization calibration procedure described in Chapter 2. The bulk compositional data of the ancient glass sample are

summarized in Table 5.2, indicating that it is a soda-lime-silicate glass in which soda-rich plant ashes were used as flux and MnO was likely applied as a decolorizing agent. Since most glass standards are not supposed to be used for microanalysis and are essentially inhomogeneous at the micrometer scale, a highly homogeneous, industrial soda-lime-silica glass (homogeneity verified by LA-ICP-MS, see Paragraph 5.5 and specifically Figure 5.6), produced by Verallia (Saint-Gobain, Italy) conform a bottle-production method, was used for validation of the 3D mapping approach.

The bulk major and minor elemental composition of this glass was determined by conventional dispersive X-ray fluorescence spectrometry (WDXRF) using a sequential X-ray spectrometer (Thermo ARL ADVANT' XP^{+}). The instrument was equipped with a rhodium tube and calibrated with international certified standard materials (Society of Glass Technology, National Bureau of Standards and BAM Federal Institute for Materials) and interlaboratory samples analyzed in the framework of the International Committee 2 “Chemical durability and analysis” (ICG-TC2).

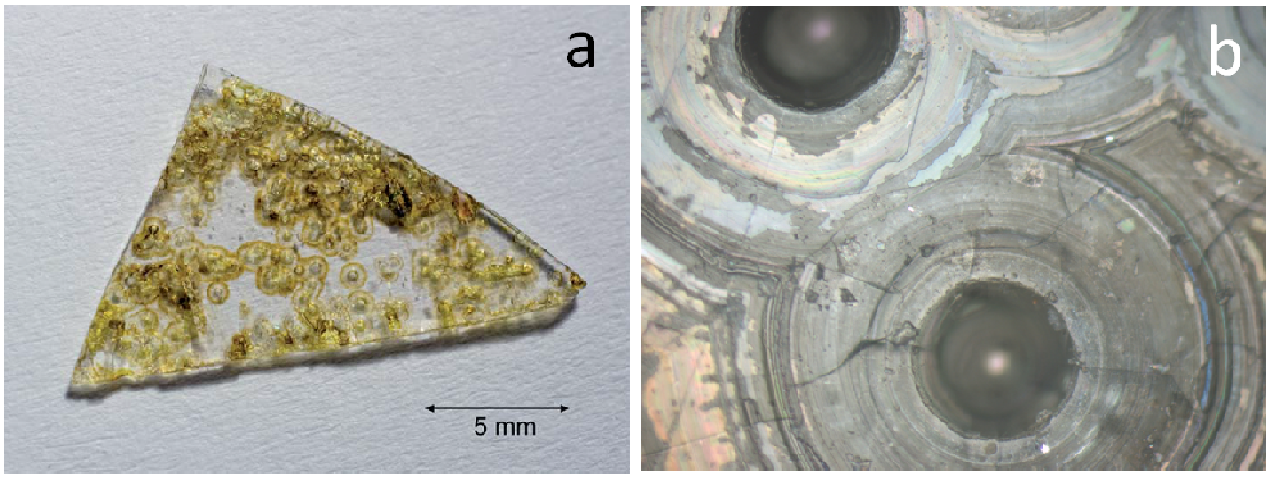

Figure 5.1. Photograph of the ancient, weathered glass (a) and optical microscope image (100X) of the weathered rings (b).

Table 5.1. LA-ICP-MS operating conditions for bulk analysis.

Laser (GeoLas 193 nm ArF* excimer-based)	
Beam diameter	120 µm
Fluence	8.8 J/cm^{-2}
Repetition rate	10 Hz
Penetration rate	ca. 0.1 µm s^{-1}
Dwell time	240 s
He flow rate	0.75 l min^{-1}
ICP-MS (Perkin-Elmer Sciex DRC ^{Plus})	
Number of elements measured	19 (^{23}Na, ^{24}Mg, ^{27}Al, ^{29}Si, ^{31}P, ^{39}K, ^{43}Ca, ^{47}Ti, ^{55}Mn, ^{57}Fe, ^{59}Co, ^{60}Ni, ^{63}Cu, ^{66}Zn, ^{88}Sr, ^{118}Sn, ^{121}Sb, ^{137}Ba, ^{208}Pb)
Total acquisition time	380 ms (1 ms per element)
Total analysis time	60-110 s
Standards	CMG B, C, D (see Chapter 2)

Table 5.2. Bulk compositional data (n=3) for the ancient corroded glass.

	Mean (% m/m)	RSD (%)
Na_2O	16.2	1.1
MgO	1.96	0.16
Al_2O_3	1.33	0.6
SiO_2	68.4	0.09
P_2O_5	0.395	3.4
K_2O	2.95	0.55
CaO	7.44	2.5
TiO_2	0.097	1.9
MnO	0.687	1.6
Fe_2O_3	0.445	3.2
CoO	0.002	3.4
NiO	0.002	5.8
CuO	0.004	3.7
ZnO	0.007	5.7
SrO	0.035	0.84
SnO_2	0.001	7.9
Sb_2O_5	0.000	89
BaO	0.018	3.2
PbO	0.001	56

5.3. Evaluation of 3D mapping procedure

An area of 1.79 mm x 1.79 mm on the weathered glass artifact (Figure 5.1), with clearly visible corroded, weathered and unweathered parts, was subjected to surface mapping by laser drilling (80 µm craters) on a 20 x 20 grid with a spacing of 90 µm (see Figure 5.2). Each crater was generated by a burst of 50 pulses, fired at a pulse rate of 1 Hz, meanwhile recording the signals (in counts per second) for 19 elements at 58 ms intervals and 1 ms dwell time per element (LA-ICP-MS operating conditions are given in Table 5.3).

Table 5.3. LA-ICP-MS operating conditions for LA-ICP-MS 3D mapping.

Laser (New Wave Research UP-213)	
Beam diameter	80 µm
Fluence	7 J/cm^{-2}
Repetition rate	1 Hz
Penetration rate	ca. 0.1 µm s^{-1}
Dwell time	1 ms per element
He flow rate	0.95 l min^{-1}
Argon	0.75 l min^{-1}
Ablation chamber	Single volume SuperCell^{TM} (New Wave Research, USA)
ICP-MS (Agilent 7500ce)	
Number of elements measured	19 (^{23}Na, ^{24}Mg, ^{27}Al, ^{29}Si, ^{31}P, ^{39}K, ^{43}Ca, ^{47}Ti, ^{55}Mn, ^{57}Fe, ^{59}Co, ^{60}Ni, ^{63}Cu, ^{66}Zn, ^{88}Sr, ^{118}Sn, ^{121}Sb, ^{137}Ba, ^{208}Pb)
Total acquisition time	58 ms (1 ms per element)
Standards	CMG B, C, D (see Chapter 2)

Although the single volume ablation chamber performs well under these conditions (washout time less than 0.5 s for the whole laser pulse, in which time the washout signal goes back to 1% of the maximum), performance may be further improved with a two volume ablation chamber exhibiting better reproducibility across the whole chamber (Müller *et al.*, 2009).

For validation of the 3D mapping procedure an area of 0.89 mm x 0.44 mm (10 x 5 grid) on the homogeneous, industrially produced glass underwent the same procedure with the exception that ^{53}Cr was added to the list of nuclides as well, making the recording interval 61 ms. By comparing the average concentrations per depth layer, the homogeneity of the industrially produced glass was verified. Short ICP-MS acquisition times were essential to be able to accurately retrieve the peak profiles for the individual laser pulses (peak widths of ca. 0.5 s) with the sequential (scanning) quadrupole-based ICP-MS instrument.

Calibration was performed with the Corning Museum of Glass reference glasses B, C and D, undergoing the same drilling procedure as the samples but then for only one spot instead of drilling on a grid, followed by a sum normalization calibration as for bulk analysis.

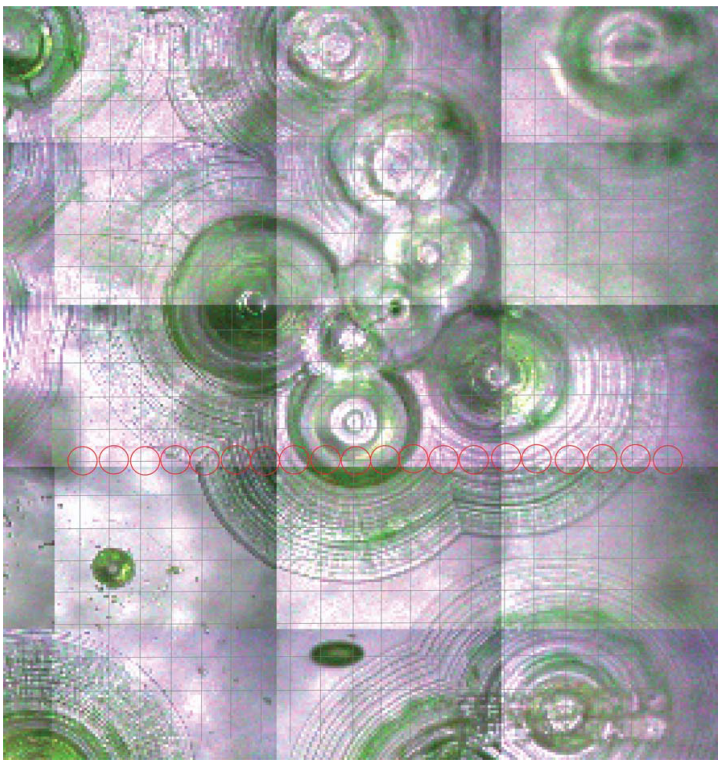

Figure 5.2. An area on the glass selected for 3D multi-elemental imaging by LA-ICP-MS. LA (50 shots) was performed on the grid points of the virtual 20x20 grid (spacing 90 µm) with the red circles indicating where detailed information was extracted in the form of cross-sectional 2D elemental maps.

5.4. Data acquisition, processing, manipulation and visualization

The laser ablation penetration rate is determined by the amount of sample removed by a single laser pulse. Measurements by optical profilometry (described in Chapter 2) showed this rate to be 0.15 ± 0.02 µm per pulse for the medieval glass sample investigated. The high linearity observed upon plotting the crater depths as a function of the number of pulses (R^2, 0.9933), for up to 50 pulses delivered at a repetition rate of 1 Hz, implies that the ablated volume per pulse is independent of the depth, what is in agreement with studies performed by Horn *et al*., 2001. They reported that the sample removal is constant over a large depth range (>100 pulses), but dependent on the properties of the material (see Chapter 3) and the laser ablation wavelength and fluence. In our case, the highly reproducible ablated volume, independent of the depth below the surface, also led to constant signals for NIST standard reference glass 612 [with a main elemental composition (Pearce *et al*., 1997) similar to that of the medieval glass under study (Table 5.2)] as can be seen from Figure 5.3.

The calculated relative standard deviation of the average peak area is 4%, suggesting that elemental fractionation phenomena during drilling are absent or negligible. When zooming in on one peak (see inset in Figure 5.3), it becomes clear that a short acquisition time for measurement of multiple elements is essential to be able to reliably determine the peak areas by integration for subsequent quantification and 3D multi-elemental imaging. However, extracting the 3D spatial elemental information of the weathered glass artifact from a 20 x 20 matrix (with a grid spacing of 90 µm), applying 50 pulses per grid point with a laser beam of 80 µm (see Figure 5.2), was challenging as in total 400 (craters) x 50 (pulses) x 19 (elements) = 380,000 peaks required processing.

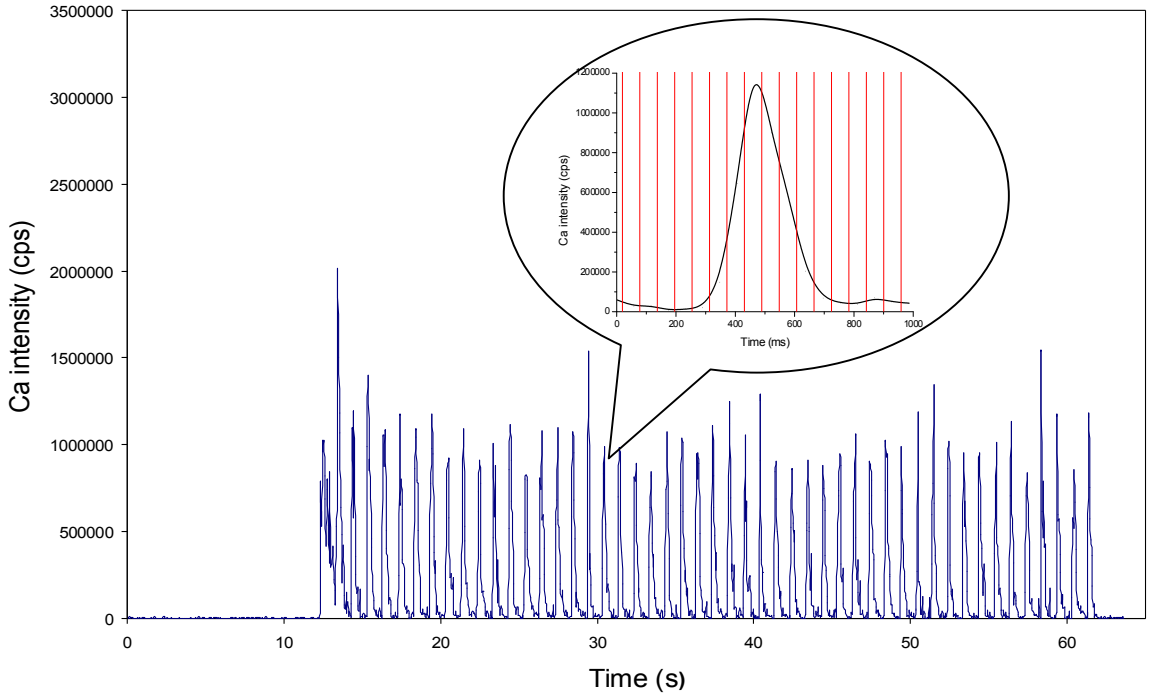

Figure 5.3. LA-ICP-MS peaks generated for Ca in NIST standard reference glass 612 upon drilling (burst of 50 pulses at a pulse rate of 1Hz). The inset shows the detail of the sequential (scanning) ICP-MS measurement for one individual peak, with the red marks indicating the dwell time/interval time for the Ca measurements (1ms/58ms); in between two red marks, the signal intensities were measured for another 18 elements, each with a dwell time of 1ms.

3D spatial elemental concentration data $c_{i,j}$ are associated with the x_i, y_i coordinates of each laser-generated crater i ($1 \leq i \geq 400$; $\Delta x = \Delta y = 90$ µm) and the ablation depth z_j as a function of the pulse number j for each pulse ($1 \leq j \geq 50$; $\Delta z = 0.15$ µm), hence the metric pixels (voxels) in the 3D images have a virtual size of 90 µm x 90 µm x 0.15 µm. A generic workflow for glass (in various software programs) was developed for data processing and manipulation based on the following key operations (illustrated in Figure 5.4 for Na or Na_2O in the weathered glass):

(a) *Subtraction* (in Microsoft® Office Excel 2003) of the gas blank signal from the raw signal (for all elements) for each crater *i*;

(b) *Integration* (in OriginLab Origin 8.1) of the 50 individual peaks (automated and unsupervised) for each pulse *j* by an adjacent-average smoothing procedure based on a 17-point window (corresponding to a summing action over an interval of ca. 1 s);

(c) *Conversion* (in Microsoft® Office Excel 2003) of the data in counts per second as obtained under (b) into wt % data using a sum normalization procedure based on summing of the oxides to 100 wt % (van Elteren *et al*., 2009) assuming that no "foreign" elements from "outside" have been introduced in the surface layers;

(d) *Manipulation* (VBA macros in Microsoft® Office Excel 2003) of 400 datasets with wt % information (for all elements) by extracting 50 2D depth maps along the z-axis and saving them as CSV files.

Visualization of the 3D images for the weathered glass artifact was carried out with the public domain software ImageJ (National Institutes of Health, USA) using the volume viewer or the animation tool. Typical 3D volume images are presented in Figure 5.5, showing different elemental distributions in the weathered glass; we limited ourselves to images of the elements Si, Mg and Mn as being representatives for three classes of leaching mechanisms.

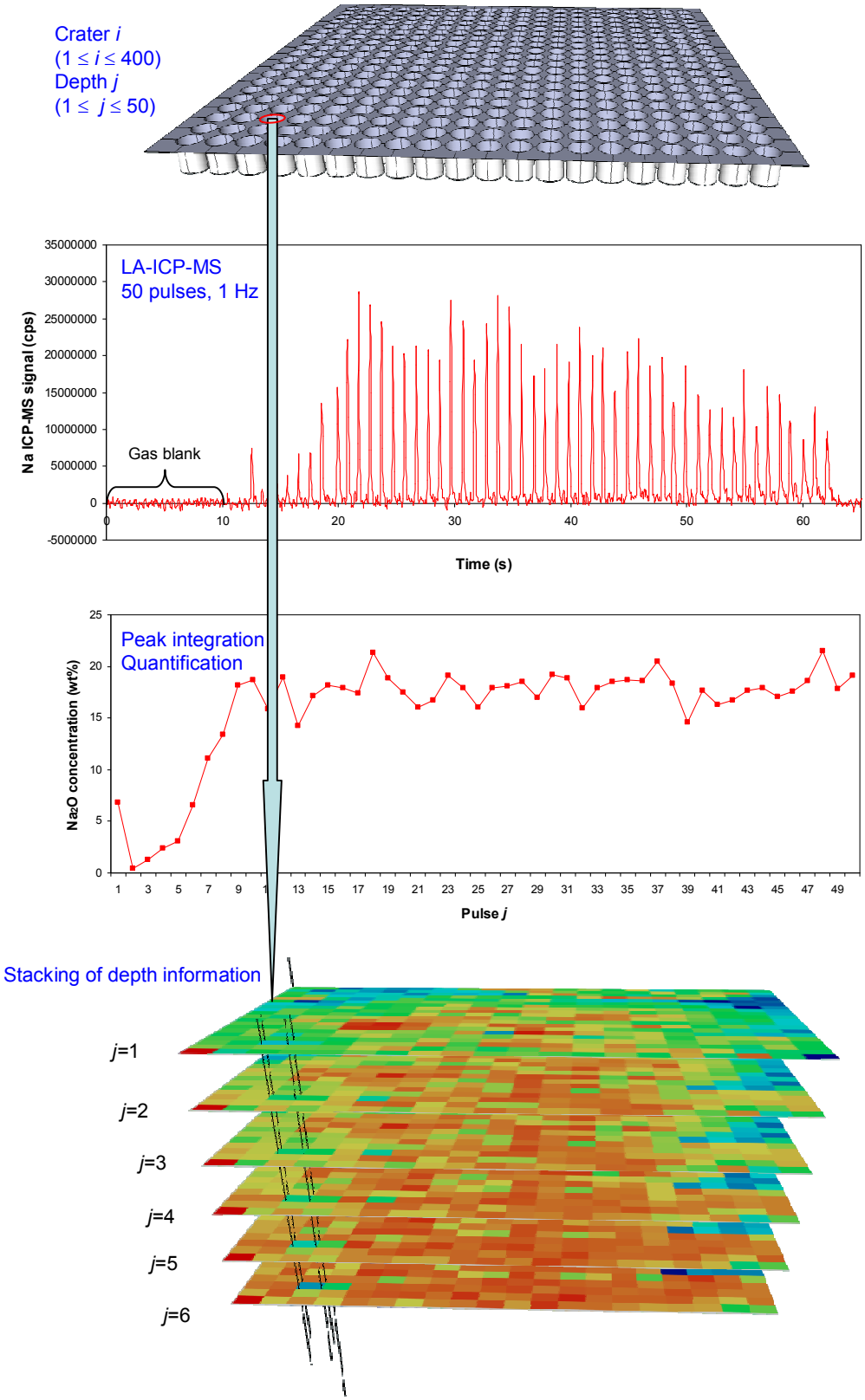

Figure 5.4. Workflow for retrieval of 3D imaging data from LA-ICP-MS analysis of the weathered area in Figure 5.2, illustrated for Na/Na_2O. The colors in the stacked maps represent Na_2O concentrations with lower concentrations mapped in "cold" colors (blue/violet) and higher concentrations in "hot" colors (orange/red). The utmost front/left pixel in each map is arbitrarily set to the maximum concentration found in the 50 maps to scale all maps similarly.

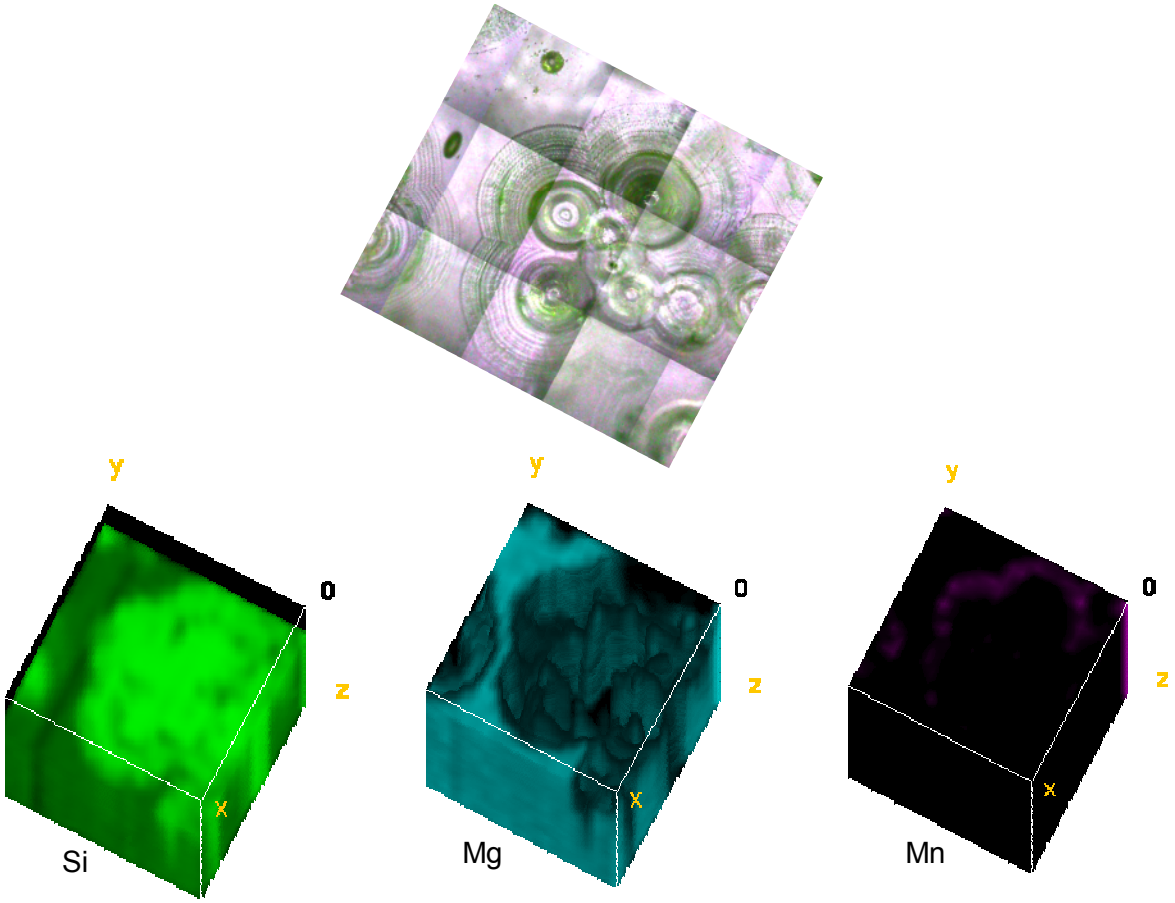

Figure 5.5. Elemental volume images for the surface of the weathered glass in Figure 5.2 (axes not to scale, i.e. lateral size is 1.79 mm x 1.79 mm and total depth size is 15 µm.

5.5. Validation and irregularities

To validate the 3D LA-ICP-MS procedure a homogeneous, industrially prepared glass (see Section 5.2) was subjected to laser drilling on a 10 x 5 grid, followed by ICP-MS measurement of 20 elements for all 50 pulses per crater. In Figure 5.6 the averaged elemental oxide data for the layers 1 to 50 (for reasons of clarity only every fifth layer is shown) are compared with bulk XRF data for major, minor and trace elements [the ratios of the (bulk XRF concentrations / LA-ICP-MS spatial concentration)] data are in the range 0.86–1.32), and are indicative of a satisfactory precision. Furthermore, the fact that the concentration data for the 50 layers (for each element) are practically indistinguishable (RSDs are in the range 0.7–5.0%) confirms that the industrially prepared glass is indeed highly homogeneous at the major, minor and trace element level. Additionally it can be concluded that the ablated volume per pulse is indeed independent of the drilling depth leading to a very high accuracy.

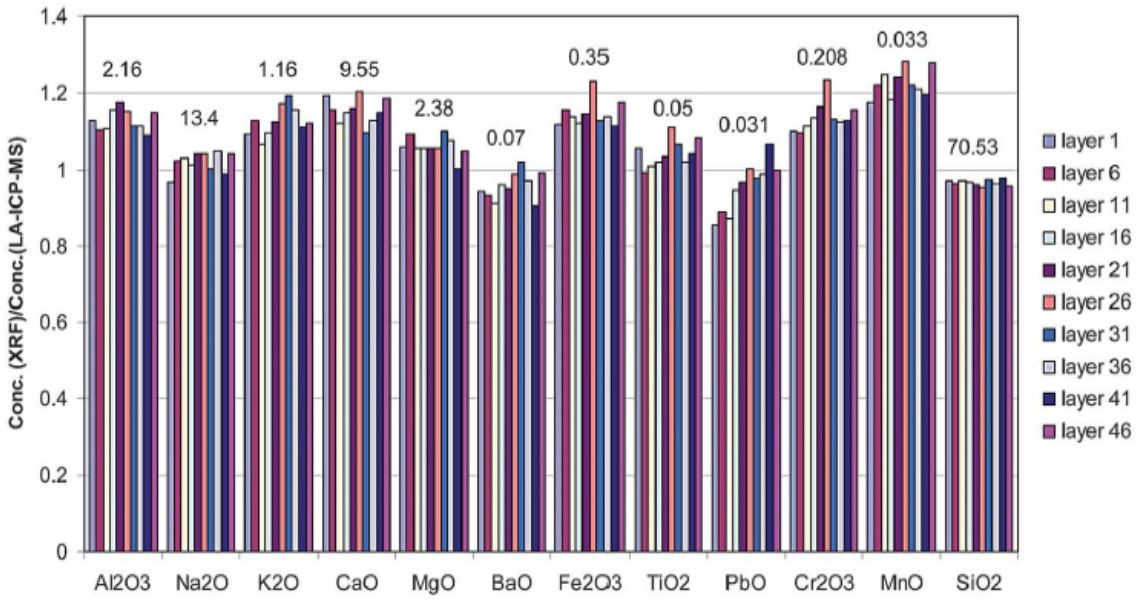

Figure 5.6. Validation of the 3D LA-ICP-MS mapping procedure by comparing the elemental oxide concentrations extracted from the various depth layers of the 3D images of the homogeneous, industrially prepared glass with those of the bulk XRF analyses; the LA-ICP-MS (layer): XRF ratios are given for the layers 1 to 50 (in steps of 5). The bulk XRF elemental oxide concentrations (in wt %) are given above each set of bar graphs.

In spite of the very convincing volume images obtained in the visualization of the 3D elemental corrosion data for the weathered glass in Section 5.4, an anomaly has occurred in the visualization of the data. Long-time weathering of the medieval glass artifact has not only led to leaching of certain elements, but also to dissolution of the network formers Si and Al, resulting in corrosion pits with a depth up to 100 µm as measured by confocal optical microscopy. During 3D mapping it is not possible to automatically correct for these height differences and therefore ablation was always on the "macro" surface of the glass, even when ablation took place in the pit. Nevertheless, from the confocal optical microscopy 3D images (Figure 5.7) of one of the corrosion pits after 3D LA-ICP-MS imaging, it can be seen that even under these unfavorable laser ablation conditions well-defined craters were obtained. Moreover, quantification of the thus retrieved elemental concentration data by the sum normalization method should result in reliable data as misfocusing on the surface not necessarily leads to inaccurate data. It has been shown that a positive or negative deviation of twice the laser beam diameter still leads to precise and accurate data (Šelih and van Elteren, 2011) In this case this implies that corrosion pits of 160 µm deep are still allowed for quantitative data retrieval. However, the 3D elemental concentration data $c_{i,j}$ in each voxel coordinate x_i,y_i,z_j (i = the number of the laser-generated crater; j = the pulse number) should still be corrected with the physical pit contour data, implying that the current z_j coordinates need to be "pushed down" by the depth of the pit at every corresponding x_i,y_i coordinate. Currently work is in progress to define and extract the exact pit contours for the area covering the whole 20 x 20 crater matrix.

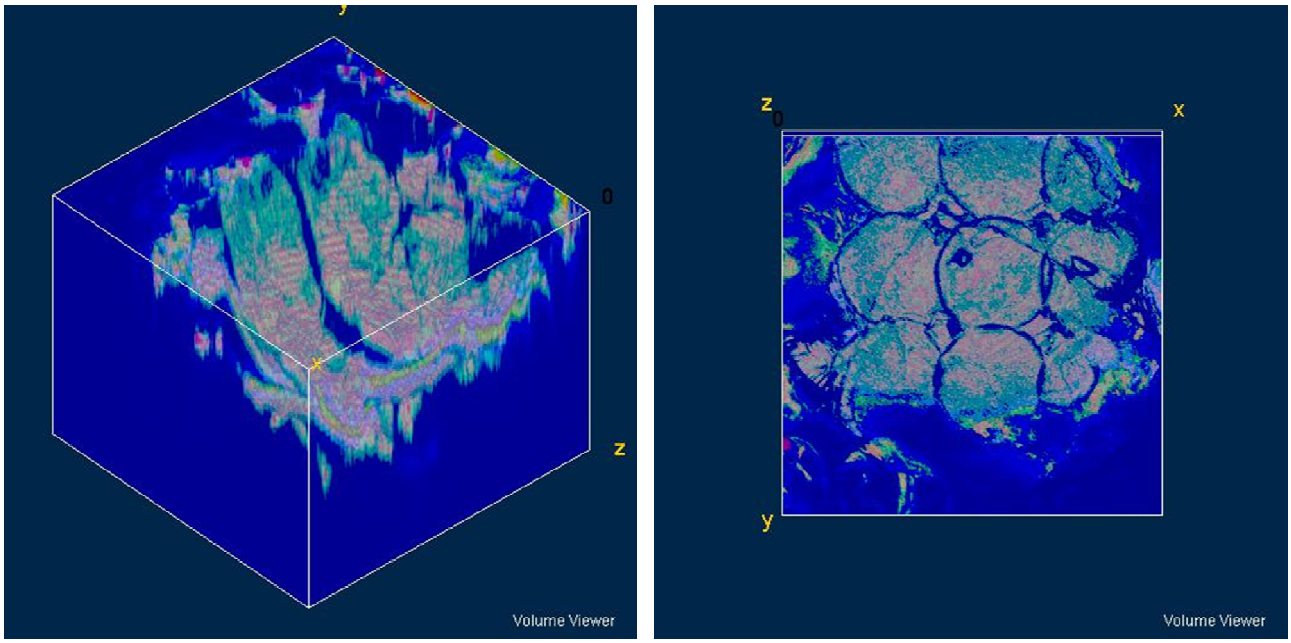

Figure 5.7. Confocal optical microscopy 3D images of one of the corrosion pits in Figure 5.2 (after laser ablation) from two different angles. The size of the laser ablation craters in the corrosion pit is 80 µm; the depth of this pit is ca. 100 µm.

5.6. Weathering mechanisms

Weathering deteriorates and subsequently dissolves a glass through two basic processes: (i) the hydrolytic attack, consisting of ion-exchange reactions (leaching or selective dissolution) between water H^+/H_3O^+ ions and the glass network soluble modifier ions such as alkalis and subsequently alkaline earth and divalent transition ions, and (ii) the silica network dissolution by hydrolysis as a consequence of the attack of the bridging oxygen by hydroxyl ions (congruent dissolution) (Cox *et al*., 1979; Newton and Fuchs, 1988; Davison, 2003; Chopinet *et al*., 2008; Verità *et al*., 2009 and Falcone *et al*., 2011). The first process leads to the formation of a hydrated and alkali-depleted glass layer, which under some conditions can act as a barrier against a further deeper leaching. When the glass surface interacts with alkaline aqueous solutions, the glass network hydrolysis predominates (at pH > 9 for sodic glass and less for potassic or mixed-alkali glass) and silicon is released into solution, causing network corrosion and dissolution, with formation of pits and cracks (Das, 1969; Das, 1980; Pohlman, 1974; Paul, 1977; Gentaz *et al*., 2011). Sometimes recombination and precipitation of some glass components leads to the formation of a silica gel layer (Doremus, 1979; Brinker, 1988). Numerous papers have been published on the weathering of archaeological glass (Newton, 1971; Brill, 1975; Davison, 2003; Kunicki-Goldfinger, 2008; Koob, 2006).

In most cases, a leached layer is found which consists of multiple sub layers, each 0.5–1 µm in thickness, (Aerts *et al*., 1999) with sometimes precipitation of a brown/black substance rich in Mn (Watkinson *et al*., 2005; Nuyts *et al*., 2013).

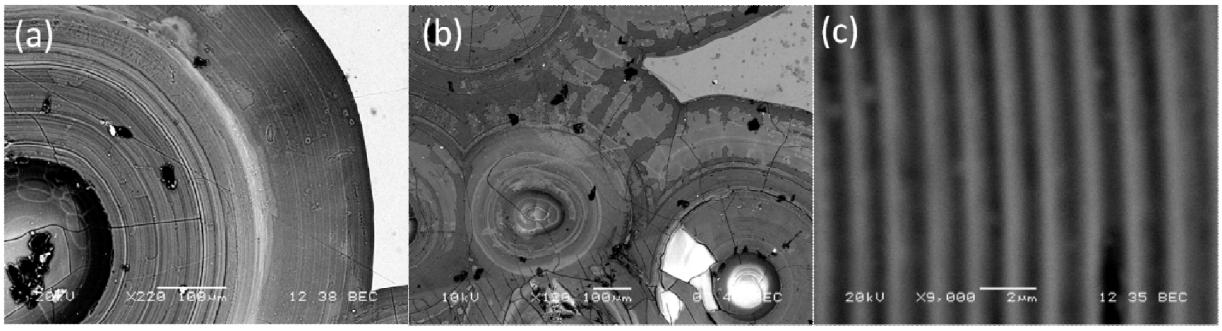

Figure 5.8. SEM images of the weathered pits and rings in the ancient glass sample (a-b); SEM image of the zoomed rings (c).

Geilmann (1956) and more recently Dal Bianco *et al*. (2005) have described this weathering process, showing rings similar to the ones found in our weathered glass (Figure 5.8). These rings are analogous to the so-called Liesegang (spatiotemporal) rings as a result of periodic precipitation of mobile ions (Liesegang, 1896) and have been a controversial means of establishing the age of a glass artifact (Brill and Hood, 1961) similar to dendrochronology (tree-ring dating). This self-organizational natural phenomenon is still not well understood, but could result from a migration of ions from the centre of the ring to the periphery, probably due to a diffusion-controlled process which favors the mobility of ions with a low charge-to-radius ratio (Scheiter *et al*., 2007). We studied the glass leaching phenomena by concentrating on a cross-section in a vertical plane of the 3D multi-elemental images already obtained (see the details in Figure 5.2). This cross section is of particular interest as it covers a part of the glass with various degrees of corrosion and traverses one single leaching crater with associated Liesegang rings. In Figure 5.9, the cross-sectional depth maps are presented as contour plots (with normalized concentrations for each map) for 19 elements and with the understanding that these maps do not take into account corrections for corrosion pit contours. Deeper ablation layers, especially on the utmost left and right hand sides of the maps where no visible corrosion is noticeable (see Figure 5.2), in principle show the bulk concentrations as reported in Table 5.2.

When comparing the elemental concentrations in these areas (extracted with the analysis tool in ImageJ) with the bulk concentrations (see Figure 5.10) we notice that for most elements the correlation is indeed good with some discrepancies at trace level concentrations, probably due to sensitivity issues. The elemental concentrations associated with the center of the glass corrosion pit, i.e. the central, vertical channels in Figure 5.9, depict practically full depletion except for the network formers Si and Al which show average oxide concentrations of 94.1 and 2.88 wt%, respectively; this is considerably higher than their bulk concentrations. The remaining elements show clear similarities/disparities in their leaching behavior as can be deduced from colocalization analysis of the elemental maps through their Pearson product-moment correlation (see Table 5.4). High Pearson correlation coefficients ($r > 0.7$) are highlighted in blue, showing two clear classes of elements with similar leaching behavior (next to the network formers Si and Al): a) Ba, Ca, K, Mg, Na, P, Sr and b) Co, Mn, Ni, Pb. Some correlations are less clear due to sensitivity issues related to low elemental contents (Zn, Cu, Ti, Sn, Sb). The numbers highlighted in red indicate which elements are anti-correlated ($r < -0.7$), clearly showing that Al and Si are behaving oppositely to the first class of elements as mentioned above. When we look in more detail, i.e. consider the depth profiling results from one spot only (spot five from the left in Figure 5.2) of the 20 spots used to construct Figure 5.9, concentration profiles as a function of depth can be easily compared for different elements.

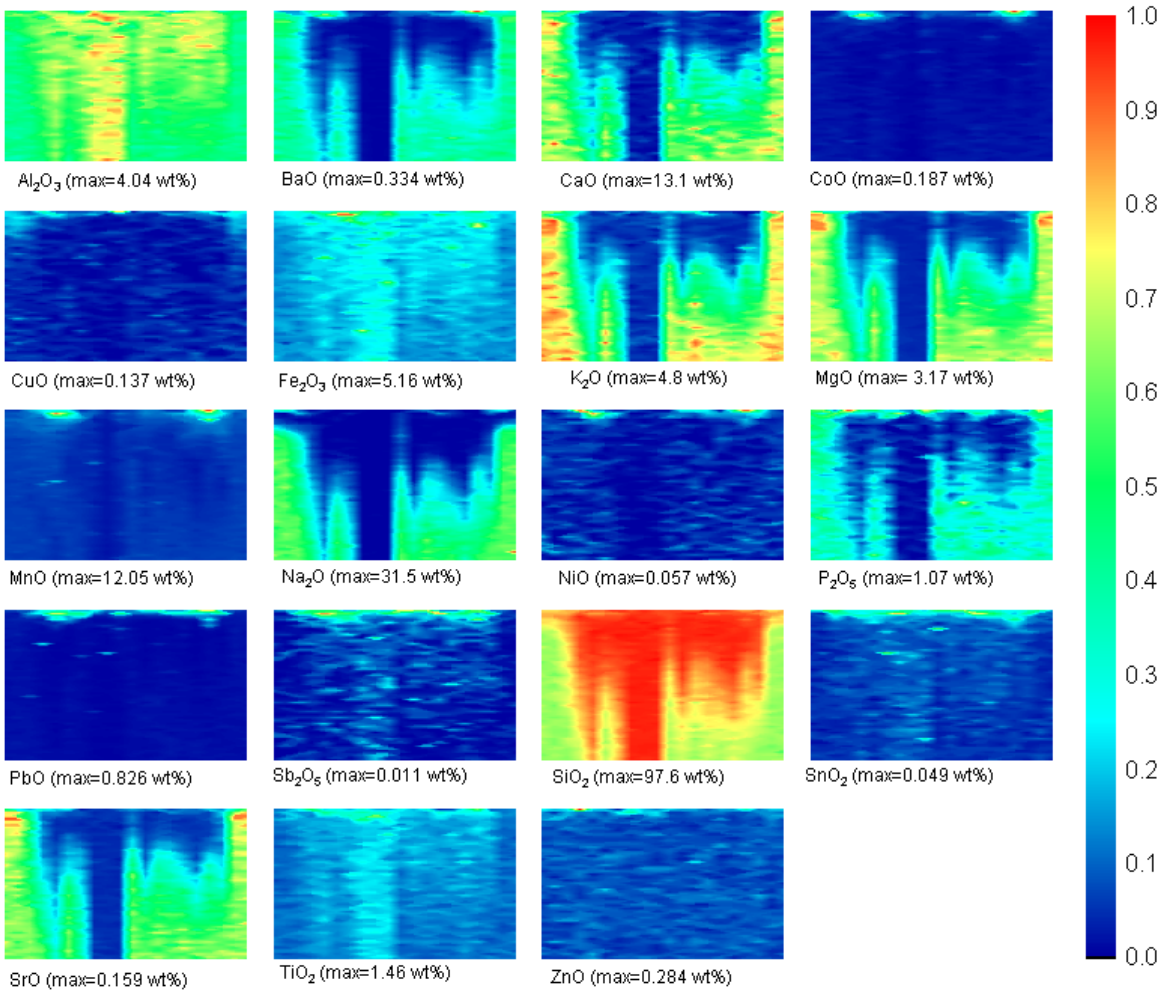

Figure 5.9. Cross-sectional contour maps with normalized concentrations for all 19 elements, extracted from the 3D elemental images in a vertical plane along a line (see Figure 5.2). The size of the individual maps is 1.79 mm (x-axis) x 7.5 µm (y-axis). Lower concentrations are mapped onto "cold" colors (blue/violet) and higher concentrations "hot" colors (orange/red). The color scale bar has a normalized concentration range from 0 to 1, thus if the actual elemental oxide concentrations in the map range from 0.2 (min) to 0.8 (max) wt %, the normalized concentrations range from 0.25 to 1 and the corresponding color palette for this map is limited from light blue to red. Since the maximal elemental oxide concentrations (in wt %) in the maps are given behind the element symbols, the actual concentrations can be deduced using the color scale bar: e.g., the color yellow resembles a normalized concentration of 0.75; when the maximal elemental oxide concentration in the map is 0.8 wt%, the normalized concentration of 0.75 resembles an actual concentration of 0.75×0.8 = 0.6 wt%.

Table 5.4. Colocalization of elemental maps through their Pearson product-moment correlation.

	Al	Ba	Ca	Co	Cu	Fe	K	Mg	Mn	Na	Ni	P	Pb	Sb	Si	Sn	Sr	Ti	Zn
Al	1.000																		
Ba	-0.733	1.000																	
Ca	-0.763	0.891	1.000																
Co	0.063	0.215	-0.080	1.000															
Cu	-0.156	0.321	0.207	0.386	1.000														
Fe	0.596	-0.459	-0.561	0.307	0.111	1.000													
K	-0.776	0.911	0.937	-0.082	0.210	-0.559	1.000												
Mg	-0.766	0.925	0.946	-0.072	0.227	-0.568	0.965	1.000											
Mn	0.046	0.229	-0.044	0.913	0.376	0.273	-0.046	-0.034	1.000										
Na	-0.762	0.834	0.866	-0.074	0.058	-0.571	0.918	0.878	-0.053	1.000									
Ni	-0.046	0.275	0.043	0.739	0.350	0.200	0.049	0.056	0.713	0.036	1.000								
P	-0.641	0.798	0.769	0.115	0.417	-0.345	0.798	0.805	0.121	0.699	0.217	1.000							
Pb	0.091	0.129	-0.131	0.849	0.409	0.424	-0.119	-0.125	0.802	-0.120	0.682	0.130	1.000						
Sb	0.341	-0.211	-0.383	0.555	0.220	0.514	-0.365	-0.384	0.541	-0.363	0.448	-0.121	0.710	1.000					
Si	0.765	-0.911	-0.942	0.004	-0.167	0.533	-0.964	-0.942	-0.029	-0.975	-0.103	-0.778	0.055	0.329	1.000				
Sn	0.338	-0.260	-0.368	0.364	0.268	0.482	-0.349	-0.370	0.361	-0.365	0.292	-0.074	0.547	0.659	0.335	1.000			
Sr	-0.761	0.937	0.944	-0.053	0.240	-0.551	0.962	0.975	-0.017	0.874	0.070	0.801	-0.112	-0.375	-0.939	-0.370	1.000		
Ti	0.667	-0.490	-0.589	0.335	0.034	0.593	-0.601	-0.608	0.271	-0.596	0.218	-0.416	0.371	0.489	0.575	0.437	-0.596	1.000	
Zn	0.108	0.083	-0.010	0.301	0.326	0.242	-0.017	0.003	0.248	-0.089	0.394	0.215	0.356	0.311	0.021	0.330	-0.042	0.257	1.000

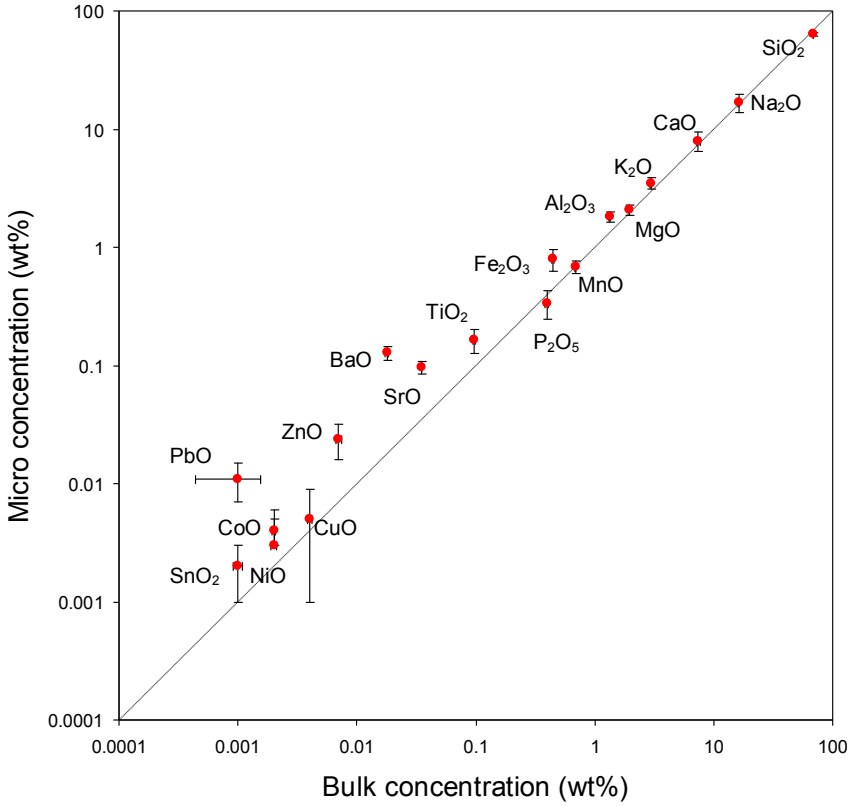

Figure 5.10. Correlation between bulk elemental concentrations and similar (micro) concentrations extracted from the cross-sectional depth maps in Figure 5.7 from deeper layers on the utmost left- and right-hand sides of the maps.

In Figure 5.11 explanatory profiles are shown for the three classes of leaching mechanisms represented by SiO_2, Na_2O and MnO. Na_2O, as a representative of the most mobile alkaline and alkaline earth ions, shows decreasing concentrations from the bulk to the surface of the glass with practically total depletion at the surface which is indicative of progressive corrosion (glass dissolution). The slight "dip" visible at a depth of ca. 1 µm might be due to a "precipitation layer", probably corresponding to the gel superficial layer, as evidenced by the presence of superficial Liesegang rings, where the outgoing mobile ions react with compounds from the environment and precipitate as insoluble compounds. SiO_2, as a representative of the network forming elements, is enriched at the surface as a result of its decreasing density due to depletion of alkaline and alkaline earth ions at the surface (see also Chapter 3). MnO, as a representative of the heavy metal ions, shows almost constant concentrations from the bulk to the "precipitation layer". However, in the precipitation layer the concentrations increase rapidly to values much higher than the bulk concentration. These superficially high concentrations suggests that this is caused by a strong contribution of the neighboring environment (soil) in which the glass artifact was immersed for several centuries.

Based on analysis of the data and inspection of the optical microscopy images we can deduce that the weathering must have occurred as a result of depletion by leaching, not only of alkali but also of alkaline earth and divalent transition elements (Farges *et al*., 2006) leading to physical tensions in the dealkalinization layers due to wet/drought cycles. Cracks must have appeared on the glass surface which grew into pits which later became interconnected as corrosion advanced (Palomar *et al*., 2012) The ion-exchange of H^+ (or H_3O^+) with glass alkaline ions in humid environment must have started the breakdown of the glass network (Si) in the pits due to OH^- ions formed during the dealkalinization process (García-Heras *et al*., 2005).

The Liesegang rings, as a manifestation of the dealkalinization process in radial direction from the pit centre (in contrast to leached layers in depth), were not probed by the laser due to the large size of the laser beam used (80 µm), thereby covering several rings upon ablation. Nevertheless, we are confident that radial leaching must have led to precipitation of elements, shown as enriched concentrations of Co, Mn, Ni and Pb located at the surface of the 2D depth maps (Figure 5.9), and associated with the edge of the Liesegang rings (Figure 5.2) and related to visible brown precipitation rings (Figure 5.1).

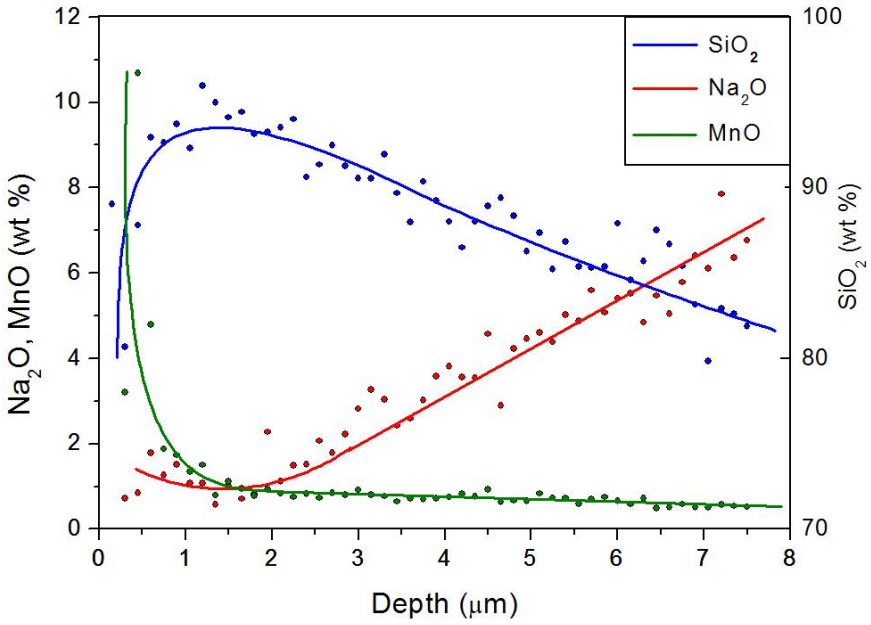

Figure 5.11. Concentration depth profiles for SiO_2, Na_2O and MnO for one single spot analysis on the glass (spot five from the left in Figure 5.2).

To better understand the effect of the weathering process and the distribution of the elements, 2D WDS mapping with a spatial resolution of ca. 1 µm was carried out at the glass surface in different zones (Figures 5.12 and 5.13). It can be seen that the Mn deposition on the surface is associated with the outer Liesegang rings and seems to be correlated with Fe and P (Figure 5.13).

Ca, K, Mg and Na are present only in one zone of the corroded radial distribution rings, more distant from the center of the pit; this is probably an uncontaminated or less corroded area. All the different areas are also recognizable in Figure 5.8 (b). The enrichment of Ca on the surface (Figure 5.12) could be from the glass itself (Willemien, 2010) or from the underground environment (Silvestri *et al*., 2005). From SEM images and from the elemental maps the Mn deposition seems to be of external provenience, e.g. the soil in which the glass has been buried for centuries. The high spatial resolution of WDS allows analysis of the morphology of the degraded glass surface, including single Liesegang rings and cracks. The heterogeneity of the sample is clearly visible in the Si map and by comparing the distribution of this element with Mn, it is evident that the rings with Mn deposition contain lower or negligible amounts of Si (Figure 5.12).

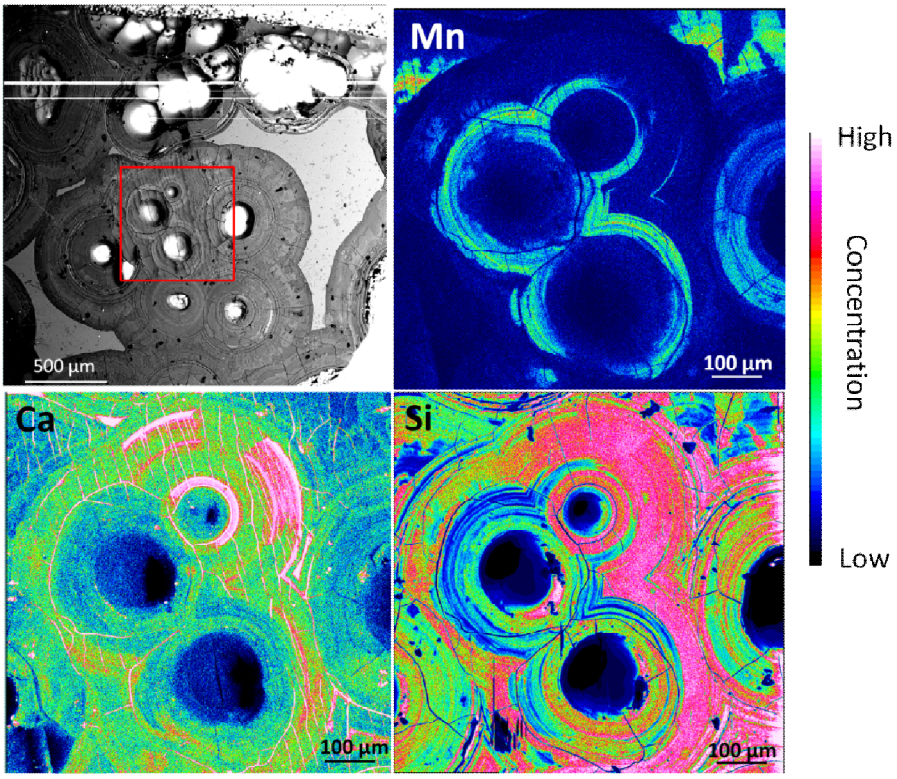

Figure 5.12. SEM image on one area of the analyzed glass sample and WDS maps of Mn, Ca and Si. The color scale from black (low concentration) to white (high concentration) is associated with different concentration ranges for different elements.

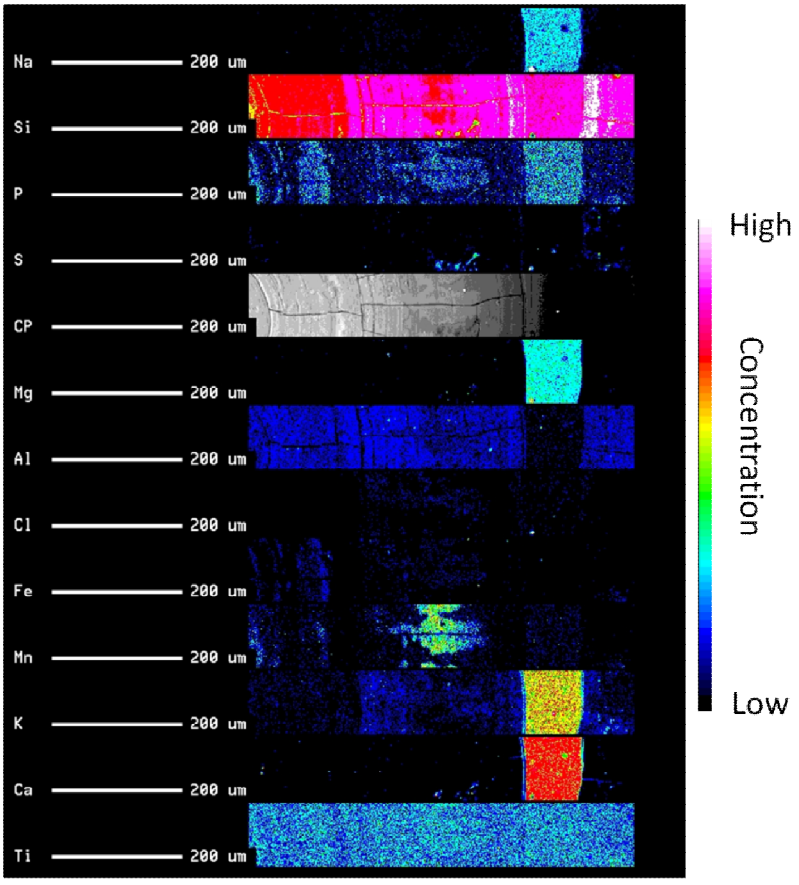

Figure 5.13. WDS maps of different elements generated on the radial distribution in corrosion growth rings and SEM image (CP) of the same area. The color scale from black (low concentration) to white (high concentration) is associated with different concentration ranges for different elements.

5.7. Conclusions

A 3D LA-ICP-MS mapping method based on laser drilling (50 pulses at 1 Hz) on a virtual grid on the surface is presented for multi-elemental surface layer analysis of “hard” samples that cannot be (cryo)microtomed. To facilitate the monitoring of transient peaks with spatial information related to individual pulses, a single volume laser ablation cell with fast signal washout was used in combination with ICP-MS monitoring via ultrashort measurement intervals. The processing and manipulation of the recorded 4D data (3D spatial + concentration) to construct 3D images with elemental concentration information required the development of several software routines to address *i*) integration of elemental peak areas related to individual pulses, *ii*) quantification of the peak areas in elemental oxide concentrations based on a sum normalization procedure and *iii*) extraction of 2D elemental depth maps to be visualized as 3D images with 4D rendering. Validation of the 3D LA-ICP-MS mapping method using a homogeneous, industrially-prepared glass, characterized by XRF, showed excellent performance characteristics with 50 practically indistinguishable layers for most elements measured. The findings obtained for the weathered, medieval glass indicate that the corrosion mechanisms can be related to dealkalinization, resulting in depleted concentrations of alkalis/earth alkalis in surface layers and enriched concentrations of network formers (Si and Al). However, over time these network formers have been dissolved leading to pits in the surface, whereas network modifiers such as Co, Ni and Pb precipitated as corrosion rings at the surface. The presence of Mn surface bodies are mainly attributed to an external contamination. Although this approach was validated and used for investigation of the multi-elemental 3D distribution in glass, its application in the study of living organisms by constructing 3D models may be advantageous as well, even for “deeper” information retrieval than presented here. Much higher depth resolutions are attainable than with the standard (cryo)microtoming method (> 10 µm) and painstaking registering is avoided.

5.8. References

Aerts A., Janssens K. and Adams F. (1999) Trace-level microanalysis of Roman glass from Khirbet Qumran, Israel, J. Archaeol. Sci., 26; pp. 883–891.

Brill R. H. and Hood H. P. (1961) A New Method for Dating Ancient Glass, Nature, 189; pp. 12–14.

Brill R.H. (1975) Crizzling - A Problem in Glass Conservation, Conservation in Archaeology and the Applied Arts, Stockholm Congress; pp. 121-134.

Brinker C. J. (1988) Hydrolysis and condensation of silicates: effects on structure, J. Non-Cryst. Solids, 100; pp. 31–50.

Casey W.H. (2008), Glass and mineral corrosion: Dynamics and durability, Nat. Mater., 7; pp. 930-932.

Chopinet M.H., Verità M., Falcone R., Lehuédé P., Vallotto M., Nardone M. and Sodo A. (2008) Soda-Lime-Silica Glass Containers: Chemical Durability and Weathering Products, Adv. Mater. Res., Vols. 39–40; pp. 305–310.

Cox G.A., Heavens O.S., Newton R.G. and Pollard A.M. (1979) A study of the weathering behavior of Medieval glass from York Minster, J. Glass. Stud., 21; pp. 54–75.

Dal Bianco B., Bertoncello R., Milanese L. and Barison S. (2005) Glass corrosion across the Alps: a surface study of chemical corrosion of glasses found in marine and ground environments, Archaeometry, 47; pp. 351–360.

Das C. R. (1969) Theoretical aspect of the corrosion of glass: Conclusion, Glass Ind., 50; pp. 422–427.

Das C.R. (1980) Diffusion-controlled attack of glass surfaces by aqueous solutions, J. Am. Ceram. Soc., 63; pp. 160–165.

Davison S. (2003) Conservation and Restoration of Glass, Butterworth-Heinemann, Oxford.

Doménech-Carbó A., Doménech-Carbó M.T. and Costa V. (2009) Electrochemical Methods in Archaeometry, Conservation and Restoration, Monographs in Electrochemistry, Springer-Verlag, Berlin, Heidelberg.

Doremus R. H. (1979) in Treatise on Materials Science and Technology, ed. Tomozawa M. and Doremus R. H., Academic Press, New York, vol. 17; pp. 41–69.

Falcone R., Licenziati F., Orsega E.F. and Verità M. (2011) The dependence of the weathering of soda–lime–silica glass on environmental parameters: a preliminary investigation, Glass Technol., 52; pp. 23–29.

Farges F., Etcheverry M.P., Haddi A., Trocellier P., Curti E. and Brown Jr G.E. (2006) Durability of ilicate glasses: an hystorical approach in Proceedings of the X-ray Absorption Fine Structure-XAFS, 13th International Conference, Stanford, California, 9–14 July 2006.

García-Heras M., Carmona N., Ruiz-Conde A., Sánchez-Soto P. and Benítez J. J. (2005) Application of atomic force microscopy to the study of glass decay, Mater. Charact., 55; pp. 272–280.

Geilmann W. (1956) Beiträge zur kenntnis alter gläser, IV: die Zersetzung der gläser im boden, Glastech. Ber., 29; pp. 145–168.

Gentaz L., Lombardo T., Loisel C., Chabas A. and Vallotto M. (2011) Early stage of weathering of medieval-like potash-lime model glass: evaluation of key factors, Environ. Sci. Pollut. Res., 18; pp. 291–300.

Horn I., Guillong M. and Günther D. (2001) Wavelength depending ablation rates for metals and silicate glasses using homogenised laser beam profiles – Implications for LA-ICP-MS, Appl. Surf. Sci., 7215; pp. 1-12.

Kanngießer B., Mantouvalou I., Malzer W., Wolff T. and Hahn O. (2008), Non-destructive, depth resolved investigation of corrosion layers of historical glass objects by 3D Micro X-ray fluorescence analysis, J. Anal. At. Spectrom., 23; pp. 814–819.

Koob S. P. (2006). Conservation and care of glass objects. Published by Archetype Publications in association with The Corning Museum of Glass, New York.

Kunicki-Goldfinger J.J. (2008). Unstable historic glass: symptoms, causes, mechanisms and conservation, Reviews in Conservation; 9; pp. 47-60.

Liesegang R.E. (1896) Naturwiss. Wochenschr., 11; pp. 353–363.

Müller W., Shelley M., Miller P. and Broude S. (2009) Initial performance metrics of a new customes-designed ArF excimer LA-ICP-MS system coupled to a two volume laser ablation cell, J. Anal. At. Spectrom., 24; pp. 209–214.

Newton R.G. (1971) The enigma of the layered crusts on some weathered glasses, a chronological account of the investigations, Archaeometry 13, I; pp. 1-9.

Newton R.G. and Fuchs D. (1988) Chemical analyses and weathering of some Medieval glass from York Minster, Glass. Technol., 29; pp. 43–48.

Nuyts G., Cagno S., Hellemans K., Veronesi G., Cotte M. and Janssens K. (2013) Study of the early stages of Mn intrusion in corroded glass by means of combined SR FTIR/µXRF imaging and XANES spectroscopy, Procedia Chemistry 8; pp. 239-247.

Palomar T., Garcia-Heras M. and Villegas M.A. (2012) Model historical glasses under simulated burial conditions, Coalition (Electronic Journal of the Network on Science and Technology for the Conservation of Cultural Heritage), 23; pp. 2–6.

Panighello S., Parello M.C., Orsega E.F. (2013) Investigation on medieval glass from Poggio Diana Castle (Sicily) by LA-ICP-MS and UV-VIS Reflectance Spectroscopy – Proceedings of the 16th Symposium on Mediterranean Archaeology, Florence, Italy, 1–3 March 2012 edited by Luca Bombardieri, Anacleto D'Agostino, Guido Guarducci, Valentina Orsi and Stefano Valentini. BAR International Series 2581 (II); pp. 1187-1195.

Paul A. (1977) Chemical durability of glass, J. Mater. Sci., 12 (11); pp. 2246–2268.

Pearce N. J. G., Perkins W. T., Westgate J. A., Gorton M. P., Jackson S. E., Neal C. R. and Chenery S. P. (1997) A compilation of new and published major and trace element data for NIST SRM 610 and NIST SRM 612 glass reference materials, Geostand. Geoanal. Res., 21 (1); pp. 115–144.

Pohlman H.J. (1974) Corrosion of lead-containing glazes by water and aqueous solutions, Glastech. Ber., 47 (12); pp. 271–276.

Scheiter D., Janssen A. and Geisler T. (2007) Formation of Liesegang rings in borosilicate glass during experimental alteration, Geochimica et Cosmochimica Acta, 71(15) Supplement 887.

Šelih V.S., van Elteren J.T. (2011) Quantitative multi-element mapping of ancient glass using a simple and robust LA-ICP-MS rastering procedure in combination with image analysis, Anal. Bioanal. Chem. 401(2); pp. 745–755.

Silvestri A., Molin G. and Salviulo G. (2005) Roman and Medieval glass from the Italian area: Bulk characterization and relationships with production technologies, J. Non-Cryst. Solids, 351(16–17); pp. 1338–49.

Van Elteren J.T., Tennent N.H. and Šelih V.S. (2009) Multi-element quantification of ancient/historic glasses by laser ablation inductively coupled plasma mass spectrometry using sum normalization calibration. Anal Chim Acta 644(1-2): 1-9.

Van Malderen S.J.M., van Elteren J.T. and Vanhaecke F. (2015) Submicrometer Imaging by Laser Ablation-Inductively Coupled Plasma Mass Spectrometry via Signal and Image Deconvolution Approaches, Anal. Chem., 87; pp. 6125−6132.

Verità M., Falcone R., Sommariva G., Chopinet M.H. and Lehuédé P. (2009) Weathering of the inner surface of soda-lime-silica glass containers exposed to the atmosphere, Glass Technol.: Eur. J. Glass Sci. Technol., Part A, 50; pp. 65–70.

Watkinson D., Weber L. and Anheuser K. (2005) Staining of archaeological glass from manganese rich environments, Archaeometry, 47; pp. 69–82.

Willemien A. (2010) Study on the formation of heterogeneous structures in leached layers during the corrosion process of glass, CeROArt.

Woodhead J., Hellstrom J., Paton C., Hergt J., Grieg A. and Maas R. (2008) In Laser Ablation-ICPMS in the Earth Sciences: Current Practices and Outstanding Issues; P.J. Sylvester, Ed.; Mineral Association of Canada, Vancouver, B.C.; pp 135-145.

CHAPTER 6
Investigation of smalt in cross-sections of 17th century paintings using elemental mapping by laser ablation ICP-MS*

Glass in a different context

* Part of this chapter was published in Panighello *et al*., 2015 and presented at Technart, Catania, Italy (2015).

6.1. Introduction

Since ancient times glass has been used in multifarious industrial (e.g. window panes, vessels, etc.), domestic (lenses, spectacles, etc.) and artistic (jewelry, sculptures, etc.,) applications. A somewhat unusual application is its use as a pigment in paintings. This pigment is called smalt, a powder of potash colored with a roasted cobalt ore (Delamare, 2009; Stege, 2004), commonly used from the 15th to the 18th century (Stege, 2004; Muhlethaler and Thissen, 1993), mainly in oil and fresco techniques (Stege, 2004; Cianchetta *et al*., 2012).

It was largely used because it was cheaper than other alternative pigments such as azurite and ultramarine (Stege, 2004; Santopadre and Verità, 2006); however, smalt is not a stable pigment and has the tendency to turn brown or greenish-gray over time. For the last fifty years the interaction between smalt and oil binding medium has been widely studied to identify processes involved in the discoloration of paintings (Cianchetta *et al*., 2012; Plesters, 1969; Noble and van Loon, 2005). There seems to be a consensus that the degradation of smalt is related to its composition. Since smalt is a high-potassium glass it has an inherent low stability, resulting in leaching of its principle alkaline component (K^+). The high surface area of the crushed smalt and the acidic environment of the drying oil facilitate the degradation process (Spring *et al*., 2005). The alteration mechanism of glass pigment was recently studied by Robinet *et al*. (2011; 2013). When the alkali in the glass structure react with the hydrogenated species from the atmosphere and from the free fatty acid of the oil, silanol species (Si-OH) are formed creating new bridging bonds and, as a result of condensation, molecular water in the glass. The loss of potassium results in a decrease in the number of charge-compensating ions in the glass network, thereby creating a charge deficiency around the cobalt atoms as well as the formation of metallic soaps by reaction of the leached K^+ with the fatty acids. Therefore the coordination geometry of Co^{2+} ions changes from a tetrahedral to an octahedral coordination state, altering the absorption in the visible region and hence the color of the pigment (Santopadre and Verità, 2006; Spring *et al*., 2005; Robinet *et al*., 2011). Furthermore, weathering of the smalt is accompanied by cracking and migration of other cations, including Co^{2+}, from the glass surface to the binding medium and even to the paint surface (Spring *et al*., 2005; Robinet *et al*., 2011). This can cause chemical and physical changes in the paint layer, e.g, formation of soaps or salts such as carbonates, sulfates or oxalates (Robinet *et al*., 2013; Spring *et al*., 2005).

6.2. 2D mapping of smalt in paintings

So far most studies on smalt have focused on degradation phenomena associated with the smalt environment, including restoration- and preservation-related activities (Spring *et al*., 2005). Smalt data related to paint cross-sections are difficult to obtain due to the small size of the smalt particles (5-30 μm) and the limited multi-element sensitivity of most microanalytical techniques (e.g. SEM-EDX and PIXE).

Consequently, only major and minor elemental concentrations have been reported, hampering the study of the provenance and the origin of the raw materials used to produce the smalt due to a lack of trace elemental data. Smalt compositional data reported in the literature are mainly obtained through SEM-EDX analysis (primarily for Si, Na, K, Co, Fe, As, Ca, Al, Ni, Pb and sometimes Bi).

Although other microanalytical techniques, e.g. Raman spectroscopy, FTIR, EPMA, XAS, XPS, etc., have been applied for smalt investigation, most of them do not quantitatively assess the elemental concentrations in smalt but identify or qualitatively analyze the elemental content.

To answer fundamental questions about smalt in paintings, including the origin of its raw materials (e.g. the cobalt ore) and the technological know-how involved in its production, and also to gain more insight

into its degradation, the retrieval of trace elemental data is crucial. The most encouraging candidate technique for trace element microanalysis of smalt in paint cross-sections is laser ablation ICP-MS due to its multi-element capabilities (most elements of the periodic table), its sensitivity (down to the low µg g^{-1} level for most elements) and extended linear range (ten orders of magnitude), facilitating the simultaneous analysis of major, minor and trace elements. Nonetheless, to the authors' knowledge laser ablation ICP-MS has not been used for the investigation of smalt as yet. The aim of this study is to elaborate the laser ablation ICP-MS technique, combined with optical microscopy (OM) and scannning electron microscopy (SEM) measurements, for multi-element mapping of paint cross-sections from three different 17th century paintings (two Dutch masters [Hendrick Avercamp and Caesar Boetius van Everdingen] and a Chinese coromandel lacquer from an unknown artist; all artifacts are from the collection of the Rijksmuseum Amsterdam) (Figure 6.1) and generate elemental distribution maps for 50-60 major, minor and trace elements. Using a suite of twelve glass standards and a sum normalization calibration protocol based on summation of the elements as their oxides to 100 wt %, elemental distribution maps with quantitative concentration data were generated for the smalt particles. Via chemometric processing procedures the elemental information in the maps was used to hypothesize questions related to cobalt ore provenance, possible deterioration mechanisms and the conservation state of the painting.

Figure 6.1. Photographs of the paintings with sampling points indicated with red arrows. Detailed information on the paintings: A) Hendrick Avercamp, *Winter landscape with ice skaters*, oil on panel, c. 1608 (Wallert and Verslype, 2010), sample codes *Aver1* and *Aver2*; B) Caesar Boetius van Everdingen, *Girl in a large Hat*, oil on canvas, c. 1645 (Weber, 2011; Smeenk-Metz *et al*., 2011), sample code *Boet*; C) Anonymous Chinese craftsmen, *Lacquer room*, Coromandel lacquer and paint on wood, c. 1695 (De Haan, 2009) sample code *Chin*. HR photographs of the paintings can be obtained at www.rijksmuseum.nl.

6.3. Samples

Micro cross-section samples from three 17th century paintings (see Figure 6.1 for detailed information on the paintings and sampling locations) were embedded in epoxy resin in small cubic holders (ca. 1×1×0.5 cm^3), followed by routine grinding/polishing. As a result of ageing of the paintings the refractive index of the binding medium increases and can become equal to the refractive index of smalt making smalt particles invisible in normal light microscopy (Plesters, 1969; Giovanoli and Mühlethaler, 1970).

However, the smalt particles are well visible under ultraviolet light; they have the typical jagged shape of crushed glass particles with different dimensions (Figure 6.2). The cross-sections in this study show differently sized smalt particles with various degrees of degradation, from pale grey to grey to blue. It seems that the largest particles are well preserved as indicated by their blue color; the small particles have mostly lost their blue color (e.g. sample *Aver1* or *Boet*).

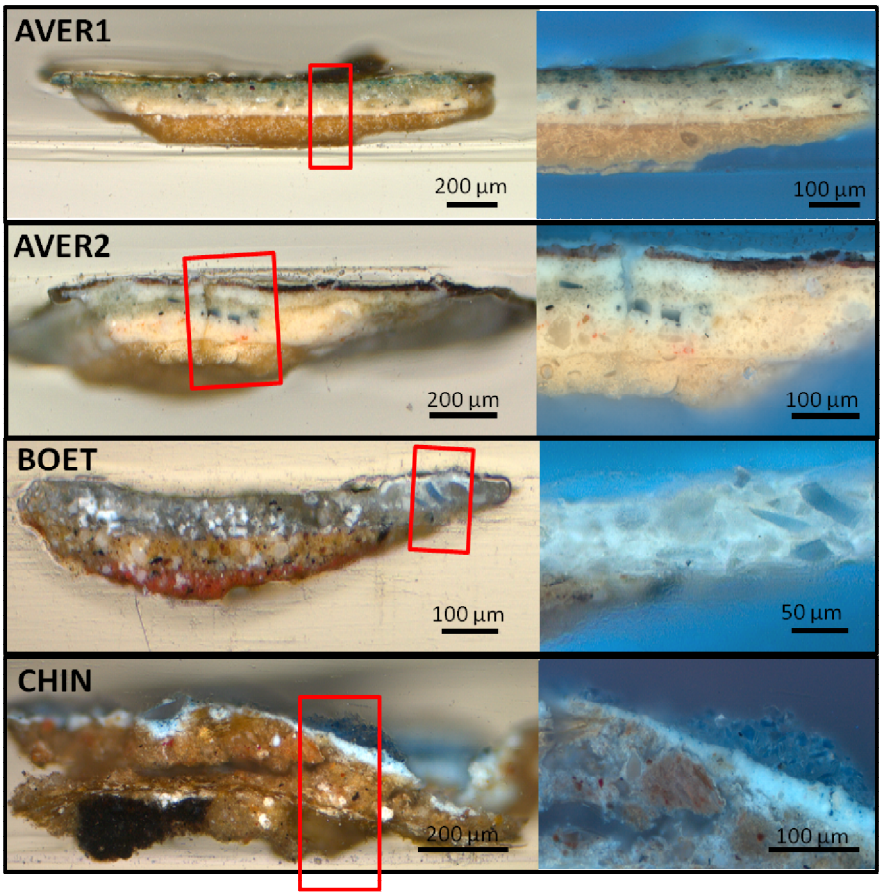

Figure 6.2. Photographs of the embedded and polished paint cross-sections images for all three paintings, under visible light (left) and under UV light (right). The red squares in the visible light images denote the areas ablated with the laser.

6.4. 2D elemental mapping procedure

All paint cross-sections were subjected to laser ablation across the painting layers, from the ground/bottom layer to the upper (varnish) surface (Figure 6.3 summarizes the microanalytical approach). Table 6.1 gives the operational parameters for elemental mapping of the smalt particles via parallel line scans, with no space between adjacent scans. A more detailed description of the LA-ICP-MS imaging protocol used in this work is given in Šelih and van Elteren (2011).

Even though the elemental stratigraphic distribution in a painting was already performed by laser ablation ICP-MS (Resano *et al.*, 2007; Syta *et al.*, 2014; Marin *et al.*, 2015), the current work is merely focusing on the study of smalt in the pigment layers. The ablation areas on the cross-sections were selected after critical observation of the smalt particles under ultraviolet light to visualize the discoloration and thus the degradation of the particles.

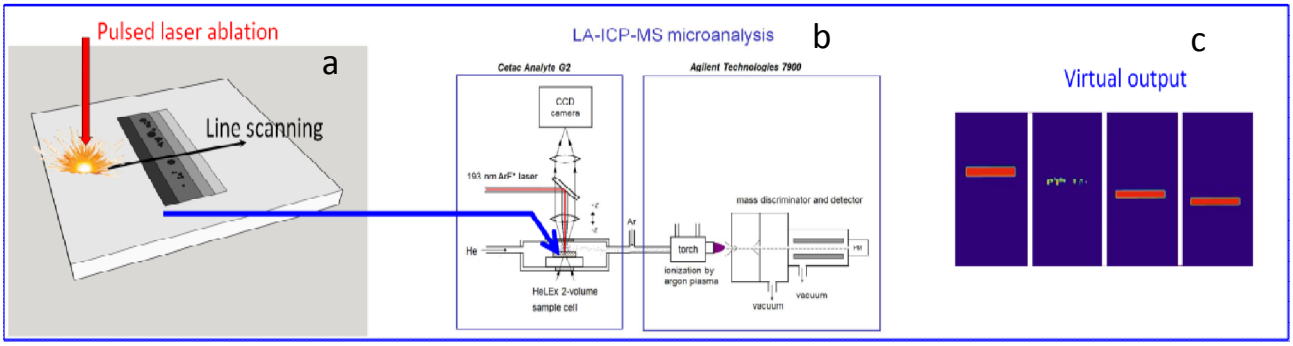

Figure 6.3. Mapping simulation of a paint cross-section (4 layers including 1 layer with smalt particles) (a), laser ablation - ICP-MS microanalysis (b) and simulated paint cross-sectional elemental maps assuming the presence of four differently distributed elements in the 4 layers (c).

Table 6.1. Operational laser ablation – ICP-MS conditions for elemental mapping of the paint cross-sections.

Laser ablation (Cetac Analyte G2)	
Wavelength	193 nm
Pulse length	<4 ns
Spot size	5 µm (square mask)
Fluence	4.08 J cm^{-2}
Repetition rate	20 Hz
He flow rate (MFC1/MFC2)	0.5/0.3 l min^{-1}
Make-up Ar flow rate	0.8 l min^{-1}
ICP-MS (Agilent 7900)	
Rf power	1500 W
Sampling depth	6.5 mm
Isotopes measured	54 isotopes
Acquisition per isotope time/mass	0.01 - 0.05 s
Total acquisition time	0.999 s
Measurement mode	Time-resolved, TRA(1)
Plasma gas flow rate	15 l min^{-1}
Auxiliary gas flow rate	1 l min^{-1}
Number of line scans/mapping sequence	20 – 50
Pixel size	5 µm × 5 µm
Mapping rate	0.15 mm^2 min^{-1}
Total analysis time/map	10 – 60 min

6.5. 2D elemental maps of paint cross-sections

The elemental maps (see the composite maps consisting of 54 element maps in Figure 6.4) obtained by laser ablation ICP-MS are very useful for visually recognizing associations between elements, in particular for the investigation of the raw materials and the manufacturing processes involved (source of silica, flux and cobalt mineral sources). The most interesting element maps were extracted from the composite maps and converted into primary color maps with shades of color representative of the pixel content. By overlaying the color maps in PyMca software (developed by the Software Group of the European Synchrotron Radiation Facility) (Solé *et al*., 2007) better and easier correlation identification is achieved. A descriptive overview of the four samples based on the extracted and overlaid elemental maps is given below (see Figure 6.7) and correlations between elements in maps are calculated via Pearson correlation coefficients (expressed as r).

Aver 1

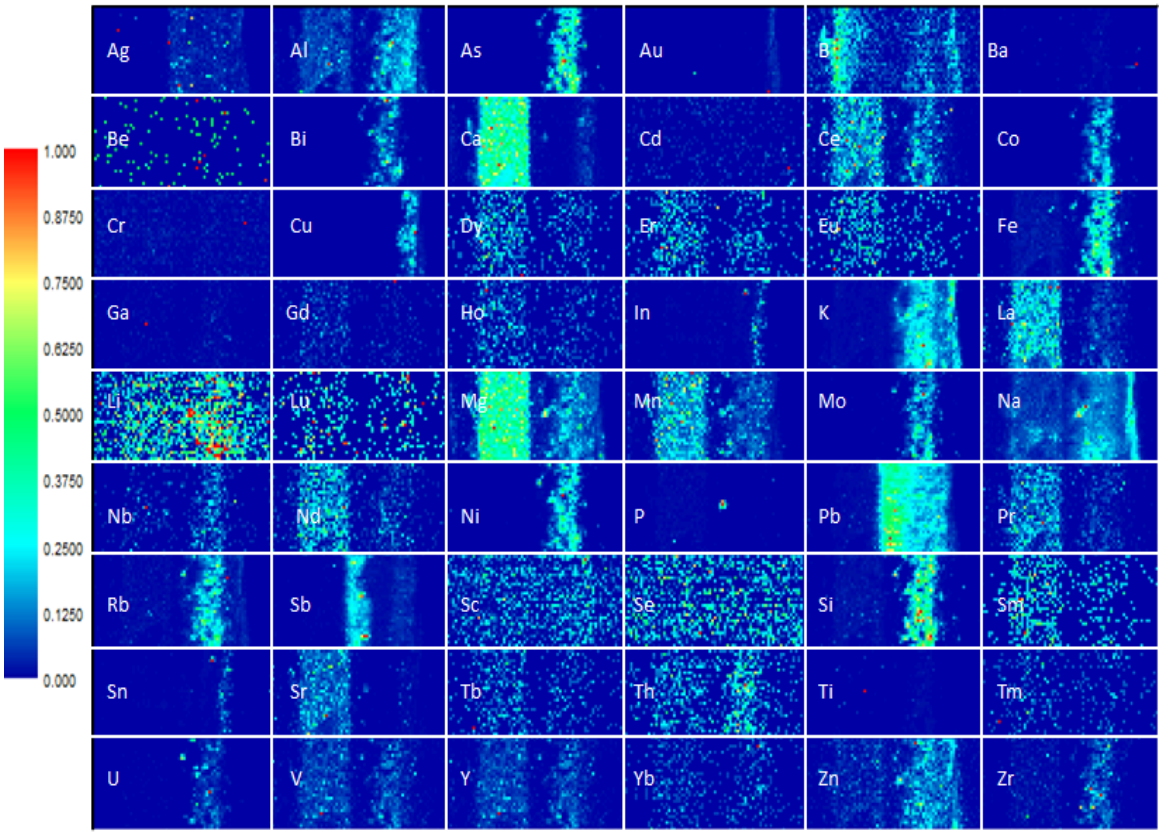

Aver2

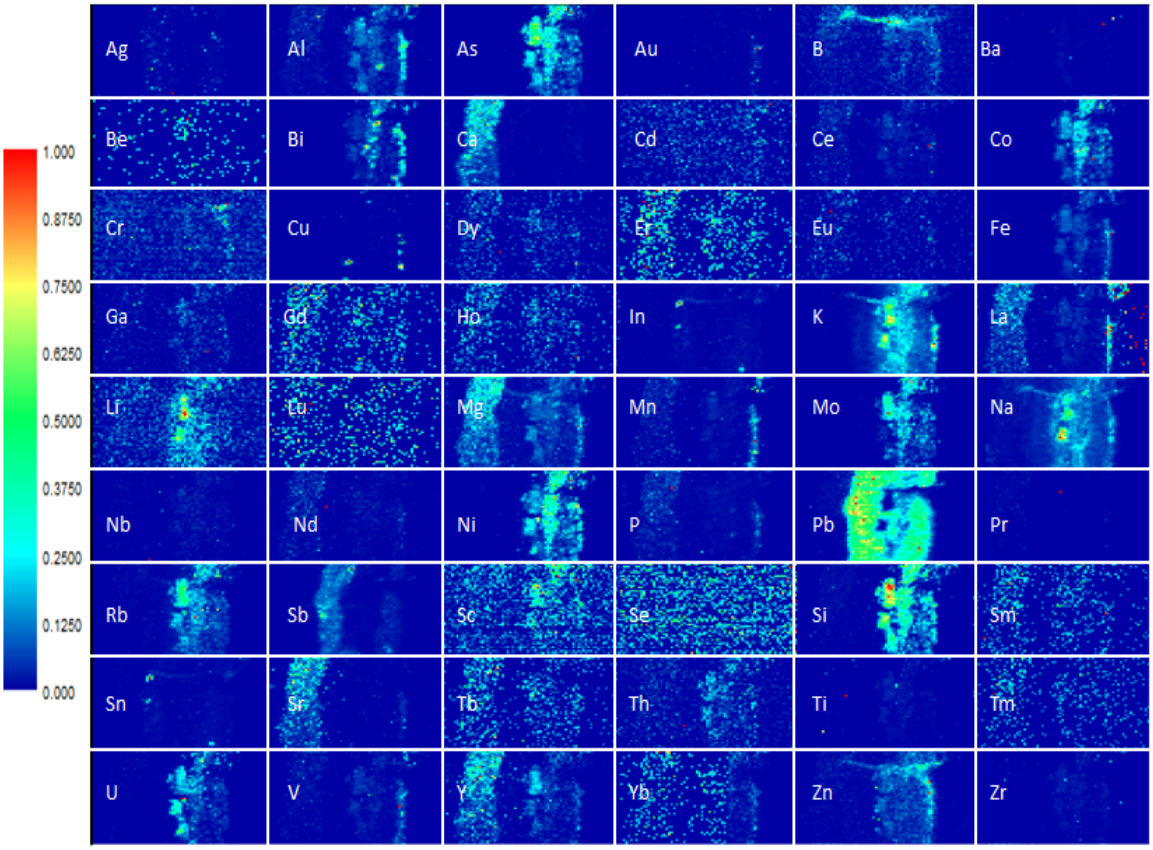

Boet

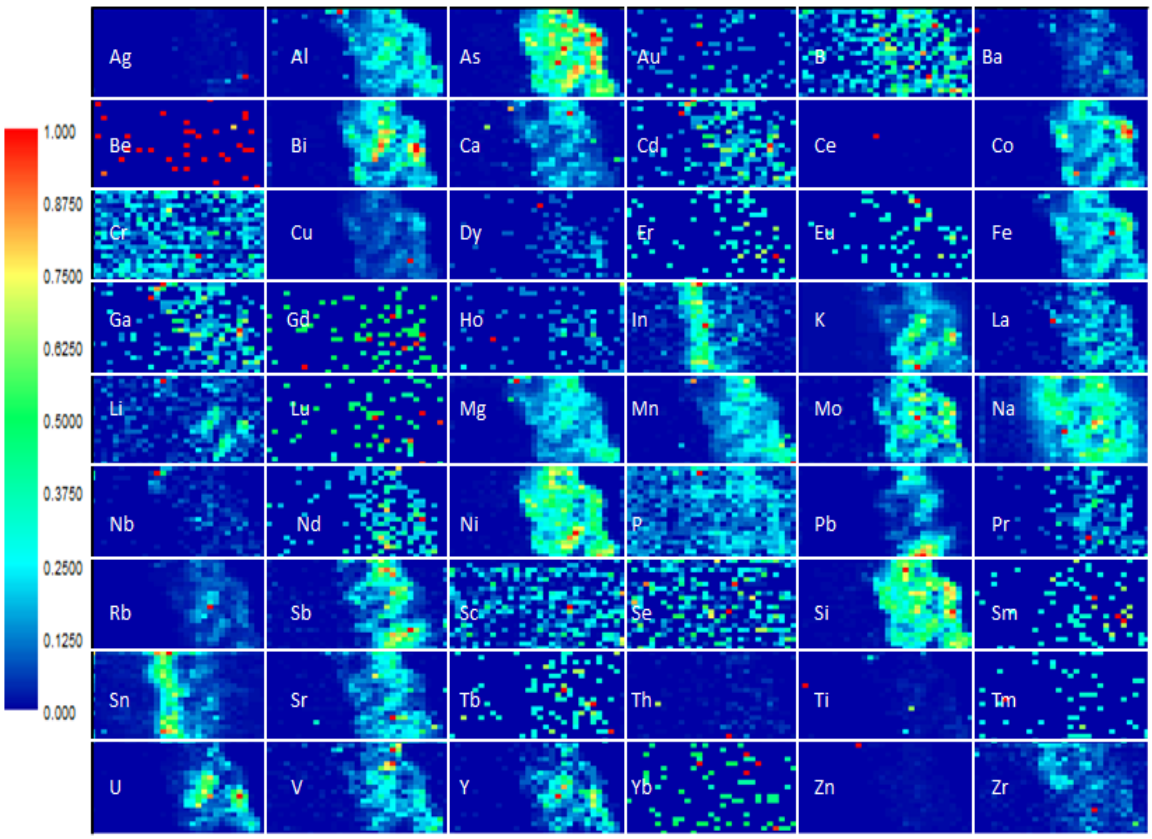

Figure 6.4. Composite maps for 54 elements for all four samples; individual maps (originally in cps) are normalized for easier comparison.

6.5.1. Sample *Aver1*

Sample *Aver1* (Figure 6.7a) shows two different paint layers, viz. a copper-based layer (probably azurite) covering a smalt-based layer (blue cobalt potash glass). Lead carbonate was used as a white pigment in the ground and paint layers. Its content is extremely high and it is spread all around the pigment particles. The Si map, together with the Co map, helps to recognize and identify the smalt particles. K is clearly leached from the particles towards the outer layer and the *imprimitura* layer of the cross-section. In the *imprimitura* layer Pb is correlated with Sb (r=0.7). Cobalt is positively correlated with As (r=0.91), Fe (r=0.89), Ni (r=0.85), Bi (r=0.59), Rb (r=0.82), Mo (r=0.86) and U (r=0.47) (Figure 6.7a). This may reflect the original provenance of the cobalt ore used to color the glass particles. Between the copper and cobalt layers we can observe Sn, probably related to a *velatura* layer of tin oxide (white).

6.5.2. Sample *Aver2*

Sample *Aver2* (Figure 6.4) shows that the major elements in the ground layer are Ca and Mg, next to traces of Sr, Y and La. This can confirm the presence of calcium carbonate and foraminifera fossils (Wallert *et al*., 2010). The *imprimitura* layer has the same composition as sample *Aver1*, mainly showing Pb and Sb (r=0.67). There are two smalt layers: one is transparent with blue or colorless glass splinters (Area 1) and the other one is semi-opaque with smaller grey or colorless glass particles (Area 2) (Figure 6.7d). The large blue particles show the highest concentrations of K, Si and Na. K and Na are also present in the utmost outer layer of the painting, probably leached out from the glass particles. Below the outer varnish a brown layer consisting of mainly Mn can be found (Wallert *et al*., 2010).

The lower Co layer consists of only three large smalt particles (Area 1), which have different elemental correlations than the upper, more condensed-like cobalt particles (Area 2). We can also observe a correlation between Co and As (r=0.79), Fe (r=0.59), Mo (r=0.79), Ni (r=0.83), Rb (r=0.55), Bi (r=0.52) and U (r=0.56). Ni, Rb and Mo correlate differently in the particles of Area 1 (Figure 6.7d). Boron is present in the cracks, possibly as a constituent of the mounting resin. U correlates with Fe and Mo in the large smalt particles in Area 1 due to its presence as a trace element in the cobalt ore. Nb correlates with As and Ni in some of the particles. Figure 6.6 shows the SEM image of the sample with the ablated area after analysis.

6.5.3. Sample *Boet*

Sample *Boet* (Figure 6.7b) shows that smalt is embedded in quartz particles as can be observed from the Si and K maps. Three large smalt particles are present in this area and from the Co map we can assume that also other smalt particles are present, probably in degraded form as their K content is very low. Cobalt is positively correlated with As (r=0.84), Fe (r=0.87), Ni (r=0.82), Mo (r=0.76) Bi (r=0.57), Rb (r=0.52) and moderately with U (r=0.34). Pb is present around the Co particles and correlates with Sb (r=0.81); even Sn is present in the layer above the smalt particles (Figure 6.7b). There is a correlation between K and Li for the most preserved particles (see the three blue marked particles in Figure 6.7b). Several particles contain U that correlates with Bi (r=0.87), Rb (r=0.61) and Mo (r=0.66).

6.5.4. Sample *Chin*

From microscopic inspection we can see that all smalt particles in sampe *Chin* (Figure 6.7c) seem to be well preserved and the pigment layer can be readily defined. Co is positively correlated with As (r=0.92), Fe

(r=0.52), Mo (r=0.88), Ni (r=0.52), Bi (r=0.55), Rb (r=0.72) and U (r=0.68) (Figure 6.6c). In the area below the Co particles there is a high content of Pb correlating with Sn and Sb. Between the lead white primer and the upper layer of paint a further layer seems to be present where a correlation between P and Ca was found.

6.6. Elemental quantification

To validate our LA-ICP-MS results, and to exclude erratic quantification arising from the surrounding paint matrix, the particles were also analyzed by SEM-EDX. SEM-EDX analysis was performed prior to laser ablation in different areas of several particles for each sample. In spite of the fact that the smalt particles are not homogeneous, the chemical composition data are in good agreement as evidenced by an overall correlation coefficient r of 0.9949 although some discrepancies can be seen for Na, K and Ca oxides (Figure 6.5). Elements as Bi and Ni were detected by SEM-EDX but not always quantifiable.

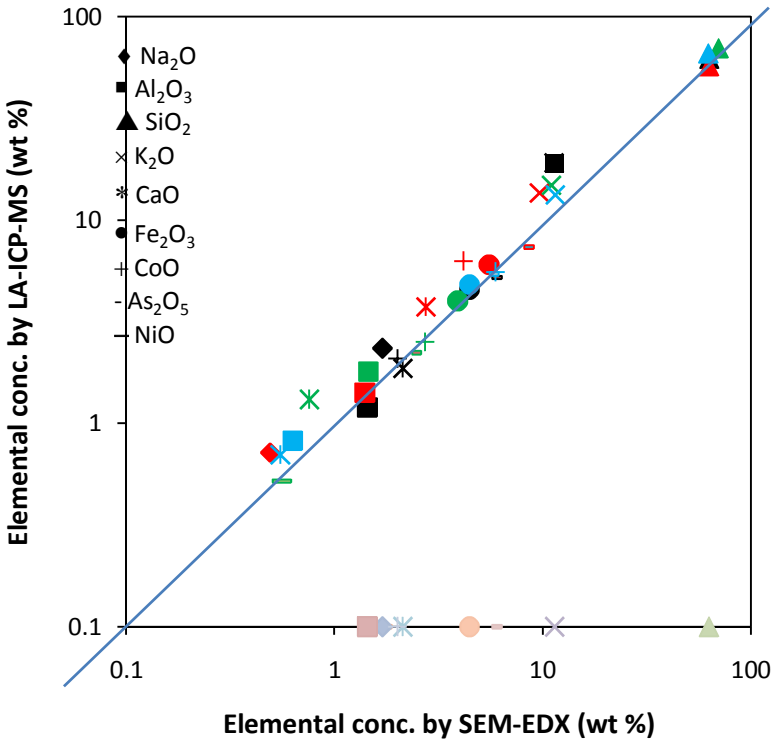

Figure 6.5. Comparison of a restricted compositional data set obtained with SEM-EDX and LA-ICP-MS; a regression line for a perfect correlation (slope=1) has been drawn. Colors refer to the smalt samples and symbols to the elemental oxides.

Quantification of elements in the maps is restricted to the smalt particles since calibration is based on the use of glass standards. In the surrounding binder material the laser ablation efficiency is much higher than in the glass particles (see the SEM images in Figure 6.6) making elemental quantification based on glass standards impossible for this material. Hence, we only quantified the elements in the glass particles using a manual particle selection method (see below) for obtaining the right pixels in the maps. After selection of the smalt particles a sum normalization approach was followed for quantification of the elements by summating *n* elements (54 major, minor and trace elements) as their oxides to 100 wt % (see Chapter 2).

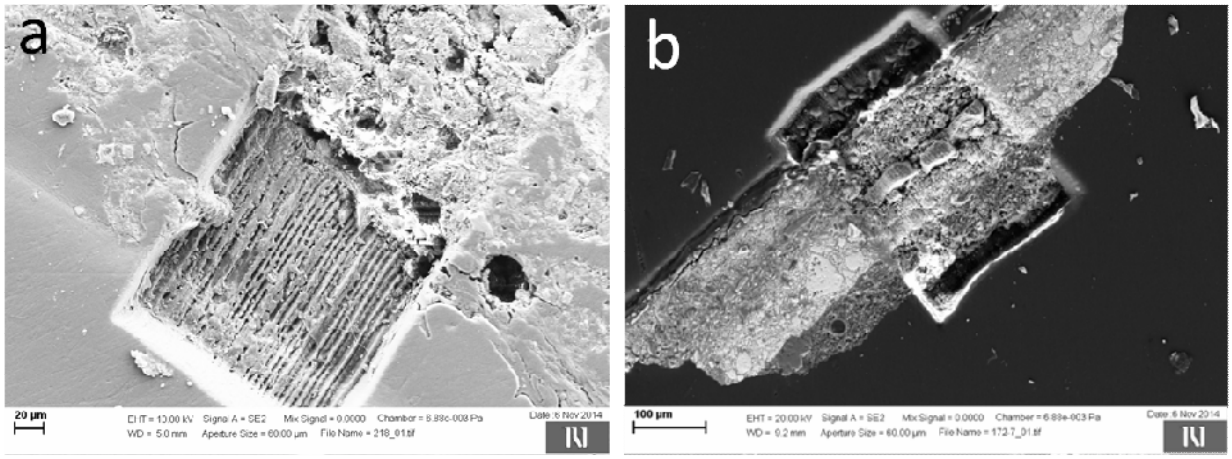

Figure 6.6. SEM images of paint cross-sections after ablation (A=*Chin* and B=*Aver2*). The line scan tracks are clearly visible in A; in B the smalt particles look as if they were dug out, as the binder material ablates much better than the glass.

Pixel selection for quantification purposes was carried out manually based on comparing the pixel content in the cobalt maps (i.e. association with the smalt particles) using the image analysis software ImageJ (Singh *et al*., 2014). To obtain insight into the degradation of smalt particles also K maps were used (see also section 6.6.3.), supported by differences (blue and gray particles) shown under UV visible light (Figure 6.2). Since lead white is the major component surrounding the smalt particles the laser beam may unintentionally ablate some of this lead white leading to corrupt elemental concentration data. Preserved smalt particles contain less than 2.5±0.4 wt % of lead oxide, as verified by EDX analysis and confirmed by literature data (Santopadre and Verità, 2006), except in a few cases (Robinet *et al*., 2011). We excluded lead from the sum normalization calculations and still obtained adequate elemental oxide concentration values deviating less than 3 % from the actual values. For sample *Chin* such lead exclusion was unnecessary as no lead white was admixed to the pigment. We did not consider elemental oxide concentrations below 0.0001 wt % (1 µg g^{-1}), i.e. the estimated average detection limit. Average concentrations of the same or different, well-preserved smalt particles, depending on the sample, are reported in Table 6.2, including their uncertainties [95 % confidence limits].

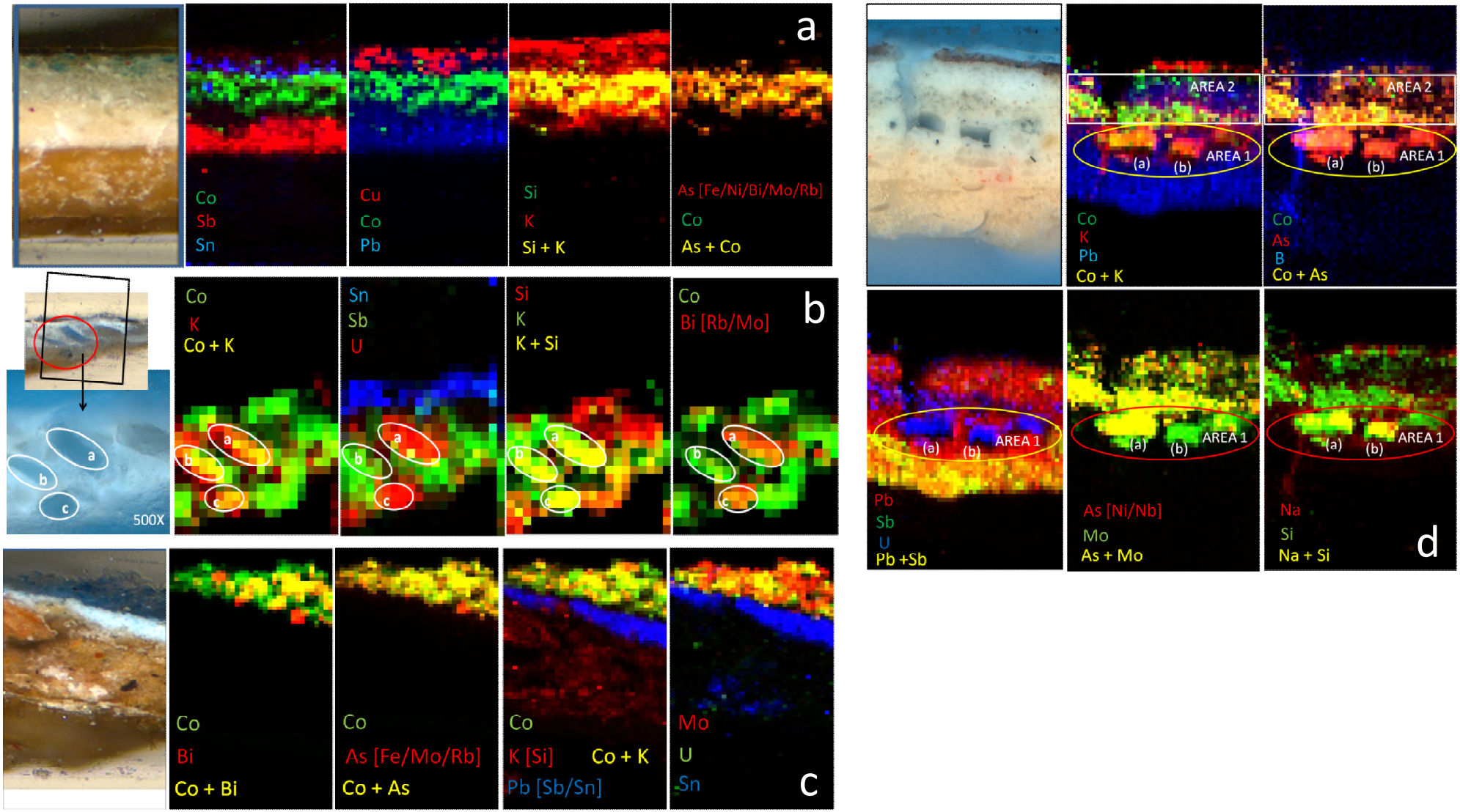

Figure 6.7. Selected areas for ablation (Figure 6.2) and relevant elemental maps extracted from Figure 6.4 were overlaid in PyMca for all four samples (a=*Aver1*, b=*Boet*, c=*Chin* and d=*Aver2*) and presented in red, green and blue (red + green = yellow).

Table 6.2. Chemical composition (mean ± uncertainty [95 % confidence limit]) of well-preserved smalt particles in different areas of the different paint cross-sections (in wt % of the major, minor and trace element oxides). Sample *Aver2* presents the average of two large blue particles (a and b) in Area1 and the average of the particles in Area 2 (see Figure 6.6b for more details); for sample *Boet* the averages of three individual, large particles are given (see Figure 6.7c for more details). Uncertainty is given by: $zs/\sqrt{n}$ (where the value of *z* depends on the degree of confidence required; *s* is the standard deviation and *n* is the size of the samples).

	Aver1		*Aver2 Area 1a*		*Aver2 Area 1b*		*Aver2 Area 2*		*Boet a*		*Boet b*		*Boet c*		*Chin*	
wt %	mean (30)	unc.	mean (17)	unc.	mean (15)	unc.	mean (14)	unc.	mean (14)	unc.	mean (13)	unc.	mean (7)	unc.	mean (15)	un.
Na_2O	0.72	0.23	1.27	0.21	2.34	0.41	1.01	0.24	0.41	0.11	0.42	0.10	0.20	0.04	0.37	0.06
MgO	0.35	0.03	0.22	0.02	0.35	0.05	0.32	0.04	0.35	0.07	0.24	0.07	0.24	0.03	0.16	0.02
Al_2O_3	1.41	0.09	1.11	0.07	1.20	0.15	1.88	1.15	1.80	0.35	1.17	0.35	1.35	0.14	0.82	0.09
SiO_2	57.01	1.45	63.63	2.15	61.95	7.98	61.47	3.11	69.91	2.30	65.67	10.63	72.40	1.71	65.74	1.61
P_2O_5	0.26	0.04	0.16	0.03	0.11	0.03	0.18	0.09	0.16	0.06	0.20	0.05	0.17	0.05	0.08	0.02
K_2O	13.58	0.98	15.91	1.20	19.04	2.41	15.14	2.07	14.79	1.81	16.87	4.09	15.12	0.88	13.27	0.83
CaO	3.74	0.45	1.38	0.18	1.86	0.27	2.91	0.75	1.31	0.46	1.67	0.45	0.43	0.06	0.70	0.17
TiO_2	0.12	0.01	0.09	0.01	0.09	0.01	0.08	0.02	0.29	0.39	0.08	0.28	0.09	0.03	0.04	0.01
Fe_2O_3	6.03	0.48	4.81	0.32	4.55	0.64	4.88	0.84	4.00	0.39	4.71	0.74	3.54	0.73	4.82	0.57
CoO	6.27	0.62	2.55	0.18	2.08	0.35	4.40	0.99	2.51	0.52	3.59	0.64	1.94	0.44	5.54	0.57
NiO	0.79	0.13	0.19	0.02	0.35	0.06	0.51	0.13	0.52	0.10	1.11	0.24	0.50	0.13	0.56	0.07
CuO	0.50	0.07	0.07	0.01	0.08	0.01	0.17	0.02	0.13	0.02	0.18	0.03	0.12	0.03	0.13	0.02
ZnO	0.03	0.01	0.03	0.01	0.03	0.01	0.04	0.01	0.04	0.01	0.04	0.01	0.02	0.01	0.02	0.01
As_2O_5	7.35	0.83	7.95	1.15	5.21	1.37	5.62	1.70	2.23	0.41	2.95	0.53	2.25	0.50	5.43	0.58
Bi_2O_3	1.31	0.27	0.32	0.04	0.47	0.08	1.00	0.45	1.16	0.36	0.73	0.32	1.39	0.64	1.37	0.29
PbO	/	/	/	/	/	/	/	/	/	/	/	/	/	/	0.63	0.22
µg/g																
Li_2O	53	14	117	17	84	21	65	12	139	25	125	40	157	83	107	24
B_2O_3	485	93	544	95	343	102	697	285	298	291	451	259	352	167	303	125
V_2O_5	75	10	59	6	66	11	62	13	96	12	57	19	104	33	37	12
Cr_2O_3	28	10	19	6	17	6	32	24	33	25	21	21	29	28	11	7
MnO	688	133	819	79	707	114	514	97	626	52	664	114	537	107	733	145
Ga_2O_3	3	1	4	1	2	1	4	2	4	1	4	2	6	6	4	2
Rb_2O	263	33	258	43	129	52	148	36	1073	552	690	400	468	88	669	127
SrO	80	13	48	8	61	10	66	20	59	23	82	24	18	13	33	10
Y_2O_3	8	2	11	1	8	2	6	2	16	5	8	4	17	7	4	1
ZrO_2	34	8	23	4	22	5	24	9	39	10	30	10	34	15	10	2
Nb_2O_5	3	1	3	1	3	1	3	2	4	2	3	2	3	2	2	1
MoO_3	343	96	238	34	31	63	217	48	179	47	149	43	157	71	455	113
Ag_2O	60	12	29	18	23	15	71	27	34	8	92	31	41	14	14	5
In_2O_3	13	2	2	1	3	2	5	2	6	3	3	2	1	1	2	1
SnO_2	2165	330	569	164	628	448	1076	312	825	252	614	229	142	51	252	143
Sb_2O_5	187	40	88	22	108	29	379	206	279	110	489	145	46	37	54	13
BaO	258	40	215	27	447	88	212	77	178	42	207	70	172	52	79	23
La_2O_3	13	2	9	2	7	2	9	2	7	2	12	3	6	3	4	1
CeO_2	15	3	17	3	17	5	12	5	15	3	15	3	12	5	9	1
UO_2	166	87	75	8	123	20	97	62	236	82	81	74	257	122	78	16

6.6.1. Cobalt ore

Typically the CoO content in smalt is variable, ranging from 3 to 9 wt % (Spring *et al*., 2005; Hartwig, 2001). The large CoO concentration range is indicative of different types of smalt; in fact the pigment was already available hundreds of years ago, from pale gray to deep blue, the color being dependent on the Co content and particle size (Muhlethaler and Thissen, 1993). In our samples the CoO concentration ranges from 1.9 wt % (in sample *Boet [c]*) to 6.3 wt % (in sample *Aver1*) (see Table 6.2). The As_2O_5 concentration is high in sample *Aver1* (7.35 wt %) and in one of the large blue particles of sample *Aver2* (7.95 wt %), but rather low in sample *Boet* (around 2 wt %). A high As content (> 4 wt %) indicates that the mineral was used without any preliminary calcination (Santopadre and Verità, 2006; Spring *et al*., 2005). The Fe_2O_3 concentration is rather high in all the samples compared to data reported in the literature; it ranges from 3.5 wt % (in sample *Boet [c]*) to 6 wt % (in sample *Aver1*). There are also low amounts of NiO (0.2 - 1.1 wt %), Bi_2O_3 (0.3 - 1.4 wt %) and CuO (0.07 - 0.5 wt %) and traces of U, Mo and Rb. Cobalt in glass is often associated with various elements incorporated in the raw cobalt-bearing materials. Gratuze and his co-workers (Soulier *et al*., 1996; Gratuze *et al*., 1996; Soulier *et al*., 1997; Gratuze *et al*., 1995) distinguished the use of four types of cobalt characteristic for different periods: 1) Co-Zn-Pb-In, 2) Co-As-Ni, 3) Co-Ni and 4) Co (Sb). The second group is characteristic for blue glass from the beginning of the 16th century with a composition comprising Co, As, Ni and traces of Bi, U and Mo (sometimes even W). The blue pigment from the 16th century is commonly associated with minerals like Smaltite, Erythrite, Safflorite and Cobaltite as found in the Saxon mining district of Schneeberg, Germany (Hartwig, 2001; Soulier *et al*., 1996).

Since Co in all samples analyzed is correlated with As, Ni, Fe, Bi, Mo and in some case with U, it can be assumed that the mineral origin coincides with group 2 (Co-As-Ni). This is illustrated in Figure 6.8a where the As_2O_5/CoO vs. NiO/CoO ratios for all samples are compared with these of group 2 by Gratuze *et al*. (1995) and some correlations are evident. It can be seen that our data fit the reported ones perfectly, representative for the composition of blue glasses from the beginning of the 16th century. It is worth to note the grouping of the data of sample *Aver2* in two clusters as a result of compositional differences in particles from Area1 a and b (Figure 6.7d). This is indicative of the heterogeneity of the mineral ore used in the fabrication of smalt, even if it originated from the same mine. Only in 1735 George Brandt introduced a chemical isolation procedure for cobalt to produce rather pure zaffre for the coloration of glass, ceramics and paint. Earlier the various minerals (Siegenite, Bieberite, Erythrite, Safflorite, Linnaeite, Chloanthite, Skutterudite and Cobaltite) from the Erzgebirge mountain range in Saxony were used in their raw form or after rough purification, resulting in an undefined product (Syta *et al*., 2014). Soulier *et al*. (1996) elaborated the correlation of As with Ni+Co for different cobalt minerals (see the black lines in Figure 6.8b) to identify the mineral ores used in the production of archaeological glazed ceramics. Our data in Figure 6.8b, based on several particles per sample, show that smalt in the paint cross-sections seems to correlate with different cobalt minerals. *Aver1* correlates well with Erythrite and *Aver2a* with Safflorite whereas *Chin* and *Aver2b* seem to be a mix of several cobalt minerals, underlining the heterogeneity of the cobalt ores used; *Boet* appears to have a different composition altogether. It is well known that cobalt in the form of smalt was imported in China for the production of ceramics until the 16th century. From about the end of the 16th century onwards probably a local “blue material” from Chekiang Erythrite was used all native Chinese cobalt ore seem to contain well-detectable contents of manganese as an impurity (Watt, 1979).

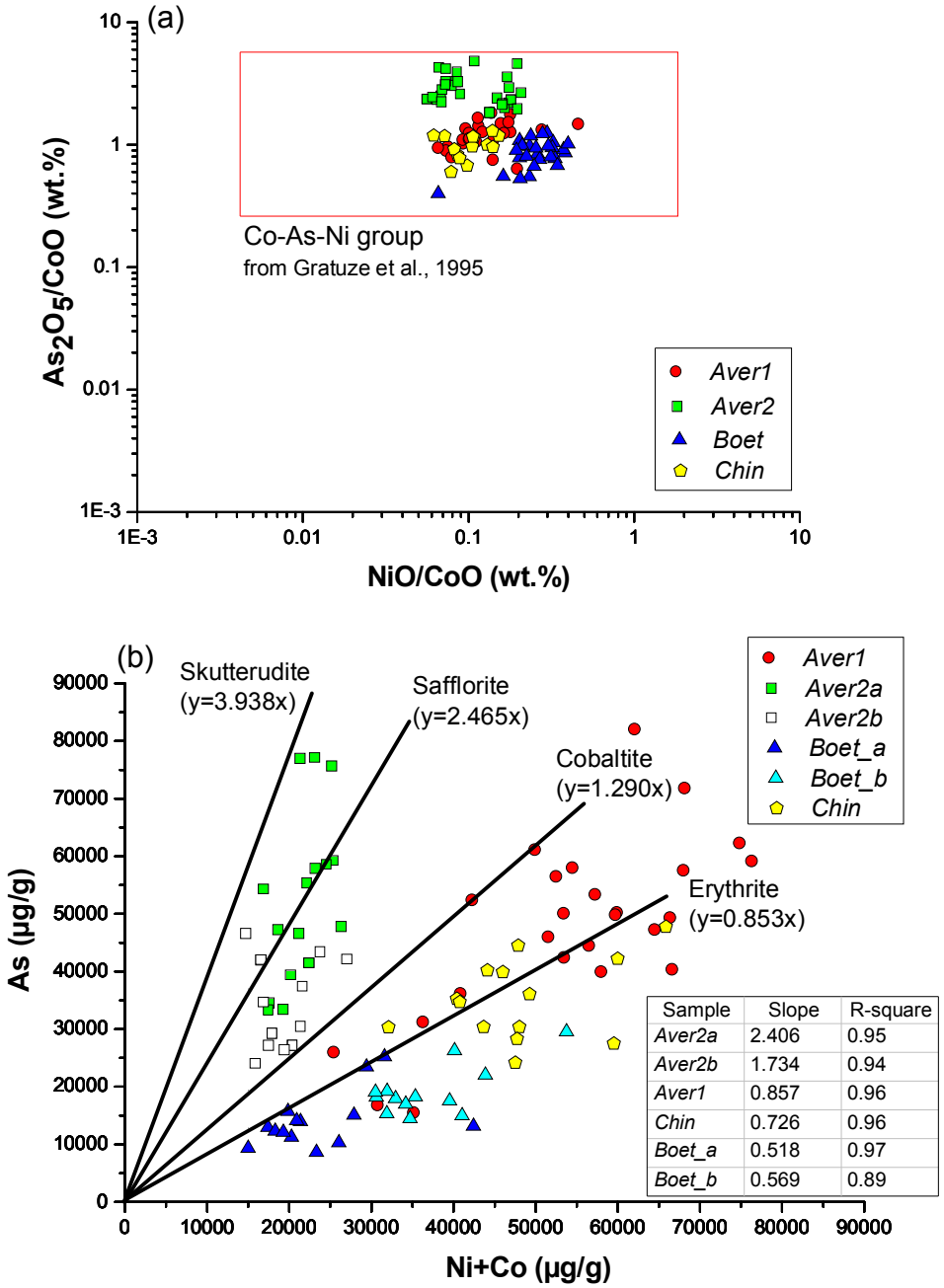

Figure 6.8. (a) Plot of As_2O_5/CoO vs. NiO/CoO (in wt %) for all four samples analyzed compared to reported data representative for the composition of blue glasses from the beginning of the 16th century (Gratuze *et al.*, 1995); (b) Plot of elemental relationships according to the function As = *f*(Ni+Co) (Soulier *et al.*, 1996) for different cobalt minerals (black lines), overlaid with our smalt data for all samples to speculate on their cobalt ore composition.

6.6.2. Smalt glass composition

The chemical composition of the glass matrix of smalt is variable; it contains approximately 66-72 wt % SiO_2 and 10-21 wt % K_2O (Muhlethaler and Thissen, 1993). For the smalt production generally a potash flux was used instead of soda because the latter makes the color blue-violet, but it is well known that the chemical stability of potassic glass is lower than that of sodic glass. We compared our smalt glass matrix data with the ones reported in the literature, specifically associated with 16th and 17th century glass originating from the Low Countries (Velde *et al*., 2010). During this period the best smalt came from Flanders and it was used in both fresco and in tempera paintings (Santopadre and Verità, 2006). The very low content of P (P_2O_5 < 0.2 wt %), Mg (MgO < 0.3 wt %) and Ca (CaO < 4 wt %) found in the smalt particles studied in the present work may indicate that wood ash was purified or, unlikely, that tartaric wine barrel deposits (*grepola*) were used (Velde *et al*., 2010; Zecchin, 1990). Potash was a classic fluxing agent in Northern Europe but, as described by several authors (Velde *et al*., 2010; Barrera and Velde, 1989; Cílová and Woitsch, 2012), it was extracted from well-burned wood ashes by washing with water. By comparing the composition of French and Low Countries glasses, Velde *et al*. (2010) discovered that a different extraction process was used by glassworkers from the Low Countries in the late 16th - early 17th century period. This new, high-potash glass with a much more purified composition is similar to the composition of our smalt samples.

Statistical analysis via two way clustering was performed on z-scaled elemental concentrations c_{scaled} in selected pixels in a particular sample using the "gplots" package in "R": $c_{scaled}=(c_i-c_{av})/c_{sd}$, with c_i the concentration in each pixel *i*, c_{av} the average concentration $\Sigma c_i/n$ (*n* is the number of pixels) and c_{sd} is the standard deviation in c_{av}. A heatmap was used to show the differences in concentrations of measured elements/elemental oxides. Two-way clustering was performed on blue particles in samples *Aver1*, *Aver2 Area 1a*, *Aver2 Area 1b*, *Boet_a*, *Boet_b* and *Chin* for the main elements (Al, Ti, Mg, P, Ca, Si, K and Na), except the ones related to the cobalt ores (Co, As, Ni, Fe, Bi, Cu). From Figure 6.9a it can be seen that discrimination based on concentration differences is poor, probably because these main elements enter the glass bulk partly via the flux which composition is predominantly related to plants ashes and dependent on the soil variability. Sample *Boet_a* has the highest contents of Ti, Al, Mg and Si, *Aver1* of P and Ca and *Aver2* of Na and K. Only sample *Chin* appears distinctly different from the other samples which is substantiated by similar two-way clustering for the trace elements (Figure 6.9b). Samples from the same cross section (*Boet_a/b* and *Aver2 Area 1a/b*) and from the same painting (*Aver1*, *Aver2 Area 1a/b*) look very similar, but sample *Chin* is still distant from the other samples. Sample *Boet_a* has the highest contents of Li, Rb, Cr, V, U, Zr, Y and Nb, *Aver* samples of Ce, Ba, Mn, B and Sr. Sb in sample *Boet_b* is not an actual smalt component but a contamination from the surrounding binder material as can be seen from the maps in Figure 6.7b.

(a)

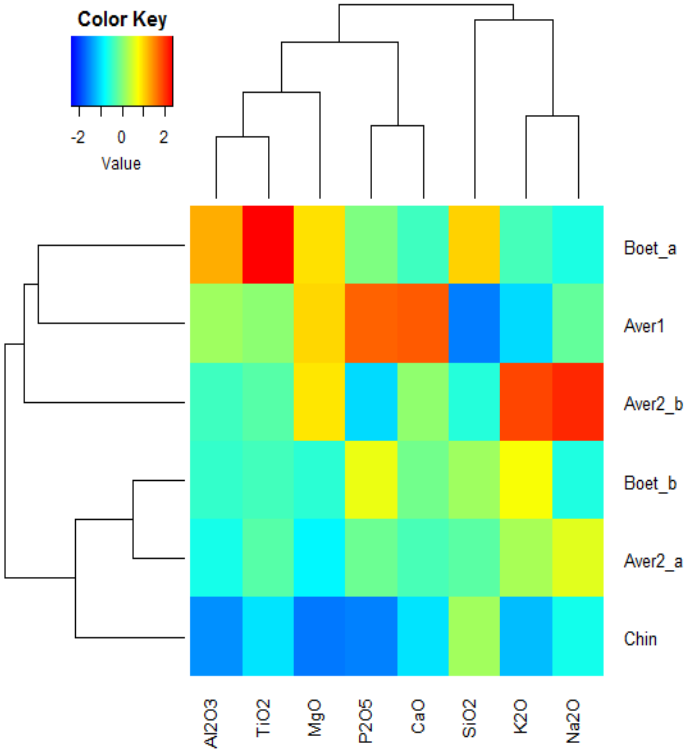

(b)

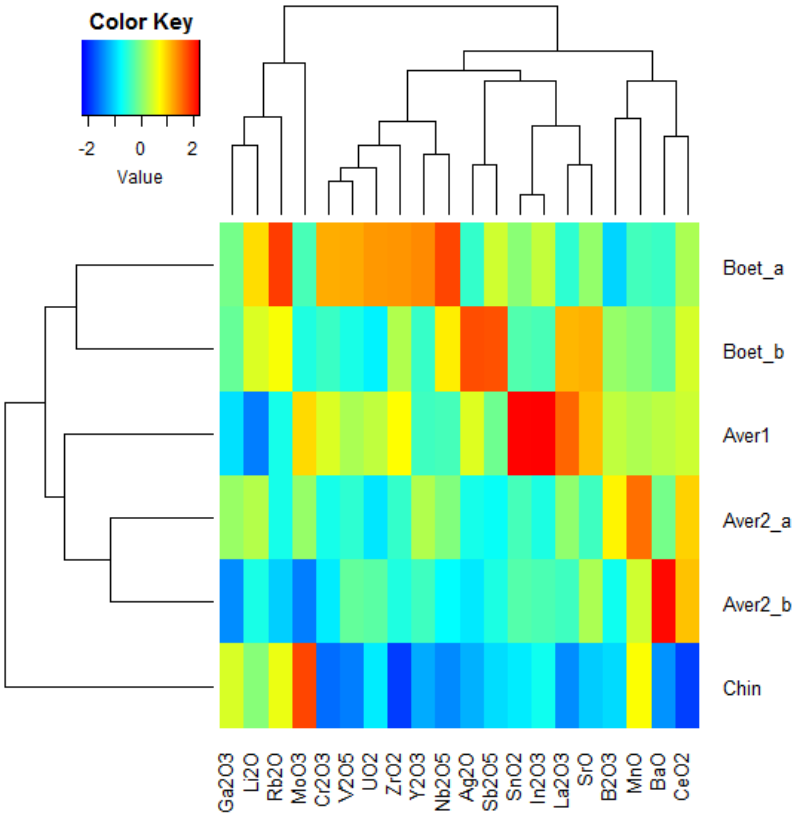

Figure 6.9. Two way clustering of the blue glass particles in paint cross-sections *Boet_a/b*, *Chin*, *Aver1* and *Aver2 Area 1a/b* for main elements (a) and minor and trace elements (b).

6.6.3. Degradation phenomena

After manual selection of suitable pixels (see Figure 6.10), expected to be related to preserved (blue color) and degraded (gray color) smalt particles in one paint layer, principal component analysis was carried out to retrieve the variability in the two clusters (preserved and degraded) using a suite of 8 elements believed to be sensitive to degradation. In Figure 6.11a it can be seen that the selected blue and gray particles in the loading plot are indeed different and form more or less separate clusters with the PC1 and PC2 factors collectively explaining 71 % of the variability. The projection of the variables (8 elements) on the factor plane (insert in Figure 6.10a) shows that Na and K dominate the dataset as one might expect from their leachability potential (Newton and Davison, 1989).

Performing the same statistical data processing routines on sample *Aver2*, a sample where the large blue particles and the small gray particles are present in different layers (Figure 6.10b), shows perfectly separated clusters with the PC1 and PC2 factors collectively explaining 75% of the variability and Na and K dominating the dataset (Figure 6.11b and insert). Although one might assume that degradation must have taken place, this is not conclusive as the painter may have used different pigments (with light and dark blue smalt particles) with initially different compositions.

For the other two samples (*Aver1* and *Chin*), pixels selected in cobalt-related areas could not be (positively) associated with preserved and degraded smalt particles. For the *Chin* sample this might be due to the painting techniques, i.e. lacquer instead of oil as binder and the absence of lead white around the particles. However, considering the age of the paintings and the conditions they were exposed to, it is unlikely that none of the smalt particles has undergone degradation, especially since in some of the samples micro cracks can be observed in the cross-sections (Figure 6.7).

This study on smalt degradation is still in progress. The main goal of this research was to show the remarkable and very promising potential of the laser ablation – ICP-MS technique that has never been applied for analysis of smalt in paint cross-sections until now.

(a) Boet

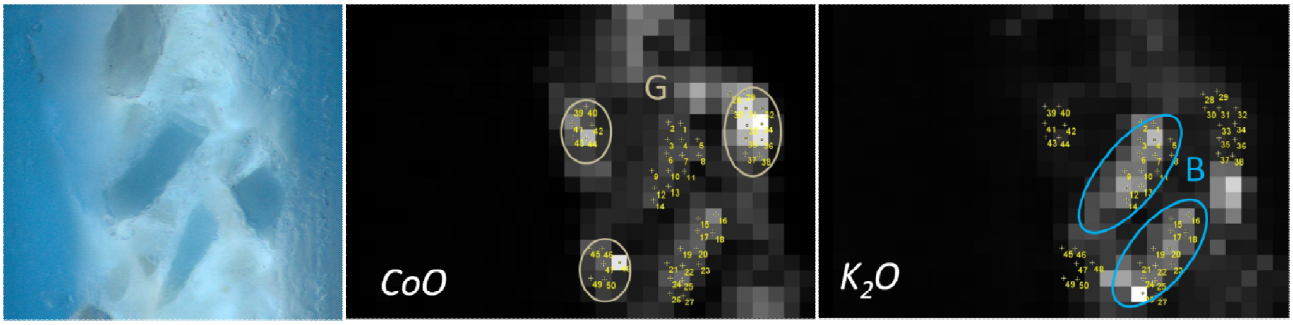

(b) Aver2

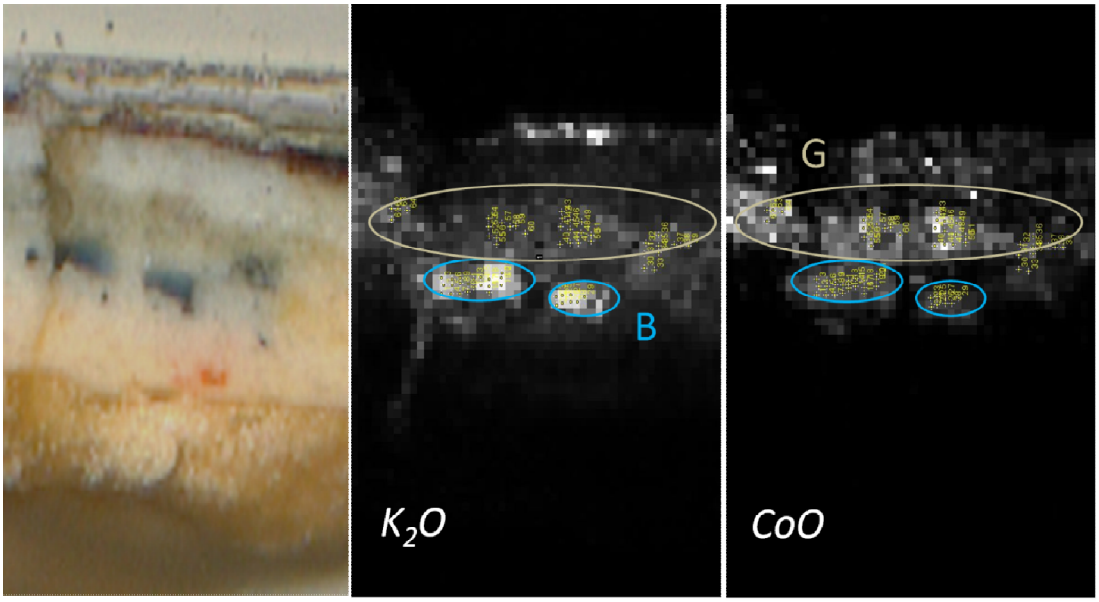

Figure 6.10. Manual pixel selection to study smalt degradation phenomena in the samples *Boet* (a) and *Aver2* (b) based on the visible light images (showing differently colored smalt particles; blue (B) and gray (G), expected to be related to preserved and degraded particles, respectively) and the CoO and K_2O maps for quantification purposes.

(a)

		Na_2O	K_2O	Fe_2O_3	CoO	NiO	CuO	As_2O_5	Bi_2O_5
***Boet* B**	mean (26)	0.41	14.53	4.36	3.03	0.80	0.16	2.53	0.95
	unc.	0.07	1.18	0.32	0.38	0.15	0.02	0.32	0.22
***Boet* G**	mean (22)	0.26	4.35	5.54	6.23	0.73	0.21	2.69	1.02
	unc.	0.07	0.63	0.54	0.80	0.14	0.04	0.40	0.42

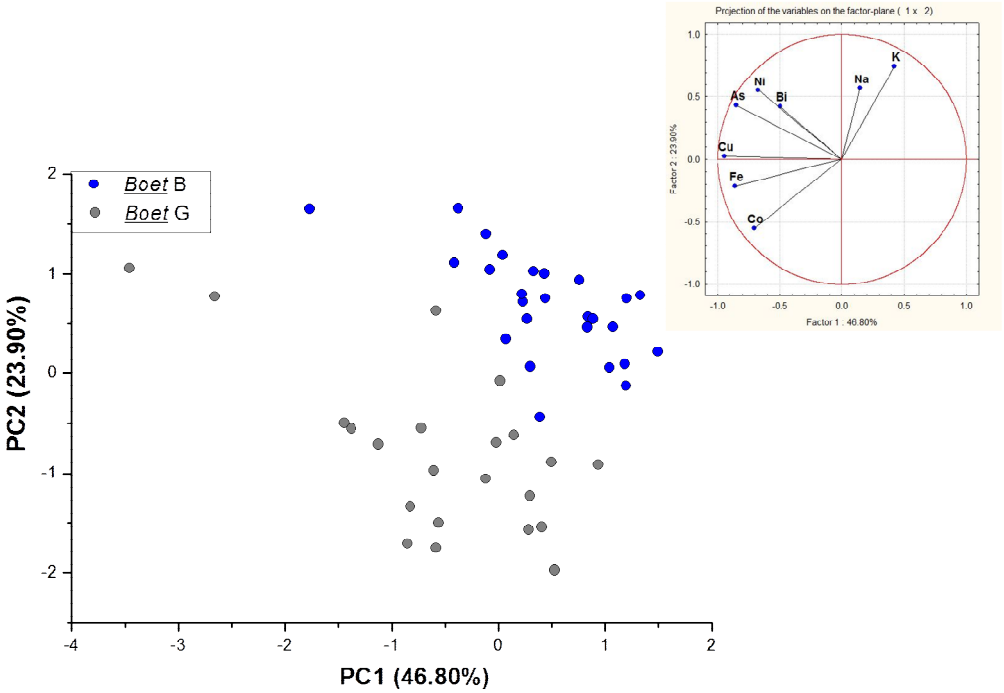

(b)

		Na_2O	K_2O	Fe_2O_3	CoO	NiO	CuO	As_2O_5	Bi_2O_5
Aver2 **B**	mean (32)	1.77	17.38	4.68	2.33	0.27	0.07	6.67	0.39
	unc.	0.24	0.88	0.23	0.15	0.04	0.01	0.82	0.05
Aver2 **G**	mean (31)	0.61	8.80	7.08	8.94	0.84	0.26	8.90	1.94
	unc.	0.07	1.01	0.56	1.45	0.10	0.03	0.92	0.71

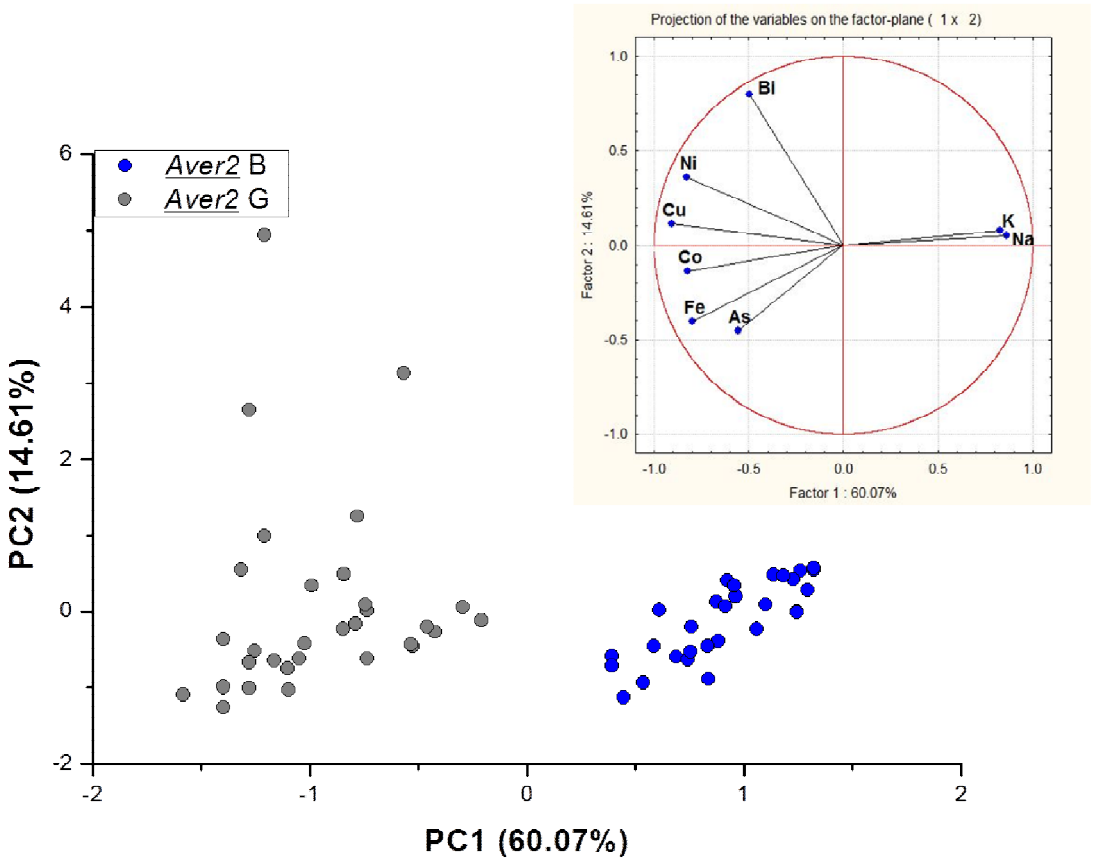

Figure 6.11. Statistical analysis via PCA to distinguish between blue (B) and grey (G) glass particles in paint cross-sections of the samples *Boet* and *Aver2* and related tables with the compositional concentration data (mean ± uncertainty [95 % confidence limit]); the inserts show the projection of the variables.

6.7. Conclusions

2D laser ablation - ICP-MS analysis is a sensitive microanalytical tool to retrieve spatial elemental correlations to obtain information on the stratigraphic composition of a painting via mapping of paint cross-sections and can aid in the understanding of smalt degradation phenomena and the provenance of the smalt pigment. It is very useful for a fast preliminary visual inspection and to collect general information about the elemental distribution in the particles; the heterogeneity of the raw materials (cobalt ores, zaffre and glass) used to manufacture the pigment will inevitable appear as irregularities in the elemental smalt maps. Quantification of elements in the particles (by selection of pixels from the Co maps) via a sum normalization approach (by summing of the elements as their oxides to 100 wt %) allows us to speculate on the provenance and origin of these raw fabrication materials.

A chemometric approach, correlating the pixel content of the elemental maps in the regions associated with smalt particles, shows no clear distinction between the elemental concentrations in four paint cross-sections of 17th century paintings. This indicates a similar provenance of the cobalt ores, suggesting a similar provenance of the pigment. The likely source of cobalt ore for the smalt particles in all paintings is the Erzgebirge in Saxony, Germany, although differences in mineral composition, even for smalt particles in the same painting, are noticeable. Nevertheless, we cannot exclude the presence of a similar cobalt ore in China as we know little about the smalt production in China in this period. The high content of K_2O and the low content of CaO, Na_2O, MgO and P_2O_5 seem to indicate the use of purified wood ashes as flux, comparable to the composition of glasses from the late 16th to early 17th century period originating from the Low Countries.

It was attempted to look at the degradation of smalt particles, based on their color under visible light microscopy, and by correlating elements (in areas of the maps associated with smalt) thought to be sensitive to leaching through corrosion of smalt. Initial findings indicate that laser ablation – ICP-MS mapping is able to distinguish between preserved and degraded smalt particles using statistical data processing routines but more work is needed to reliably study smalt corrosion in paintings.

6.8. References

Barrera J. and Velde B. (1989) A study of French Medieval glass composition, JGS 31; pp. 48-54.

Cianchetta I., Colantoni I., Talarico F., d'Acapito F., Trapananti A., Maurizio C., Fantacci S. and Davoli I. (2012) Discoloration of the smalt pigment: experimental studies and ab initio calculations, J. Anal. At. Spectrom. 27; pp. 1941-1948.

Cílová Z. and Woitsch J. (2012) Potash – a key raw material of glass batch for Bohemian glasses from 14th-17th centuries?, J. Archaeol. Sci. 39; pp. 371-380.

De Haan J. (2009) The Leeuwarden Lacquer Room: a Royal Puzzle, The Rijksmuseum Bulletin 57; pp. 151-167.

Delamare F. (2009) Aux origines des bleus de cobalt : les débuts de la fabrication du saffre et du smalt en Europe occidentale, CRAI 153; pp. 297-315.

Giovanoli R. and Mühlethaler B. (1970) Investigation of discoloured smalt, Stud. Conserv. 15; pp. 37-44.

Gratuze B., Soulier I., Barrandon J.N. and Foy D. (1995) The origin of cobalt blue pigments in French glass from the thirteenth to the eighteenth centuries, in: D.R. Hook and D.R.M. Gaimster, Trade and Discovery: the scientific study of artefacts from Post-Medieval Europe and Beyond, British Museum Occasional Paper 109; pp. 123-132.

Gratuze B., Soulier I., Bler M. and Vallauri L. (1996) De l'origine du cobalt: du verre a la ceramique, Revue d'Archéometrie 20; pp. 77-94.

Hartwig J. (2001) De la fabrication et de l'utilisation du safre ou zaffera (cobalt) et du smalte, par les verriers Durant les XVI Ème, XVII Ème et XVIII Ème siècles. Verre 7; pp. 1-12.

Marin E., Padro´ A., Miquel A. and Garcia J.F. (2015) Characterization of paintings by Laser Ablation-Inductively Coupled Plasma-Mass Spectrometry, Anal. Lett. 48; pp. 167-179.

Muhlethaler B., Thissen J. (1993) Smalt, in Artists' Pigments, A handbook of their history and characteristics, ed. A. Roy, Washington, Vol 2, pp. 113-130.

Newton R.G. and Davison S. (1989) Deterioration of glass, in: R.G. Newton and S. Davison (Eds.), Conservation of Glass, Butterworths, London; pp. 135-164.

Noble P. and van Loon A. (2005) New Insights into Rembrandt's Susanna, Art Matters – Netherlands Technical Studies in Art 2; pp. 76-96.

Plesters J. (1969) A Preliminary Note on the Incidence of Discolouration of Smalt in Oil Media, Stud. Conserv. 14; pp. 62-74.

Resano M., García-Ruiz E., Alloza R., Marzo M. P., Vandenabeele P. and Vanhaecke F. (2007) Spectrometry for the Characterization of Pigments in Prehistoric Rock Art Discussion of the quantitative data, Anal. Chem. 79; pp. 8947-8955.

Robinet L., Spring M., Pagès-Camagna S., Vantelon D. and Trcera N. (2011) Investigation of the Discoloration of Smalt Pigment in Historic Paintings by Micro-X-ray Absorption Spectroscopy at the Co K-Edge, Anal. Chem. 83; pp. 5145-5152.

Robinet L., Spring M. and Pagès-Camagna S. (2013) Vibrational spectroscopy correlated with elemental analysis for the investigation of smalt pigment and its alteration in paintings, Anal. Methods 5; pp. 4628-4638.

Santopadre P. and Verità M. (2006) A Study of Smalt and its Conservation Problems in two Sixteenth-century Wall Paintings, Stud. Conserv. 51; pp. 29-40.

Šelih V.S. and van Elteren J.T. (2011) Quantitative multi-element mapping of ancient glass using a simple and robust LA-ICP-MS rastering procedure in combination with image analysis, Anal Bioanal Chemistry 401; pp. 745-755.

Singh S.P., Vogel-Mikuš K., Vavpetič P., Jeromel L., Pelicon P., Kumar J. and Tuli R. (2014) Spatial X-ray fluorescence micro-imaging of minerals in grain tissues of wheat and related genotypes, Planta 240; pp. 277–289.

Smeenk-Metz E., Zeldenrust M. and Wallert A. (2011) Young Woman in a Broad – Brimmed Hat. Painting Technique and Restoration, The Rijksmuseum Bulletin 59; 223-235.

Solé V.A., Papillon E., Cotte M., Walter Ph., Susini J. (2007) A multiplatform code for the analysis of energy-dispersive X-ray fluorescence spectra, Spectrochim. Acta Part B 62; pp. 63-68.

Soulier I., Gratuze B. and Barrandon J.N. (1996) The origin of cobalt blue pigments in French glass from the Bronze age to the eighteenth century, in: S. Demirci, A.M. Ozer, G.D. Summer (Eds.), Proceedings of the International Symposium on Archaeometry, Tubitak Ankara; pp. 133-140.

Soulier I., Blet M. and Gratuze B. (1997) Verres et Céramiques glaçurées archéologiques: complémentarité entre les texts et les resultants d'analyses, in: H.J. Braun and A. Herlea (Eds.), Proceedings of the XXth International Congress of History of Science, Liège; pp. 211-228.

Spring M., Higgitt C. and Saunders D. (2005) Investigation of Pigment-Medium Interaction Processes in Oil Paint containing Degraded Smalt, National Gallery Technical Bulletin 26; pp. 56-70.

Stege H. (2004) Out of the blue? Considerations on the early use of smalt as blue pigment in European easel painting, ZKK 18; pp. 121-142.

Syta O., Rozum K., Choińska M., Zielińska D., Żukowska G. Z., Kijowska A. and Wagner B. (2014) Analytical procedure for characterization of medieval wall-paintings by X-ray fluorescence spectrometry, laser ablation inductively coupled plasma mass spectrometry and Raman spectroscopy, Spectrochim. Acta B 101; pp. 140-148.

Velde B., Janssens K., de Raedt I. and Veekman J. (2010) Potassic glass compositions in the Low Countries: 15 – 17th centuries, in: K. Janssens, P. Degryse, P. Cosyns, J. Caen and L. Van't Dack (Eds.), Annales of the 17th Congress of the International Association for the History of Glass: Annales du 17e Congres de l'Association Internationale pour l'Histoire du Verre, Antwerp, 2010; pp. 594-601.

Wallert A. and Verslype I. (2010) IJzige luchten, luchtig ijs, in: P. Roelofs, et al. (Eds.), Hendrick Avercamp, De meester van het ijsgezicht, Rijksmuseum, Amsterdam & Nieuw Amsterdam Uitgevers; pp. 129-140.

Watt J.C.Y. (1979) Notes on the Use of Cobalt in Later Chinese Ceramics. Ars Orientalis 11; pp. 63-85.

Weber G.J.M. (2011) Young Woman in a Broad – Brimmed Hat. A Newly Acquired Painting by Caesar Boetius van Everdingen, The Rijksmuseum Bulletin 59; pp. 211-220.

Zecchin L. (1990) Vetro e vetrai di Murano, vol. III, Arsenale, Venice.

CHAPTER 7
Analysis of polychrome Iron Age glass vessels from Mediterranean I, II and III groups by LA-ICP-MS*

A case study

* Part of this chapter was published in Panighello *et al*., 2012.

7.1. Introduction

In this chapter LA-ICP-MS is applied to analyze polychrome glass vessels from the Iron Age found at an Etruscan archaeological site near Adria (Northern Italy). The glass samples were analyzed by LA-ICP-MS in line scanning mode in order to generate quantitative, bulk elemental data to retrieve information about glass production during the Iron Age and in general to answer specific, archaeological questions. The samples belong to the so-called Mediterranean Groups I, II and III and date back to the 5th, 3rd and 2nd century BC, respectively. To date, analytical data for only two sets of vessels of the Iron Age have been discussed in the literature. In spite of the low number of available samples, this is the first time that vessels of all three periods are analytically compared. Elemental concentration data show that the samples can be classified as low-magnesia-low potash (LMLK) soda-lime-silica glasses, with low phosphorus and titanium contents, in agreement with data for similar samples of the same age. Bivariate and multivariate analyses of the contents of many elements characterizing the siliceous sands showed three distinct sets corresponding to the three periods. Since the sets indicate different provenances of the sands it seems reasonable to assume that different glassmaking locations were involved. Chromophores and opacifiers of the blue bodies and the yellow, white and turquoise decorations of the vessels were analytically identified, while the nature of the corresponding ores was hypothesized.

So far only a limited number of studies on the chemical composition of glass from the Iron Age have been carried out (Hartmann *et al*., 1997; Gratuze and Billaud, 2003; Gratuze and Lorenzi, 2006; Towle and Henderson, 2007; Zorn and Brill, 2007; Oikonomou *et al*., 2008; Gratuze, 2009; Reade *et al*., 2009; Shortland and Schroeder, 2009; Arletti *et al*., 2008, 2010, 2011). Only the last four cited papers deal with Mediterranean glass vessels. They originate from the Northern Italy Etruscan sites of Spina and Bologna, (Arletti *et al*., 2008, 2010, 2011) and from a Greek settlement on the Black Sea coast of modern Georgia (Shortland and Schroeder, 2009). The towns of Bologna and Spina are situated near Adria and have been Etruscan centers (dating from the first half of the 6th century BC to the 3rd century BC). Arletti *et al*. (2010, 2011) noted that all the samples from Bologna and Spina are silica-soda-lime glass produced with a natron flux and that there is no link between these glass samples and the northern Italian glass produced during the final Bronze Age; moreover, all the finds from Bologna and Spina seem to have a common origin. The chemical composition of these vessels from Groups I and II suggests that similar raw materials and recipes of production were used. Shortland and Schroeder observed that the type of vessels from the Black Sea was very common in the Mediterranean, with the exception of the colonies of the Eastern Black Sea, although they were prevalent in Rhodes. They pointed out also that the remarkable stylistic similarity of these vessels with some found on Rhodes suggests their provenance from some workshops of this island and that they present an elemental composition very similar to the Roman Levantine glass reported by Freestone *et al*. (2002a, 2002b); Freestone (2006).

7.2. Samples

Twenty samples from seven different vessels were selected for this study. All the vessels, produced with the core-forming technique, belong to the so-called Mediterranean Groups I, II and III.

Types and features of the samples are indicated in Table 7.1. Since the analysis by LA-ICP-MS and SEM-EDS requires very small samples, subsamples from the fragments of the artifacts were taken with linear dimensions of 1-5 mm. Sub-sampling was performed only on those vessels already damaged. In Figure 7.1 cross-sections of samples 52 and 53 are shown.

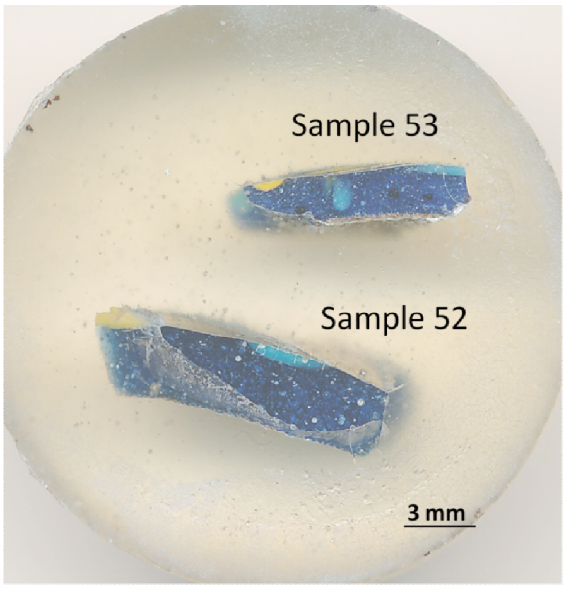

Figure 7.1. Cross sections of samples 52 and 53 incorporated in epoxy resin. Turquoise and yellow decorations are visible with bubbles and black inclusions (sample 53).

Table 7.1. Dating, color and typology of the glass samples.

Typology	Date	Provenance	Samples	
Fragment of Aryballos	5th century B.C.	Adria - Bocchi collection	51b	Blue
			51y	Yellow
			51t	Turquoise
Fragment of Aryballos	5th century B.C.	Adria - Bocchi collection	52b	Blue
			52y	Yellow
			52t	Turquoise
Fragment of Aryballos	5th century B.C.	Adria	53b	Blue
			53t	Turquoise
			53y	Yellow
Fragment of Aryballos	5th century B.C.	Adria	54b	Blue
			54t	Turquoise
Fragment of Oinochoe	3rd century. B.C.	Adria - Bocchi collection	3b	Blue
			3w	White
Fragment of balsamar	2nd century B.C.	Adria – cemetery of Canal Bianco	21b	Blue
			21w	White
			21ya	Yellow
			21yb	Yellow
Fragment of balsamar	2nd century B.C.	Adria – cemetery of Canal Bianco	22b	Blue
			22ya	Yellow
			22yb	Yellow

7.3. Analytical approach and findings

Table 7.3 reports the elemental analysis data of the samples by LA-ICP-MS. The table presents the contents of 54 elemental oxides analyzed in the samples (LA-ICP-MS operating conditions are given in Table 7.2), although most of them will be not taken in consideration for this discussion and are presented here for future comparison.

Reduced composition values were calculated with the procedure explained in Chapter 2. The subtracted oxides were Fe, Co, Cu, Sn, Sb and Pb. Iron oxide was not subtracted for the white and turquoise samples, whose Fe_2O_3 content (0.4-0.9 wt %) can be considered a constituent of the sands. For the blue and yellow samples, where iron oxide ranges from 1.6 to 4.1 wt %, concentrations exceeding 0.65 wt % were subtracted. In ancient glasses the Fe_2O_3 associated with the sands generally ranges from 0.3 to 1.0 wt %. So, the choice of the average value of 0.65 wt % minimizes the discrepancies between this value and the real content of iron in the sands, with negligible errors for the reduced compositions.

The Iron Age glasses investigated here present high contents of lead, iron, copper and antimony, mainly in the decorations. These oxides have a clear correlation the minerals added as chromophores and opacifiers. The values of the reduced oxides are in many cases markedly different from the original values, especially for the yellow-colored samples.

Table 7.2. LA-ICP-MS operating conditions for quantitative analysis of the glass samples.

LA	***New Wave Research UP 213***
Wavelength (nm)	213
Laser ablation chamber	Standard (New Wave Research)
Ablation mode	Continuous
Line length (mm)	0.75–1.5
Sampling events (line)	5
Beam diameter (μm)	100
Fluence (Jcm^{-2})	7.5
Repetition rate (Hz)	10
Scanning speed (μms^{-1})	5-10
Carrier gas flow rate ($L\ min^{-1}$)	0.95 (He)
Make-up flow rate ($Lmin^{-1}$)	0.75 (Ar)
ICP-MS	***Agilent 7500ce***
RF power (W)	1500
Isotopes measured	7Li, 9Be, 11B, 23Na, 24Mg, 27Al, 29Si, 31P, 39K, 43Ca,45Sc, 47Ti, 51V, 53Cr, 55Mn, 56Fe, 57Fe, 59Co, 60Ni, 63Cu,66Zn, 69Ga, 75As, 82Se, 85Rb, 88Sr, 89Y, 90Zr, 93Nb,95Mo, 107Ag, 111Cd, 115In, 118Sn, 121Sb, 137Ba, 139La, 140Ce, 141Pr, 146Nd, 147Sm, 153Eu, 157Gd, 159Tb, 163Dy, 165Ho, 166Er, 169Tm, 172Yb, 175Lu, 197Au, 208Pb, 209Bi, 232Th, 238U
Acquisition time/mass (s)	0.3 (peak hopping)
Points/mass	3
Plasma gas flow rate ($Lmin^{-1}$)	15 (Ar)
Auxillary gas flow rate ($L\ min^{-1}$)	1 (Ar)

7.3.1. Sand and flux composition

High levels of Na, together with low K, Mg and P oxides, show that all the finds were produced with an inorganic sodic flux, probably natron. This is in agreement with the other analytical studies of Iron Age glass samples (Hartmann *et al*., 1997; Gratuze and Billaud, 2003; Gratuze and Lorenzi, 2006; Towle and Henderson, 2007; Zorn and Brill, 2007; Gratuze, 2009; Reade *et al*., 2009; Shortland and Schroeder, 2009; Arletti *et al*., 2010, 2011). Reduced values for all the elements concerning investigation and comparison of the sands have been considered. The results obtained for the analysis of the siliceous sands used to make the glass vessels from Adria have been compared, through the values of some reduced oxides, with the glass vessels from the Black Sea coast of the 5th century BC (Shortland and Schroeder, 2009) and with the ones from two Etruscan sites in Northern Italy (Bologna and Spina, ca. 50 km from Adria) dating from the first half of the 6th century BC to the 3rd century BC (Arletti *et al*., 2010, 2011). For the sake of simplicity, in the remainder of the text data from these references will simply be referred to as Shortland and Arletti data. Reduced composition calculations were also carried out on the Shortland and Arletti data in order to compare their samples with the ones of the present study regarding the characterization of sands and fluxes.

All the samples analyzed are soda-lime-silica glasses, with potash and magnesia contents below 1.5 wt %. According to Sayre and Smith (1961), Freestone (2006) and Reade *et al*. (2009), they may be classified as low-magnesia-low potash (LMLK) glasses (Figure 7.2a). The bivariate plot of P_2O_5 vs. MgO (Figure 7.2b) shows a good distinction of the samples of the three periods (5th, 3rd and 2nd century BC, corresponding to Mediterranean I, II and III Groups, respectively) in separate clusters, suggesting different compositions of the sands used and hence their different provenances.

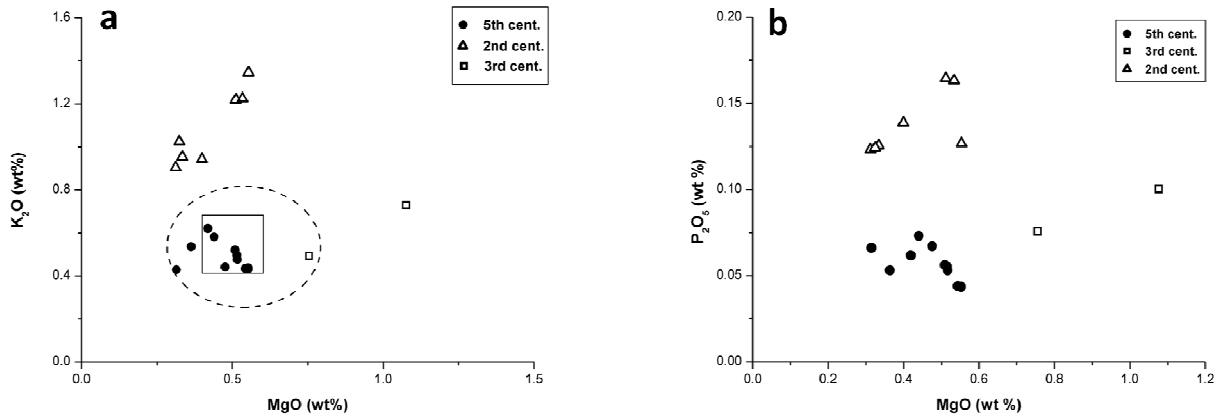

Figure 7.2. Magnesia vs. potash in the glass samples, in comparison with the data of Shortland and Schroeder, 2009 (rectangle) and Arletti *et. al*., 2010, 2001 (ellipse) (a); P_2O_5 vs. MgO for the samples under investigation (b). Reduced compositions.

All the samples exhibit a low content (<0.20 wt %) of phosphorus oxide, besides the above cited low potash and magnesia. These features are typical of glasses made with natron as fluxing agent (Shortland *et al.*, 2006b). All the samples show also very low Mn oxide content (<0.1% wt), with some differences between the average contents for the three Groups. Figure 7.3 shows that the amount of alumina and lime is extended in wide ranges (1.4-2.4 wt % and 3.1-10.6 wt %, respectively). The 5th century BC samples appear restricted in a tight cluster.

In both the plots of Figures 7.2b and 7.3, 5th century BC data match well with the ones published by Shortland and Schroeder samples (Shortland and Schroeder, 2009), and fall inside the larger cluster of Arletti samples (Arletti *et al*., 2010, 2011), dating from 6th to 4th century BC. The 2nd and 3rd century BC samples show a wider distribution, mainly due to their lower alumina content. From this plot a separation of the three compositional groups is evident. In particular the white decoration of the 3rd century BC sample presents a content of calcium oxide (7.6 wt %) which is significantly different from the blue body (~10.6 wt %). This might be an indication of the different provenances between the glass decoration and the blue bulk, without excluding the hypothesis of the use of colored glass ingots imported from different primary glass producers (Henderson *et al*., 2010).

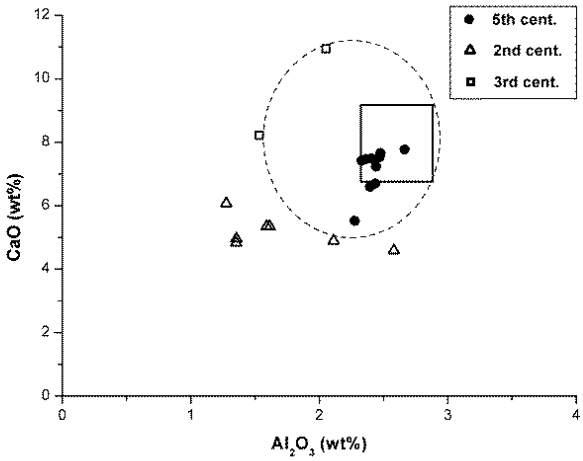

Figure 7.3. Alumina vs. lime data compared with data by Shortland and Schroeder, 2009 (rectangle) and Arletti *et. al*., 2010, 2001 (ellipse). Reduced compositions.

Samples from the 5th century BC present lower titanium oxide values (<0.1 wt %) than the samples of the 3rd and 2nd century BC, where TiO_2 ranges from 0.13 to 0.19 wt %. In general, glasses produced in these periods and from 100 BC to 300 AD (Aerts *et al*., 2003) show a low content of TiO_2.

A flawless separation of the samples from the three different periods results also from the plots of ZrO_2 vs. SrO (Figure 7.4a) and BaO vs. SrO (not reported here). The BaO content is associated with feldspathic minerals present in the sands (Fischer and Puchelt, 1969; Silvestri, 2008). It should be noted that the 5th century BC data result in tight and well-separated clusters, with a good overlap with Shortland's data.

The 5th century BC samples have high SrO (>400 ppm) and low ZrO_2 (<52 ppm) contents, while samples of the 2nd century BC show high ZrO_2 (>190 ppm) and low SrO (<200 ppm) contents with a good linear correlation. Samples from the 3rd century BC present intermediate values for these oxides (SrO, ~300 ppm; ZrO_2, ~100 ppm). SrO in ancient glass is mainly associated with the lime bearing material, such as shells, limestone or plant ash. It has been demonstrated that natron has no significant influence on the SrO content in glass (Freestone *et al*., 2003). It is known that calcium substitution by strontium ions is easier in the structure of aragonite than calcite (Mirti *et al*., 2008). Glass produced using Mediterranean coastal sand has typically low ZrO_2 (<100 ppm) and high SrO (>300 ppm) contents, due to the aragonite of the shells in beach sand (Wedepohl and Baumann, 2000; Freestone *et al*., 2003; Mirti *et al*., 2008; Dungworth *et al*., 2009). Glass made from inland sand, containing calcium carbonate derived from limestone, consists of less SrO (<200 ppm) but more ZrO_2 (>150 ppm) (Freestone *et al*., 2000; Silvestri *et al*., 2008).

Data in Figure 7.4a seem to indicate a coastal origin for the sands from the 5th century BC samples, similar to Shortland's samples, and continental sands from the 2nd century BC samples. Samples from the

3th century can be considered to be border-line between coastal and continental sands, with a lower content of BaO (feldspathic minerals).

Figure 7.4b shows a linear correlation between SrO and CaO with different slopes for samples from the 5th and 2nd century BC, in agreement with the previous results. In particular, the yellow samples from the 2nd century BC contain besides low SrO levels also very low CaO levels.

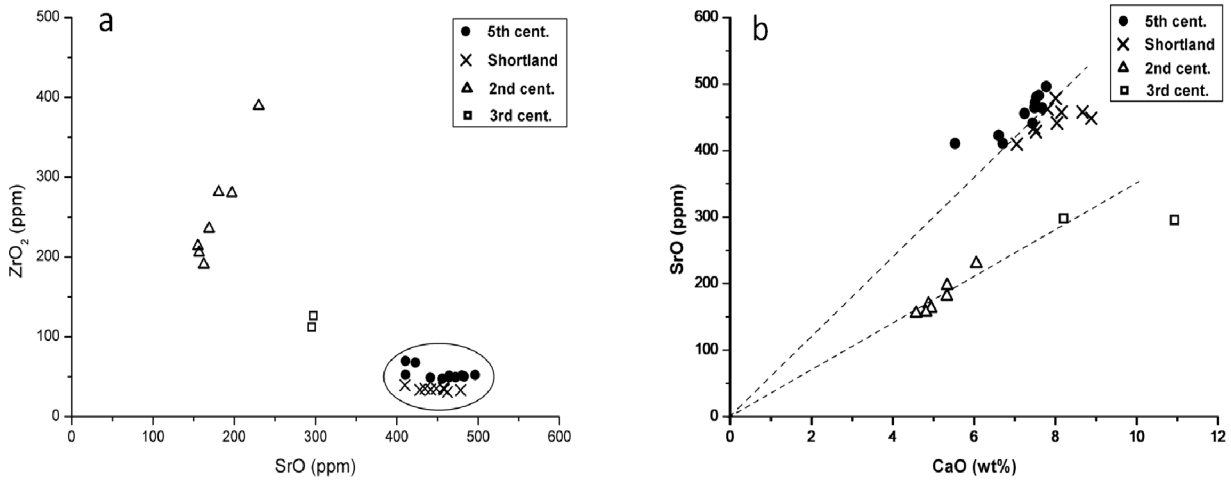

Figure 7.4. SrO vs. ZrO_2 in comparison with the data of Shortland and Schroeder (2009) (a); SrO vs. lime in comparison with the data of Shortland and Schroeder (2009) (b); reduced compositions.

7.3.2. Statistical analysis

Hierarchical clustering of all the glass samples was performed taking into account the reduced concentrations for a set of oxides coming mainly from the sands: Be, B, Mg, Si, P, K, Ca, Ga, Rb, Sr, Y, Ba.

The results in Figure 7.5 show at least two well-separated clusters and maybe three clusters, corresponding to the periods of production of the glass samples, viz. 2nd, 3rd and 5th century. As a countercheck, two other cluster analyses were performed on subsets of the major and minor elements (Mg, Al, Si, P, K, Ca) and of the trace elements (Be, B, Ga, Rb, Sr, Y, Zr, Ba). These cluster analyses gave analogous subdivisions of the samples. This analysis is in agreement with the bivariate ones discussed above and gives a strong indication of the different provenances of the sands used for the three types of glasses. The minor and trace element contents associated with the sands show a good differentiation based on the three periods of glass production, strongly indicating different production sites, at least of the raw glasses, for Mediterranean I, II and III samples studied here. The very limited number of samples does not allow to generalize, but this is the first time that samples from the 2nd century BC are compared with ones of the other two periods. The results might be indicative of a change in raw material sources for glassmaking during the Iron Age, while the glass working techniques and esthetic features seem to have remained largely unchanged.

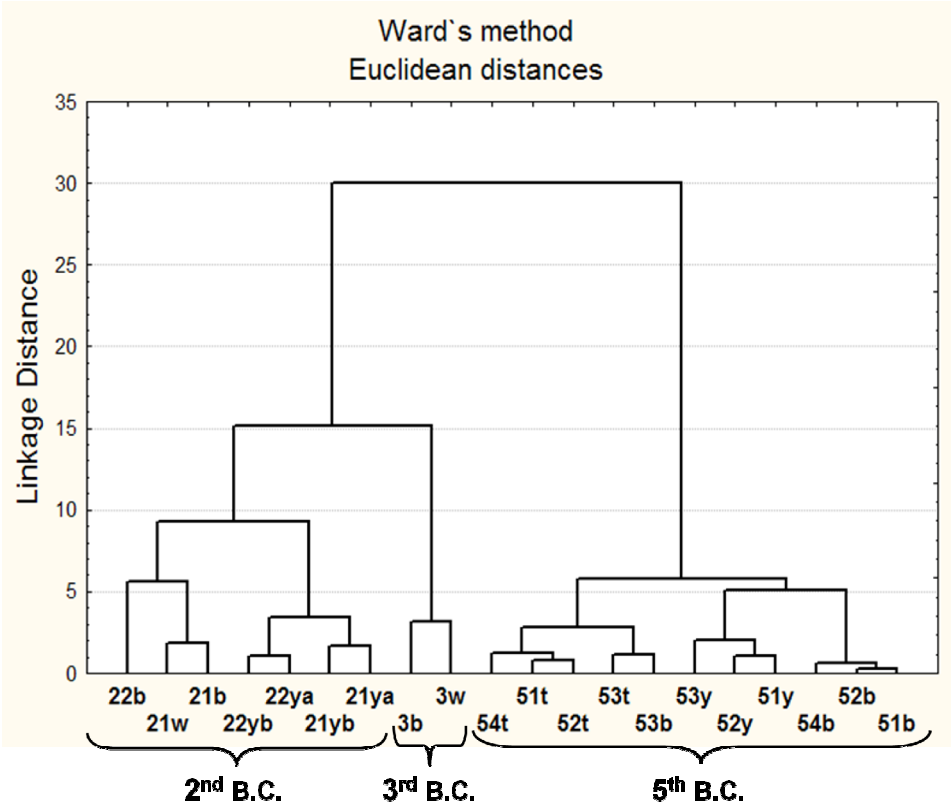

Figure 7.5. Cluster analysis for the samples under investigation, performed on some major, minor and trace elements associated with the sands; reduced compositions.

7.3.3. Chromophores and opacifiers

Blue body glasses. The ground body color of the vessels is a translucent blue that seems opaque due to the presence of bubbles and devitrification crystals. The color is caused by the presence of cobalt, a very powerful colorant.

Several previous studies investigated the nature and origin of the cobalt minerals used to obtain deep blue glass. They were based on analysis of the elements associated with cobalt, such as Al, Cu, Mn, Fe, Ni, Zn, As, Sb and Pb (Gratuze *et al*., 1992; Soulier *et al*., 1994; Gratuze, 1997; Towle *et al*., 2001; Rehren, 2001; Reade *et al*., 2005; Shortland *et al*., 2006a; Gratuze and Picon, 2006). The correlations between heavy metal oxides and CoO do not offer straightforward answers about the origin of the cobalt sources. The blue samples in this study contain CoO concentrations in the range from 0.077 to 0.026 wt % and significant contents of Fe, Cu and Zn oxides.

For the cobalt-based blue samples in this work the Al and Mg contents are on the same or lower level than in the cobalt-free samples, excluding the use of cobaltiferous alums as a source of cobalt (Lilyquist *et al*., 1993; Shortland and Tite, 2000; Rehren, 2001; Tite and Shortland, 2003; Gratuze, 2006; Gratuze and Picon, 2006; Walton *et al*., 2009), in agreement with Arletti *et al*. (2011). The absence of any correlation between Co and Sb, and the very low levels of Mn, As and Ni oxides in all the blue samples (except for Ni in the only blue sample from Group II), also seems to exclude the use of cobalt sources containing manganese or antimony, as reported for other Iron Age glasses (Nicholson and Henderson, 2000; Arletti *et al*., 2011), and arsenic-nickel cobalt ore (Gratuze *et al*., 1992). In the blue samples from the 5th century BC (Group I) cobalt appears to be correlated with copper (R^2 = 0.97) and zinc (R^2 = 0.94) (Figure 7.6) and less so with iron (R^2 = 0.74). Iron is usually present in ancient glass as a natural component of sand when it is less than 1 wt % (Caley, 1962; Mirti *et al*., 1993, 2008; Henderson *et al*., 2004). Fe_2O_3 in the blue samples ranges from 1.6

to 2.3% wt, while only one among seventeen Arletti's Mediterranean I and II blue vessel samples showed an iron content over 1.1%. It seems reasonable to assume that most of the iron is associated with a cobalt-bearing ore. Some inclusions containing all these four elements, with very high iron oxide content (50-95 % wt oxide), were found by SEM-EDS.

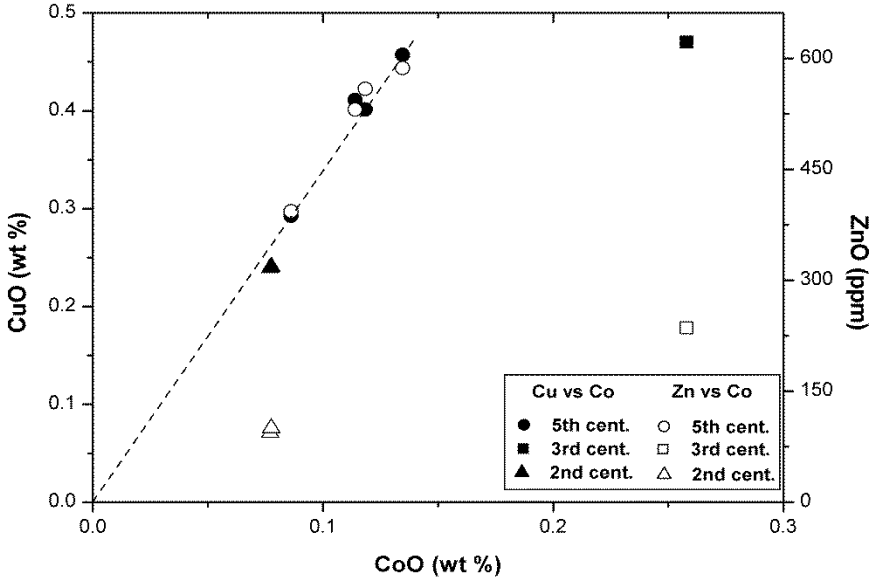

Figure 7.6. CuO and ZnO vs. CoO for the samples under investigation.

It is worth to note that the good linear correlation between copper and zinc (R^2 = 0.94) with a Cu/Zn ratio of about 7.5, for the blue samples of Group I, is consistent with an addition of copper in the form of brass (Pollard and Heron, 2008, pp. 197-201). This Cu/Zn ratio, together with the very high correlation between Co and Cu, could indicate that cobalt ingots (Henderson *et al*., 2010) were produced adding cobalt ore with scraps of brass to the batch. The copper addition could have been made to vary the hue of the blue color (Shortland and Schroeder, 2009). For the blue samples of Group I the addition as a colorant in the form of an ore or combination of ores containing Co, Fe, Zn and/or Cu may be the most reliable hypothesis, especially since various metal sulfides are often associated with natural deposits.

Since only two blue samples can be linked to the 2nd century BC (Group III) and only one from the 3rd century BC (Group II), one cannot give conclusive evidence about their cobalt sources. Just like all other samples the blue samples show significant amount of Cu, Fe, Zn and Co (~0.08 wt %). The blue sample from the 3rd century BC presents the highest Co, Cu, Fe, Ti, Cr Sc and V levels, whereas the amount of Ni is much higher than in the other blue samples. Zn amounts for Groups II and III are considerably lower than for Group I.

The ratios between Co, Cu, Zn and Fe are different for the three Groups, except for the Co/Cu ratio which is similar for Groups I and III and the Cu/Zn ratio which is the similar for Groups II and III, but three times higher than for Group I. Unfortunately, the lack of data about zinc for Arletti's blue vessels and the absence of numerical data about Shortland's blue vessels did not allow any comparison with the data in this work. In summary, the above results suggest different provenances of the cobalt ores for the three different Groups of glasses, in agreement with the different provenances of the sands.

Yellow, turquoise and white decorations. The opaque white, turquoise and yellow glass decorations contain opacifiers based on antimony, whose oxide ranges between 2 and 6 wt %. Opacity is due to the presence of

a dispersion of crystals in a translucent glass matrix (Nicholson and Henderson, 2000) (Figure 7.7). White calcium antimonate and yellow lead antimonate are well-known opacifiers in ancient glass used from the beginning of glass production in the Near East and Egypt around 1500 BC (Tite *et al*., 2008). Yellow decorations are present on the vessels from the 5th and 2nd century BC (Groups I and III, respectively). For each one of the two vessels of the Group III, two different yellow decorative filaments were analyzed (samples 21ya, 21yb and 22ya, 22yb, respectively) for comparison purposes, since they seemed to present different hues of yellow at a visual inspection.

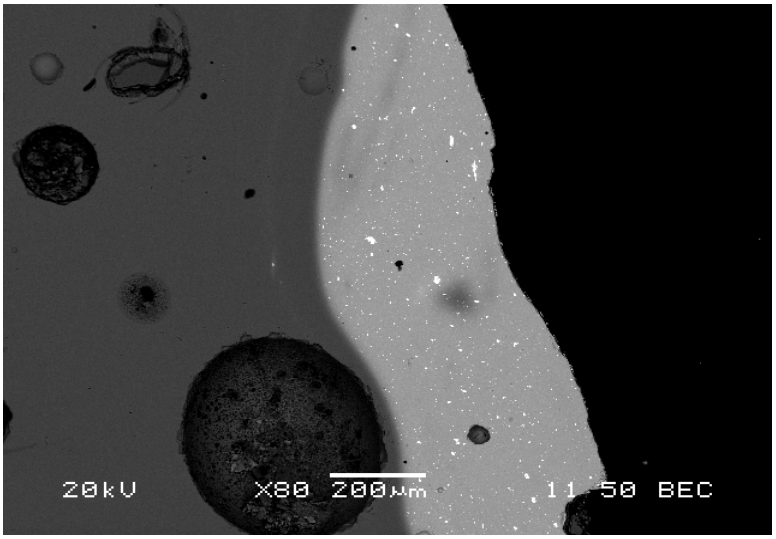

Figure 7.7. SEM/BSE image of the yellow decoration (with crystalline aggregates) and the blue bulk (with bubbles) of sample 51.

Lead antimonate, $Pb_2Sb_2O_7$, acts as chromophore and opacifier in the yellow glasses, as indicated by the high contents of PbO and Sb_2O_5. The PbO/Sb_2O_5 ratios varies in the ranges 7.1-10.6 and 7.2-7.7 wt % for Groups I and III, respectively, although they do not follow the lead antimonate stoichiometry.

Pb was probably added in excess to obtain lead antimonate crystals by cooling the melting mass at a temperature below 850^{o} C (Shortland, 2002). As for the blue samples, it is rather difficult to state the origin of the significant presence of iron oxide in the yellow samples of Groups I (1.4-1.8 wt %) and III (3.4-4.0 wt %). Fe oxide shows good correlations with both Sb and Pb oxides for both the Groups, but with different slopes and intercepts. These results suggest the addition of ores with different Pb-Sb-Fe stoichiometries for the yellow decorations of Groups I and III. The opacity of the turquoise and white glasses, where the Sb_2O_5 level is higher than 1.5 wt %, is due to the presence of calcium antimonate crystals ($Ca_2Sb_2O_7$ or $Ca_2Sb_2O_6$). Nicholson and Henderson (2000), with reference to Egyptian Bronze Age core forming glass, hypothesized that to produce an opaque turquoise glass, antimony was added to a translucent turquoise glass. The color of the turquoise samples (Group I) was obtained by a mixture of aquamarine blue CuO (2.5-3.6 wt %), and white calcium antimonate, with a possible minor contribution of yellow lead antimonate. SEM analysis detected lead antimonate crystals, which could contribute to the turquoise color with a light yellow component. The absence of significant correlations between CuO and other elements did not allow any hypothetical claim about the copper source for the turquoise samples. The turquoise glasses from Group I contain also ~2 wt % of lead oxide, much higher than in the blue samples (<0.30 wt %). It appears likely that lead addition at this level in the turquoise glasses was intentional. Arletti *et al*. (2008, 2010) ascribe the addition of lead to a possible purpose of improving the fluidity of the melt. This could favor the application of glass decorations on the vessel body, but the lead contents in Arletti's turquoise vessels are randomly distributed over a wide range (0.05-2.03 wt %), associated with samples dating from the first half of the 6th

to the 3rd century BC. In the turquoise samples of this study antimony is present together with comparable amounts of lead (Pb/Sb = 1.25-1.57).

Addition of lead antimonate such as bindheimite or some ores containing sulfides such as stibnite (Sb_2S_3) or galena (PbS) could explain these results. Low levels of lead oxide are also present in the blue glasses (<0.30 wt %), similar to levels reported for other Iron Age glasses (Arletti *et al*., 2010). It is difficult to state whether the lead entered the batch with the cobalt ore or was added intentionally.

7.4. Conclusions

The vessels investigated in this chapter, assigned to the so-called Mediterranean Groups I, II and III, were made from soda-lime-silica glass, in agreement with the ones of the same age reported in the literature. The close similarity of the 5th century BC glasses with the ones coming from the Black Sea analyzed by Shortland and Schroeder (2009) supports the hypothesis of their origin from Rhodes island, which was probably the major production center in the Aegean Sea of the Mediterranean Group I glass vessels. The siliceous sands used to make these glasses appear to be of coastal origin with a composition similar to the ones of the Roman glasses from the first Imperial Era.

The bivariate and multivariate analyses of a wide set of major, minor and trace reduced oxides associated with the sands gave a strong indication of the different provenances of the sands of the three sets of vessels, i.e. from the 5th, 3rd and 2nd century BC, archaeologically classified as Mediterranean Groups I, II and III, respectively. The glasses of Groups I and III were made with coastal and inland sands respectively, while the ones from Group II appear of uncertain origin.

Although the number of the samples in this study is very limited, the analytical results constitute a first comparison of the three different Mediterranean Groups of vessels, previously classified on the basis of stylistic considerations only. This seems to indicate three differently located glassmaking traditions along the Mediterranean Iron Age, although the majority of the vessels of the Mediterranean Groups present clear typological and esthetic similarities. Only further analytical studies on larger sets of vessels from the three periods, performed on a set of elements mainly associated with the sands, may strengthen the hypotheses here presented. The contents of heavy metal oxides, such as cobalt, iron, antimony, copper and zinc found in the samples of the three periods, seem to indicate that different ores have been added as chromophores and opacifiers, although the nature appears rather difficult to interpret.

Table 7.3. Chemical composition of the bulk samples (in wt.% of the major and minor oxides and in μg g^{-1} of the trace elemental oxides); the mean and standard deviation for 5 measurements is given.

Sample	Na_2O	MgO	Al_2O_3	SiO_2	P_2O_5	K_2O	CaO	TiO_2	MnO	Fe_2O_3	CoO	CuO	Sb_2O_5	PbO
	wt.%	wt.%	wt.%	wt.%	wt.%	wt.%	wt.%	wt.%	wt.%	wt.%	wt.%	wt.%	wt.%	wt.%
51b	17.9	0.5	2.4	68.6	0.0	0.4	7.5	0.1	0.01	1.7	0.12	0.4	0.0	0.1
52b	18.0	0.5	2.4	68.2	0.0	0.4	7.4	0.1	0.01	1.6	0.11	0.4	0.0	0.0
53b	16.9	0.4	2.4	69.5	0.1	0.6	7.1	0.1	0.01	2.0	0.09	0.3	0.2	0.3
54b	17.4	0.5	2.4	68.9	0.0	0.4	7.3	0.1	0.01	1.9	0.13	0.5	0.0	0.2
52t	16.4	0.5	2.2	63.3	0.1	0.5	6.8	0.1	0.01	0.6	0.00	3.0	3.5	2.2
51t	16.8	0.5	2.4	62.9	0.1	0.4	7.0	0.1	0.01	0.5	0.00	2.7	4.2	2.1
53t	17.1	0.4	2.1	64.2	0.1	0.5	6.8	0.1	0.01	0.4	0.00	3.6	3.0	1.9
54t	16.5	0.5	2.2	64.2	0.0	0.4	6.9	0.1	0.01	0.5	0.00	2.5	3.3	1.9
51y	10.7	0.3	1.6	48.1	0.0	0.3	4.4	0.1	0.01	1.8	0.00	0.1	4.0	28.9
52y	10.4	0.2	1.6	47.3	0.0	0.3	4.3	0.1	0.01	1.9	0.00	0.1	3.6	29.6
53y	13.8	0.3	1.8	59.4	0.0	0.4	4.5	0.1	0.01	1.4	0.00	0.1	1.5	16.2
3b	15.1	1.0	2.0	66.7	0.1	0.7	10.6	0.2	0.04	2.3	0.26	0.5	0.0	0.2
3w	17.5	0.7	1.4	64.4	0.1	0.5	7.6	0.1	0.02	0.9	0.03	0.1	6.5	0.0
2b1	15.3	0.5	1.6	73.6	0.2	1.2	5.3	0.1	0.02	1.6	0.08	0.2	0.0	0.0
2b2	16.4	0.5	1.6	70.6	0.2	1.2	5.3	0.1	0.02	1.6	0.08	0.2	0.0	0.0
21ya	10.2	0.2	1.7	50.9	0.1	0.6	3.1	0.1	0.01	4.1	0.01	0.1	3.4	25.2
21yb	11.0	0.3	1.6	55.8	0.1	0.7	3.6	0.1	0.01	3.4	0.02	0.1	2.7	20.5
22ya	10.2	0.2	0.9	51.0	0.1	0.6	3.3	0.1	0.01	3.8	0.00	0.1	3.4	26.2
22yb	10.3	0.2	0.9	48.9	0.1	0.7	3.1	0.1	0.01	4.0	0.01	0.1	3.8	27.7
21w	15.5	0.5	1.2	70.5	0.1	1.3	5.8	0.2	0.01	0.8	0.00	0.0	3.8	0.0

Sample	Li_2O	BeO	B_2O_3	Sc_2O_3	V_2O_5	Cr_2O_3	CoO	NiO	ZnO	Ga_2O_3	As_2O_5	SeO_2	Rb_2O	SrO	Y_2O_3	ZrO_2	Nb_2O_5	MoO_3	Ag_2O	CdO	In_2O_3	SnO_2
	µg/g	µg/g	µg/g	µg/g	µg/g	µg/g	µg/g	µg/g	µg/g	µg/g	µg/g	µg/g	µg/g	µg/g	µg/g	µg/g	µg/g	µg/g	µg/g	µg/g	µg/g	µg/g
51b	6.5	0.7	207	2.5	12.5	12.7	1184	10.8	559	19.9	23.5	14.7	7.9	455.6	9.0	50.1	1.7	1.1	4.2	0.3	1.3	4.0
52b	6.3	0.7	208	2.5	12.5	12.1	1139	10.7	531	19.7	23.4	13.9	7.9	473.8	8.9	49.5	1.7	1.0	4.3	0.3	1.3	4.1
53b	6.5	0.6	233	2.2	10.8	11.8	862	8.5	393	17.9	17.8	11.9	10.6	444.8	8.2	46.4	1.7	1.3	1.3	0.2	1.1	13.0
54b	5.2	0.6	203	2.7	12.5	11.7	1345	11.9	587	20.7	25.1	11.8	7.8	469.1	9.0	50.3	1.7	1.0	2.2	0.2	1.4	12.2
52t	5.8	0.6	159	2.2	11.4	12.0	37	19.0	29	5.7	134.8	14.4	9.0	429.7	8.5	45.1	1.7	0.8	32.7	0.3	5.4	1521.9
51t	5.6	0.7	160	2.3	11.7	12.2	38	19.5	31	5.8	133.1	13.0	8.9	450.2	8.9	47.3	1.8	0.9	32.6	0.5	6.3	2015.2
53t	6.3	0.6	263	2.0	11.3	11.4	18	14.0	21	5.5	97.1	11.6	9.9	403.8	7.8	44.8	1.6	0.2	12.0	0.3	1.8	392.3
54t	5.2	0.6	164	2.3	14.5	11.5	48	18.1	34	5.7	194.7	9.6	8.2	264.5	6.0	45.6	1.6	0.4	56.6	0.2	5.9	1577.3
51y	4.0	0.5	121	2.4	14.5	11.3	31	9.1	26	4.2	106.8	9.8	5.5	269.0	6.3	45.6	1.5	0.4	53.7	0.5	0.1	20.3
52y	4.0	0.5	119	2.1	9.4	10.8	30	13.3	26	5.5	110.1	9.6	5.3	397.2	7.6	44.1	1.5	0.4	11.6	0.5	0.1	335.5
53y	4.9	0.6	216	3.6	19.4	15.7	6	6.3	17	4.8	51.0	15.8	7.8	220.4	7.5	42.8	4.3	0.2	2.4	0.5	0.0	1.7
3b	19.1	0.9	643	4.7	36.8	21.9	2581	366.8	236	11.8	44.0	9.8	7.7	286.8	6.9	108.9	4.2	1.5	1.2	0.2	11.6	38.9
3w	18.9	0.6	592	3.6	21.8	17.1	286	49.3	51	4.1	28.0	10.1	7.2	276.4	6.5	117.5	3.1	0.5	0.8	0.4	1.5	6.6
2b1	12.5	0.6	991	4.2	21.7	16.2	771	26.3	94	7.1	64.2	16.5	10.4	194.0	8.1	275.6	3.8	3.0	1.4	0.2	1.3	8.7
2b2	12.4	0.7	984	4.1	21.7	15.9	775	24.3	95	71.1	64.5	16.5	10.3	195.0	8.1	276.8	3.8	3.0	1.2	0.2	1.3	8.6
21ya	6.8	1.0	429	3.8	19.0	17.4	79	11.1	49	4.1	137.4	12.0	6.4	104.9	8.1	144.4	4.2	0.6	54.0	0.7	0.3	54.5
21yb	8.0	0.9	560	3.6	19.0	15.8	235	14.0	64	4.5	116.9	12.5	7.0	124.5	8.0	173.5	3.5	1.1	54.1	0.8	0.6	43.2
22ya	7.4	0.7	430	2.9	15.4	10.5	15	8.3	40	2.5	125.8	12.1	6.2	108.8	7.1	127.7	2.4	0.3	69.5	0.6	0.2	55.1
22yb	6.6	0.9	403	2.7	15.1	9.9	55	8.6	41	2.5	136.6	11.4	6.0	101.6	7.3	133.1	2.3	0.5	49.5	0.6	0.3	58.1
21w	13.7	0.5	1010	3.6	19.4	15.7	6	6.3	45	3.7	51.0	15.8	9.9	220.4	7.5	373.0	4.3	1.0	2.4	0.3	0.0	1.7

Sample	BaO	La_2O_3	Ce_2O	Pr_2O_3	Nd_2O_3	Sm_2O_3	Eu_2O_3	Gd_2O_3	Tb_2O_3	Dy_2O_3	Ho_2O_3	Er_2O_3	Tm_2O_3	Yb_2O_3	Lu_2O_3	Au_2O_3	Bi_2O_3	ThO_2	UO_2
	µg/g	µg/g	µg/g	µg/g	µg/g	µg/g	µg/g	µg/g	µg/g	µg/g	µg/g	µg/g	µg/g	µg/g	µg/g	µg/g	µg/g	µg/g	µg/g
51b	202.0	7.5	13.8	1.8	7.5	1.5	0.5	1.4	0.2	1.4	0.3	0.8	0.1	0.7	0.1	0.1	0.1	1.0	14.1
52b	201.4	7.5	13.8	1.7	7.5	1.5	0.5	1.4	0.2	1.3	0.3	0.7	0.1	0.7	0.1	0.1	0.1	1.0	14.1
53b	222.3	6.9	12.6	1.6	6.9	1.4	0.4	1.3	0.2	1.2	0.3	0.7	0.1	0.7	0.1	0.0	0.3	0.9	1.6
54b	196.0	7.3	13.4	1.7	7.3	1.5	0.4	1.4	0.2	1.3	0.3	0.7	0.1	0.7	0.2	0.7	0.3	1.0	13.3
52t	191.6	7.2	13.2	1.6	7.2	1.4	0.4	1.4	0.2	1.3	0.3	0.7	0.1	0.7	0.1	0.8	34.0	1.0	8.0
51t	200.2	7.5	13.8	1.7	7.3	1.5	0.4	1.5	0.2	1.4	0.3	0.8	0.1	0.7	0.1	0.7	38.2	1.0	8.4
53t	214.0	6.6	11.6	1.5	6.4	1.3	0.4	1.2	0.2	1.2	0.2	0.6	0.1	0.6	0.1	0.6	1.2	0.9	1.6
54t	186.8	7.0	12.9	1.6	6.9	1.4	0.4	1.3	0.2	1.2	0.3	0.7	0.1	0.6	0.1	0.6	35.4	0.9	8.4
51y	132.2	8.5	17.4	1.6	5.9	1.1	0.3	1.0	0.2	1.0	0.2	0.5	0.1	0.5	0.1	0.1	3.7	1.0	6.0
52y	131.3	6.4	11.0	1.4	6.4	1.4	0.3	1.2	0.2	1.1	0.2	0.5	0.1	0.6	0.1	0.1	3.8	0.9	1.5
53y	163.9	8.9	17.8	1.9	7.8	1.5	0.3	1.2	0.2	1.2	0.2	0.7	0.1	0.8	0.1	0.0	0.0	2.3	1.6
3b	94.6	9.2	18.5	2.0	8.3	1.6	0.4	1.3	0.2	1.2	0.2	0.6	0.1	0.6	0.1	0.0	0.2	1.9	2.1
3w	91.0	8.2	16.2	1.8	7.4	1.5	0.3	1.2	0.2	1.0	0.2	0.6	0.1	0.6	0.1	0.0	0.1	1.8	2.4
2b1	155.1	8.8	18.2	2.0	8.3	1.6	0.4	1.4	0.2	1.2	0.3	0.7	0.1	0.8	0.1	0.0	0.1	2.1	1.6
2b2	145.5	8.9	18.2	2.0	8.4	1.6	0.4	1.4	0.2	1.3	0.3	0.7	0.1	0.7	0.1	0.0	0.1	2.2	1.6
21ya	88.5	7.5	17.3	1.8	7.6	1.6	0.4	1.5	0.2	1.3	0.3	0.7	0.1	0.7	0.1	0.1	6.3	2.0	1.0
21yb	101.6	7.3	16.4	1.8	7.3	1.6	0.3	1.5	0.2	1.3	0.3	0.7	0.1	0.6	0.1	0.1	4.9	1.9	1.2
22ya	90.7	5.9	12.5	1.4	6.3	1.4	0.3	1.3	0.2	1.2	0.2	0.6	0.1	0.6	0.1	0.1	6.1	1.5	0.9
22yb	84.9	5.8	12.4	1.4	6.2	1.4	0.3	1.4	0.2	1.2	0.2	0.6	0.1	0.6	0.1	0.1	6.7	1.5	0.9
21w	139.8	8.9	17.8	1.9	7.8	1.5	0.3	1.2	0.2	1.2	0.2	0.7	0.1	0.8	0.1	0.1	0.0	2.3	1.6

7.5. References

Aerts A., Velde B., Janssens K., Dijkman W. (2003) Change in silica sources in Roman and post-Roman glass, Spectrochim. Acta Part B 58; pp. 659-667.

Arletti R., Vezzalini G., Quartieri S., Ferrari D., Merlini M., Cotte M. (2008) Polychrome glass from Etruscan sites: first non-destructive characterization with synchrotron m-XRF, m-XANES and XRPD, Appl Phys A Mater Sci. Process., 92; pp. 127-135.

Arletti R., Maiorano C., Ferrari D., Vezzalini G., Quartieri S. (2010) The First archaeometric data on polychrome Iron Age glass from sites located in northern Italy. J. Archaeol. Sci. 37; pp. 703-712.

Arletti R., Rivi L., Ferrari D., Vezzalini G. (2011) The Mediterranean Group II: analyses of vessels from Etruscan contexts in northern Italy, J. Archaeol. Sci. 38; pp. 2094-2100.

Caley E.R. (1962) Analysis of Ancient Glasses, The Corning Museum of Glass, Corning, New York; pp. 1790-1957.

Dungworth D., Degryse P., Schneider J. (2009) Kelp in historic glass: the application of strontium isotope analysis. In: Degryse P., Henderson J., Hodgins G. (Eds.), Isotopes in Vitreous Materials, Studies in Archaeological Sciences. Leuven University Press; pp. 113-130.

Fischer K., Puchelt H. (1969) Barium. In: Wedepohl K.H. (Ed.), Handbook of Geochemistry, Elements Kr(36) to Ba(56). Springer, Berlin, 56A1.

Freestone I.C. (2006) Glass production in Late Antiquity and the early Islamic period: a geochemical perspective, geomaterials in cultural heritage. In: Maggetti M., Messiga B. (Eds.), Geological Society of London, Special Publications, vol. 207; pp. 201-216.

Freestone I.C., Gorin Rosen Y., Hughes M.J. (2000) Primary glass from Israel and the production of glass in Late Antiquity and the Early Islamic period. In: Nenna, M.D. (Ed.), La Route du Verre. Travaux de la Maison de l'Orient Méditerranéan, Lyon; pp. 65-83.

Freestone I.C., Greenwood R., Gorin-Rosen Y. (2002a) Byzantine and early Islamic glassmaking in the eastern Mediterranean: production and distribution of primary glass. In: Kordas, G. (Ed.), 1st International Conference Hyalos-Vitrum- Glass. History, Technology and Conservation of Glass in the Hellenic World, Athens; pp. 167-174.

Freestone I.C., Ponting M., Hughes M.J. (2002b) The origins of Byzantine glass from Maroni Petrera, Cyprus. Archaeometry 44; pp. 257-272.

Freestone I.C., Leslie K.A., Thirlwall M., Gorin-Rosen Y. (2003) Strontium isotopes in the investigation of early glass production Byzantine and early Islamic glass from the Near East, Archaeometry 45 pp. 19-32.

Gratuze B. (1997) L'apport des analyses de verres archéologiques: études de cas, Techne, 6: Verres-émaux e glaçures; pp. 8-18.

Gratuze B. (2006) Les premiers verres au natron retrouvés en Europe occidentale: composition chimique et chrono-typologie, Annales du 17e Congrès de l'Association Internationale pour l'Histoire du Verre (AIHV), Antwerp (Belgium) 4-10 Sep 2006.

Gratuze B. (2009) Les premiers verres au natron retrouvés en Europe occidentale: composition chimique et chrono-typologie. In: Janssens K., Degryse P., Cosyns P., Caen J., Van't dack L. (Eds.), Annales du 17eme Congres de l'Association Internationale pour l'Histoire du Verre, Antwerp; pp. 8-14.

Gratuze B. and Billaud Y. (2003) La circulation des perles en verre dans le Bassin Méditerranéen, de l'Age du Bronze moyen jusqu'au Hallstatt. In: Foy D., Nenna M.D. (Eds.), Echanges et commerce du verre dans le monde antique. Actes colloque AFAV, Aix-en-Provence et Marseille 2001, Mergoil Editor, Montagnac; pp. 11-15.

Gratuze B. and Lorenzi F. (2006) Les éléments de parure en verre du site de Lumaca (Âge du Fer, Centuri, Haute-Corse): compositions et typochronologie. Bulletin de la Société préhistorique française 103 (2); pp. 379-384.

Gratuze B., Picon M. (2006) Utilisation par l'industrie verrière des sels d'aluns des oasis égyptiennes au début du premier millénaire avant notre ère. In: Brun, J.-P. (Ed.), L'Alun de Mediterranie. Institut Français de Naples; pp. 269-276.

Gratuze B., Soulier I., Barrandon J.N., Foy D. (1992) De l'origine du cobalt dans les verres. Revue d'Archéométrie 16; pp. 97-108.

Hartmann G., Kappel I., Grote K., Arnold B. (1997) Chemistry and technology of prehistoric glass from Lower Saxony and Hesse. J. Archaeol .Sci 24; pp. 547-559.

Henderson J., McLoughlin S.D., McPhail D.S. (2004) Radical changes in Islamic glass technology: evidence for conservatism and experimentation with new glass recipes from early and middle Islamic Raqqa, Syria. Archaeometry 46; pp. 439-468.

Henderson J., Evans J., Nikita K. (2010) Isotopic evidence for the primary production, provenance and trade of Late Bronze Age glass in the Mediterranean, Mediterranean Archaeology and Archaeometry 10 (1); pp. 1-24.

Lilyquist C., Brill R.H., Wypyski M.T. (1993) Studies in Early Egyptian Glass. The Metropolitan Museum of Art, New York.

Mirti P., Casoli A., Appolonia L. (1993) Scientific analysis of Roman glass from Augusta Praetoria, Archaeometry 35; pp. 225-240.

Mirti P., Pace M., Negro Ponzi M.M., Aceto M. (2008) ICP-MS analysis of glass fragments of Parthian and Sasanian epoch from Seleucia and Veh Ardasir (Central Iraq), Archaeometry 50 (3); pp. 429-450.

Nicholson P.T. and Henderson J. (2000) Glass. In: Nicholson P.T., Shaw I. (Eds.), Ancient Egyptian Materials and Technology. Cambridge University Press; pp. 195-224.

Oikonomou Ar., Triantafyllidis P., Beltsios K., Zacharias N., Karakassides M. (2008) Raman structural study of ancient glass artifact from the island of Rhodes, J. Non-Cryst. Solids 354; pp. 768-772.

Pollard M.A. and Heron C. (2008), Archaeological Chemistry, second ed. RSC Publishing.

Reade W., Freestone I.C., Simpson St. J. (2005) Innovation or continuity? Early first millennium BCE glass in the Near East: the cobalt blue glasses from Assyrian Nimrud. Annales du 16e Congres de l'Association Internationale pour l' Histoire du Verre; pp. 23-27.

Reade W., Freestone I.C., Bourke S. (2009) Innovation and continuity in Bronze and Iron Age glass from Pella in Jordan. In: Annales du 17eme Congres de l'Association Internationale pour l'Histoire du Verre pp. 47-54.

Rehren Th. (2001) Aspects of the production of cobalt-blue glass in Egypt, Archaeometry 43; pp. 483-489.

Sayre E.V., Smith R.W. (1961) Compositional categories of ancient glass. Science 133; pp. 1824-1826.

Shortland A.J. (2002) The use and origin of antimonate colorants in early Egyptian glass, Archaeometry 44; pp. 517-530.

Shortland A.J., Schroeder H. (2009) Analysis of first millennium BC Glass vessels and beads from the Pichvnari Necropolis, Georgia, Archaeometry 51 (6); pp. 947-965.

Shortland A., Tite M. (2000) Raw materials of glass from Amarna and implications for the origins of Egyptian glass, Archaeometry 42; pp. 141-151.

Shortland A.J., Tite M.S., Ewart I. (2006a) Ancient exploitation and use of cobalt alums from the western oases of Egypt, Archaeometry 48 (1); pp. 153-168.

Shortland A., Schachner L., Freestone I., Tite M. (2006b) Natron as a flux in the early vitreous materials industry: sources, beginnings and reason for decline, J. Archaeol. Sci. 33; pp. 521-530.

Silvestri A. (2008) The coloured glass of Iulia Felix, J. Archaeol. Sci. 35; pp. 1489-1501.

Silvestri A., Molin G., Salviulo G. (2008) The colourless glass of Iulia Felix, J. Archaeol. Sci. 35; pp. 331-341.

Soulier I., Gratuze B., Barrandon J.N. (1994) The Origin of Cobalt Blue Pigments in French Glass from the Bronze Age to the Eighteenth Century. In: Archaeometry 94: Proceedings of the 29th International Symposium on Archaeometry, Ankara; pp. 97-108.

Tite M., Shortland A. (2003) Production technology for copper and cobalt blue vitreous materials from the New Kingdom site of Amarna e a reappraisal, Archaeometry 45; pp. 285-312.

Tite M., Pradell T., Shortland A. (2008) Discovery, production and use of tin based opacifiers in glasses, enamels and glazes from the Late Iron Age onwards: a reassessment, Archaeometry 50; pp. 67-84.

Towle A., Henderson J. (2007) The glass bead game: archaeometric evidence for the existence of an Etruscan glass industry. Etruscan studies, Journal of the Etruscan Foundation 10; pp. 47-66.

Towle A., Henderson J., Bellintani P., Gambacurta G. (2001) Frattesina and Adria: Report of Scientific Analyses of Early Glass from the Veneto, in PADUSA, Bollettino del Centro Polesano di studi storici, archeologici ed etnografici; anno XXXVII Rovigo; pp. 7-57.

Walton M.S., Shortland A., Kirk S., Degryse P. (2009) Evidence for the trade of Mesopotamian and Egyptian glass to Mycenaean Greece, J. Archaeol. Sci. 36; pp. 1496-1503.

Wedepohl K.H., Baumann A. (2000) The use of marine molluscan shells in the Roman glass and local raw glass production in the Eifel area (Western Germany), Naturwissenschaften 87; pp. 129-132.

Zorn J.R., Brill R.H. (2007) Iron Age, glass from Tel Dor, Israel (notes). J. Glass Stud. 49; pp. 256-259.

CHAPTER 8

CONCLUSIONS

8.1. Conclusions

The investigations presented within this thesis provide new insights into the development and application of LA-ICP-MS in the study of glass. Laser ablation ICP-MS can be used in different modes with the aim to investigate diverse aspects of a sample (surface degradation, bulk chemical composition, inclusions, diverse compositional layers, etc.). Different analytical parameters (detection modes, data acquisition, uptake time, analytical time, laser repetition rate, number of analytical menus, etc.) and their application have been discussed. The major conclusions that can be drawn from these studies are as follow:

- LA-ICP-MS operated in drilling mode with a low and/or a high repetition rate can generate depth profiles with quantitative elemental information for all the compositional layers of a glass sample. In spite of the fact that corrosion can be deeper than a few micrometers, laser ablation operating in drilling mode is a useful tool to obtain the pristine glass composition with minimal damage to the artifact. Nevertheless, so far it is difficult to perform depth calibration of the depth profiles due to different ablation characteristics of degraded glasses compared to standard glasses. More work is needed to further understand the relationship between laser sampling conditions (for depth profiling) and the associated ablation rate for corroded glasses comprising pure glass structures and "gel" layers.

- To get insight into the relationship between laser efficiency and glass density, a novel procedure to indirectly measure the volumetric mass density along the glass depth for high-silica content glasses was demonstrated. Volumetric mass density measurements relating the wt% and vol% elemental concentration depth profiles, allow to measure the density of the alteration layers, a property normally not easily retrieved.

- Operating laser ablation in line scanning mode (or with more complicated patterns as "raster") for elemental image mapping, can be useful to retrieve detailed elemental correlations on the glass surface. A computational-experimental strategy was used with the help of virtual mapping software to obtain the best image in the shortest analysis time and the highest spatial resolution. Using these virtually optimized parameters we are able to predict LA-ICP-MS conditions for optimal 2D elemental image mapping. When set up properly this process should take no longer than ca. one hour but might save many hours of analysis time or even prevent one from choosing the wrong LA-ICP-MS parameters; one should also be aware that the mapping process cannot be repeated again on the same glass surface, and therefore choosing optimal parameters in advance is particularly valuable.

- Elemental mapping can contribute to the overall information retrieval on elemental distribution and homogeneity in the glass surface to gain insight into the presence of chromophores, opacifiers and their associated ores in an easy way, i.e. by visual inspection of the maps.

- Laser drilling on a virtual grid on the surface of a glass sample can be used to generate 3D maps. The processing and manipulation of the recorded 4D data (3D spatial + concentration) to construct 3D images with elemental concentration information required the development of several software routines to address *i*) integration of elemental peak areas related to individual pulses, *ii*) quantification of the peak areas in elemental oxide concentrations based on a sum normalization

procedure and *iii*) extraction of 2D elemental depth maps to be visualized as 3D images with 4D rendering.
The application of multi-elemental 3D mapping to investigate the elemental distribution in glass, can be suitable to study corrosion mechanisms to prevent glass deterioration.

- Finally, the potential of LA-ICP-MS for archaeometric research was presented among different samples from diverse contexts: buried glass vessels, smalt pigment in paintings and contemporary industrial glasses (Appendix 3). The versatility of this technique combined with other techniques as SEM-EDX allows to achieve meaningful information in glass investigations.

- On-going developments in the field of LA-ICP-MS such as its application for isotope ratio analysis with MC-ICP-MS instruments and the use of fs lasers for reduction of interferences are expected to lead to even faster adoption in the fields of archaeology, biology and forensics.

Figure 8.1 summarizes the sequence of steps in the glass investigation, from the choice of the analytical mode to the interpretation of the data.

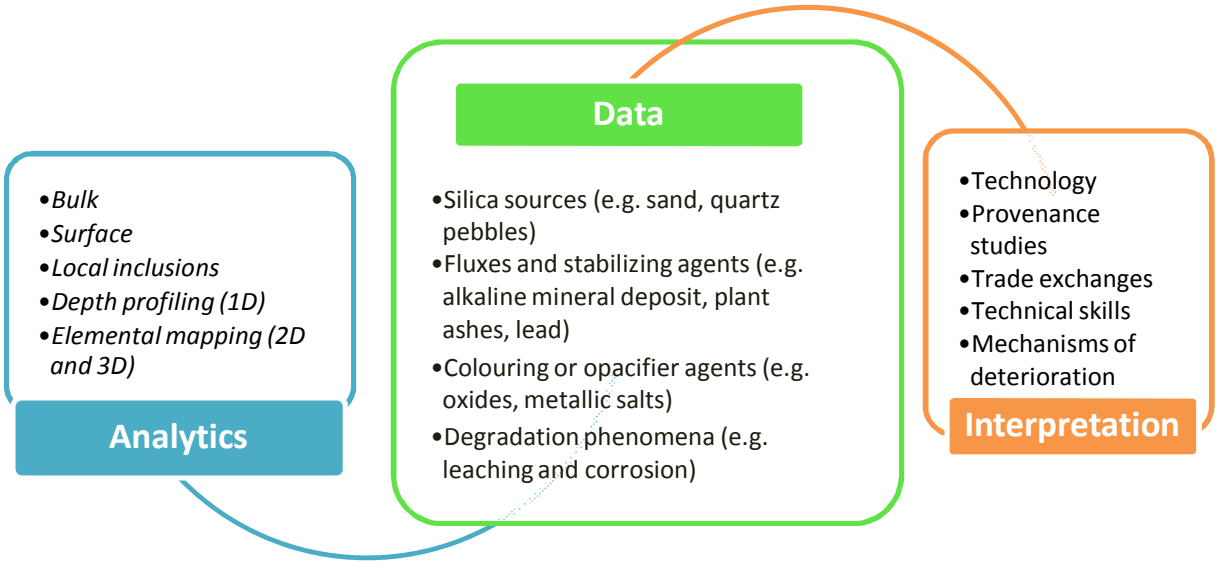

Figure 8.1. Schematic illustration of the "problem setting" using LA-ICP-MS for degraded glass analysis.

CHAPTER 9
APPENDICES

Appendix 1: Investigation of Medieval Glass from Sicily by UV-Vis Reflectance Spectroscopy♦

1.1 Introduction

Several medieval and post-medieval glass fragments from the Southwestern Sicily were analyzed by ICP-MS with laser ablation solid sampling and UV-Vis Reflectance Spectroscopy (elemental analysis results are summarized below). The samples originate from the excavation of a dump found in the Castle of Poggio Diana and from an excavation campaign at the archaeological site of Castello Nuovo of Sciacca, both built from the end of the 14th century.

Poggio Diana Castle samples. The elemental analysis data show that the glass samples were produced using sodic vegetable ashes as fluxing agents (see Table 2.1), except for one potassic glass. In order to recognize the silica sources, focusing on the contents of alumina and other oxides, different groups have been identified. The blue-colored glass samples seem to have a Venetian origin and can be dated after the second half of 16th century. They also present an anomalous content of lead and tin, similar to enamelled glass (Panighello *et al*., 2013).

Castello Nuovo of Sciacca samples. The elemental analysis data show that all the glass samples are soda-lime silica glasses, except for a potassic one and four mixed alkali glasses. Al and Ba data, together with trace elemental data, seem to indicate the use of different sands for preparing glasses (see Table 2.2). These differences could be related to the use of diverse glassmaker recipes, to the trading of different raw materials for glass making and/or to the import of glass artifacts from other countries, like Venice, Tuscany and Northern Europe (Orsega *et al*., 2013).

An in-depth analysis of the data for both archaeological sites is still in progress in order to get a clearer insight into the production of glass and the evolution of the use of raw materials in the Southwestern Sicily.

In this Appendix only UV-VIS reflectance spectroscopy analysis for glass chromophores identification will be presented.

1.2 UV-Vis spectra

The color of glass is determined by the oxidation state and electronic configuration of the associated ions or compounds (Weyl, 1953; Nassau, 1983). In Table 2.3 the coloring effects of different metal ions and compounds under different redox melting conditions are listed. The most representative colors of the samples, ranging from purple and blue to green to yellow and colorless, were analyzed primarily by UV-VIS Reflectance Spectrophotometry. UV-VIS absorbance spectra, together with elemental analysis data from LA-ICP-MS, allowed the identification of the chromophores and highlighted the role of the transition metal ions, such as those of iron (Fe^{2+}/Fe^{3+}), cobalt (Co^{2+}) and manganese (Mn^{3+}) and of the Fe-S complex, as discussed in the following paragraphs.

As shown in the colorimetric plan of Figure 2.1 the medieval samples are mostly distributed over two quadrants, - a*, + b* (green-yellow) and - a*, - b* (blue-green). The UV-Vis absorbance spectra are useful for the identification of the chromophores, as discussed below. The detected reflectance spectra were

♦ Part of this Appendix was published in Panighello *et al*., 2013 and Orsega *et al*., 2013 and presented at the Symposium on Mediterranean Archaeology (SOMA), Florence, Italy, 1–3 March 2012.

converted into (pseudo) absorbance spectra (K/S) of Kubelka Munk (Kubelka and Munk, 1931) according to the relation:

$$K/S = \frac{(R_{N-1})^2}{2R_N}$$

where
K is the Absorption Coefficient
S is the Scattering Coefficient
R_N is the normalized reflectance in the range 0 - 1

Table 1.3. Principal chromophores and their coloring effects under different redox melting conditions.

Element/compound	*Colour*	
	Oxidizing conditions	*Reducing conditions*
Cobalt	Blue	
Copper	Aquamarine	Uncolored or red
Manganese	Violet	
Manganese (high concentration)	Black	
Iron	Yellow	Light blue
Lead antimonate	Opaque yellow	
Calcium antimonate	Opaque white	
Lead stannate	Opaque yellow	
Tin oxide	Opaque white	
Sulphur-Iron		Amber-yellow
Sulphur-Iron (high concentration)		Brown

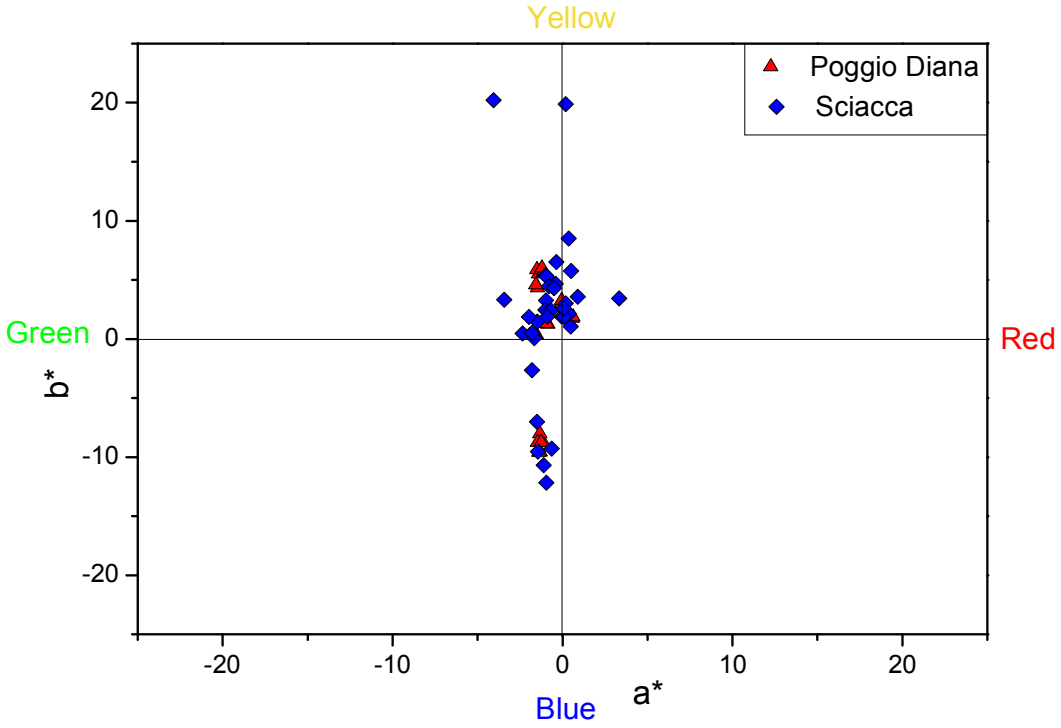

Figure 1.1. Colorimetric plane of chromaticity coordinates a*b* of all the samples from the two Medieval castles.

The blue color is due to the presence of the cobalt Co^{2+} ion. Cobalt is the most powerful colorant for glass and very low levels of cobalt oxide (tens of μg g^{-1}) are sufficient to color a glass. Elemental analysis shows that CoO ranges from 1500 to 2300 μg g^{-1} in the dark blue samples under investigation. They present the three typical absorption bands of Co^{2+} at 535, 590 and 640nm; in combination with the absorption band of Mn^{2+} at about 490nm, the blue glass gets a violet hue (Figure 2.2).

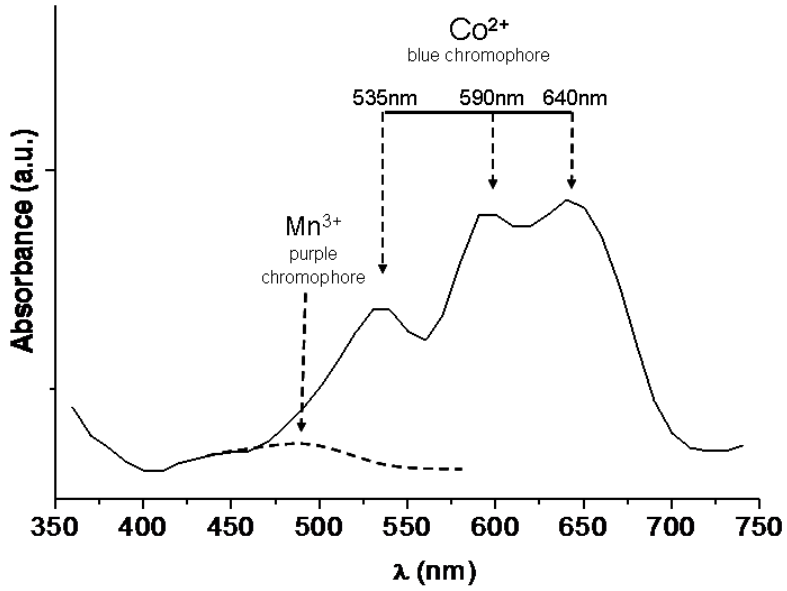

Figure 1.2. UV-Vis absorbance spectrum for one blue sample of Sciacca castle. The maximum of the absorption band for Mn^{3+} lies between 470 and 520 nm, depending on the base glass.

A pure green glass chromophore did not exist until the use of chromium minerals at the end of the 18th century. The green color was due to a combination of a light blue chromophore, such as reduced iron (Fe^{2+}) or oxidized copper (Cu^{2+}), and of yellow oxidized iron (Fe^{3+}). Iron is always present in ancient glasses as a natural impurity of sand. The UV-VIS spectra show that both the two iron ions are present in the samples here discussed producing a color variable from blue-green to yellow, through different yellow-green hues, depending on the Fe^{3+}/Fe^{2+} ratio (Figure 2.3).

The UV-VIS spectra of the dark green, olive green, intense green-yellow and amber yellow samples present a strong absorption band at about 408nm (Figure 2.4), typical of the Fe^{3+} - S^{2-} complex, the so-called *amber chromophore*, obtained under strongly reducing melting conditions (Weyl, 1953; Schreurs and Brill, 1984). The presence of *amber chromophore* in a green glass sample is explained by the residual fraction of Fe^{2+} (light blue) that modifies the amber colour into a green hues. Green samples in Figure 2.5 show the spectral features of iron ions together with slight characteristic cobalt bands.

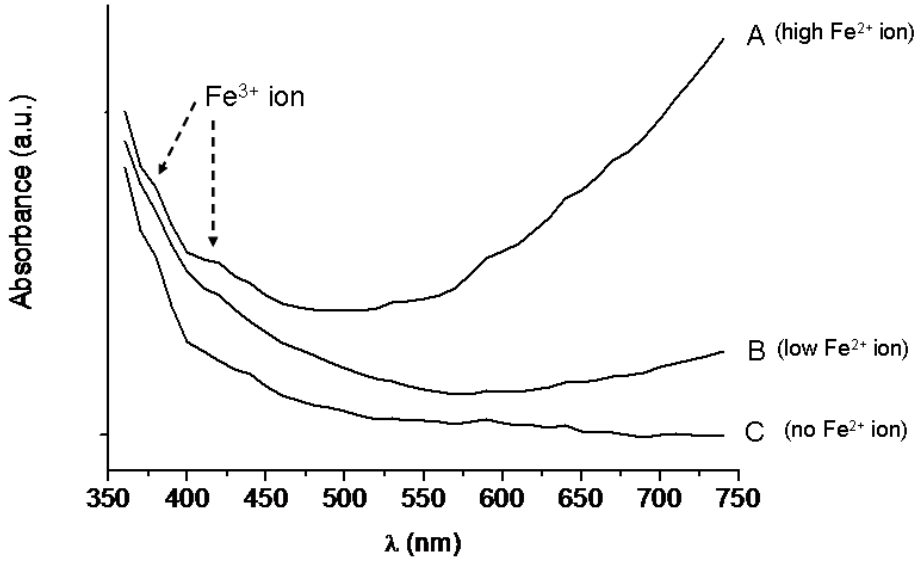

Figure 1.3. UV-Vis absorbance spectrum for three typical iron-colored samples.

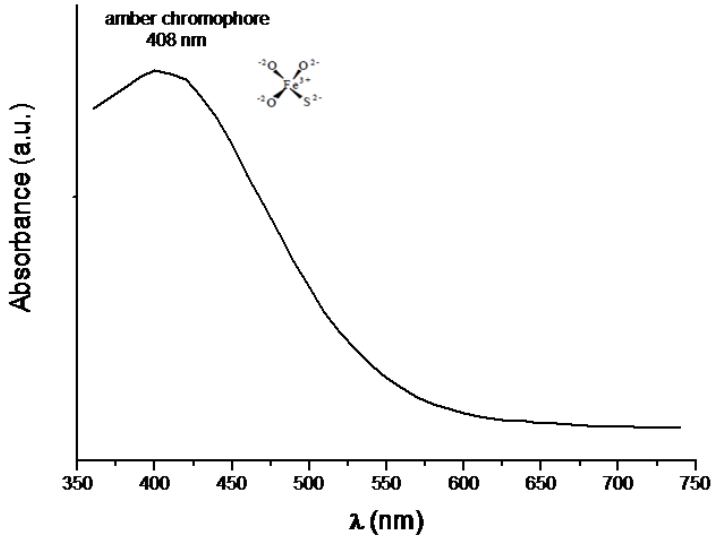

Figure 2.4. UV-Vis absorbance spectrum for an amber-colored sample.

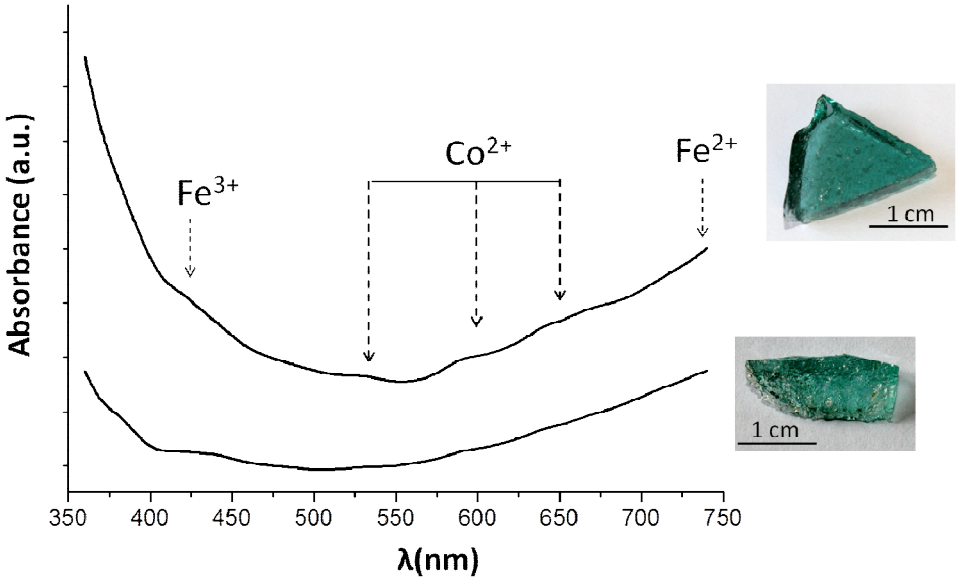

Figure 1.5. UV-Vis absorbance spectrum for green-colored samples shown in the inserts.

1.3 Conclusions

The main goal of this study was to prove that with a simple spectroscopic technique it is possible to identify the transition metals present in ancient glass, even when their concentrations are very low (e.g. <0.01 % of CoO).

The Medieval glass samples from two Sicilian castles were first classified on the base of the color and then analyzed with LA-ICP-MS. The main metal ions involved in coloring the glasses blue, light blue, yellow, purple, green or amber were Co^{2+}, Fe^{2+}, Fe^{3+}, Mn^{3+} and the iron-sulfur complex.

Apart from being a non-destructive method, which is important in analysis of cultural heritage artifacts, reflectance spectroscopy has another remarkable advantage, viz. it is possible to distinguish between valency states of some elements, induced by the (reducing or oxidizing) conditions in the furnace. Consequently, it is possible to retrieve information about some conditions of glass melting process.

Table 1.1. Chemical composition of the bulk of Poggio Diana samples (in wt.% of the major and minor oxides and in μg g^{-1} of the trace elemental oxides); the mean and standard deviation for 5 measurements is given.

Wt.%	Colour	Na_2O	MgO	Al_2O_3	SiO_2	P_2O_5	K_2O	CaO	TiO_2	MnO	Fe_2O_3	CoO	NiO	CuO	SnO_2	PbO
P1	Blue	10.57	2.87	1.42	60.87	0.38	4.52	8.72	0.07	0.13	1.37	0.21	0.06	0.61	3.28	4.41
sd		0.07	0.03	0.01	0.38	0.01	0.05	0.12	0.01	0.01	0.01	0.01	0.01	0.01	0.08	0.06
P2	Blue	11.45	3.00	1.48	57.60	0.42	5.13	9.80	0.08	0.14	1.44	0.24	0.07	0.65	3.45	4.47
sd		0.11	0.03	0.02	0.20	0.01	0.07	0.09	0.01	0.01	0.02	0.01	0.01	0.01	0.06	0.08
P3	Blue	11.53	3.05	1.52	57.08	0.39	5.17	9.98	0.08	0.14	1.47	0.24	0.07	0.64	3.52	4.57
sd		0.05	0.04	0.01	0.25	0.01	0.08	0.10	0.01	0.01	0.01	0.01	0.01	0.01	0.02	0.07
P4	Blue	11.54	3.09	1.56	56.57	0.42	5.34	10.21	0.09	0.14	1.48	0.25	0.07	0.65	3.55	4.47
sd		0.08	0.03	0.02	0.24	0.01	0.03	0.05	0.01	0.01	0.01	0.01	0.01	0.01	0.02	0.17
P5	Blue	11.53	3.03	1.50	56.74	0.41	5.17	9.94	0.08	0.14	1.48	0.24	0.07	0.67	3.59	4.82
sd		0.07	0.01	0.01	0.18	0.01	0.03	0.06	0.01	0.01	0.01	0.01	0.01	0.01	0.02	0.07
P6	Light blue	3.41	0.33	1.44	69.88	0.04	12.55	11.31	0.10	0.06	0.69	0.01	0.01	0.02	0.01	0.01
sd		0.16	0.02	0.14	1.54	0.01	0.46	0.69	0.01	0.01	0.09	0.01	0.01	0.01	0.01	0.01
P7	Light blue	14.62	2.63	4.97	63.83	0.42	4.74	7.33	0.10	0.59	0.58	0.005	0.003	0.005	0.001	0.004
sd		0.54	0.05	0.10	0.68	0.01	0.04	0.22	0.01	0.02	0.02	0.001	0.001	0.001	0.001	0.001
P8	Pink	14.20	2.69	4.66	62.07	0.43	6.06	8.06	0.10	0.88	0.60	0.002	0.002	0.004	0.012	0.013
sd		0.58	0.07	0.17	1.37	0.02	0.21	0.30	0.01	0.04	0.02	0.001	0.001	0.001	0.001	0.001
P9	Green	9.21	4.06	5.71	57.91	0.75	4.73	14.00	0.33	0.86	2.17	0.001	0.003	0.004	0.001	0.002
sd		0.07	0.04	0.05	0.22	0.02	0.05	0.13	0.01	0.02	0.01	0.001	0.001	0.001	0.001	0.001
P10	Yellow	12.90	2.44	5.18	64.53	0.38	5.32	7.71	0.09	0.75	0.51	0.002	0.002	0.003	0.001	0.004
sd		0.60	0.10	0.15	1.21	0.01	0.17	0.28	0.01	0.03	0.02	0.001	0.001	0.001	0.001	0.001
P11	Yellow-green	9.56	4.09	5.45	57.42	0.79	5.13	14.01	0.31	0.90	2.09	0.001	0.003	0.005	0.001	0.001
sd		0.11	0.03	0.04	0.28	0.01	0.10	0.08	0.01	0.02	0.01	0.001	0.001	0.001	0.001	0.001
P12	Yellow	13.54	2.11	5.91	64.94	0.54	4.72	7.00	0.12	0.89	0.71	0.002	0.002	0.003	0.001	0.003
sd		0.66	0.14	0.40	2.21	0.03	0.33	0.39	0.01	0.06	0.06	0.001	0.001	0.001	0.001	0.001
P14	Yellow	14.29	3.16	4.95	56.96	0.34	6.18	11.15	0.10	1.93	0.68	0.014	0.005	0.008	0.004	0.010
sd		0.25	0.05	0.12	0.71	0.01	0.12	0.16	0.01	0.05	0.02	0.001	0.001	0.001	0.001	0.001
P16	Yellow	13.58	2.40	5.56	63.55	0.61	5.07	7.46	0.11	0.80	0.66	0.002	0.002	0.003	0.001	0.002

sd		0.86	0.06	0.17	0.97	0.02	0.16	0.19	0.00	0.03	0.02	0.001	0.001	0.001	0.001	0.001
P17	Yellow	9.14	3.66	5.38	62.05	0.52	4.50	11.18	0.34	1.16	2.13	0.001	0.003	0.005	0.000	0.002
sd		0.14	0.22	0.36	1.17	0.03	0.17	0.57	0.02	0.07	0.12	0.001	0.001	0.001	0.001	0.001
P18	Colourless	10.97	2.98	1.42	65.21	0.32	4.87	12.27	0.13	1.00	0.60	0.006	0.004	0.003	0.001	0.001
sd		0.31	0.06	0.05	0.72	0.01	0.09	0.27	0.01	0.03	0.02	0.001	0.001	0.001	0.001	0.001
P20	Colourless	11.22	2.60	5.92	64.07	0.65	5.17	8.48	0.12	0.91	0.72	0.003	0.003	0.004	0.000	0.004
sd		0.84	0.03	0.10	1.51	0.02	0.12	0.09	0.01	0.01	0.01	0.001	0.001	0.001	0.001	0.001
P21	Colourless	12.80	3.75	1.35	61.36	0.28	2.64	15.15	0.16	1.62	0.58	0.015	0.007	0.003	0.005	0.005
sd		0.20	0.04	0.01	0.38	0.01	0.02	0.17	0.01	0.02	0.01	0.001	0.001	0.001	0.001	0.001
P22	Colourless	17.56	2.14	0.81	64.89	0.18	6.45	7.11	0.03	0.36	0.32	0.001	0.001	0.020	0.003	0.005
sd		0.67	0.10	0.07	1.37	0.01	0.29	0.47	0.01	0.01	0.01	0.001	0.001	0.001	0.001	0.001

µg/g	**Li_2O**	**BeO**	**B_2O_3**	**Sc_2O_3**	**V_2O_5**	**Cr_2O_3**	**ZnO**	**Ga_2O_3**	**As_2O_5**	**SeO_2**	**Rb2O**	**SrO**	**Y_2O_3**	**ZrO_2**	**Nb_2O_5**	**MoO_3**	**Ag_2O**	**CdO**	**In_2O_3**	**Sb_2O_5**
P1	30.2	0.78	335.7	21.91	18.69	16.48	37.26	6.19	2089	69.68	23.89	470.5	4.72	51.32	2.47	34.25	7.28	0.40	124.5	47.65
sd	1.0	0.05	23.7	0.23	0.33	0.98	1.88	0.35	53	6.31	0.85	13.1	0.18	1.44	0.06	1.40	0.17	0.02	2.7	1.58
P2	38.3	0.57	242.5	15.31	21.14	17.93	57.41	5.14	2709	25.00	28.94	530.9	5.20	57.00	2.77	38.95	6.93	0.37	130.8	54.26
sd	1.1	0.03	6.5	0.19	0.28	1.27	2.63	0.18	50	2.00	0.38	6.8	0.19	0.68	0.11	0.61	0.35	0.03	2.7	1.98
P3	36.7	0.59	221.6	15.07	21.18	19.15	54.54	5.25	2637	16.39	29.03	547.2	5.43	58.06	2.84	38.80	6.29	0.34	133.1	55.13
sd	0.6	0.06	5.6	0.25	0.23	0.73	1.38	0.12	18	1.08	0.34	3.5	0.10	0.41	0.09	0.81	0.21	0.05	1.5	1.00
P4	38.5	0.58	214.4	14.85	22.28	18.48	58.64	5.41	2691	14.03	30.75	566.5	5.70	60.56	2.92	40.27	5.90	0.39	135.5	55.24
sd	0.3	0.06	5.8	0.18	0.36	0.55	3.14	0.18	109	1.03	0.32	11.1	0.14	0.30	0.08	0.65	0.18	0.02	0.4	0.75
P5	38.5	0.77	218.8	14.89	21.34	17.60	54.71	5.32	2824	15.89	29.10	546.8	5.45	58.22	2.74	39.14	7.25	0.38	136.0	56.88
sd	1.9	0.05	4.6	0.42	0.32	0.67	2.34	0.10	40	0.68	0.54	3.8	0.16	0.66	0.06	1.39	0.26	0.07	0.6	0.30
P6	114.0	1.97	46.6	20.16	21.56	10.97	39.39	9.60	2.8	13.87	44.08	200.4	13.75	38.54	4.52	0.14	0.04	0.26	0.02	0.25
sd	5.3	0.09	2.6	0.50	1.45	0.87	3.24	0.31	0.2	1.02	0.79	10.8	1.30	3.36	0.28	0.03	0.01	0.03	0.01	0.02
P7	42.4	1.27	324.8	17.04	16.01	14.84	81.56	13.48	50.3	32.28	56.44	415.2	14.45	157.43	5.56	3.09	0.31	0.43	0.05	1.77
sd	1.0	0.08	5.3	0.65	0.60	1.27	4.83	0.42	2.3	1.11	0.98	6.4	0.53	4.06	0.21	0.21	0.03	0.00	0.01	0.14
P8	46.0	2.01	290.8	15.64	20.72	17.00	68.29	16.40	36.2	58.07	64.30	481.9	18.72	203.72	5.39	1.98	0.30	1.01	0.44	2.13
sd	1.9	0.26	9.0	0.43	0.76	2.51	6.61	0.74	4.3	4.91	2.41	17.8	0.95	7.71	0.35	0.22	0.05	0.23	0.05	0.27
P9	65.6	2.12	305.5	20.25	88.51	62.19	130.79	13.86	12.3	19.30	41.44	911.7	19.51	392.92	13.57	2.28	0.23	0.85	0.07	1.96
sd	0.7	0.22	17.0	0.15	1.52	4.77	6.85	0.37	1.6	1.86	0.66	12.3	0.44	4.72	0.19	0.21	0.01	0.05	0.01	0.17

P10	38.6	1.32	292.4	16.26	19.05	12.16	86.23	15.21	20.53	23.80	67.08	397.0	16.13	157.69	5.06	1.39	0.19	0.52	0.03	1.37
sd	1.2	0.14	13.2	0.92	0.46	1.18	3.07	0.68	1.96	1.91	2.58	15.2	0.66	6.24	0.25	0.07	0.02	0.13	0.01	0.12
P11	67.7	1.83	348.0	19.77	87.70	56.73	141.54	13.66	12.61	67.29	46.01	903.6	18.89	381.94	13.05	2.17	0.22	1.36	0.04	2.97
sd	1.9	0.24	12.0	0.73	1.35	3.30	5.63	0.68	1.24	7.59	0.71	9.1	0.50	3.58	0.34	0.21	0.02	0.11	0.01	0.18
P12	35.7	1.38	317.5	17.29	20.66	16.83	107.03	16.00	9.81	21.97	55.00	318.2	15.92	190.64	6.60	4.40	0.12	0.25	0.04	4.99
sd	1.3	0.13	23.8	0.89	0.64	1.19	5.82	0.43	0.36	2.29	1.85	11.5	0.77	13.99	0.67	0.14	0.01	0.01	0.00	0.48
P14	61.4	1.53	173.9	14.77	23.24	16.00	62.67	15.05	293.40	25.13	78.38	614.5	16.00	161.44	5.14	2.05	0.41	0.46	0.16	1.48
sd	0.7	0.09	3.1	0.51	0.65	0.76	3.16	0.39	3.98	2.17	1.63	12.3	0.40	3.55	0.14	0.15	0.04	0.04	0.01	0.14
P16	34.8	1.39	405.4	16.56	22.92	15.76	114.19	16.75	7.30	60.96	60.61	331.1	17.17	166.10	5.77	7.77	0.12	0.13	0.03	3.04
sd	1.6	0.18	12.7	0.36	1.84	0.97	3.92	0.43	0.64	4.87	1.74	7.1	0.36	3.65	0.39	0.29	0.01	0.02	0.01	0.15
P17	66.7	1.39	278.0	19.93	80.80	58.71	104.07	13.28	10.16	25.32	41.16	681.2	17.50	374.94	13.86	2.09	0.59	0.27	0.05	2.37
sd	4.9	0.11	17.8	0.87	2.14	3.49	2.49	0.57	0.76	1.76	1.43	32.3	0.74	24.39	0.70	0.23	0.02	0.04	0.01	0.14
P18	46.0	0.53	212.0	16.28	22.27	23.08	30.99	7.99	138.19	36.29	23.10	794.9	8.16	281.75	4.88	1.45	0.17	0.31	0.04	0.76
sd	1.3	0.04	9.2	0.31	0.83	2.16	1.71	0.49	4.67	2.90	0.63	15.5	0.22	10.37	0.36	0.07	0.01	0.07	0.01	0.07
P20	32.3	1.58	378.0	16.10	24.11	21.75	147.07	17.87	7.30	24.23	65.02	367.3	18.54	176.03	6.13	9.05	0.14	0.46	0.03	3.54
sd	2.3	0.10	6.4	0.49	0.47	2.12	2.88	0.27	0.35	2.08	0.61	3.7	0.22	2.41	0.27	0.78	0.01	0.01	0.01	0.15
P21	27.0	0.66	257.8	14.95	28.97	25.02	56.77	12.39	268.30	31.66	21.23	958.9	10.32	410.56	6.05	3.67	0.20	0.45	0.23	0.62
sd	0.6	0.04	8.9	0.31	0.53	1.40	2.22	0.13	11.58	1.57	0.36	8.7	0.27	4.98	0.13	0.30	0.01	0.03	0.02	0.06
P22	23.5	0.54	184.8	14.05	14.47	6.82	22.96	4.25	9.38	11.84	36.37	453.3	2.90	20.73	1.32	1.05	0.07	0.22	0.12	1.02
sd	0.8	0.01	8.5	0.37	0.43	0.53	1.96	0.29	0.67	3.25	0.94	31.8	0.22	1.77	0.11	0.07	0.01	0.01	0.01	0.08

µg/g	**BaO**	**La_2O_3**	**CeO_2**	**Pr_2O_3**	**Nd_2O_3**	**Sm_2O_3**	**Eu_2O_3**	**Gd_2O_3**	**Tb_2O_3**	**Dy_2O_3**	**Ho_2O_3**	**Er_2O_3**	**Tm_2O_3**	**Yb_2O_3**	**Lu_2O_3**	**HfO_2**	**Au_2O_3**	**Bi_2O_3**	**ThO_2**	**UO_2**
P1	141.2	4.51	8.98	1.04	4.20	0.79	0.18	0.82	0.13	0.68	0.15	0.40	0.06	0.42	0.05	1.10	0.06	1400	1.18	0.99
sd	3.6	0.13	0.29	0.03	0.19	0.04	0.01	0.04	0.01	0.05	0.01	0.03	0.01	0.03	0.01	0.06	0.01	25	0.03	0.03
P2	153.3	4.75	9.65	1.13	4.21	0.82	0.18	0.79	0.15	0.70	0.14	0.44	0.06	0.43	0.05	1.22	0.08	1508	1.31	1.13
sd	2.5	0.07	0.18	0.05	0.27	0.07	0.02	0.06	0.01	0.05	0.01	0.01	0.01	0.03	0.01	0.05	0.01	34	0.05	0.05
P3	154.7	4.83	9.76	1.16	4.33	0.88	0.21	0.77	0.11	0.72	0.13	0.45	0.05	0.43	0.06	1.16	0.05	1456	1.31	1.12
sd	2.1	0.16	0.09	0.05	0.08	0.07	0.01	0.07	0.01	0.05	0.02	0.04	0.01	0.04	0.01	0.05	0.01	17	0.04	0.02
P4	160.1	5.05	9.99	1.13	4.51	0.96	0.19	0.90	0.12	0.78	0.16	0.47	0.07	0.45	0.07	1.18	0.06	1502	1.36	1.16
sd	2.4	0.16	0.15	0.04	0.12	0.09	0.01	0.09	0.01	0.04	0.01	0.04	0.01	0.04	0.01	0.05	0.01	59	0.04	0.03
P5	154.8	4.86	9.56	1.13	4.39	0.77	0.18	0.63	0.12	0.71	0.14	0.44	0.06	0.41	0.05	1.17	0.07	1537	1.31	1.12

sd	1.9	0.10	0.12	0.07	0.23	0.07	0.02	0.04	0.01	0.09	0.01	0.04	0.01	0.02	0.01	0.11	0.01	24.44	0.06	0.05
P6	185.3	11.25	20.62	2.61	9.74	1.92	0.50	1.92	0.23	1.68	0.30	0.93	0.13	0.81	0.10	0.68	0.01	0.02	1.14	0.39
sd	12.8	1.04	1.80	0.14	1.00	0.14	0.05	0.01	0.03	0.17	0.04	0.10	0.01	0.08	0.01	0.03	0.01	0.01	0.06	0.03
P7	407.0	11.21	22.61	2.44	9.40	1.90	0.36	1.80	0.26	1.77	0.40	1.19	0.17	1.35	0.21	2.66	0.03	15.56	4.13	1.79
sd	9.5	0.28	0.84	0.13	0.45	0.14	0.02	0.19	0.02	0.10	0.03	0.10	0.01	0.09	0.02	0.08	0.01	1.30	0.14	0.05
P8	579.2	13.83	27.42	3.08	12.00	2.23	0.37	2.34	0.35	2.35	0.51	1.60	0.25	1.77	0.27	3.38	0.10	8.55	5.17	2.01
sd	21.9	0.54	1.14	0.14	0.84	0.27	0.05	0.18	0.03	0.32	0.03	0.14	0.03	0.11	0.02	0.32	0.01	0.36	0.22	0.08
P9	244.3	23.25	48.63	5.18	19.35	3.71	0.76	3.25	0.46	2.73	0.54	1.56	0.21	1.55	0.26	7.54	0.01	0.16	6.09	1.63
sd	3.0	0.44	0.96	0.14	0.62	0.19	0.02	0.19	0.03	0.12	0.04	0.04	0.02	0.11	0.03	0.21	0.00	0.05	0.17	0.07
P10	508.9	11.74	23.56	2.71	10.05	2.04	0.38	1.75	0.30	2.03	0.45	1.33	0.22	1.50	0.21	2.87	0.03	4.30	4.20	1.73
sd	20.6	0.47	0.85	0.12	0.57	0.15	0.04	0.16	0.03	0.10	0.03	0.12	0.02	0.10	0.03	0.33	0.01	0.29	0.20	0.07
P11	244.6	22.83	47.14	4.98	18.93	3.57	0.72	3.05	0.42	3.03	0.57	1.62	0.22	1.53	0.26	7.06	0.08	0.17	5.88	1.56
sd	6.6	0.26	0.87	0.13	0.58	0.34	0.08	0.25	0.03	0.32	0.02	0.09	0.03	0.13	0.03	0.28	0.01	0.02	0.13	0.15
P12	485.0	12.16	24.99	2.80	10.20	2.18	0.40	1.80	0.29	2.21	0.45	1.33	0.22	1.32	0.22	3.34	0.01	0.15	4.99	1.78
sd	33.9	0.72	1.20	0.16	0.55	0.13	0.02	0.17	0.02	0.17	0.03	0.11	0.02	0.08	0.02	0.19	0.01	0.01	0.36	0.09
P14	499.5	12.13	24.06	2.74	10.41	2.07	0.36	1.95	0.29	2.04	0.44	1.37	0.22	1.31	0.22	2.88	0.04	106.44	4.41	1.91
sd	10.7	0.19	0.57	0.12	0.51	0.20	0.01	0.14	0.02	0.16	0.04	0.09	0.02	0.12	0.01	0.08	0.01	3.34	0.09	0.05
P16	516.4	13.01	26.78	3.04	11.12	2.22	0.38	2.04	0.30	2.32	0.46	1.45	0.22	1.55	0.24	3.03	0.03	0.06	4.41	1.74
sd	13.0	0.31	0.60	0.11	0.39	0.22	0.03	0.09	0.01	0.09	0.03	0.06	0.02	0.13	0.01	0.17	0.01	0.01	0.15	0.10
P17	208.0	21.70	48.16	5.05	18.65	3.43	0.73	2.62	0.37	2.44	0.49	1.38	0.20	1.44	0.22	6.82	0.01	0.11	5.48	1.59
sd	10.4	0.92	2.64	0.26	1.13	0.14	0.06	0.04	0.05	0.16	0.04	0.07	0.01	0.13	0.02	0.42	0.01	0.01	0.39	0.08
P18	312.0	8.75	18.44	2.02	7.19	1.37	0.33	1.28	0.17	0.96	0.21	0.61	0.12	0.63	0.12	4.84	0.01	32.97	2.28	0.94
sd	10.2	0.40	0.57	0.09	0.52	0.09	0.03	0.12	0.02	0.09	0.02	0.06	0.01	0.10	0.01	0.26	0.01	1.41	0.03	0.04
P20	573.6	14.01	28.41	3.16	11.76	2.43	0.42	2.22	0.34	2.32	0.47	1.58	0.23	1.59	0.25	3.09	0.01	0.09	4.76	1.89
sd	7.6	0.22	0.51	0.03	0.31	0.10	0.03	0.20	0.02	0.17	0.05	0.06	0.02	0.08	0.02	0.11	0.01	0.01	0.16	0.09
P21	611.9	10.29	20.29	2.25	8.20	1.67	0.37	1.16	0.19	1.42	0.28	0.86	0.10	0.79	0.14	7.10	0.04	69.28	2.26	0.82
sd	6.7	0.27	0.16	0.12	0.34	0.07	0.03	0.03	0.03	0.08	0.03	0.07	0.01	0.07	0.01	0.37	0.01	3.49	0.07	0.04
P22	147.6	2.69	5.70	0.66	2.47	0.51	0.09	0.43	0.07	0.42	0.09	0.17	0.04	0.24	0.03	0.36	0.40	4.69	0.77	0.33
sd	8.5	0.24	0.17	0.04	0.20	0.04	0.01	0.02	0.01	0.03	0.01	0.02	0.01	0.01	0.01	0.05	0.04	0.48	0.07	0.01

Table 2.2. Chemical composition of the bulk of Sciacca samples (in wt.% of the major and minor oxides and in μg g^{-1} of the trace elemental oxides); the mean and standard deviation for 5 measurements is given.

wt.%	Colour	Na_2O	MgO	Al_2O_3	SiO_2	P_2O_5	K_2O	CaO	TiO_2	MnO	Fe_2O_3	CoO	NiO	CuO
S1	Blue	18.72	1.96	5.01	60.68	0.48	4.76	5.66	0.10	0.87	1.20	0.192	0.091	0.102
sd		0.10	0.02	0.04	0.18	0.01	0.02	0.05	0.01	0.01	0.01	0.002	0.001	0.001
S2	Blue	13.59	3.24	4.49	57.54	0.48	6.88	10.64	0.08	0.94	1.00	0.092	0.003	0.229
sd		0.11	0.04	0.05	0.32	0.01	0.08	0.11	0.00	0.01	0.03	0.003	0.001	0.015
S3	Blue	10.28	2.03	5.99	68.82	0.54	4.11	6.18	0.15	0.72	1.39	0.150	0.066	0.068
sd		0.39	0.16	0.26	1.98	0.02	0.26	0.47	0.01	0.05	0.05	0.010	0.006	0.004
S14	Dark green	22.98	2.23	9.94	48.58	0.49	4.47	5.89	1.18	0.10	3.92	0.002	0.003	0.004
sd		0.43	0.02	0.06	0.44	0.00	0.06	0.07	0.01	0.01	0.04	0.001	0.001	0.001
S10	Pink	19.55	0.21	0.11	69.38	0.09	0.73	9.28	0.02	0.03	0.09	0.001	0.001	0.001
sd		0.76	0.00	0.00	0.96	0.01	0.01	0.26	0.01	0.01	0.01	0.001	0.001	0.001
S4	Blue	19.15	1.99	5.07	59.76	0.51	4.93	5.78	0.10	0.88	1.24	0.188	0.096	0.113
sd		0.08	0.02	0.03	0.15	0.01	0.04	0.07	0.01	0.01	0.01	0.001	0.001	0.000
S11	Light green	11.99	4.03	1.96	60.92	0.36	3.45	14.91	0.18	1.10	0.83	0.003	0.002	0.012
sd		0.12	0.04	0.02	0.35	0.01	0.02	0.20	0.01	0.03	0.02	0.001	0.001	0.001
S17	Pink	8.00	2.07	6.28	70.21	0.45	4.69	5.98	0.14	1.14	0.86	0.005	0.005	0.005
sd		0.61	0.04	0.16	0.74	0.01	0.16	0.17	0.00	0.09	0.03	0.001	0.001	0.001
S18	Violet	11.86	4.58	2.69	56.49	0.83	7.39	13.58	0.24	1.03	0.73	0.002	0.002	0.044
sd		0.13	0.03	0.03	0.21	0.00	0.06	0.12	0.00	0.01	0.01	0.001	0.001	0.001
S15	Dark amber	10.79	8.74	2.64	50.15	1.80	10.77	13.51	0.19	0.38	0.78	0.001	0.001	0.009
sd		0.19	0.03	0.03	0.39	0.05	0.21	0.08	0.00	0.00	0.01	0.001	0.001	0.001
S19	Blue	12.02	2.62	5.88	61.79	0.64	6.31	7.77	0.12	1.10	1.35	0.072	0.038	0.050
sd		0.43	0.04	0.18	0.53	0.01	0.15	0.15	0.00	0.03	0.03	0.001	0.001	0.004
S20	Colourless	15.95	2.56	4.66	62.31	0.47	5.44	7.16	0.12	0.63	0.50	0.002	0.002	0.002
sd		0.82	0.06	0.09	1.10	0.01	0.13	0.17	0.00	0.03	0.01	0.001	0.001	0.001
S21	Yellow-green	14.36	3.28	2.47	61.03	0.40	3.21	11.54	0.19	2.18	1.14	0.002	0.002	0.003
sd		0.17	0.04	0.07	0.24	0.01	0.06	0.10	0.00	0.05	0.01	0.001	0.001	0.001
S22	Light blue	9.46	4.60	1.54	60.46	1.13	10.10	10.89	0.17	0.74	0.63	0.001	0.001	0.003

sd		0.11	0.15	0.05	0.39	0.02	0.12	0.24	0.01	0.03	0.02	0.001	0.001	0.001
S23	Light blue	13.77	3.85	1.73	63.61	0.35	3.37	11.59	0.13	0.78	0.63	0.001	0.001	0.004
sd		0.20	0.03	0.03	0.32	0.00	0.06	0.10	0.01	0.01	0.01	0.001	0.001	0.001
S38	Yellow-green	9.51	4.16	3.13	63.27	0.75	5.80	10.62	0.23	1.11	1.18	0.001	0.002	0.003
sd		0.16	0.05	0.07	0.61	0.02	0.15	0.21	0.01	0.01	0.02	0.001	0.001	0.001
S24	Colourless	9.72	6.55	2.17	54.73	1.20	10.70	12.61	0.18	1.06	0.71	0.001	0.001	0.004
sd		0.10	0.10	0.03	0.33	0.01	0.10	0.13	0.00	0.01	0.01	0.001	0.001	0.001
S25	Colourless	14.61	3.92	1.23	64.93	0.29	3.30	10.57	0.06	0.44	0.51	0.001	0.001	0.005
sd		0.29	0.17	0.04	0.62	0.01	0.06	0.17	0.00	0.02	0.02	0.001	0.001	0.001
S27	Light green	12.76	3.25	1.79	64.74	0.30	2.64	12.34	0.14	1.07	0.80	0.002	0.002	0.004
sd		0.18	0.03	0.02	0.32	0.01	0.04	0.15	0.00	0.02	0.01	0.001	0.001	0.001
S28	Colourless	6.27	2.52	5.62	71.85	0.56	4.40	7.36	0.09	0.59	0.58	0.001	0.001	0.003
sd		0.67	0.07	0.18	0.54	0.02	0.11	0.16	0.01	0.01	0.02	0.001	0.001	0.001
S29	Light green	13.33	4.10	1.16	66.35	0.29	3.56	9.67	0.09	0.65	0.51	0.001	0.001	0.004
sd		0.34	0.11	0.09	0.67	0.01	0.09	0.43	0.01	0.10	0.03	0.001	0.001	0.001
S34	Blue	12.67	6.40	1.31	64.58	0.30	3.53	9.85	0.08	0.08	0.76	0.111	0.044	0.135
sd		0.25	0.11	0.03	0.22	0.01	0.18	0.18	0.01	0.01	0.02	0.006	0.004	0.006
S33	Light green	15.39	3.09	5.18	58.84	0.81	5.55	8.30	0.12	1.54	0.97	0.001	0.002	0.008
sd		0.20	0.04	0.05	0.25	0.02	0.05	0.11	0.01	0.02	0.01	0.001	0.001	0.001
S30	Green	16.98	3.44	2.80	62.04	0.59	2.92	9.00	0.12	0.80	1.06	0.005	0.005	0.019
sd		0.21	0.03	0.05	0.31	0.01	0.03	0.09	0.01	0.01	0.02	0.001	0.001	0.002
S40	Colourless	20.12	2.03	1.28	64.72	0.43	3.60	6.78	0.06	0.32	0.55	0.001	0.001	0.003
sd		0.55	0.04	0.05	0.73	0.01	0.07	0.17	0.01	0.01	0.02	0.001	0.001	0.001
S36	Emerald green	16.67	3.66	5.46	57.05	0.62	3.85	10.52	0.23	0.64	1.06	0.007	0.002	0.022
sd		0.10	0.03	0.05	0.09	0.01	0.04	0.05	0.01	0.01	0.01	0.001	0.001	0.001
S12	Colourless	17.72	2.67	3.31	63.27	0.62	2.97	7.75	0.14	0.56	0.83	0.003	0.002	0.006
sd		0.19	0.04	0.04	0.23	0.02	0.04	0.07	0.00	0.01	0.02	0.001	0.001	0.001
S13	Yellow-green	6.04	3.62	2.52	56.10	1.88	12.95	15.05	0.23	0.16	0.94	0.002	0.002	0.005
sd		0.07	0.04	0.02	0.22	0.01	0.09	0.18	0.01	0.01	0.02	0.001	0.001	0.001

µg/g	Li_2O	BeO	B_2O_3	Sc_2O_3	V_2O_5	Cr_2O_3	ZnO	Ga_2O_3	As_2O_5	SeO_2	Rb_2O	SrO	Y_2O_3	ZrO_2	Nb_2O_5	MoO_3	Ag_2O	CdO	In_2O_3	SnO_2
S1	54.30	1.73	324.2	21.43	20.12	14.47	141.4	12.11	135.7	24.79	54.04	265.7	13.70	134.57	4.71	162.5	1.92	0.35	0.07	14.79
sd	0.40	0.21	7.2	0.29	0.24	0.41	3.0	0.30	2.7	1.80	0.73	1.2	0.25	0.89	0.04	4.2	0.17	0.02	0.01	0.23
S2	60.30	1.17	276.6	19.93	26.79	15.12	698.9	15.03	24.2	23.61	107.34	650.7	10.68	91.85	3.52	3.35	0.88	0.21	46.84	185.0
sd	0.94	0.09	7.0	0.50	0.41	0.73	29.5	0.20	0.9	2.49	0.84	3.7	0.33	1.70	0.11	0.20	0.04	0.04	1.90	9.0
S3	28.84	1.33	306.0	24.73	22.06	20.59	110.7	14.04	34.3	13.95	46.70	268.6	17.56	212.37	6.51	120.9	0.93	0.61	0.16	36.40
sd	2.57	0.10	27.1	0.92	1.70	0.72	8.4	0.61	2.5	0.65	2.61	18.7	0.63	9.37	0.37	9.4	0.13	0.07	0.01	2.91
S14	36.98	3.03	212.3	36.93	273.41	166.18	62.3	21.70	4.5	17.91	15.45	283.5	29.25	336.09	20.67	1.12	0.29	0.51	0.07	4.12
sd	0.60	0.20	5.1	0.40	3.27	2.38	3.4	0.25	0.2	2.14	0.31	3.7	0.44	4.83	0.40	0.12	0.02	0.06	0.00	0.50
S10	25.77	0.62	212.3	24.76	5.54	5.95	5.7	0.73	4280	412.35	1.22	28.6	1.37	37.62	0.48	0.22	0.16	0.36	0.01	0.94
sd	1.27	0.04	18.4	1.26	0.50	1.03	0.4	0.08	132	17.36	0.10	0.5	0.10	0.97	0.02	0.03	0.02	0.14	0.00	0.11
S4	61.90	2.31	360.8	23.38	20.52	15.60	129.9	12.37	152.1	45.15	56.62	276.2	14.42	138.92	4.77	174.4	2.12	0.50	0.09	14.71
sd	1.65	0.26	11.0	0.66	0.46	0.81	3.9	0.70	5.1	3.96	1.52	3.0	0.36	1.92	0.21	4.9	0.12	0.16	0.01	0.50
S11	40.00	1.22	277.4	24.67	37.53	31.40	97.2	8.22	7.86	29.87	30.62	1038	9.74	373.87	6.12	1.82	0.52	0.84	1.60	11.43
sd	0.82	0.13	5.4	0.53	0.63	0.98	10.9	0.13	0.45	1.50	1.84	10	0.26	4.43	0.17	0.17	0.06	0.08	0.11	0.54
S17	38.41	1.56	166.3	27.09	36.52	21.03	96.8	13.82	10.19	20.74	47.41	379.1	19.01	201.10	6.35	18.49	0.25	1.89	0.07	8.52
sd	2.48	0.11	5.6	0.74	3.72	1.68	10.5	0.44	0.49	1.71	1.91	13.4	0.67	4.49	0.26	1.49	0.04	0.10	0.01	0.52
S18	123.08	1.11	383.3	23.54	41.84	21.76	76.4	9.50	9.88	22.07	40.35	3802	13.84	438.03	7.01	4.38	0.21	1.36	0.06	1.85
sd	1.73	0.16	6.4	0.51	0.45	0.59	3.4	0.21	0.42	1.98	0.54	51	0.27	2.31	0.12	0.25	0.01	0.22	0.01	0.11
S15	74.17	1.37	437.0	20.69	31.51	15.20	76.8	9.33	5.34	36.62	73.24	975	8.75	249.80	6.83	3.98	0.39	0.64	0.03	4.05
sd	1.04	0.18	15.8	0.57	0.47	1.47	2.4	0.26	0.70	3.28	1.90	5	0.20	2.71	0.23	0.40	0.03	0.10	0.01	0.15
S19	63.39	1.98	362.9	23.68	28.73	16.29	115.9	18.44	20.09	22.44	61.53	347.8	15.56	151.18	5.43	386.27	1.10	0.43	0.05	8.45
sd	3.01	0.10	11.8	0.61	0.66	0.43	3.1	0.24	1.00	2.20	1.15	4.0	0.41	3.82	0.19	5.06	0.12	0.04	0.01	0.18
S20	50.19	1.41	385.0	24.18	15.38	11.23	77.8	12.06	20.85	51.01	54.12	330.2	24.00	295.78	6.20	1.05	0.22	0.43	0.03	2.85
sd	0.86	0.19	12.9	1.01	0.59	0.20	2.4	0.31	2.00	2.42	1.41	8.8	0.82	9.03	0.21	0.05	0.02	0.01	0.01	0.24
S21	49.03	1.04	237.2	26.03	56.85	29.66	50.6	7.21	7.44	28.53	19.62	702.6	9.86	146.75	5.75	2.21	0.49	0.34	0.03	3.19
sd	0.95	0.09	8.7	0.31	0.70	1.10	2.3	0.30	0.53	1.97	0.45	5.9	0.18	1.09	0.11	0.18	0.05	0.01	0.01	0.20
S22	62.57	0.43	424.2	23.10	24.45	17.71	57.6	4.73	3.87	29.07	42.52	1545.5	7.82	319.21	5.83	3.89	0.26	0.80	0.01	0.89
sd	1.57	0.00	6.7	0.49	0.79	2.15	2.4	0.23	0.34	2.49	0.83	32.3	0.21	6.68	0.26	0.59	0.02	0.13	0.00	0.08
S23	32.88	1.08	302.6	24.54	26.93	16.87	51.8	5.40	5.96	27.63	32.31	747.1	7.96	239.42	4.82	1.38	0.79	0.93	0.03	5.85

sd	0.72	0.13	5.3	0.53	0.86	1.30	2.0	0.30	0.27	1.19	0.42	5.1	0.23	2.59	0.11	0.16	0.07	0.07	0.00	0.19
S38	77.04	1.32	455.0	27.09	44.45	29.11	70.7	9.40	4.96	123.81	27.86	737.9	10.43	310.66	7.46	1.49	0.19	0.18	0.02	1.06
sd	2.77	0.11	42.0	0.41	1.00	0.66	3.7	0.68	0.47	11.52	1.25	21.2	0.40	11.99	0.37	0.12	0.01	0.05	0.01	0.10
S24	65.86	0.50	382.0	21.72	26.12	16.10	57.5	8.75	3.23	35.46	75.74	2156.4	8.36	319.12	6.01	4.45	0.33	0.55	0.03	2.04
sd	1.24	0.05	10.2	0.34	0.45	0.72	1.3	0.20	0.09	1.80	1.27	46.5	0.16	6.05	0.22	0.28	0.02	0.03	0.01	0.16
S25	29.50	0.92	288.6	24.21	16.82	16.78	73.9	4.68	6.41	29.28	21.82	508.2	4.00	24.82	2.16	1.63	0.47	0.40	0.12	34.66
sd	1.06	0.13	6.2	0.88	0.35	0.56	2.0	0.09	0.58	4.10	0.79	10.1	0.08	0.57	0.12	0.16	0.01	0.02	0.01	1.13
S27	28.04	0.96	234.5	19.62	37.51	24.02	47.4	6.19	5.32	23.42	21.35	780.1	8.58	192.59	4.72	1.28	0.39	0.20	0.05	8.15
sd	0.59	0.09	4.4	0.47	0.58	1.45	2.3	0.31	0.10	1.58	0.39	17.3	0.25	4.29	0.17	0.12	0.04	0.04	0.01	0.43
S28	24.30	1.63	323.0	20.40	15.20	13.27	102.5	11.91	14.79	17.33	65.64	273.6	18.41	188.29	5.31	0.68	0.25	0.42	0.03	3.73
sd	1.00	0.23	7.4	0.23	0.86	0.36	5.3	0.42	0.90	2.23	2.00	7.2	0.67	4.64	0.09	0.06	0.01	0.05	0.01	0.32
S29	20.80	0.55	299.4	19.48	20.23	14.74	42.5	3.70	3.65	23.10	20.92	602.5	5.37	121.42	3.42	1.79	0.23	0.41	0.04	3.19
sd	1.22	0.01	9.4	0.51	1.24	1.14	4.1	0.20	0.28	3.52	0.72	32.0	0.58	14.80	0.26	0.16	0.01	0.03	0.01	0.64
S34	21.26	0.57	349.7	19.11	26.43	17.57	35.5	5.94	37.77	42.15	15.75	498.7	5.52	164.41	3.23	41.68	0.74	0.72	0.05	1.91
sd	0.56	0.05	11.4	0.30	0.39	1.13	1.3	0.22	2.36	2.99	0.33	8.6	0.14	3.98	0.15	2.49	0.04	0.08	0.01	0.24
S33	76.27	2.27	273.4	19.30	29.80	21.06	110.6	14.37	15.21	27.07	62.04	498.6	15.23	147.05	5.62	2.35	2.27	0.56	0.14	29.62
sd	0.89	0.03	20.0	0.39	0.38	2.20	4.5	0.35	1.80	2.92	0.87	7.0	0.34	1.64	0.24	0.28	0.25	0.09	0.01	0.61
S30	103.27	1.93	412.3	20.66	29.48	13.38	118.0	12.24	9.63	23.58	19.84	442.2	10.05	79.85	4.05	5.37	2.44	0.53	0.56	79.56
sd	1.24	0.21	11.7	0.35	0.56	0.69	1.7	0.39	0.66	2.14	0.64	4.3	0.16	1.37	0.11	0.59	0.26	0.04	0.06	3.10
S40	31.42	1.10	311.0	20.12	12.76	9.65	104.6	4.49	2.83	21.30	13.46	352.1	3.78	22.95	1.84	1.75	0.05	0.23	0.02	1.64
sd	1.66	0.08	9.5	0.71	0.55	0.83	2.2	0.10	0.28	2.70	0.29	10.8	0.18	0.69	0.11	0.14	0.01	0.03	0.01	0.30
S36	80.45	2.15	434.4	20.83	36.98	18.31	104.0	13.29	14.27	27.29	40.15	491.2	14.48	155.00	7.45	3.75	1.15	0.23	2.84	59.32
sd	0.83	0.27	5.0	0.16	0.47	0.77	3.6	0.30	0.67	1.13	0.92	2.5	0.28	2.34	0.29	0.53	0.06	0.01	0.15	1.43
S12	61.99	1.25	429.8	21.89	25.50	13.29	142.9	9.08	4.15	80.24	20.55	294.6	10.12	83.29	4.48	2.59	0.16	0.45	0.65	18.13
sd	1.01	0.24	10.1	0.39	0.54	0.66	7.2	0.26	0.29	6.96	0.63	5.6	0.24	1.37	0.09	0.25	0.02	0.13	0.11	0.62
S13	53.76	1.15	479.9	20.51	33.47	16.76	65.2	9.86	3.97	25.00	69.38	3401.9	11.01	422.70	10.15	5.27	0.22	0.56	0.03	3.92
sd	0.56	0.11	10.8	0.34	0.40	1.04	2.5	0.43	0.66	3.49	1.05	33.4	0.28	4.75	0.16	0.27	0.04	0.00	0.01	0.21

µg/g	Sb_2O_5	BaO	La_2O_3	CeO_2	Pr_2O_3	Nd_2O_3	Sm2O3	Eu_2O_3	Gd_2O_3	Tb_2O_3	Dy2O3	Ho_2O_3	Er_2O_3	Tm_2O_3	Yb_2O_3	Lu_2O_3	HfO_2	Au_2O_3	PbO	Bi_2O_3	ThO_2	UO_2
S1	26.74	289.6	11.34	22.44	2.62	9.71	1.95	0.35	1.80	0.30	1.96	0.41	1.26	0.21	1.35	0.21	2.64	0.03	73.53	0.05	4.29	1.67
sd	0.33	1.3	0.09	0.35	0.10	0.21	0.18	0.02	0.15	0.02	0.17	0.03	0.06	0.02	0.09	0.02	0.15	0.01	1.83	0.00	0.14	0.06
S2	44.75	522.9	8.40	16.34	1.96	7.40	1.47	0.35	1.51	0.22	1.57	0.34	1.01	0.16	1.03	0.17	1.92	0.03	5129.58	0.23	2.75	1.22
sd	1.38	13.0	0.29	0.24	0.08	0.43	0.09	0.02	0.09	0.02	0.12	0.02	0.08	0.00	0.02	0.01	0.12	0.01	227.97	0.02	0.08	0.03
S3	13.55	291.3	14.62	29.89	3.33	12.35	2.47	0.43	2.35	0.38	2.62	0.52	1.69	0.27	1.85	0.31	3.92	0.04	975.62	1.34	5.78	2.12
sd	0.68	19.1	0.69	1.25	0.15	0.54	0.19	0.02	0.18	0.01	0.22	0.03	0.12	0.02	0.10	0.01	0.29	0.00	89.21	0.23	0.30	0.11
S14	0.94	345.8	24.86	57.85	6.36	26.19	5.49	1.49	5.41	0.81	4.94	0.91	2.74	0.38	2.43	0.38	7.02	0.03	70.64	0.04	5.00	7.59
sd	0.05	2.9	0.36	0.12	0.08	0.68	0.38	0.09	0.36	0.04	0.25	0.05	0.11	0.03	0.07	0.02	0.24	0.00	4.68	0.00	0.09	0.21
S10	6.65	33.0	1.12	1.88	0.22	0.71	0.28	0.02	0.10	0.02	0.24	0.04	0.15	0.03	0.26	0.04	0.90	0.09	5.21	0.12	0.26	0.19
sd	0.54	2.0	0.09	0.09	0.01	0.09	0.05	0.01	0.00	0.00	0.01	0.00	0.02	0.01	0.03	0.01	0.07	0.01	0.19	0.01	0.03	0.02
S4	28.78	301.4	11.75	22.93	2.70	10.09	1.88	0.32	2.11	0.31	2.15	0.43	1.28	0.15	1.18	0.25	2.58	0.04	67.80	0.05	4.08	1.52
sd	0.17	4.1	0.40	0.36	0.16	0.29	0.18	0.02	0.13	0.02	0.22	0.04	0.13	0.00	0.27	0.03	0.13	0.01	1.08	0.01	0.12	0.05
S11	3.49	329.3	11.14	22.42	2.44	9.23	1.79	0.38	1.71	0.23	1.33	0.31	0.85	0.14	0.82	0.16	7.03	0.05	37.08	0.05	2.58	1.07
sd	0.24	6.3	0.16	0.35	0.08	0.52	0.15	0.05	0.19	0.02	0.12	0.02	0.08	0.01	0.08	0.00	0.40	0.00	4.64	0.01	0.06	0.09
S17	4.62	405.6	14.53	32.28	3.30	12.48	2.43	0.41	2.45	0.41	2.67	0.55	1.71	0.27	1.92	0.25	3.60	0.04	75.67	0.08	5.33	2.08
sd	0.47	16.9	0.34	0.87	0.13	0.30	0.20	0.04	0.07	0.03	0.10	0.05	0.12	0.02	0.17	0.01	0.24	0.00	3.99	0.01	0.07	0.08
S18	4.88	350.9	14.10	29.27	3.20	12.55	2.66	0.50	2.34	0.31	1.78	0.42	1.17	0.19	1.33	0.21	8.80	0.08	9.88	0.04	3.74	1.04
sd	0.29	1.81	0.20	0.26	0.15	0.44	0.11	0.03	0.15	0.03	0.10	0.03	0.12	0.02	0.10	0.01	0.19	0.01	0.25	0.01	0.04	0.06
S15	1.16	347.6	12.03	24.91	2.83	11.15	2.42	0.53	2.04	0.30	1.50	0.31	0.71	0.13	1.01	0.13	5.00	0.07	9.94	0.03	2.65	0.73
sd	0.04	3.1	0.31	0.36	0.15	0.37	0.13	0.03	0.22	0.01	0.10	0.04	0.09	0.01	0.04	0.02	0.12	0.01	0.72	0.01	0.08	0.08
S19	4.99	577.5	12.52	25.41	2.89	10.52	2.10	0.42	1.93	0.33	2.19	0.46	1.43	0.23	1.46	0.23	2.94	0.03	90.65	0.06	4.29	1.68
sd	0.34	9.4	0.40	0.51	0.07	0.55	0.17	0.02	0.12	0.03	0.16	0.02	0.16	0.02	0.07	0.01	0.16	0.01	2.63	0.01	0.13	0.04
S20	0.95	373.4	16.53	33.04	3.67	13.63	2.68	0.37	2.47	0.46	3.16	0.64	2.34	0.31	2.39	0.37	4.92	0.04	28.77	7.12	6.01	2.38
sd	0.06	9.4	0.47	0.82	0.10	0.38	0.21	0.02	0.13	0.05	0.15	0.06	0.17	0.03	0.18	0.05	0.39	0.01	0.63	0.19	0.12	0.12
S21	2.94	205.3	11.19	22.59	2.59	9.96	1.96	0.51	1.82	0.23	1.48	0.28	0.84	0.11	0.81	0.13	2.99	0.04	276.64	0.05	2.20	0.91
sd	0.12	2.6	0.38	0.44	0.10	0.41	0.19	0.05	0.17	0.02	0.13	0.02	0.11	0.01	0.07	0.01	0.15	0.00	8.46	0.01	0.07	0.09
S22	0.96	146.5	10.07	21.76	2.24	8.67	1.41	0.33	1.55	0.22	1.13	0.22	0.69	0.12	0.67	0.13	6.13	0.03	16.22	0.04	2.43	0.70
sd	0.11	3.2	0.24	0.38	0.05	0.33	0.16	0.01	0.03	0.02	0.10	0.01	0.06	0.01	0.05	0.01	0.21	0.01	0.43	0.01	0.07	0.06
S23	1.59	176.6	11.96	24.10	2.52	9.47	1.60	0.40	1.42	0.20	1.15	0.24	0.61	0.10	0.60	0.08	4.59	0.03	19.81	0.04	3.02	0.99

sd	0.18	3.3	0.27	0.25	0.13	0.52	0.16	0.02	0.10	0.01	0.10	0.02	0.03	0.01	0.05	0.01	0.22	0.01	0.62	0.01	0.18	0.05
S38	0.50	159.3	12.49	26.01	2.77	10.47	1.80	0.38	1.82	0.26	1.50	0.31	0.84	0.12	0.89	0.15	5.80	0.03	4.29	0.04	3.19	0.87
sd	0.05	9.8	0.65	1.18	0.10	0.63	0.19	0.02	0.16	0.03	0.09	0.02	0.06	0.01	0.07	0.01	0.21	0.01	0.23	0.01	0.14	0.03
S24	0.86	326.9	10.70	22.32	2.34	8.84	1.59	0.39	1.52	0.21	1.20	0.25	0.76	0.12	0.83	0.12	6.16	0.04	14.41	0.03	2.68	0.74
sd	0.09	3.3	0.15	0.27	0.10	0.32	0.12	0.03	0.14	0.01	0.09	0.02	0.05	0.01	0.09	0.01	0.15	0.01	0.30	0.01	0.10	0.05
S25	3.57	159.7	3.86	7.98	0.87	3.31	0.77	0.14	0.69	0.09	0.52	0.11	0.31	0.04	0.34	0.05	0.51	0.14	66.09	0.20	0.81	0.39
sd	0.24	5.2	0.10	0.17	0.03	0.19	0.04	0.01	0.08	0.01	0.06	0.01	0.03	0.01	0.01	0.01	0.04	0.01	2.98	0.02	0.04	0.02
S27	1.79	195.8	9.49	20.02	2.19	8.82	1.77	0.37	1.50	0.22	1.27	0.24	0.74	0.12	0.62	0.12	3.91	0.02	25.60	0.05	2.11	0.82
sd	0.14	2.3	0.15	0.31	0.06	0.16	0.09	0.03	0.17	0.02	0.12	0.02	0.07	0.01	0.06	0.01	0.21	0.01	0.98	0.01	0.07	0.05
S28	16.47	314.0	14.78	28.81	3.28	12.32	2.34	0.37	2.25	0.38	2.54	0.55	1.65	0.25	1.81	0.29	3.45	0.02	26.73	0.04	5.40	2.07
sd	0.42	7.2	0.49	0.73	0.17	0.45	0.11	0.03	0.18	0.02	0.19	0.04	0.13	0.03	0.08	0.03	0.15	0.01	3.59	0.01	0.15	0.08
S29	1.09	117.8	7.01	15.77	1.67	6.46	1.11	0.24	0.92	0.14	0.76	0.16	0.53	0.07	0.40	0.08	2.88	0.04	11.87	0.06	1.56	0.56
sd	0.10	8.9	0.55	0.55	0.12	0.67	0.13	0.02	0.09	0.01	0.09	0.02	0.01	0.01	0.01	0.01	0.24	0.01	0.93	0.01	0.17	0.03
S34	1.28	123.1	8.12	16.35	1.75	6.73	1.22	0.29	1.08	0.12	0.94	0.14	0.57	0.06	0.47	0.10	3.39	0.02	3.78	0.04	1.95	0.66
sd	0.06	5.1	0.28	0.42	0.02	0.21	0.15	0.03	0.11	0.01	0.06	0.01	0.04	0.01	0.05	0.01	0.19	0.01	0.24	0.01	0.09	0.05
S33	22.39	450.1	17.12	27.16	3.34	12.58	2.19	0.46	2.17	0.33	2.11	0.46	1.34	0.22	1.43	0.23	2.97	0.04	110.76	0.06	4.28	1.72
sd	1.03	11.6	0.30	0.44	0.07	0.62	0.13	0.06	0.24	0.03	0.12	0.03	0.11	0.02	0.10	0.02	0.12	0.01	9.26	0.01	0.13	0.22
S30	2.36	483.7	10.48	20.51	2.34	9.01	1.85	0.42	1.77	0.26	1.51	0.30	0.83	0.13	0.81	0.13	1.73	0.08	195.65	0.35	2.93	1.43
sd	0.20	7.0	0.21	0.32	0.09	0.52	0.16	0.04	0.16	0.02	0.09	0.02	0.06	0.01	0.09	0.03	0.13	0.01	3.24	0.02	0.10	0.06
S40	0.50	137.6	4.16	8.62	0.94	3.54	0.68	0.17	0.66	0.12	0.58	0.11	0.33	0.06	0.31	0.04	0.51	0.02	4.40	0.03	1.24	0.77
sd	0.10	4.4	0.12	0.30	0.06	0.20	0.07	0.02	0.08	0.01	0.05	0.01	0.02	0.00	0.02	0.00	0.05	0.01	0.30	0.00	0.06	0.02
S36	4.52	304.7	17.86	38.55	4.37	16.64	3.24	0.62	2.90	0.38	2.27	0.47	1.35	0.18	1.31	0.17	3.29	0.08	92.16	0.17	5.70	2.20
sd	0.23	3.6	0.33	0.81	0.14	0.81	0.13	0.06	0.11	0.03	0.13	0.04	0.14	0.01	0.10	0.02	0.11	0.01	1.39	0.02	0.06	0.09
S12	1.14	218.6	10.91	22.26	2.51	10.21	1.96	0.44	1.90	0.25	1.57	0.29	0.86	0.11	0.83	0.12	1.77	0.03	39.43	0.08	3.08	1.45
sd	0.04	2.2	0.26	0.22	0.08	0.35	0.25	0.04	0.15	0.02	0.16	0.01	0.07	0.02	0.06	0.01	0.18	0.01	2.21	0.01	0.13	0.04
S13	0.89	343.2	14.93	29.83	3.24	11.98	2.19	0.47	2.03	0.27	1.61	0.34	1.05	0.17	1.12	0.18	8.41	0.02	6.30	0.05	3.81	1.04
sd	0.11	4.0	0.21	0.49	0.11	0.29	0.19	0.02	0.27	0.02	0.12	0.02	0.05	0.01	0.13	0.01	0.15	0.01	0.24	0.01	0.08	0.05

1.4 References

Kubelka P. and F. Munk (1931) Ein Beitrag zur Optik der Farbanstriche. Z. Technol. Phys. 12; pp. 593–620.

Nassau K. (1983) The Physics and Chemistry of Color, the Fifteen Causes of Color, New York, Wiley.

Orsega E.F., Caminneci V., Panighello S., Rizzo M.S. (2013) Physicochemical analysis of medieval glass from 14th-16th centuries found in the Sciacca Castle site (Sicily) by LA-ICP-MS and UV-VIS Reflectance Spectroscopy – Proceedings of the 16th Symposium on Mediterranean Archaeology, Florence, Italy, 1–3 March 2012 edited by Luca Bombardieri, Anacleto D'Agostino, Guido Guarducci, Valentina Orsi and Stefano Valentini. *BAR International Series*, 2581 (II), Oxford University Press.

Panighello S., Parello M.C., Orsega E.F. (2013) Investigation on medieval glass from Poggio Diana Castle (Sicily) by LA-ICP-MS and UV-VIS Reflectance Spectroscopy – Proceedings of the 16th Symposium on Mediterranean Archaeology, Florence, Italy, 1–3 March 2012, edited by Luca Bombardieri, Anacleto D'Agostino, Guido Guarducci, Valentina Orsi and Stefano Valentini. *B.A.R. International Series* 2581 (II), Oxford University.

Schreurs J.W.H. and Brill R.H. (1984) Iron and sulphur related colors in ancient glasses, Archaeometry 26; pp. 199-209.

Weyl W.A. (ed.) (1953) Coloured Glasses. Society of Glass Technology, Sheffield.

Appendix 2: Development of artificial aging and measurement protocols for glass

2.1. Introduction

This research is focused on the development of an alternative method to study the chemical stability of glass; especially the chemical stability of inert glass is difficult to study with conventional methods. The protocol is based on artificial aging of a piece of the glass in an aqueous solution by microwave-assisted leaching under high-temperature/pressure regimes. Various pH values will be used to target different chemical stability criteria, i.e. leaching via ion exchange with H_3O^+ ions or dissolution of the silica bonds at high pH values (see also Chapter 1).

By analyzing the leachates and the leached glasses separately by conventional solution ICP-OES and -MS and depth profiling via LA-ICP-MS, respectively, a better understanding of the durability (leaching kinetics) of various glass compositions as a function of the surrounding environment can be obtained.

2.2. Samples

Several industrial glasses (cubes of 1x1x1 cm) with a range of chemical compositions (see Table 2.1) were selected for this study. They are soda-lime-silica glasses used in the production of hollow glass (containers, bottles) as T1 and T2 and varieties of glass used for tableware and manual artistic production (lead crystal and Venetian c*ristallo).* Technical glasses like neutral pharmaceutical glass were also included. They are borosilicate glasses containing significant amounts of boric oxide, aluminium oxide alkali and/or alkaline earth oxides and defined as Type I glass[♣]. Due to its composition neutral glass has a high hydrolytic resistance and a high thermal shock resistance. One is amber colored and may be used for substances known to be light-sensitive.

The chemical durability of these kind of glasses should be unquestionable due to their connection with human health, e.g., lead can migrate from crystal glass containers to food and drinks in contact with them (Hynesa and Jonsonb, 1997; Ahmed *et al*., 1998). Also the corrosion of ampoules in the presence of some pharmaceutical compounds still remains an unsolved problem (Iacocca *et al.*, 2010).

A further topic of study concerns the durability of *cristallo* glass (different from the above-cited lead crystal glass) produced in Venice from the 15th century till today. It is a high-quality colorless glass, but rather unstable (low durability) due to low concentrations of stabilizing components. The lack of satisfactory studies on the chemical stability of *cristallo* glass produced today makes it an interesting subject of investigation, the more that we can compare the results obtained with similar glass from decades or centuries ago for crizzling phenomena (Brill, 1975; Koob, 2006).

[♣]For the purposes of pharmaceutical packaging, three types of glass are defined by USP General Chapter <660> Containers—Glass. Type I (borosilicate glass) is suitable for most products for injectable and noninjectable use. Type II is treated soda-lime glass, and Type III is soda-lime glass on the basis of the hydrolytic resistance of the glass.

2.2. Accelerated microwave aging process

Artificial aging was achieved through microwave-assisted leaching under high temperature/pressure regimes and various pH environments (see Table 2.2). Leaching occurs in a controlled manner using sealed Teflon vessels in a Milestone microwave (ETHOS 1 - Advanced Microwave Digestion Labstation) and by monitoring and controlling the temperature and the pressure in the vessels.

Before microwave aging the glass samples were weighed and then placed in the teflon vessels with 10 ml 0.01 mol l^{-1} of HNO_3 (Experiment 1) or 10 ml of 0.01 mol l^{-1} LiOH (Experiment 2) at a temperature of 121^{o}C for 5 hours. This temperature was chosen according to the ISO norm for the chemical stability of glass (ISO 719: 1985 and ISO 720: 1985). Different kinds of samples with different kinds of chemical resistance were selected for the two experiments (see Table 2.2). Neutral glasses (inert pharmaceutical glasses) were not considered in the first experiment due to their great resistance to hydrolytic attack. Conversely, Venetian *cristallo* glasses were not considered in the second experiment as being too "weak" for these aggressive conditions.

After microwave aging the leached glasses were weighed again and then analyzed by depth profiling for up to 20 elements via LA-ICP-MS (see Chapter 3) and the leachates by conventional solution ICP-MS/ICP-OES (for the main elements as Si, B, Na, K and Pb).

Table 2.1. Chemical composition (wt %) and relative standard deviation (RSD, %) of different current-day industrial glass investigated in this study (n=3).

	Cristallo		**T2**		**T1**		**Lead Crystal**		**Neutral**		**Neutral**	
Glass type	Muranese		Soda lime		Soda lime				Borosilicate		Borosilicate	
Uses	Table, artistic		Bottle		Bottle		Table ware		USP Type I*		USP Type I*	
Color	Transparent not colored		Transparent not colored		Transparent not colored		Transparent not colored		Transparent not colored		Transparent Amber	
		RSD,%	wt %	RSD,%	wt %	RSD,%	wt %	RSD,%	wt %	RSD,%	wt %	RSD,%
Na_2O	14.59	3.47	12.64	0.04	13.37	0.93	3.45	0.14	7.71	1.96	6.33	0.12
MgO	0.04	1.83	0.55	0.81	1.76	0.75	0.01	3.57	0.02	3.87	0.04	0.46
Al_2O_3	0.73	3.06	1.78	0.06	2.27	0.65	0.04	1.67	6.03	1.03	5.08	2.05
SiO_2	73.02	0.47	72.65	0.02	71.82	0.07	57.27	1.95	70.59	0.15	73.81	0.06
P_2O_5	0.01	1.04	0.02	0.01	0.02	3.44	0.01	9.51	0.03	2.22	0.03	2.65
K_2O	3.95	0.57	1.17	0.49	0.04	6.24	11.85	3.01	1.07	0.53	1.33	0.27
CaO	6.77	2.22	11.07	0.13	10.67	1.38	0.06	17.38	1.26	1.28	0.88	0.37
MnO	0.01	3.71	0.01	3.33	0.01	4.05	0.01	17.04	0.01	0.23	0.01	0.52
Fe_2O_3	0.02	7.89	0.08	1.95	0.05	0.81	0.01	11.88	0.04	4.79	0.82	3.37
CuO	0.01	2.56	0.01	0.01	0.01	1.28	0.01	7.67	0.01	3.85	0.01	3.26
ZnO	0.01	5.77	0.01	7.85	0.01	4.77	1.14	2.76	0.01	15.19	0.01	18.21
SnO_2	0.01	37.34	0.01	0.85	0.01	8.89	0.01	14.94	0.01	4.05	0.01	14.44
Sb_2O_5	0.87	2.73	0.01	0.01	0.01	5.53	0.48	2.39	0.01	11.91	0.01	7.45
BaO	0.01	4.53	0.03	0.97	0.01	0.65	0.01	2.34	1.13	0.04	1.14	0.11
PbO	0.01	0.79	0.01	1.62	0.01	1.16	25.73	3.08	0.01	17.87	0.01	6.25
B_2O_3	nd	nd	nd	nd	0.01	5.28	nd	nd	11.83	1.78	10.52	0.59

Table 2.2. Conditions for accelerated leaching of different types of glass (Table 2.1).
Abbreviations: C=Venetian *cristallo*; L= crystal lead; T= soda lime bottle (T1 and T2);
N1= not colored neutral; N2=amber neutral.

Experiment	*pH solution*	*Time*	*Temperature*	*Energy (microwave digestion unit)*	*Glass types*
1	pH=2 (HNO_3)	5h	121°C	1200W	C, L, T
2	pH=12 (LiOH)	5h	121°C	1000W	L, T, N1, N2

2.3. Glass stability results

Preliminary results for leaching of Na in Experiments 1 and 2 are given in Tables 2.3 and 2.4; work is in progress to get a full picture of glass deterioration related to element, deterioration conditions, depth of leaching, degree of corrosion, etc.

Table 2.3. Preliminary results for Experiment 1 (Table 2.2) for the elements leached out of the glass samples described in Table 3.1, expressed in amount per area (µg cm^{-2}). nd =not detected (by ICP-MS).

	N1	**N2**	**L**	**T1**	**T2**	**C**
B (µg cm^{-2})	0.18	0.11	nd	nd	nd	0.11
sd	0.03	0.03	nd	nd	nd	0.05
Na (µg cm^{-2})	0.58	0.383	7.01	3.15	2.84	39.65
sd	0.03	0.11	0.59	0.665	0.39	7.89
Al (µg cm^{-2})	0.13	0.07	nd	0.055	0.04	nd
sd	0.03	0.02	nd	0.01	0.01	nd
K (µg cm^{-2})	0.133	0.13	19.28	nd	0.12	6.92
sd	0.05	0.05	12.07	nd	0.03	1.78
Ca (µg cm^{-2})	0.07	0.05	nd	0.37	0.37	0.62
sd	0.01	0.01	nd	0.11	0.06	0.17
Pb (µg cm^{-2})	nd	nd	9.74	nd	nd	nd
sd	nd	nd	1.86	nd	nd	nd
Zn (µg cm^{-2})	nd	nd	0.31	nd	nd	nd
sd	nd	nd	0.02	nd	nd	nd
Mg (µg cm^{-2})	nd	nd	nd	0.08	nd	nd
sd	nd	nd	nd	0.02	nd	nd

Table 2.4. Preliminary results for Experiment 2 (Table 2.2) studying the elements dissolved in the glass samples, expressed in amount per area (μg cm^{-2}). nd = not detected (by ICP-OES).

Samples	B (ppm)	K (ppm)	Na (ppm)	Pb (ppm)	Si (ppm)
T2	u.v.	u.v.	0.799	u.v.	37.738
L	u.v.	4.938	0.084	5.235	8.519
L	u.v.	4.349	0.065	5.006	7.445
N1	2.071	0.502	0.229	u.v.	22.531
N2	3.196	0.938	0.326	u.v.	36.770
N2	2.765	0.836	0.273	u.v.	32.404
N1	2.934	0.672	0.331	u.v.	31.165
T1	0.030	u.v.	0.654	u.v.	35.058
T1	u.v.	0.603	0.468	u.v.	26.044

In Figures 2.1 and 2.2 the leachability of Na in Experiment 1 and the dissolution of Si in Experiment 2, respectively, is expressed as the percentage lost from the glass.

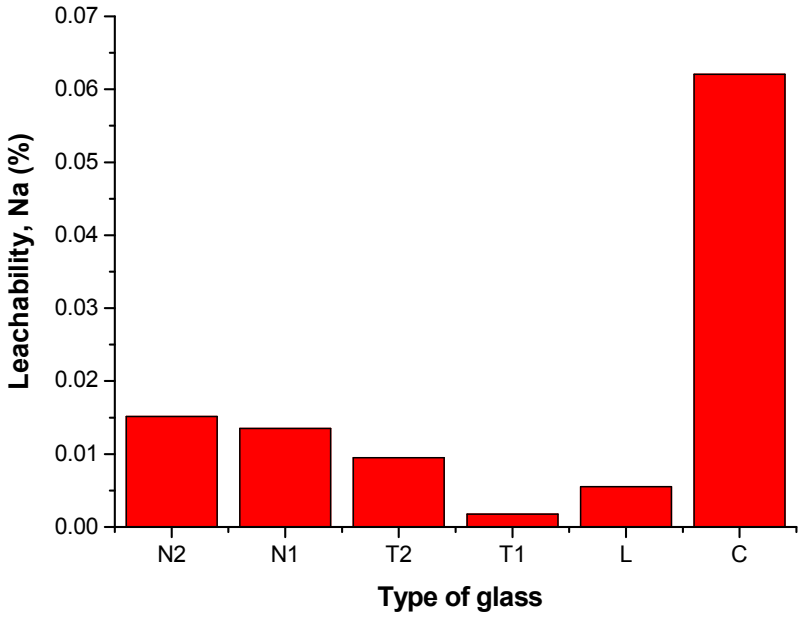

Figure 2.1. Leachability of Na (in %) for the different glasses subjected to conditions in Experiment 1 (Table 22.2).

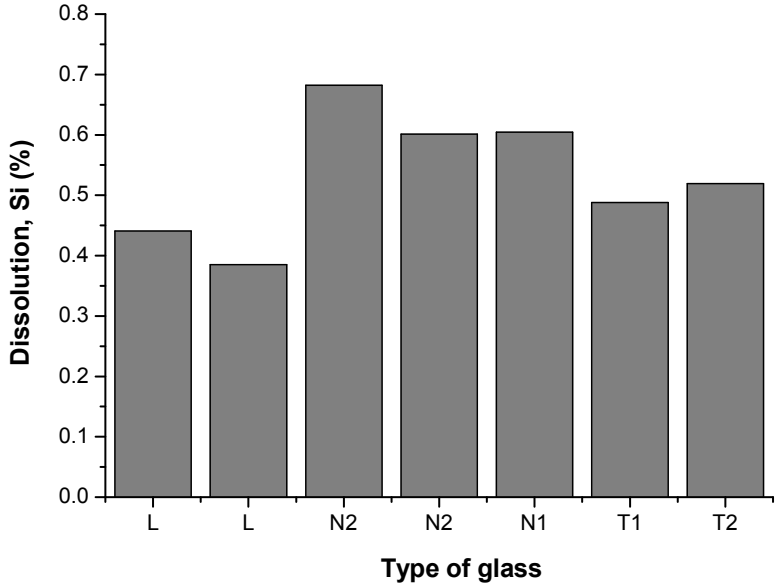

Figure 2.2. Dissolution of Si (in %) for the different glasses subjected to conditions in Experiment 2 (Table 2.2).

2.4. Discussion

The main elements leached from the Venetian *cristallo* glass (Na, K, Ca) (Table 2.3) indicate significant losses in the surface layer compared to the other glasses; however, when the leached glass is analyzed by LA-ICP-MS depth profiling it becomes clear that only the utmost surface layer (< 20 µm) has lost certain elements (illustrated for Na_2O in Figure 22.3), although K_2O and CaO were leached out to a lesser extent (data not shown). Due to depletion of Na_2O in the outer glass layer the SiO_2 concentration increases since the total elemental oxide concentration stays 100 wt % in the sum normalization calibration protocol used in the quantification. However, in Chapter 3 it is explained that the increase in the SiO_2 concentration can be associated with a volumetric mass density decrease towards the outer glass layer.

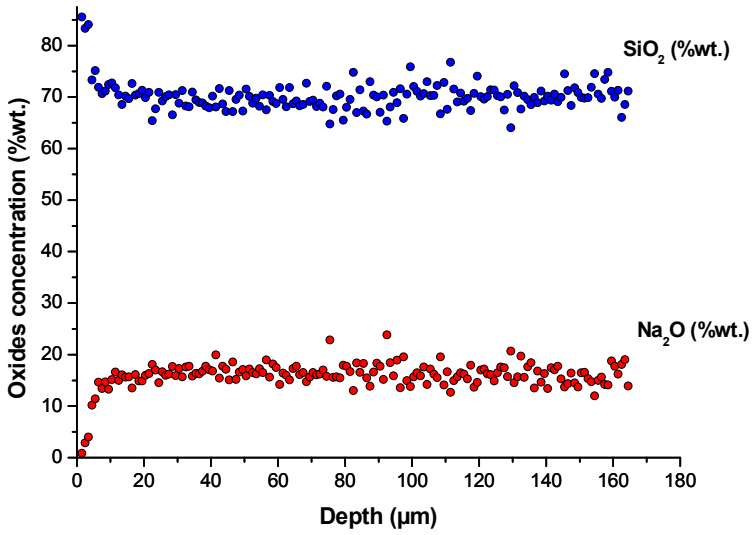

Figure 2.3. SiO_2 and Na_2O depth profiles in the glass after microwave leaching (Experiment 1).

From SEM-EDX analysis (Figure 2.4) it is evident that the microwave accelerated leaching process has led to heterogeneous deposits of Si-Ca-K-Na on the surface of the glass after degradation.

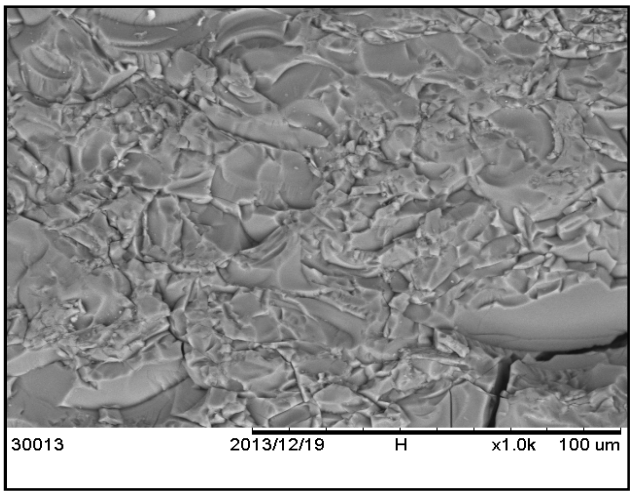

Figure 2.4. Morphology of the deposits observed on the glass surface after the microwave leaching process assessed by SEM-EDX.

2.5. References

Ahmed A.A., Youssof I.M., Abbas A.F. and Abou Eleinen O. (1998) Inhibition of Pb-leaching from lead crystal glass by coating with films preparated by the sol-gel method; Journal of the Sol-Gel Science and Technology, 13; pp. 753-756.

Brill R. H. (1975) Crizzling - A Problem in Glass Conservation; Conservation in Archaeology and the Applied Arts, Stockholm Congress; pp. 121-134.

Hynesa Michael J. and Jonson B. (1997) Lead, Glass and the Environment; Chemical Society Reviews; pp. 133-146.

Koob Stephen P. (2006) Conservation and Care of Glass Objects, London : Archetype Publications.

Iacocca Ronald G., Toltl N., Allgeier M., Bustard B., Dong X., Foubert M., Hofer J., Peoples S. and Shelbourn T. (2010) Factors Affecting the Chemical Durability of Glass Used in the Pharmaceutical Industry, American Association of Pharmaceutical Scientists, 11; pp. 1340-1349.